The Extended Discontinuous Galerkin Method for Evaporation and Contact Lines

Zur Erlangung des akademischen Grades Doktor-Ingenieur (Dr.-Ing.)
Genehmigte Dissertation von Matthias Rieckmann aus Seligenstadt
Tag der Einreichung: 20.07.2024, Tag der Prüfung: 29.10.2024

1. Gutachten: Prof. Dr.-Ing. M. Oberlack
2. Gutachten: Prof. Dr.-Ing. P. Stephan
Darmstadt, Technische Universität Darmstadt

TECHNISCHE UNIVERSITÄT DARMSTADT

Fachbereich Maschinenbau
Fachgebiet für Strömungsdynamik

The Extended Discontinuous Galerkin Method for Evaporation and Contact Lines

Genehmigte Dissertation von Matthias Rieckmann

Tag der Einreichung: 20.07.2024
Tag der Prüfung: 29.10.2024

Darmstadt, Technische Universität Darmstadt

Bitte zitieren Sie dieses Dokument als:
URN: urn:nbn:de:tuda-tuprints-286262
URL: https://tuprints.ulb.tu-darmstadt.de/id/eprint/28626
DOI: https://doi.org/10.26083/tuprints-00028626
Jahr der Veröffentlichung auf TUprints: 2024

Dieses Dokument wird bereitgestellt von tuprints,
E-Publishing-Service der TU Darmstadt
https://tuprints.ulb.tu-darmstadt.de
tuprints@ulb.tu-darmstadt.de

Erklärungen laut Promotionsordnung

§ 8 Abs. 1 lit. c PromO

Ich versichere hiermit, dass die elektronische Version meiner Dissertation mit der schriftlichen Version übereinstimmt.

§ 8 Abs. 1 lit. d PromO

Ich versichere hiermit, dass zu einem vorherigen Zeitpunkt noch keine Promotion versucht wurde. In diesem Fall sind nähere Angaben über Zeitpunkt, Hochschule, Dissertationsthema und Ergebnis dieses Versuchs mitzuteilen.

§ 9 Abs. 1 PromO

Ich versichere hiermit, dass die vorliegende Dissertation – abgesehen von den in ihr ausdrücklich genannten Hilfen – selbstständig verfasst wurde und dass die „Grundsätze zur Sicherung guter wissenschaftlicher Praxis an der Technischen Universität Darmstadt“ und die „Leitlinien zum Umgang mit digitalen Forschungsdaten an der TU Darmstadt“ in den jeweils aktuellen Versionen bei der Verfassung der Dissertation beachtet wurden.

§ 9 Abs. 2 PromO

Die Arbeit hat bisher noch nicht zu Prüfungszwecken gedient.

Darmstadt, 20.07.2024

M. Rieckmann

Abstract

In many technical and industrial applications, the wetting of surfaces by various fluids plays a decisive role. The interplay of wetting and evaporation processes, for example in drying processes, is also of particular importance. A good understanding of the underlying physical principles is therefore crucial in order to precisely control these processes.

In this work, a numerical solver based on the extended discontinuous Galerkin (XDG) method is developed for the calculation of multiphase flows with evaporation and contact lines. The basis functions used, which are adapted to the phase boundaries, allow the highly accurate representation of the solution fields for pressure, velocity and temperature. By using a sharp interface model and corresponding jump conditions, discontinuities in the solution fields can be represented directly at the interfaces. The interfaces themselves are represented in the solver by the level set method. The movement of the contact line is enabled and modeled by using the generalized Navier boundary condition (GNBC).

The developed solver is then used to simulate various multiphase problems. When investigating the flow through the nip between two printing cylinders, the behavior of the solution fields with vanishing nip width and the occurrence of viscous vortices in the nip can be mapped. The implementation of the coupled momentum and energy balance, including evaporation at the phase boundary, is then verified with established test cases. In investigations of the moving contact line, the behavior of the contact line in the implementation can then be confirmed according to the boundary conditions used. In particular, singular behavior can be observed in the solution fields when unsuitable boundary conditions are employed. This is of particular importance when considering contact lines and evaporation at the same time, where a contradiction can be identified in the model used. This inconsistency leads to a drastic reduction in the convergence order of the method. By using slip on the phase boundary, a possible resolution of the contradiction is then tested, and the convergence order is partially restored. Finally, a real experiment is considered in a highly simplified form. During the dewetting of a heated wall pulled out of a liquid bath, a reduction of the liquid film on the wall can be observed with increasing evaporation.

The XDG method extended in this work for evaporation and contact line problems allows a highly accurate simulation of the pressure, velocity and temperature fields, especially in the vicinity of interfaces and contact lines. However, this higher order method is very sensitive to contradictory boundary conditions or irregular solutions. Nevertheless, this sensitivity allows the method to be used to develop and test novel models, especially for modeling contact line motion.

Zusammenfassung

In vielen technischen und industriellen Anwendungen spielt die Benetzung von Oberflächen durch verschiedene Fluide eine entscheidende Rolle. Von besonderer Bedeutung ist dabei auch das Zusammenspiel von Benetzungs- und Verdampfungsvorgängen, beispielsweise bei Trocknungsprozessen. Ein gutes Verständnis der zugrundeliegenden physikalischen Prinzipien ist daher entscheidend, um diese Prozesse präzise zu kontrollieren.

Im Rahmen dieser Arbeit wird ein numerischer Löser auf Basis der erweiterte diskontinuierliche Galerkin (XDG) Methode zur Berechnung von Mehrphasenströmungen mit Verdampfung und Kontaktlinien entwickelt. Die dazu verwendeten, an die Phasengrenzen angepassten Basisfunktionen erlauben die hochgenaue Darstellung der Lösungsfelder für Druck, Geschwindigkeit und Temperatur. Durch die Verwendung eines scharfen Interface Modells und entsprechenden Sprungbedingungen können so insbesondere Unstetigkeiten in den Lösungsfeldern direkt an den Grenzflächen abgebildet werden. Die Grenzflächen selbst werden in dem Löser durch die Level Set Methode dargestellt. Die Bewegung der Kontaktlinie wird durch die generalisierte Navier Randbedingung (GNBC) ermöglicht und modelliert.

Mit dem entwickelten Löser erfolgt dann die Simulation verschiedener Mehrphasenprobleme. Bei der Untersuchung der Strömung durch den Spalt zwischen zwei Druckwalzen kann das Verhalten der Lösungsfelder bei verschwindender Spaltbreite, sowie das Auftreten von viskosen Wirbeln im Druckspalt, abgebildet werden. Anschließend wird die Implementierung von Verdampfung an der Phasengrenze mit etablierten Testfällen verifiziert. Bei Untersuchungen der bewegten Kontaktlinie kann dann das Verhalten der Kontaktlinie in der Implementierung entsprechend der verwendeten Randbedinungen bestätigt werden. Insbesondere kann singuläres Verhalten in den Lösungsfeldern bei der Verwendung von ungeeigneten Randbedingungen beobachtet werden. Von besonderer Bedeutung ist dies bei der gleichzeitigen Berücksichtigung von Kontaktlinien und Verdampfung, bei welcher ein Widerspruch in dem verwendeten Modell festgestellt werden kann. Dieser führt zu einer drastischen Reduktion der Konvergenzordnung des Verfahrens. Durch die Verwendung von Schlupf auf der Phasengrenzfläche wird dann eine mögliche Auflösung des Widerspruchs getestet, und es gelingt die Konvergenzordnung zum Teil wiederherzustellen. Zuletzt folgt die Betrachtung eines realen Experiments in stark vereinfachter Form. Bei der Entnetzung einer aus einem Flüssigkeitsbad herausgezogenen, beheizten Wand kann so eine Reduktion des Flüssigkeitsfilms auf der Wand bei zunehmender Verdampfung beobachtet werden.

Die in dieser Arbeit für Verdampfungs- und Kontaktlinienprobleme erweiterte XDG Methode erlaubt eine hochgenaue Simulation von Druck-, Geschwindigkeits- und Temperaturfeldern, insbesondere in der Nähe von Grenzflächen und Kontaktlinien. Diese Methode höherer Ordnung ist allerdings sehr sensitiv gegenüber widersprüchlichen Randbedingungen beziehungsweise irregulären Lösungen. Dies ermöglicht jedoch eine Verwendung der Methode um neuartige Modelle, vor allem zur Modellierung der Kontaktlinienbewegung, zu entwickeln und zu erproben.

Danksagung

Als ich meine Arbeit an der Universität zu Beginn der Corona Pandemie begonnen habe, wusste ich noch nicht, welche enorme mentale Belastung die fordernde Forschung und digitale Isolation für mich darstellen würde. In dieser Anfangszeit und bis Zuletzt konnte ich mich vollkommen auf meine Familie verlassen, die mein sicherer Hafen war und ist. Neben meinen Eltern und Geschwistern möchte ich meinen besonderen Dank auch meiner Tante aussprechen. Mehrfach hast du mich bei dir aufgenommen und mir dein Heim als Refugium zur Verfügung gestellt.
Der Austausch mit meinen Weggefährten im SFB, die wie ich an numerischen Projekten arbeiteten, war für mich sehr wichtig. Vor allem Suraj und Francisco möchte ich für die Gespräche und Späße, die den oft aufkommenden Frust entschärften, danke sagen. Überhaupt möchte ich mich gerne bei den Mitgliedern und Leitungsteam des SFB 1194 bedanken, die stets bereit waren zu unterstützen und nicht zuletzt meine Arbeit überhaupt erst ermöglichten.
An dieser Stelle kann ich kaum untertreiben, wenn ich hervorheben welche enorme Stütze meine Kollegen am FDY für mich waren. Besonders herzlich bedanken möchte ich mich bei - Schahin, dessen aufbauenden Worte mir immer wieder Mut gemacht haben, wenn es schleppend voranging - Simon, die vielen Bahnen, die wir im Schwimmbad oder auf dem Rad gezogen haben, waren für mich ein allzu notwendiger Ausgleich. Ich freue mich, dass daraus in den letzten Jahren eine für mich sehr wertvolle Freundschaft entstanden ist - Martin, der mich in einer Art Mentoring mit einem offenen Ohr und gutem fachlichen Rat begleitet hat - Lauritz, mit dem ich die längste Zeit gemeinsam die TM1 und insbesondere die verrückten Klausuren während Corona betreut und so manchen Frust geteilt habe. Ebenfalls danke sagen möchte ich auch meinen Betreuern. Florian der mich als Projektverantwortlicher anleitete und dessen Tür stets offenstand, wenn ich Bugs oder fachliche Probleme diskutieren wollte. Herr Professor Oberlack, der mich immer wieder ermutigte auch über den Tellerrand hinauszuschauen und dessen anhaltende Begeisterung für die Forschung auch für mich ein großer Motivationsschub war.
Vielen Dank auch an meine Freunde, die mir halfen, mich zu erden. Zu der Zeit, in der man sich kaum mit jemandem treffen durfte, halfen mir die Spaziergänge mit David nicht durchzudrehen. Mit Oliver ließ ich beim regelmäßigen Zocken Dampf ab und er war auch bereit meinen Nerdtalk anzuhören, wenn mir ein Thema nicht aus dem Kopf ging.
Viel Unterstützung erfuhr ich ebenfalls aus meiner Kirchengemeinde. Roland hat sich Zeit für meine Anliegen genommen und ist ein gutes Vorbild für mich. In meinem Hauskreis konnte ich mich austauschen und Fürbitte empfangen. Leo nahm mich in den Kreis seiner Familie auf, ihr seid unersetzlich für mich geworden. Bedanken möchte ich mich auch bei Rocksolid. Zeit mit euch zu verbringen, bereitet mir große Freude und erfrischt meinen Geist, was so manchen Freitag Abend dringend notwendig war.
Psalm 40,3 - Danke!

Funding

I kindly acknowledge the financial support by the Deutsche Forschungsgemeinschaft (DFG, German Research Foundation) – Project-ID 265191195 – Collaborative Research Center 1194 (CRC 1194) 'Interaction between Transport and Wetting Processes', project B06. Additionally, this work is supported by the Graduate School CE within the Centre for Computational Engineering at TU Darmstadt.

Data availability

The simulation software *BoSSS* further developed and used in this work is open-source and available at Kummer et al. (2023). The raw simulation results themselves are compiled in several data sets accessible at Rieckmann (2024), sorted by the section they appear in. The data for Section 5.1 and Section 6.4 is published separately and available at Rieckmann et al. (2023d) and Rieckmann et al. (2023b).

Contents

List of Figures

List of Tables

List of symbols

a	Capillary length, [m]
$\hat{c}$	Specific heat capacity, [J/(kg K)]
$\boldsymbol{f}$	Volume force, [N/kg]
$\boldsymbol{g}$	Gravitational acceleration, $\left[\mathrm{m/s^2}\right]$
$\hat{h}$	Specific enthalpy, [J/kg]
h	Cell size
$\hat{h}_{vap}$	Specific enthalpy of evaporation, [J/kg]
k	Polynomial order
$\hat{k}$	Specific heat conductivity, [W/(m K)]
$\dot{m}$	Mass flux, $\left[\mathrm{kg/(m^2\,s)}\right]$
m	Mass, [kg]
$\boldsymbol{n}$	Unit normal vector
$\hat{\boldsymbol{n}}^L$	Contact line normal vector, tangential to the (rigid) fluid-solid interface
$\boldsymbol{n}^\Gamma$	Edge normal vector
$\boldsymbol{n}^L$	Contact line normal vector, tangential to the fluid-fluid interface
$\boldsymbol{n}^\Sigma$	Interface normal vector
$\boldsymbol{n}^{\partial\Omega}$	Boundary normal vector
$\boldsymbol{n}^{(i)}$	Normal vector to boundary of phase $\Omega^{(i)}$
$\boldsymbol{n}^{(i,j)}$	Normal vector to boundary of the interface between phases $\Omega^{(i)}, \Omega^{(j)}$
$\boldsymbol{p}$	Momentum, [kg m/s]
p	Pressure, [Pa]
$\boldsymbol{q}$	Heat flux, $\left[\mathrm{W/m^2}\right]$
q	Continuity equation test function
$q_{\partial\Omega}$	Boundary heat flux, $\left[\mathrm{W/m^2}\right]$
r	Heat equation test function
$\hat{r}$	Radiant energy transfer, or volumetric energy sink/source, [W/kg]
$\boldsymbol{s}$	Boundary velocity, [m/s]
$\boldsymbol{s}^{(i)}$	Boundary velocity of $\partial\Omega^{(i)}$, [m/s]
$\boldsymbol{s}^{(i,j)}$	Boundary velocity of $\partial\Sigma^{(i,j)}$, [m/s]
t	Time coordinate, [s]
$\boldsymbol{t}$	Unit tangent vector
$\boldsymbol{t}^L$	Contact line tangent vector
$\boldsymbol{t}^\Sigma$	Interface tangent vector, at contact lines equal to $\boldsymbol{n}^L$

$\hat{u}$	Specific inner energy, [J/kg]
$\boldsymbol{u}$	Velocity, [m/s]
$\boldsymbol{u}^L$	Contact line velocity, [m/s]
$\boldsymbol{u}_{\text{ext}}$	Extension velocity, [m/s]
$\boldsymbol{u}^\Sigma$	Interface velocity, [m/s]
$\boldsymbol{v}$	Momentum eqution test function
$\boldsymbol{x}$	Spatial (cartesian) coordinate vector, [m]
$\boldsymbol{z}$	Solution vector
Ca	Capillary number
E	Energy, [J]
$\boldsymbol{F}$	Force, rate of momentum transmission, [N]
Fr	Froude number
K	Computational cell
K^{X}	Cut-cell
$K^{\text{X}}_{,\mathfrak{s}}$	Phase-cell of species $\mathfrak{s}$
L	Contact line(s)
L_Σ	Interfacial slip length, [m]
$L^{(i,j,k)}$	Contact line between phases $\Omega^{(i)}$, $\Omega^{(j)}$ and $\Omega^{(k)}$
M	Mobility coefficient, $\left[\text{m}^2/\text{s}\right]$
N_K	Number of cells
N_Γ	Number of edges
N_k	Number of polynomial basis functions per cell
N_Ω	Number of phases
$\mathbf{P}$	Projection tensor
P	Mechanical power, [W]
$\mathbf{P}^L$	Contact line normal projection tensor
$\mathbf{P}^\Sigma$	Interface normal projection tensor
$\mathbf{P}^{\partial\Omega}$	Boundary normal projection tensor
$\mathbf{P}^{\boldsymbol{t}}$	Contact line tangential projection tensor
Q	Rate of energy transmission, [W]
Re	Reynolds number
$\mathbf{T}$	Stress tensor, [Pa]
T	Temperature, [K]
$T_{\partial\Omega}$	Boundary temperature, [K]
T_{sat}	Saturation temperature, [K]
We	Weber number
β	Friction coefficient, [Pa s/m]
β_L	Contact line friction coefficient, $\left[\text{Pa s/m}^2\right]$
β_N	Wall normal friction coefficient, [Pa s/m]
β_T	Thermal resistance, $\left[\text{W}/(\text{m}^2\,\text{K})\right]$
β_Σ	Interfacial friction coefficient, [Pa s/m]
ϵ	Volume viscosity, [Pa s]
η	Numerical penalty parameter
γ	Chemical potential
κ	Mean curvature, [1/m]
$\hat{\lambda}$	Bulk viscosity, [Pa s]
μ	Shear viscosity, [Pa s]

ρ	Density, $[\mathrm{kg/m^3}]$
σ	Surface tension, $[\mathrm{N/m}]$
$\boldsymbol{\tau}$	Traction (stress) vector, [Pa]
$\boldsymbol{\tau}_{\partial\Omega}$	Boundary stress, [Pa]
θ	Contact angle, $[^\circ]$
θ_{adv}	Advancing contact angle, $[^\circ]$
θ_{rec}	Receding contact angle, $[^\circ]$
θ_{stat}	Static contact angle, $[^\circ]$
φ	Level set field or phase field
$\boldsymbol{\xi}$	Reference space coordinate vector
ξ	Gradient energy coefficient, or transition length, [m]
Δt	Time-step size, [s]
Γ	Computational edge
Γ_{D}	Edge with Dirichlet B.C.
Γ_{int}	Inner edge
Γ_{N}	Edge with Neumann B.C.
Γ_{out}	Outer (boundary) edge
Γ_{R}	Edge with Robin B.C.
Ω	Physical or computational domain
$\Omega^{(i)}$	Domain of phase (i)
Φ	Basis function
$\boldsymbol{\Phi}$	Vector of basis functions
Φ^{X}	Cut-cell basis function
$\boldsymbol{\Phi}^{\mathrm{X}}$	Vector of cut-cell basis functions
Ψ^{L}	Arbitrary contact line scalar/vector/tensor quantity
Ψ^{Σ}	Arbitrary surface scalar/vector/tensor quantity
$\Psi^{(i)}$	Arbitrary bulk scalar/vector/tensor quantity in phase $\Omega^{(i)}$
$\Psi^{(i,j)}$	Arbitrary interface scalar/vector/tensor quantity on $\Sigma^{(i,j)}$
Σ	Phase interface
$\Sigma^{(i,j)}$	Interface between phases $\Omega^{(i)}$ and $\Omega^{(j)}$
$\partial\Omega$	Domain boundary
$\mathfrak{s}$	Species/phase identifier
$\mathfrak{A}$	Domain of phase A - usually fluid
$\mathfrak{B}$	Domain of phase B - usually vapor/gas
$\mathbb{P}_k^C$	Cell local polynomial space of order k
$\mathfrak{K}_h$	Numerical mesh
$\mathfrak{K}_h^{\mathrm{X}}$	Numerical cut-cell mesh
$\mathbb{P}_k$	Global polynomial space of order k
$\mathbb{P}_k^{\mathrm{X}}$	Broken cut polynomial space of order k
$\mathfrak{S}$	Domain of phase S - usually solid
$\mathbb{V}_{\boldsymbol{k}}^{\mathrm{X}}$	Broken cut solution space
$\langle(1),(2)\rangle_{L^2(\Omega)}$	L^2 product of (1) and (2) over the domain Ω
$[\![\cdot]\!]$	Jump operation at an interface
$\{\{\cdot\}\}$	Average operation at an interface
$((\cdot))$	Jump operation at a contact line

$\nabla_\Sigma(\cdot)$	Surface gradient
$\nabla_\Sigma \cdot (\cdot)$	Surface divergence
$\|(1)\|_{(2)}$	Norm of (1) with respect to the specified space (2)
$\|(1)\|_{(2)}$	Semiorm of (1) with respect to the specified space (2)

List of abbreviations

ALE arbitrary Lagrangian-Eulerian

AMR adaptive mesh refinement

BC boundary condition

BDF backward differentiation formula

BoSSS Bounded Support Spectral Solver

BPC bipolar coordinate

CFL Courant-Friedrichs-Lewy

DAE differential-algebraic equation

DG discontinuous Galerkin

DOF degree of freedom

DOFs degrees of freedom

EOC experimental order of convergence

FD finite difference

FE finite element

FEM finite element method

FFT Fast Fourier Transformation

FV finite volume

FVM finite volume method

GNBC generalisierte Navier Randbedingung

GNBC generalized Navier boundary condition

LBM Lattice Boltzmann Method

LHS left-hand side

MD molecular dynamics

MKT molecular kinetic theory

ODE ordinary differential equation

PDE partial differential equation

RHS right-hand side

RK Runge Kutta

SDIRK singly diagonal implicit Runge Kutta

SFB/CRC 1194 Sonderforschungsbereich/Collaborative Research Center 1194

SIP symmetric interior penalty

SPH smoothed particle hydrodynamics

TVD total variation diminishing

VOF volume-of-fluid

XDG erweiterte diskontinuierliche Galerkin

XDG extended discontinuous Galerkin

1 Introduction

1.1 Motivation

To give an intuitive understanding of the topic of this thesis we want to start with an everyday example, water in a glass. Along the inner surface of the glass a line is visible, where air, water and glass meet. This is called three-phase contact line. At this line, three distinct phases can be distinguished, these being the air, water and glass phases. Further, between each phase in contact with another phase an interface forms, e.g. the air-water interface. It is clear from everyday experience, that the contact line and interfaces influence how the water moves in the glass, e.g. through the formation of a so-called meniscus near the walls, where the water rises slightly above the gauge further away from the wall. This behavior how the fluid (water) wets the wall is what is known as wetting or dewetting (if the fluid recedes).
Wetting and dewetting, eventually in combination with evaporation, play an important role in many industrial and natural processes. As common examples the coating of surfaces or drying of liquid films can be mentioned. The dynamics of such processes are determined by the behavior of the three-phase contact line, between the liquid, air and the solid. To date the mechanics governing the behavior of the contact line are still not fully understood. As part of the Sonderforschungsbereich/Collaborative Research Center 1194 (SFB/CRC 1194), where the interaction between transport and wetting processes is investigated, this work aims to close this gap a little further.

1.1.1 Aim

To understand and predict the mechanisms taking place at the contact line it is necessary to develop practical mathematical models. These range from molecular models (molecular kinetic theory (MKT)/molecular dynamics (MD)), focusing on microscopic scales ($<$ µm), to hydrodynamic models, focusing more on the macroscopic scale ($>$ µm). Some survey works on these models include the works of Blake (2006), Bonn et al. (2009), and Snoeijer and Andreotti (2013). In the design of such models special attention has to be paid with regard to conditions on the boundaries and interfaces. Through numerous works it is known that careless modeling can result in singularities at the contact line, as is the case for example when the wall is modeled as a no-slip wall (Huh and Scriven, 1971; Sprittles and Shikhmurzaev, 2011). If in reality the wall really does not allow slip, the contact line could not move. To resolve this issue a commonly employed adaption in the model is to allow slip between the fluid and the wall as well as the contact line and the wall.
Introducing heat transport and evaporation into the model can give rise to additional singularities. For example the most basic evaporation models assume the fluid-fluid interface to keep a constant

temperature. Bringing such an interface in contact with a super-heated or sub-cooled wall (meaning the wall temperature is higher or lower than the saturation temperature of the liquid-vapor interface) would result in infinitely large heat fluxes (and consequently mass fluxes through evaporation/condensation) at the contact line (Colinet and Rednikov, 2011). This example illustrates that successful modeling of contact lines is decisive. The non-trivial task in modeling is to find the appropriate balance between simplicity and accuracy for the respective application. Related to the evaporation example it is possible to get rid of the singularities by including several microscopic effects, like the Kelvin-Thomson effect or the Hertz-Knudsen kinetic theory in Rednikov and Colinet (2013) and Rednikov and Colinet (2019). However, these approaches are very likely to require a much finer resolution then one would like when solving a macroscopic problem. Therefore, it may be suitable to implement a model that is less accurate, but computationally more efficient. For example, introducing a thermal resistance at the fluid-solid interface would limit the heat flux to a large but finite amount.
The objective of this work is to model and simulate contact lines, including momentum and heat transfer, using the extended discontinuous Galerkin (XDG) method (Kummer, 2017; Smuda and Kummer, 2021; Rieckmann et al., 2023e). The method can then be used as a kind of magnifying glass to zoom into the contact line and visualize for example temperature or velocity fields there. The assumption is that by investigating scales not accessible in experiments further insight into the contact line dynamics can be generated. The future perspective is then to have the method available as a tool to evaluate and develop new models to describe and predict the contact line hydrodynamics.

1.1.2 Novelty

The main novelty of this work lies in the implementation of the coupled momentum and heat transfer, including evaporation, in the XDG method, while also simulating moving contact lines. To this end the already existing XDG solver Bounded Support Spectral Solver (BoSSS), see (Kummer, 2017; Smuda and Kummer, 2021; Smuda and Kummer, 2022; Kummer et al., 2023), is expanded in its capability. Results using this extension are compiled in Sections 6.4, 7.1 and 7.3 in particular. As minor advancements two level set methods, an adapted one and a new one, are presented in this work, Section 4.3, and a suggestion for an extended sharp interface model for evaporation is made in Section 7.2.
As a side project, which slightly deviates from the main topic of this work as no interface is present, Chapter 5 covers numerical solutions of a Stokes flow through the nip between to rotating cylinders, as the distance between these asymptotically approaches zero. Furthermore, homogeneous solutions to the same problem are determined analytically, which in that extend has not been previously attempted.

1.2 Review of modeling and computational methods

In the latter motivation already a few buzz words were mentioned that may not be commonly known. To further explain and also give an overview of the state of the art regarding the simulation of fluids, interfaces and contact lines, this section will review the mathematical description and also numerical solution of such problems. Some of the discussed presented here were part of the introduction in Rieckmann et al. (2023e).

1.2.1 Modeling of multiphase flows

To be able to calculate and predict the movement of fluids, interfaces and contact lines it is necessary to adopt a mathematical model. In principle we need to make two major choices, how to represent the fluid bulk and how to treat the interface. These choices are considered in this subsection.

Continuum mechanics It is common knowledge that the matter around us consists of discrete particles, molecules, atoms and the subatomic particles they consist of. However, this view is somewhat in conflict with our everyday experience, where these particles are not perceptible and instead matter usually presents itself as homogeneous and continuous, like the water in a bottle. Therefore, two different approaches arise when trying to describe the behavior of real materials. The first based on discrete interacting particles is explored in the fields of classical mechanics (using Lagrange or Hamilton equations), statistical physics and quantum mechanics, e.g. (Baus and Tejero, 2021). For wetting problems this approach is taken for example in the work of Blake (2006) in the framework of MKT.
The second, which we adapt in this work, is the continuum model giving rise to the overarching field of continuum mechanics. In this approach matter is not viewed as the collection of discretely distributed molecules or similar, but as the name suggests as a continuous distribution, a so-called continuum. This model is less accurate than the molecular approach, but through its simplicity allows to calculate much larger systems. It should be noted, however, that this "continuum hypothesis" is not always applicable (Holland and Bragg, 1995).

Interface modeling When following the continuum consideration for the description of multiple interacting materials, e.g. water and air at the surface of an ocean, it is again possible to distinguish two broad classes of models for the interface. In the first class, called diffuse interface models, such phase transitions are continuous. The second class, so-called sharp interface models, which are used in this work, regard the transition regions between phases as sharp interfaces of zero-thickness. In reality, the transition between phases is known to be rapid but continuous, which justifies either approach to be taken.
A good introduction to the first class of interface models, the diffuse interface models, is given by Anderson et al. (1998). To sum up, the interface is smeared out over a region of finite thickness, and additional equations, which are only applicable at the interface, are integrated into the bulk equations. Thus, the solution is obtained by solving a unified set of equations that applies to the entire domain. These approaches give rise to very elegant one-fluid models, such as the Cahn-Hilliard Navier-Stokes equations, cf. Gal and Grasselli (2010). A sharp-interface limit, is only obtained in the asymptotic limit of vanishing interface thickness, as shown for example in the work on contact lines by Yue et al. (2010).
In recent years, many numerical methods, some of which differ greatly from one another, have been adapted and used for the simulation of two-phase fluid flow and heat transfer during pool boiling. A review is given by Dhir et al. (2013). In this context, the diffuse interface method was, e.g., successfully applied to pool boiling of single bubbles by Kunkelmann and Stephan (2009) and Kunkelmann and Stephan (2010), Wang and Cai (2017) or Franz et al. (2021). However, the diffuse interface approach has the inherent disadvantage of not providing sharp solutions in the interface region, which typically leads to an inaccurate computation of the local interface shape. This directly affects the temperature gradients near the interface and thus the liquid-vapor phase

change rates. Furthermore, an inaccurate calculation of the interface curvature might lead to spurious currents near the interface (Franz et al., 2021). All these inaccuracies are specifically high for small vapor bubbles with high surface tension. As a consequence, applying diffuse interface methods to such boiling configurations at least requires extremely small mesh sizes and therefore a high use of computational resources to reach an acceptable accuracy. Compared with diffuse interface methods, sharp interface methods do not have these inherent disadvantages. In this work, we adopt the sharp interface approach to circumvent the aforementioned limitations. The transition between phases occurs on a length scale much smaller than the resolution of numerical methods. Therefore, the interface is modeled as a lower dimensional manifold of zero thickness, embedded in the domain, and a separate set of equations is employed in each phase. Suitable couplings between the phases are established at the interface.

Contact line modeling As part of this thesis the behavior of three-phase contact lines in combination with evaporation is to be simulated. To this end, a good understanding of the contact line hydrodynamics is necessary. Therefore, we want to compile here a list of some influential works dealing with the dynamics of contact lines. Some of the earliest works dealing with hydrodynamic modeling of three-phase contact lines are those by Huh and Scriven (1971) and Voinov (1976) investigating the hydrodynamics of contact lines in creeping flows. More recent review works include (Blake, 2006; Snoeijer and Andreotti, 2013) comparing different contact line models, not necessarily limited to hydrodynamic ones. In the work of Lukyanov and Pryer (2017), on the other hand, the interface is not regarded to be massless, as is usually the case. From the aforementioned works it is known that careless modeling of boundary conditions and contact line behavior can lead to singularities at the contact line. These singularities are investigated in (Rednikov and Colinet, 2013; Rednikov and Colinet, 2019). Finally, Deegan et al. (2000) and Marengo and Coninck (2022) review the influence of evaporation on the wetting behavior.

1.2.2 Computational fluid dynamics

From the mathematical description of the problem it is usually not possible to directly obtain solutions for these models. Therefore, a numerical scheme is needed to achieve this task. At this point it should be mentioned that there exist also meso-scale methods, which work on scales between the microscopic molecular approach and the macroscopic continuum approach. Examples for such methods are the particle based Lattice Boltzmann Method (LBM) or the smoothed particle hydrodynamics (SPH). Apart from these two methods Fig. 1.2 shows a “two-fluid” and “one-fluid” model. “Two-fluid” models are a separate descriptor to a class of models where a kind of mixture model is used to describe the multiphase flow. Thus, not a single but multiple fluid equations are solved in the domain, which are extended by suitable interaction terms, see also Prosperetti and Tryggvason (2009) and Ishii and Hibiki (2011). In contrast, in so-called “one-fluid” models from Mirjalili et al. (2017), a single set of equations for each fluid region is used. From here on we focus solely on these latter models, which additionally necessitate a scheme to treat the interface numerically.

Computational methods For the molecular approach a very common numerical method is MD, for which a good overview is given in Marengo and Coninck (2022). However, as specified in the last paragraphs the focus in this work lies on continuum models for multiphase flows within a

sharp interface formulation. To solve these kind of models numerically a variety of numerical methods exist, for which we want to give a short overview of the most common ones, including a very rough sketch of the schemes. The mathematical description of the multiphase problem leads to a set of coupled differential equations called partial differential equation (PDE) or system of PDEs. The most intuitive approach to solve such systems is to construct a grid of equidistant points and approximate the derivatives arising in the PDE at each of these points using a difference scheme. E.g. the forward difference

$$\left.\frac{\partial \boldsymbol{f}(\boldsymbol{x})}{\partial x}\right|_{\boldsymbol{x}_i} \approx \frac{\boldsymbol{f}(\boldsymbol{x}_{i+1}) - \boldsymbol{f}(\boldsymbol{x}_i)}{\boldsymbol{x}_{i+1} - \boldsymbol{x}_i} \tag{1.1}$$

uses the value of the function at two neighboring grid points. The so constructed method is called a finite difference (FD) method. We refer to Tryggvason et al. (1998) for an example of a so-devised scheme for multiphase flow.
Another approach is called finite volume method (FVM). In this method the domain in which the flow is to be solved is divided into many cells or elements. In each element an approximation of the average value of the solution variable is determined as the solution to the problem. To this end, the PDE system, e.g. for a variable u, is integrated over the whole mesh and Gauss's theorem is applied to get rid of derivatives $\partial \boldsymbol{f}(\boldsymbol{x},u)/\partial \boldsymbol{x}$ of the so-called fluxes $\boldsymbol{f}(\boldsymbol{x},u)$. Subsequently, a suitable numerical flux $\hat{\boldsymbol{f}}$ is employed using values from multiple cells to approximate the flux across element boundaries, giving

$$\nabla\cdot(\boldsymbol{f}(\boldsymbol{x},u)) = g(\boldsymbol{x}) \rightarrow \sum_{K\in\Omega}\int_K \nabla\cdot(\boldsymbol{f})\ \mathrm{d}V \approx \sum_{K\in\Omega}\int_{\partial K} \hat{\boldsymbol{f}}\cdot\boldsymbol{n}^{\partial K}\ \mathrm{d}S = \int_\Omega g\ \mathrm{d}V. \tag{1.2}$$

In this way, in each element a constant value is obtained for the solution variable. This value can change discontinuously across element boundaries. By clever construction of the numerical fluxes, methods which uphold conservation properties can be constructed. A few examples of multiphase solvers employing the FVM (with evaporation) are given by Gibou et al. (2007), Tanguy et al. (2007), Bureš and Sato (2021a), and Bureš and Sato (2021b).
The finite element method (FEM) follows a very similar approach. However, instead of constant values the solution variables are given as a series expansion of a basis for a finite dimensional functionspace in each element. Usually this function space is globally continuous, meaning the solution does not have discontinuities across cell boundaries. Again the PDE is transferred to a variational formulation, however this time the arising integrals are weighted by so called test functions v. This gives

$$\nabla\cdot(\boldsymbol{f}(\boldsymbol{x},u)) = g(\boldsymbol{x}) \rightarrow \sum_{K\in\Omega}\int_K \nabla\cdot(\boldsymbol{f}(x,u))\,v\ \mathrm{d}V = \sum_{K\in\Omega}\int_K -\boldsymbol{f}\cdot\nabla v\ \mathrm{d}V = \int_\Omega gv\ \mathrm{d}V. \tag{1.3}$$

Due to the continuity of the solution and test functions the fluxes on element boundaries usually vanish, when summing over all elements (boundary treatment is omitted here for brevity). A few works employing the FEM to simulate multiphase flow with contact lines and/or evaporation are those of Gerbeau and Lelièvre (2009), Diddens (2017), and Reusken et al. (2017).
A sub-type of the FEM and a mix between the continuous finite element (FE) and discontinuous finite volume (FV) methods is the discontinuous Galerkin (DG) method. It also makes use of higher order basis functions like the FEM. However, these are locally defined and the solution can have discontinuities across element boundaries as in the FVM. This necessitates the use of numerical fluxes, once again enabling the relatively easy construction of a conservative scheme.

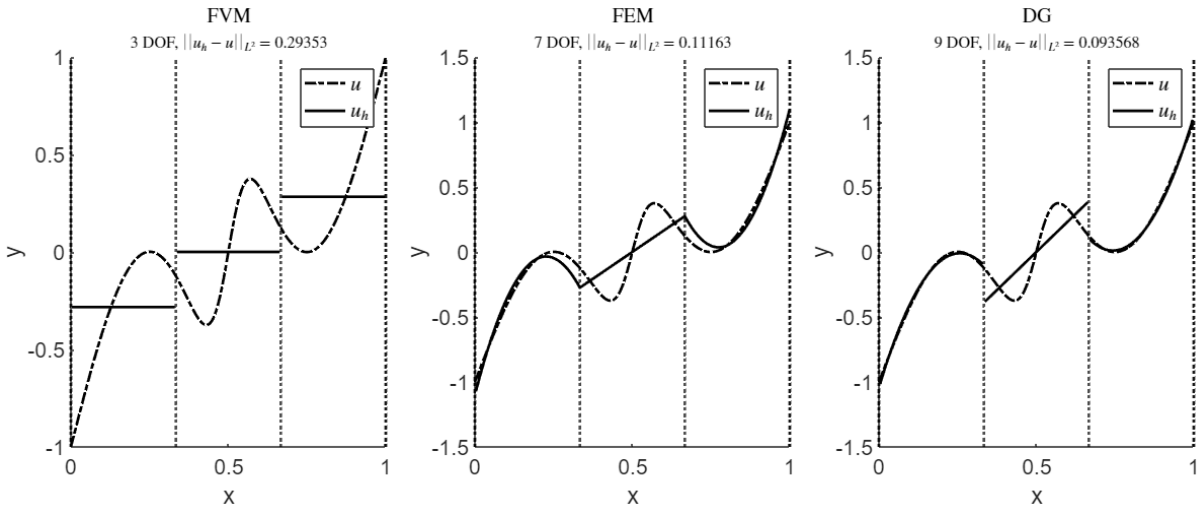

Figure 1.1: Comparison of the projections $u_h(x)$ of the function $u(x) = \tanh(5\pi x) + \sin(2\pi x)$ onto the FV, FE and DG approximation spaces. Above each plot the global L^2-error and total number of DOFs is displayed.

Apart from that a variational formulation is used again, with the same basis for the test functions as used for the solution. This class of methods was first developed by Reed and Hill (1973) and became popular for (hyperbolic) conservation laws, cf. Marsden et al. (2008). It has also been further developed for elliptic problems (Arnold et al., 2002; Dolejší and Feistauer, 2015) and employed for the Navier-Stokes equations (Di Pietro and Ern, 2012; Dolejší and Feistauer, 2015). When applying DG methods it is possible to achieve high order convergence, while still employing simple numerical fluxes. Additionally, the local nature of the functional basis makes mesh refinement and parallelization much easier. For this reason, DG is used in the preliminary works of this thesis in the context of multiphase flows with evaporation or wetting (Kummer, 2017; Smuda and Kummer, 2021; Rieckmann et al., 2023e).
Figure 1.1 shows a comparison of the projection of a given function $u(x)$ onto the solution spaces of the FV, FE and DG methods, using 3 elements and second order polynomials for the higher order methods. For the FVM the element-wise constant values of the projection $u_h(x)$ are clearly visible. For the FE space, on the other hand, it can be seen that $u_h(x)$ is globally continuous, while there are jumps in the DG approximation. The slight improvement in accuracy for the DG method comes at the cost of an increase in degrees of freedom (DOFs).

Interface treatment

In Fig. 1.2 an overview of several models for two-phase flow is given. For the “one-fluid” models it is visible that the numeric interface treatment can be divided into two approaches as either interface-tracking (e.g. splines, particles, markers) or interface-capturing (e.g. volume-of-fluid, level set) techniques, depending on whether they explicitly or implicitly discretize the interface location. Even though the “two-fluid” models also use PDE systems, usually no explicit interface treatment is necessary as the surface effects are included in the interaction terms, for example an additional term in the momentum balance for the liquid fraction of a gas-liquid mixture to consider interfacial momentum transfer. A discussion and good starting point for further inquiries

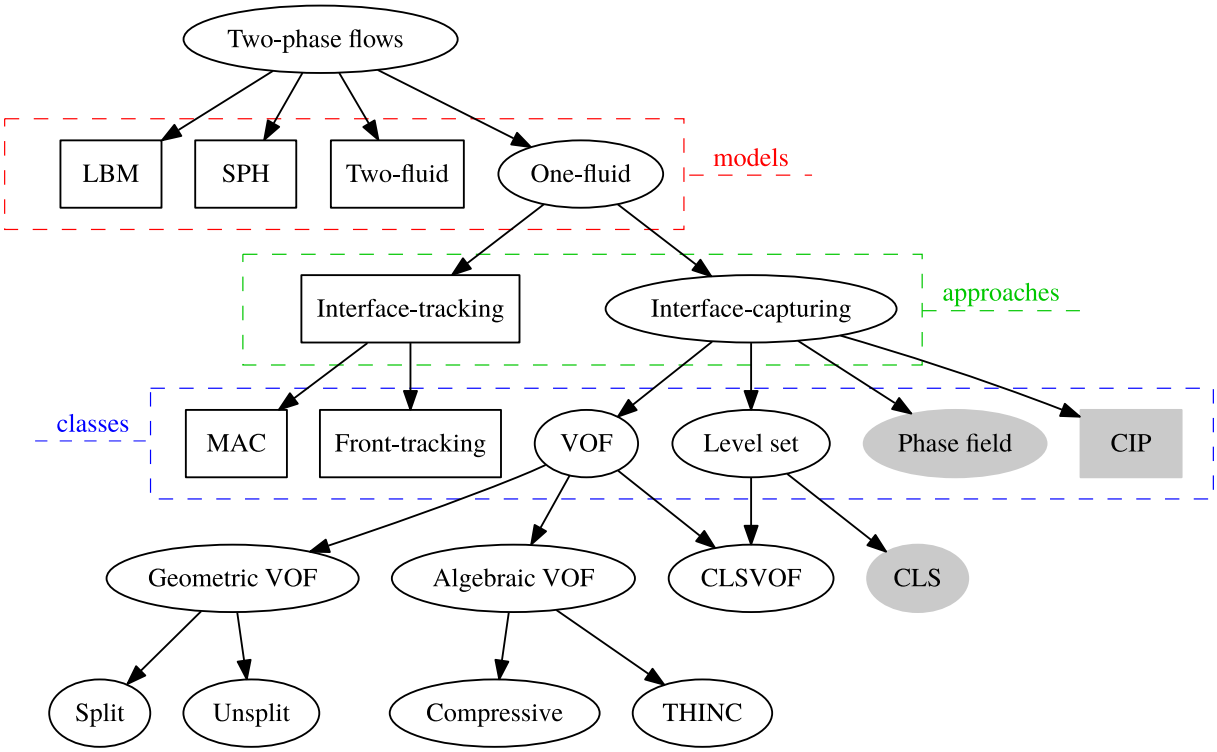

Figure 1.2: Overview of different mathematical models and their interface representation from Mirjalili et al. (2017). For the abbreviations not specified here, we refer to the original work. Shaded gray methods are diffuse interface methods. All other follow the sharp interface approach.

can be found in the work of Mirjalili et al. (2017).
To summarize, interface-tracking implies explicit tracking of the interface, for example by markers that are advected with the flow or a body-fitted mesh as for arbitrary Lagrangian-Eulerian (ALE) methods. On the other hand, interface capturing describes an implicit description of the interface. Common examples are the usage of auxiliary volume fraction field describing how much of a certain fluid is contained in any cell in the volume-of-fluid (VOF) method or a level set field, whose zero set marks the position of the interface. In that categorization the phase field in the aforementioned Cahn-Hilliard Navier-Stokes model is another example of the interface-capturing approach in the diffuse interface context.
In a certain sense a variant of the interface-tracking approach is used for a single simulation in Section 7.1, where the interface is described by a spline and the interpolation points of the spline are advected explicitly. Apart from this exception we will use a level set method with some adaptations regarding the special needs of our DG based method throughout this work. The level set method was first proposed by Osher and Sethian (1988), see also Osher and Fedkiw (2001). The idea is to represent the interface as the zero (or level) set of a scalar field. This field is typically required to be a signed-distance function w.r.t. the interface. However, in general, this property is lost when advecting the interface, thus necessitating the need for a reinitialization procedure. To this end, we adopt the approach given by Basting and Kuzmin (2013).
It should also be mentioned that another way to categorize the interface representation would be as whether the method uses a body-fitted mesh or an unfitted mesh, as done here. For further

insights, refer to the benchmark study of Gründing et al. (2020), where representatives of both approaches are compared.
Summarizing, we can note that to discretize the set of equations in each phase, we use the discontinuous Galerkin (DG) method. The approach suggested in this work follows the ideas of the extended finite element method (XFEM) proposed by Mos et al. (1999), and in analogy to this is known as extended discontinuous Galerkin (XDG) method, or otherwise known as unfitted DG (Bastian and Engwer, 2009). Unlike many finite volume based sharp interface methods that rely on reconstructing values and gradients at the interface, e.g, the ghost fluid method used by Bureš and Sato (2021a), the XDG method represents the solution using high-order functions in each phase, eliminating the need for such reconstruction. Instead the high-order functions can be directly evaluated at the interface.

1.3 Content

To conclude the brief introduction to the topic of this thesis, we want to give a short summary of the structure and content of this work.

In Chapter 2 the hydrodynamic model(s), which will be used subsequently, is presented. From the fundamental conservation laws for mass, momentum and energy we will go through the steps to derive a differential form of these laws including especially the necessary extensions for interfaces and contact lines. By clearly highlighting which assumptions and simplifications are used, this should give a good overview of how to model the contact line hydrodynamics in a sharp interface setting.

After having specified which model is used, it is usually wanted to obtain analytical or numerical solutions for it. In this work this task is accomplished numerically by use of the XDG method. The working principle and a coarse heuristic derivation for which is presented in Chapter 3.

To actually compute solutions with the XDG method a working implementation as a computer software is necessary. Such a software to solve the coupled continuity, momentum and heat equations including evaporation at interfaces and contact lines is first implemented in this work. The building blocks of this algorithm are described in Chapter 4, which gives an overview of how to obtain a solvable linear system starting from the differential equations of the hydrodynamic model.

At this point all necessary tools are available to actually solve fluid dynamic problems. The results obtained during this work are compiled as three separate chapters. In Chapter 5 a pure single-phase flow through the gap between two cylinders is considered. There are no interfaces or contact lines involved yet. In Chapter 6, on the other hand, two-phase simulations are presented including interfaces, but no contact lines. The main result of this chapter is the validation of the evaporation implementation. Finally, Chapter 7 also includes contact lines. Several parameter studies give insights into the behavior of the fluids near the contact line in the used model and implementation.

In Chapter 8 the achieved progress and findings are summarized, concluding the work and evaluating the fulfillment of the postulated goal.

At last an expanded presentation of the XDG discretization is presented in Appendix A, as well as further details for the implementation of a slip on the fluid-fluid interface used in Section 7.2.

2 Conservation equations for incompressible multiphase flows with thermal evaporation

The different approaches of modeling the behavior of materials have already been briefly presented in Section 1.2.1. As mentioned the present work follows the continuum approach. In the following sections a summary of the continuum mechanical description of incompressible multiphase flows, within a sharp interface context, will be given. The presentation is heavily leaned on the work of Slattery et al. (2007). The focus lies on the conservation equations for mass, momentum and energy and especially the description of those at phase interfaces and contact lines. The derivation is limited to dividing interfaces embedded into $\mathbb{R}^3$. The chapter will close with considerations regarding the necessary closure relations, also called constitutive equations and a presentation of the so obtained models used later in this work.

2.1 Preliminaries

Before beginning the discussion of the continuum description of multiphase flows a few fundamental results from the study of continuums are given. In the form they occur in this work the sum of some quantity at the dividing interfaces and contact lines may appear. These special sums are called jumps and are defined as follows:

Definition 2.1 (Jump operators). *On the dividing interface $\Sigma^{(i,j)}$ between phase $\Omega^{(i)}$ and $\Omega^{(j)}$ the jump operator for some variable Ψ is defined as*

$$\left[\!\left[\Psi \boldsymbol{n}^{\Sigma}\right]\!\right] = \Psi^{(i)}\boldsymbol{n}^{(i)} + \Psi^{(j)}\boldsymbol{n}^{(j)}. \tag{2.1}$$

The normal vector $\boldsymbol{n}^{(i)}$ is pointing outward from $\Omega^{(i)}$. Without loss of generality, it is assumed from here on that $\boldsymbol{n}^{\Sigma} = \boldsymbol{n}^{(i)}$ uniquely along an interface, such that additionally

$$\left[\!\left[\Psi \boldsymbol{n}^{\Sigma}\right]\!\right] = \Psi^{(i)}\boldsymbol{n}^{\Sigma} - \Psi^{(j)}\boldsymbol{n}^{\Sigma} = \left[\!\left[\Psi\right]\!\right]\boldsymbol{n}^{\Sigma}. \tag{2.2}$$

The jump operator at the three phase contact line $L^{(i,j,k)}$, where three phases $\Omega^{(i)}$, $\Omega^{(j)}$ and $\Omega^{(k)}$ meet, is defined as

$$\left(\!\left(\Psi^{\Sigma}\boldsymbol{n}^{L}\right)\!\right) = \Psi^{(i,j)}\boldsymbol{n}^{(i,j)} + \Psi^{(i,k)}\boldsymbol{n}^{(i,k)} + \Psi^{(j,k)}\boldsymbol{n}^{(j,k)}, \tag{2.3}$$

taking into account the surface quantity Ψ^{Σ} on the intersecting interfaces. Here, the normal vector $\boldsymbol{n}^{(i,j)}$ is tangential and outwards facing to the interface $\Sigma^{(i,j)}$. Note that $\boldsymbol{n}^{(i,j)} = \boldsymbol{n}^{(j,i)}$. This situation is depicted in Fig. 2.1.

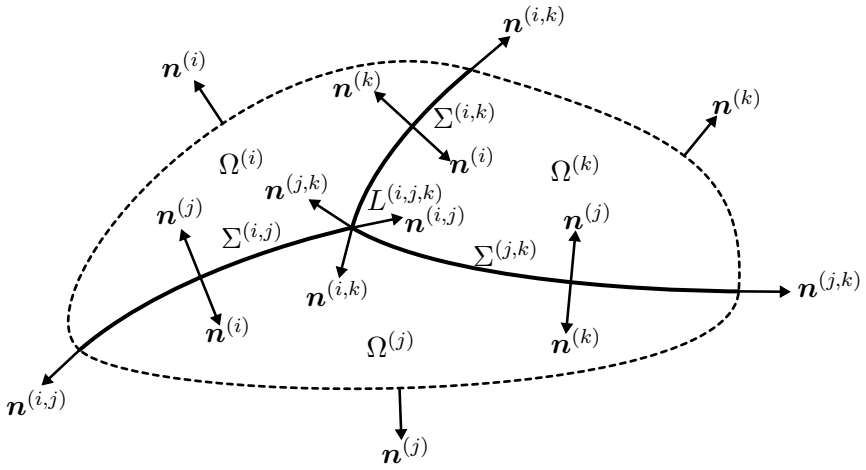

Figure 2.1: Depiction of three phases with the respective dividing interfaces and three phase contact line.

To make the text easier to understand, it should be noted that in contrast to the presentation in (Slattery et al., 2007) the direction of interface normals is reversed. Here, it is assumed that e.g. $\boldsymbol{n}^{(i)}$ is the outer normal of the phase $\Omega^{(i)}$, while in (Slattery et al., 2007) inner normals are used.

One fundamental result of continuum mechanics are the so-called transport theorems. These are useful to pull the material time derivative of an integral of some quantity into said integral.

Definition 2.2 (Bulk transport theorem). *For the volume term the transport theorem for some bulk (scalar, vector or tensor) quantity Ψ is (Slattery et al., 2007, p. 68ff.)*

$$\frac{d}{dt}\int_{\Omega}\Psi\ dV = \int_{\Omega}\frac{\partial\Psi}{\partial t} + \nabla\cdot(\Psi\otimes\boldsymbol{u})\ dV - \int_{\Sigma}\left[\!\left[\Psi(\boldsymbol{u}-\boldsymbol{u}^{\Sigma})\cdot\boldsymbol{n}^{\Sigma}\right]\!\right]\ dS, \tag{2.4}$$

using the material velocity $\boldsymbol{u}$ and the interface velocity $\boldsymbol{u}^{\Sigma}$.

To arrive at this result consider the decomposition of the full volume into the separate phases $\Omega = \sum_{i=1}^{N_\Omega}\Omega^{(i)}$:

$$\frac{\mathrm{d}}{\mathrm{d}t}\int_{\Omega}\Psi\ \mathrm{d}V = \sum_{i=1}^{N_\Omega}\frac{\mathrm{d}}{\mathrm{d}t}\int_{\Omega^{(i)}}\Psi^{(i)}\ \mathrm{d}V. \tag{2.5}$$

For each of these phases the transport theorem in the following form is valid (Slattery et al., 2007, p. 68):

$$\begin{aligned}\frac{\mathrm{d}}{\mathrm{d}t}\int_{\Omega^{(i)}}\Psi^{(i)}\ \mathrm{d}V = &\int_{\Omega^{(i)}}\frac{\partial\Psi^{(i)}}{\partial t}\ \mathrm{d}V + \int_{\partial\Omega^{(i)}}\Psi^{(i)}\boldsymbol{s}^{(i)}\cdot\boldsymbol{n}^{(i)}\ \mathrm{d}S \\ &+ \sum_{j=1,j\neq i}^{N_\Omega}\int_{\Sigma^{(i,j)}}\Psi^{(i)}\boldsymbol{s}^{(i,j)}\cdot\boldsymbol{n}^{(i)}\ \mathrm{d}S.\end{aligned} \tag{2.6}$$

The normals are chosen to point outwards from $\Omega^{(i)}$. $\boldsymbol{s}^{(i)}$ and $\boldsymbol{s}^{(i,j)}$ denote the velocities of the boundary $\partial\Omega^{(i)}$, excluding the phase interfaces, and of these interfaces $\Sigma^{(i,j)}$. In the next step the

divergence theorem

$$\int_{\partial\Omega^{(i)}} \Psi^{(i)}\boldsymbol{s}^{(i)}\cdot\boldsymbol{n}^{(i)}\ \mathrm{d}S = \int_{\Omega^{(i)}} \nabla\cdot\left(\Psi^{(i)}\boldsymbol{s}^{(i)}\right)\ \mathrm{d}V - \sum_{j=1,j\neq i}^{N_\Omega}\int_{\Sigma^{(i,j)}} \Psi^{(i)}\boldsymbol{s}^{(i)}\cdot\boldsymbol{n}^{(i)}\ \mathrm{d}S \tag{2.7}$$

is used and the phases and dividing interfaces are combined again. Then, Eq. (2.5) can be rewritten to

$$\frac{\mathrm{d}}{\mathrm{d}t}\int_\Omega \Psi\ \mathrm{d}V = \int_\Omega \frac{\partial\Psi}{\partial t} + \nabla\cdot(\Psi\boldsymbol{s})\ \mathrm{d}V - \int_\Sigma \left[\!\left[\Psi(\boldsymbol{s}-\boldsymbol{u}^\Sigma)\cdot\boldsymbol{n}^\Sigma\right]\!\right]\ \mathrm{d}S. \tag{2.8}$$

Finally, the volume is assumed to be material and it is possible to identify $\boldsymbol{s}=\boldsymbol{u}$ as the fluid velocity. However, the internal interfaces $\Sigma^{(i,j)}$ are not necessarily material and $\boldsymbol{u}^\Sigma = \boldsymbol{s}^{(i,j)} = \boldsymbol{s}^{(j,i)} \neq \boldsymbol{u}$. With these assumptions Eq. (2.4) is obtained. In the derivation of the transport theorem for the dividing interfaces the same approach is used. I.e. decomposing the combined interface into separate parts $\Sigma = \sum_{i=1}^{N_\Omega}\sum_{j=i+1}^{N_\Omega}\Sigma^{(i,j)}$ and obtaining the occurring jumps by later recombination of these partial interfaces.

Definition 2.3 (Surface transport theorem). *The transport theorem for the dividing interfaces is (Slattery et al., 2007, p. 75ff.)*

$$\begin{aligned}\frac{d}{dt}\int_\Sigma \Psi^\Sigma\ dS = &\int_\Sigma \frac{\partial\Psi^\Sigma}{\partial t} - \nabla_\Sigma\Psi^\Sigma\cdot\boldsymbol{v}^\Sigma + \nabla_\Sigma\cdot\left(\Psi^\Sigma\otimes\boldsymbol{u}^\Sigma\right)\ dS\\ &- \int_L \left(\left(\Psi^\Sigma(\boldsymbol{u}^\Sigma-\boldsymbol{u}^L)\cdot\boldsymbol{n}^L\right)\right)\ dl.\end{aligned} \tag{2.9}$$

The meaning of the velocity $\boldsymbol{v}^\Sigma$ is not easy to grasp. The velocity $\boldsymbol{u}^\Sigma = \boldsymbol{v}^\Sigma + \boldsymbol{w}^\Sigma$ of a surface particle consists of the speed of displacement of a surface point $\boldsymbol{v}^\Sigma$ and the intrinsic surface velocity $\boldsymbol{w}^\Sigma$ related to the reference configuration of the surface (Slattery et al., 2007, p. 19 ff.).

In principle it would be possible to extend this discussion even further to (four phase) contact points. However, in this work such models are not considered, which is why no point jumps occur in the line transport theorem:

Definition 2.4 (Line transport theorem). *Analogous to the transport theorem at interfaces a transport theorem for the contact lines can be obtained (Slattery et al., 2007, p. 75ff.). This is given as*

$$\frac{d}{dt}\int_L \Psi^L\ dl = \int_L \frac{\partial\Psi^L}{\partial t} - \nabla_L\Psi^L\cdot\boldsymbol{v}^L + \nabla_L\cdot\left(\Psi^L\otimes\boldsymbol{u}^L\right)\ dl. \tag{2.10}$$

As will be visible later, that it is also necessary to transform integrals of the flux of a quantity over the boundary of some manifold to integrals of the divergence of that quantity over the volume of the manifold. To do this the divergence theorem, also known as Gauss's theorem, as a special form of the generalized Stokes theorem can be used. This is a classical result of multivariate calculus and we state it here in specific forms useful for this work, limited to flat (volume) spaces (usually $\Omega\subseteq\mathbb{R}^3$) and embedded surfaces and lines, that may be curved.

Definition 2.5 (Divergence theorem). *For a bulk vector or tensor[1] quantity the divergence theorem states, that the divergence of that quantity over some volume equals its flux through the boundary of that volume. For a body containing dividing interfaces it can be formulated as*

$$\int_\Omega \nabla \cdot (\boldsymbol{\Psi}) \ dV = \int_{\partial\Omega} \boldsymbol{\Psi} \cdot \boldsymbol{n} \ dS + \int_\Sigma \left[\!\left[\boldsymbol{\Psi} \cdot \boldsymbol{n}^\Sigma\right]\!\right] \ dS. \tag{2.11}$$

Definition 2.6 (Surface divergence theorem). *For a surface tensor[2] or vector quantity the surface divergence theorem states, that the divergence of that quantity over some surface equals its flux through the boundary of that surface. Additionally, such a surface is not usually flat, which is why the mean curvature[3]*

$$\kappa = \nabla_\Sigma \cdot \left(\boldsymbol{n}^\Sigma\right) \tag{2.12}$$

is also taken into account. For a body containing intersecting dividing interfaces it can be formulated as

$$\int_\Sigma \nabla_\Sigma \cdot \left(\boldsymbol{\Psi}^\Sigma\right) - \kappa \boldsymbol{\Psi}^\Sigma \cdot \boldsymbol{n}^\Sigma \ dS = \int_{\partial\Sigma} \boldsymbol{\Psi}^\Sigma \cdot \boldsymbol{n}_{\partial\Sigma} \ dl + \int_L \left(\!\left(\boldsymbol{\Psi}^\Sigma \cdot \boldsymbol{n}^L\right)\!\right) \ dl. \tag{2.13}$$

The proof of the surface divergence theorem relies on the decomposition of $\boldsymbol{\Psi}^\Sigma$ in a surface tangential and normal part,

$$\nabla_\Sigma \cdot \left(\boldsymbol{\Psi}^\Sigma\right) = \nabla_\Sigma \cdot \left(\mathbf{P}^\Sigma \cdot \boldsymbol{\Psi}^\Sigma + (\boldsymbol{n}^\Sigma \otimes \boldsymbol{n}^\Sigma) \cdot \boldsymbol{\Psi}^\Sigma\right), \tag{2.14a}$$

$$\nabla_\Sigma \cdot \left((\boldsymbol{n}^\Sigma \otimes \boldsymbol{n}^\Sigma) \cdot \boldsymbol{\Psi}^\Sigma\right) = \underbrace{\nabla_\Sigma \cdot \left(\boldsymbol{n}^\Sigma\right) \boldsymbol{\Psi}^\Sigma \cdot \boldsymbol{n}^\Sigma}_{=\kappa \boldsymbol{\Psi}^\Sigma \cdot \boldsymbol{n}^\Sigma} + \underbrace{\nabla_\Sigma (\boldsymbol{\Psi}^\Sigma \cdot \boldsymbol{n}^\Sigma) \cdot \boldsymbol{n}^\Sigma}_{=0}, \tag{2.14b}$$

by using the surface projection tensor $\mathbf{P}^\Sigma = \mathbf{I} - \boldsymbol{n}^\Sigma \otimes \boldsymbol{n}^\Sigma$. For the surface divergence of the tangential part Gauss's theorem can be applied (Slattery et al., 2007, p. 669ff.):

$$\int_\Sigma \nabla_\Sigma \cdot \left(\mathbf{P}^\Sigma \cdot \boldsymbol{\Psi}^\Sigma\right) \ \mathrm{d}S = \int_{\partial\Sigma} (\mathbf{P}^\Sigma \cdot \boldsymbol{\Psi}^\Sigma) \cdot \boldsymbol{n}_{\partial\Sigma} \ \mathrm{d}l + \int_L \left(\!\left((\mathbf{P}^\Sigma \cdot \boldsymbol{\Psi}^\Sigma) \cdot \boldsymbol{n}^L\right)\!\right) \ \mathrm{d}l. \tag{2.15}$$

Noticing that the scalar product of the normal part and the $\boldsymbol{n}_{\partial\Sigma}, \boldsymbol{n}^L$ vectors vanish gives the final result of Eq. (2.13).

Definition 2.7 (Line divergence theorem). *The line divergence theorem gives a similar result. Here, we made use of the decomposition of some vector or tensor property on the contact lines into a line normal and tangential part, using the projection tensor in line tangent direction $\mathbf{P}^L$:*

$$\int_L \nabla_L \cdot \left(\boldsymbol{\Psi}^L\right) - \nabla_L \cdot \left((\mathbf{I} - \mathbf{P}^L) \cdot \boldsymbol{\Psi}^L\right) \ dl = \int_{\partial L} \boldsymbol{\Psi}^L \cdot \boldsymbol{n}_{\partial L} \ ds. \tag{2.16}$$

The integral on the right hand side is evaluated at the two end points of the line, if it is not closed. Using differential geometric results, the normal component of $\boldsymbol{\Psi}^L$ could probably be further expanded in terms of a curvature tensor, as has been done for surfaces using the mean curvature.

[1] This generalization is possible for cartesian spaces.

[2] The generalization at this point is possible due to the special structure of the regarded problem. If not surfaces embedded in $\mathbb{R}^3$ are considered alternative ways to derive the balance of momentum may have to be explored, see e.g. (Marsden and Hughes, 1994).

[3] also $\nabla_\Sigma \cdot \left(\mathbf{P}^\Sigma\right) = -\kappa \boldsymbol{n}^\Sigma$

2.2 Mass conservation

The meaning of mass conservation is probably the most intuitive of the various conservation laws employed in physics and reflects an everyday observation, that : “Things come not into being out of nothing.” Mathematically speaking the mass is obtained by integrating the density of any body over its volume. This is intuitive to grasp, if we deviate for a moment from the continuum hypothesis, e.g. (Baus and Tejero, 2021), we could think of that body as the sum of a finite amount of particles. In that setting the mass of the body is the sum of all the masses of the particles and its volume their distribution in space. As long as the body consists of the same particles as in the beginning its mass does not change, no matter their configuration in space:

$$\frac{\mathrm{d}m}{\mathrm{d}t} = \frac{\mathrm{d}}{\mathrm{d}t}\int_{\Omega(t)} \rho \ \mathrm{d}V = 0. \tag{2.17}$$

In the continuum setting instead of directly counting particles we average beforehand over an infinitesimal small domain and call the resulting quantity a density. In what follows we expand this consideration to surface and line densities. The complete body under investigation consists now of the union of phases $\Omega = \sum_{i=1}^{N_\Omega} \Omega^{(i)}$, dividing interfaces between these phases $\Sigma = \sum_{i=1}^{N_\Omega}\sum_{j=i+1}^{N_\Omega} \Sigma^{(i,j)}$ and three phase contact lines $L = \sum_{i=1}^{N_\Omega}\sum_{j=i+1}^{N_\Omega}\sum_{k=i+2}^{N_\Omega} L^{(i,j,k)}$, where the phase interfaces intersect. With associated densities on each of these manifolds the total mass in the system is

$$m = \int_\Omega \rho \ \mathrm{d}V + \int_\Sigma \rho^\Sigma \ \mathrm{d}S + \int_L \rho^L \ \mathrm{d}l. \tag{2.18}$$

By employing the transport theorems, Definitions 2.2 to 2.4, to Eqs. (2.17) and (2.18) the time derivative can be drawn under the integrals, to obtain

$$\begin{aligned}\frac{\mathrm{d}m}{\mathrm{d}t} = &\int_\Omega \frac{\partial \rho}{\partial t} + \nabla\cdot(\rho\boldsymbol{u}) \ \mathrm{d}V \\ &+ \int_\Sigma \frac{\partial \rho^\Sigma}{\partial t} - \nabla_\Sigma\rho^\Sigma\cdot\boldsymbol{v}^\Sigma + \nabla_\Sigma\cdot\left(\rho^\Sigma\boldsymbol{u}^\Sigma\right) - \left[\!\left[\rho(\boldsymbol{u}-\boldsymbol{u}^\Sigma)\cdot\boldsymbol{n}^\Sigma\right]\!\right] \ \mathrm{d}S \\ &+ \int_L \frac{\partial \rho^L}{\partial t} - \nabla_L\rho^L\cdot\boldsymbol{v}^L + \nabla_L\cdot\left(\rho^L\boldsymbol{u}^L\right) - \left(\!\left(\rho^\Sigma(\boldsymbol{u}^\Sigma-\boldsymbol{u}^L)\cdot\boldsymbol{n}^L\right)\!\right) \ \mathrm{d}l = 0.\end{aligned} \tag{2.19}$$

This result is known as the integral mass balance for material volumes, containing intersecting dividing interfaces. Equation (2.19) holds for every material volume, therefore, two observations can be made. Firstly, each of the integrals has to be fulfilled separately. Secondly, the volume can be chosen arbitrarily small. Through these observations we obtain the bulk mass balance in differential form, commonly known as continuity equation

$$\frac{\partial \rho}{\partial t} + \nabla\cdot(\rho\boldsymbol{u}) = 0, \tag{2.20}$$

the differential jump mass balance on dividing interfaces

$$\frac{\partial \rho^\Sigma}{\partial t} - \nabla_\Sigma\rho^\Sigma\cdot\boldsymbol{v}^\Sigma + \nabla_\Sigma\cdot\left(\rho^\Sigma\boldsymbol{u}^\Sigma\right) - \left[\!\left[\rho(\boldsymbol{u}-\boldsymbol{u}^\Sigma)\cdot\boldsymbol{n}^\Sigma\right]\!\right] = 0, \tag{2.21}$$

and the jump mass balance at common lines

$$\frac{\partial \rho^L}{\partial t} - \nabla_L\rho^L\cdot\boldsymbol{v}^L + \nabla_L\cdot\left(\rho^L\boldsymbol{u}^L\right) - \left(\!\left(\rho^\Sigma(\boldsymbol{u}^\Sigma-\boldsymbol{u}^L)\cdot\boldsymbol{n}^L\right)\!\right) = 0. \tag{2.22}$$

2.3 Momentum conservation

Momentum conservation is arguably the core insight of classical "Newtonian" mechanics (Smith, 2008). It describes that a body changes its motion as the result of forces acting on said body. The motion of a body can be quantified by the linear momentum, the product of mass and velocity of the body. Put in terms of a momentum density for the bulk, dividing surfaces and contact lines this becomes

$$\boldsymbol{p} = \int_\Omega \rho \boldsymbol{u} \ \mathrm{d}V + \int_\Sigma \rho^\Sigma \boldsymbol{u}^\Sigma \ \mathrm{d}S + \int_L \rho^L \boldsymbol{u}^L \ \mathrm{d}l, \tag{2.23}$$

and the axiom can be written as

$$\frac{\mathrm{d}\boldsymbol{p}}{\mathrm{d}t} = \boldsymbol{F}. \tag{2.24}$$

The forces acting on the body can be distinguished as "volume" forces acting over the volume of the manifolds and "surface" forces acting on their boundaries (Slattery et al., 2007, p. 113ff.):

$$\boldsymbol{F} = \boldsymbol{F}_V + \boldsymbol{F}_S, \tag{2.25a}$$

$$\boldsymbol{F}_V = \int_\Omega \rho \boldsymbol{f} \ \mathrm{d}V + \int_\Sigma \rho^\Sigma \boldsymbol{f}^\Sigma \ \mathrm{d}S + \int_L \rho^L \boldsymbol{f}^L \ \mathrm{d}l, \tag{2.25b}$$

$$\boldsymbol{F}_S = \int_{\partial\Omega} \boldsymbol{\tau} \ \mathrm{d}S + \int_{\partial\Sigma} \boldsymbol{\tau}^\Sigma \ \mathrm{d}l + \int_{\partial L} \boldsymbol{\tau}^L \ \mathrm{d}s. \tag{2.25c}$$

By employing Cauchy´s stress principle (Slattery et al., 2007, p. 114ff.) the forces acting on the boundaries, in terms of traction vectors, can be represented by respective bulk, surface and line stress tensors

$$\boldsymbol{\tau} = \mathbf{T} \cdot \boldsymbol{n}^{\partial\Omega}, \tag{2.26a}$$

$$\boldsymbol{\tau}^\Sigma = \mathbf{T}^\Sigma \cdot \boldsymbol{n}_{\partial\Sigma}, \tag{2.26b}$$

$$\boldsymbol{\tau}^L = \mathbf{T}^L \cdot \boldsymbol{n}_{\partial L}, \tag{2.26c}$$

which are tangential tensor fields, w.r.t to their respective manifold. Finally, combining Eqs. (2.23) to (2.26), making use of the transport theorems Definitions 2.2 to 2.4, divergence theorems Definitions 2.5 to 2.7 and the continuity equations Eqs. (2.20) to (2.22) the momentum conservation in the following form is found:

$$\begin{aligned}
0 = &\int_\Omega \rho \left(\frac{\partial \boldsymbol{u}}{\partial t} + \boldsymbol{u} \cdot \nabla \boldsymbol{u} \right) - \rho \boldsymbol{f} - \nabla \cdot (\mathbf{T}) \ \mathrm{d}V \\
&+ \int_\Sigma \rho^\Sigma \left(\frac{\partial \boldsymbol{u}^\Sigma}{\partial t} + (\boldsymbol{u}^\Sigma - \boldsymbol{v}^\Sigma) \cdot \nabla_\Sigma \boldsymbol{u}^\Sigma \right) - \rho^\Sigma \boldsymbol{f}^\Sigma - \nabla_\Sigma \cdot \left(\mathbf{T}^\Sigma \right) \\
&- \left[\!\left[\left(\rho (\boldsymbol{u} - \boldsymbol{u}^\Sigma)(\boldsymbol{u} - \boldsymbol{u}^\Sigma) - \mathbf{T} \right) \cdot \boldsymbol{n}^\Sigma \right]\!\right] \ \mathrm{d}S \\
&+ \int_L \rho^L \left(\frac{\partial \boldsymbol{u}^L}{\partial t} + (\boldsymbol{u}^L - \boldsymbol{v}^L) \cdot \nabla_L \boldsymbol{u}^L \right) - \rho^L \boldsymbol{f}^L - \nabla_L \cdot \left(\mathbf{T}^L \right) \\
&- \left(\left(\left(\rho^\Sigma (\boldsymbol{u}^\Sigma - \boldsymbol{u}^L)(\boldsymbol{u}^\Sigma - \boldsymbol{u}^L) - \mathbf{T}^\Sigma \right) \cdot \boldsymbol{n}^L \right) \right) \ \mathrm{d}l.
\end{aligned} \tag{2.27}$$

From Eq. (2.27) we can immediately conclude that

$$\rho \left(\frac{\partial \boldsymbol{u}}{\partial t} + \boldsymbol{u} \cdot \nabla \boldsymbol{u} \right) = \rho \boldsymbol{f} + \nabla \cdot (\mathbf{T}) \tag{2.28}$$

on the bulk. On the dividing interfaces we find

$$\begin{aligned}\rho^{\Sigma}\left(\frac{\partial \boldsymbol{u}^{\Sigma}}{\partial t}+(\boldsymbol{u}^{\Sigma}-\boldsymbol{v}^{\Sigma})\cdot\nabla_{\Sigma}\boldsymbol{u}^{\Sigma}\right)-\left[\!\left[(\rho(\boldsymbol{u}-\boldsymbol{u}^{\Sigma})(\boldsymbol{u}-\boldsymbol{u}^{\Sigma})-\mathbf{T})\cdot\boldsymbol{n}^{\Sigma}\right]\!\right]\\ =\rho^{\Sigma}\boldsymbol{f}^{\Sigma}+\nabla_{\Sigma}\cdot\left(\mathbf{T}^{\Sigma}\right).\end{aligned} \tag{2.29}$$

And finally on contact lines

$$\begin{aligned}\rho^{L}\left(\frac{\partial \boldsymbol{u}^{L}}{\partial t}+(\boldsymbol{u}^{L}-\boldsymbol{v}^{L})\cdot\nabla_{L}\boldsymbol{u}^{L}\right)-\left(\!\left(\left(\rho^{\Sigma}(\boldsymbol{u}^{\Sigma}-\boldsymbol{u}^{L})(\boldsymbol{u}^{\Sigma}-\boldsymbol{u}^{L})-\mathbf{T}^{\Sigma}\right)\cdot\boldsymbol{n}^{L}\right)\!\right)\\ =\rho^{L}\boldsymbol{f}^{L}+\nabla_{L}\cdot\left(\mathbf{T}^{L}\right)\end{aligned} \tag{2.30}$$

should uphold.

2.4 Energy conservation

The notion of energy conservation follows along the lines of momentum conservation. However, in addition to energy related to the macroscoping movement of the system, called kinetic energy, the microscoping state of the system contributes to its energy. This contribution is called called inner energy. The total energy contained in the system is then

$$E=\int_{\Omega}\rho\left(\hat{u}+\frac{1}{2}|\boldsymbol{u}|^{2}\right)\,\mathrm{d}V+\int_{\Sigma}\rho^{\Sigma}\left(\hat{u}^{\Sigma}+\frac{1}{2}|\boldsymbol{u}^{\Sigma}|^{2}\right)\,\mathrm{d}S+\int_{L}\rho^{L}\left(\hat{u}^{L}+\frac{1}{2}|\boldsymbol{u}^{L}|^{2}\right)\,\mathrm{d}l. \tag{2.31}$$

The rate at which the energy in the system changes is identified as the work performed by the forces and an additional rate of energy transfer. With these assumptions the energy change rate becomes

$$\frac{\mathrm{d}E}{\mathrm{d}t}=P+Q, \tag{2.32}$$

which is commonly known as the first law of thermodynamics. Recognizing the findings of Section 2.3, the work done by the external forces is defined as

$$P=P_{V}+P_{S}, \tag{2.33a}$$

$$P_{V}=\int_{\Omega}\rho\boldsymbol{u}\cdot\boldsymbol{f}\,\mathrm{d}V+\int_{\Sigma}\rho^{\Sigma}\boldsymbol{u}^{\Sigma}\cdot\boldsymbol{f}^{\Sigma}\,\mathrm{d}S+\int_{L}\rho^{L}\boldsymbol{u}^{L}\cdot\boldsymbol{f}^{L}\,\mathrm{d}l, \tag{2.33b}$$

$$P_{S}=\int_{\partial\Omega}\boldsymbol{u}\cdot(\mathbf{T}\cdot\boldsymbol{n}^{\partial\Omega})\,\mathrm{d}S+\int_{\partial\Sigma}\boldsymbol{u}^{\Sigma}\cdot(\mathbf{T}^{\Sigma}\cdot\boldsymbol{n}_{\partial\Sigma})\,\mathrm{d}l+\int_{\partial L}\boldsymbol{u}^{L}\cdot(\mathbf{T}^{L}\cdot\boldsymbol{n}_{\partial L})\,\mathrm{d}s. \tag{2.33c}$$

In analogy to the forces the energy transfer is postulated to have a volumetric, radiant energy transmission, and boundary contribution, called contact energy transmission (Slattery et al., 2007, p. 288ff.). The derivation is somewhat abbreviated here, but finally this energy transfer rate is expressed in terms of a rate of radiant energy transmission and the energy flux vector:

$$Q=Q_{V}+Q_{S}, \tag{2.34a}$$

$$Q_{V}=\int_{\Omega}\rho\hat{r}\,\mathrm{d}V+\int_{\Sigma}\rho^{\Sigma}\hat{r}^{\Sigma}\,\mathrm{d}S+\int_{L}\rho^{L}\hat{r}^{L}\,\mathrm{d}l, \tag{2.34b}$$

$$Q_{S}=\int_{\partial\Omega}-\boldsymbol{q}\cdot\boldsymbol{n}^{\partial\Omega}\,\mathrm{d}S+\int_{\partial\Sigma}-\boldsymbol{q}^{\Sigma}\cdot\boldsymbol{n}_{\partial\Sigma}\,\mathrm{d}l+\int_{\partial L}-\boldsymbol{q}^{L}\cdot\boldsymbol{n}_{\partial L}\,\mathrm{d}s. \tag{2.34c}$$

From multiplying Eqs. (2.28) to (2.30) by the respective velocities, the energy balances for the kinetic energy can be obtained:

$$\rho \boldsymbol{u} \cdot \left(\frac{\partial \boldsymbol{u}}{\partial t} + \boldsymbol{u} \cdot \nabla \boldsymbol{u} \right) = \rho \boldsymbol{u} \cdot \boldsymbol{f} + \boldsymbol{u} \cdot \nabla \cdot (\mathbf{T}) \,, \tag{2.35}$$

$$\begin{aligned} \rho^{\Sigma} \boldsymbol{u}^{\Sigma} \cdot \left(\frac{\partial \boldsymbol{u}^{\Sigma}}{\partial t} + (\boldsymbol{u}^{\Sigma} - \boldsymbol{v}^{\Sigma}) \cdot \nabla_{\Sigma} \boldsymbol{u}^{\Sigma} \right) - \left[\!\left[\boldsymbol{u}^{\Sigma} \cdot \left(\rho (\boldsymbol{u} - \boldsymbol{u}^{\Sigma})(\boldsymbol{u} - \boldsymbol{u}^{\Sigma}) - \mathbf{T} \right) \cdot \boldsymbol{n}^{\Sigma} \right]\!\right] \\ = \rho^{\Sigma} \boldsymbol{u}^{\Sigma} \cdot \boldsymbol{f}^{\Sigma} + \boldsymbol{u}^{\Sigma} \cdot \nabla_{\Sigma} \cdot \left(\mathbf{T}^{\Sigma} \right) , \end{aligned} \tag{2.36}$$

$$\begin{aligned} \rho^{L} \boldsymbol{u}^{L} \cdot \left(\frac{\partial \boldsymbol{u}^{L}}{\partial t} + (\boldsymbol{u}^{L} - \boldsymbol{v}^{L}) \cdot \nabla_{L} \boldsymbol{u}^{L} \right) - \left(\left(\boldsymbol{u}^{L} \cdot \left(\rho^{\Sigma} (\boldsymbol{u}^{\Sigma} - \boldsymbol{u}^{L})(\boldsymbol{u}^{\Sigma} - \boldsymbol{u}^{L}) - \mathbf{T}^{\Sigma} \right) \cdot \boldsymbol{n}^{L} \right) \right) \\ = \rho^{L} \boldsymbol{u}^{L} \cdot \boldsymbol{f}^{L} + \boldsymbol{u}^{L} \cdot \nabla_{L} \cdot \left(\mathbf{T}^{L} \right) . \end{aligned} \tag{2.37}$$

The energy balance for internal energy can be obtained by combining Eqs. (2.31) to (2.34), applying the transport, Definitions 2.2 to 2.4, and divergence theorems, Definitions 2.5 to 2.7, and using Eqs. (2.20) to (2.22) as well as Eqs. (2.35) to (2.35). Using the same argument as before to separate bulk, interface and line contributions it is possible to obtain the bulk energy balance

$$\rho \left(\frac{\partial \hat{u}}{\partial t} + \boldsymbol{u} \cdot \nabla \hat{u} \right) = \rho \hat{r} + \nabla \cdot (-\boldsymbol{q}) + \mathrm{tr}(\mathbf{T} \cdot \nabla \boldsymbol{u}), \tag{2.38}$$

the interface or jump energy balance

$$\begin{aligned} \rho^{\Sigma} \left(\frac{\partial \hat{u}^{\Sigma}}{\partial t} + (\boldsymbol{u}^{\Sigma} - \boldsymbol{v}^{\Sigma}) \cdot \nabla_{\Sigma} \hat{u}^{\Sigma} \right) \\ - \left[\!\left[\boldsymbol{q} \cdot \boldsymbol{n}^{\Sigma} - (\boldsymbol{u} - \boldsymbol{u}^{\Sigma}) \cdot \mathbf{T} \cdot \boldsymbol{n}^{\Sigma} + \rho \left((\hat{u} - \hat{u}^{\Sigma}) + \frac{1}{2} (\boldsymbol{u} - \boldsymbol{u}^{\Sigma})^2 \right) (\boldsymbol{u} - \boldsymbol{u}^{\Sigma}) \cdot \boldsymbol{n}^{\Sigma} \right]\!\right] \\ = \rho^{\Sigma} \hat{r}^{\Sigma} + \nabla_{\Sigma} \cdot \left(-\boldsymbol{q}^{\Sigma} \right) + \mathrm{tr}(\mathbf{T}^{\Sigma} \cdot \nabla_{\Sigma} \boldsymbol{u}^{\Sigma}), \end{aligned} \tag{2.39}$$

and finally the line energy balance

$$\begin{aligned} \rho^{L} \left(\frac{\partial \hat{u}^{L}}{\partial t} + (\boldsymbol{u}^{L} - \boldsymbol{v}^{L}) \cdot \nabla_{L} \hat{u}^{L} \right) \\ - \left(\left(\boldsymbol{q}^{\Sigma} \cdot \boldsymbol{n}^{L} - (\boldsymbol{u}^{\Sigma} - \boldsymbol{u}^{L}) \cdot \mathbf{T}^{\Sigma} \cdot \boldsymbol{n}^{L} + \rho^{\Sigma} \left((\hat{u}^{\Sigma} - \hat{u}^{L}) + \frac{1}{2} (\boldsymbol{u}^{\Sigma} - \boldsymbol{u}^{L})^2 \right) (\boldsymbol{u}^{\Sigma} - \boldsymbol{u}^{L}) \cdot \boldsymbol{n}^{L} \right) \right) \\ = \rho^{L} \hat{r}^{L} + \nabla_{L} \cdot \left(-\boldsymbol{q}^{L} \right) + \mathrm{tr}(\mathbf{T}^{L} \cdot \nabla_{L} \boldsymbol{u}^{L}). \end{aligned} \tag{2.40}$$

2.5 Constitutive equations

In this section the various conservation laws are complemented with constitutive equations, introducing the specific behavior of the materials to be calculated. In essence, there are various arguments that can be made to justify the choice of constitutive equation. This includes phenomenological material behavior, i.e., observations made in experiments. But also considerations regarding the entropy inequality or independence from the observer (i.e. frame indifference). Here, we will not dive into the details of such considerations, which can be found e.g. in Slattery et al. (2007, p. 304-382), but specify the modeling assumptions used in this work.

2.5.1 Bulk behavior

First, the behavior of the bulk shall be specified. From looking at Eqs. (2.20), (2.28) and (2.38) one can gather the dependent bulk variables

$$V^* := \{\rho, \boldsymbol{u}, \hat{u}, \boldsymbol{f}, \hat{r}, \mathbf{T}, \boldsymbol{q}\}\,. \tag{2.41}$$

It is immediately clear, that there are more variables than bulk equations available and the system is unclosed. The first assumption is to identify the external forcings $\boldsymbol{f}, \hat{r}$ to be given functionals depending on $\boldsymbol{x}$ and t. Next, the stress tensor is specified as that of a Newtonian fluid (Slattery, 2005, p. 41):

$$\mathbf{T} = \left(-p + \hat{\lambda}\nabla\cdot(\boldsymbol{u})\right)\mathbf{I} + \mu\left(\nabla\boldsymbol{u} + \nabla\boldsymbol{u}^T\right). \tag{2.42}$$

This reduces the number of unknowns in the system, but at the same time introduces the pressure p, volume viscosity $\epsilon = \hat{\lambda} + 2/3\mu$ and shear viscosity μ. For the heat flux Fourier's law states (Stephan et al., 2013, p. 211)

$$\boldsymbol{q} = -\hat{k}\nabla T, \tag{2.43}$$

making a connection between heat flux and temperature gradients, using the heat conductivity $\hat{k}$. At last, several thermodynamic/caloric relations are employed to reduce the number of variables. Usually, a connection of the form $\rho = f(p,T)$ is made to define the density as a function of temperature and pressure. In this work we will exclusively consider incompressible fluids, in which case

$$\rho = \text{const.}, \tag{2.44}$$

is a known quantity. The inner energy of an incompressible material is specified by the caloric equation

$$\hat{u} = \hat{c}T \tag{2.45}$$

in dependence of the temperature and heat capacity $\hat{c}$. The newly introduced material properties $\rho, \mu, \hat{c}$ and $\hat{k}$ are assumed to be constant throughout this work. More generally they could be defined as functions of e.g. temperature and pressure. Thus the conservation equations for the bulk of an incompressible, single component, Newtonian fluid with Fourier's law of heat conductivity are given in terms of the dependent variables

$$V := \{p, \boldsymbol{u}, T\}\,, \tag{2.46}$$

to be

$$\nabla\cdot(\boldsymbol{u}) = 0, \tag{2.47}$$

$$\rho\left(\frac{\partial\boldsymbol{u}}{\partial t} + \boldsymbol{u}\cdot\nabla\boldsymbol{u}\right) = \rho\boldsymbol{f} - \nabla p + \nabla\cdot\left(\mu\left(\nabla\boldsymbol{u} + \nabla\boldsymbol{u}^T\right)\right), \tag{2.48}$$

$$\rho\left(\frac{\partial\hat{c}T}{\partial t} + \boldsymbol{u}\cdot\nabla\hat{c}T\right) = \rho\hat{r} + \nabla\cdot\left(\hat{k}\nabla T\right) + \mathrm{tr}(\mathbf{T}\cdot\nabla\boldsymbol{u}). \tag{2.49}$$

The last term in the energy equation, often called viscous dissipation, describes the conversion of kinetic into thermal energy and is often neglected, also in this work, indicated by the grayed-out color.

2.5.2 Surface behavior

In similar fashion as for the bulk the behavior of the dividing interfaces can be specified. The model used in this work makes some rigorous assumptions. First, the surface is assumed to be mass-less, i.e.,

$$\rho^{\Sigma} = 0. \tag{2.50}$$

Based on this assumption the (material) derivatives of surface density, momentum and inner energy vanish, as well as volume forces or radiant energy transfer acting on the interface. What remains is to define the surface stress tensor and surface heat transfer. In Slattery et al. (2007, p. 358ff.) the constitutive modeling of these is discussed in more detail. In this work the surface stress is modeled as isotropic and inviscid as the special case of the more general Boussinesq surface fluid (Slattery et al., 2007, p. 359) as

$$\mathbf{T}^{\Sigma} = \left(\sigma + \hat{\lambda}^{\Sigma}\nabla_{\Sigma}\cdot\left(\boldsymbol{u}^{\Sigma}\right)\right)\mathbf{P}^{\Sigma} + \mu^{\Sigma}\left(\mathbf{P}^{\Sigma}\cdot\nabla_{\Sigma}\boldsymbol{u}^{\Sigma} + \nabla_{\Sigma}\boldsymbol{u}^{\Sigma^{T}}\cdot\mathbf{P}^{\Sigma}\right), \tag{2.51}$$

introducing the surface tension σ, to gather asymmetric molecular interactions in the interface region on the sharp dividing interface. Note the similarity to the modeling of stresses for a Newtonian fluid Eq. (2.42). In this sense, surface tension on the interface plays a similar role to pressure in the bulk. Heat (energy) flux on the surface is not taken into account:

$$\boldsymbol{q}^{\Sigma} = 0. \tag{2.52}$$

With these assumptions and by recognizing that at any point of the surface the massflux from either bulk phase to the interface is $\dot{m} = \dot{m}^{(i)} = \rho^{(i)}(\boldsymbol{u}^{(i)} - \boldsymbol{u}^{\Sigma})\cdot\boldsymbol{n}^{\Sigma}$ the surface continuity equation becomes

$$\left[\!\left[\rho(\boldsymbol{u} - \boldsymbol{u}^{\Sigma})\cdot\boldsymbol{n}^{\Sigma}\right]\!\right] = \left[\!\left[\dot{m}\right]\!\right] = 0. \tag{2.53}$$

Using this result it is possible to simplify the surface momentum equation Eq. (2.29) to

$$-\dot{m}\left[\!\left[\boldsymbol{u}\right]\!\right] + \left[\!\left[\mathbf{T}\cdot\boldsymbol{n}^{\Sigma}\right]\!\right] = -\sigma\kappa\boldsymbol{n}^{\Sigma} + \nabla_{\Sigma}\sigma. \tag{2.54}$$

Equation (2.54) can be further divided into an interface normal and tangential part:

$$-\dot{m}\left[\!\left[\boldsymbol{u}\cdot\boldsymbol{n}^{\Sigma}\right]\!\right] + \left[\!\left[\left(\mathbf{T}\cdot\boldsymbol{n}^{\Sigma}\right)\cdot\boldsymbol{n}^{\Sigma}\right]\!\right] = -\sigma\kappa, \tag{2.55a}$$

$$-\dot{m}\left[\!\left[\mathbf{P}^{\Sigma}\boldsymbol{u}\right]\!\right] + \left[\!\left[\mathbf{P}^{\Sigma}\left(\mathbf{T}\cdot\boldsymbol{n}^{\Sigma}\right)\right]\!\right] = \nabla_{\Sigma}\sigma. \tag{2.55b}$$

This presentation highlights the effect which further assumptions have on these jump conditions. In the remainder of this work the σ is assumed to be constant. The interfaces are not necessarily material ($\dot{m} \neq 0$) and no-slip between bulk phases is assumed ($\left[\!\left[\mathbf{P}^{\Sigma}\boldsymbol{u}\right]\!\right] = \mathbf{0}$, with the exception of Section 7.2). Finally, the energy equation is investigated. Under the assumption of a mass-less, non energy conducting interface Eq. (2.39) can be simplified to

$$-\left[\!\left[\boldsymbol{q}\cdot\boldsymbol{n}^{\Sigma} + \dot{m}\left(\frac{p}{\rho} + \hat{u} + \frac{1}{2}(\boldsymbol{u} - \boldsymbol{u}^{\Sigma})^{2}\right) - (\boldsymbol{u} - \boldsymbol{u}^{\Sigma})\cdot\left(\mu(\nabla\boldsymbol{u} + \nabla\boldsymbol{u}^{T})\right)\cdot\boldsymbol{n}^{\Sigma}\right]\!\right] = \mathrm{tr}(\mathbf{T}^{\Sigma}\cdot\nabla_{\Sigma}\boldsymbol{u}^{\Sigma}),$$

where the model for the bulk stress tensor is already inserted. The terms marked in gray are neglected, as usually thermal effects and pressure-volume work are much greater than energy

transfer associated with the bulk viscous or surface stresses. At last, the enthalpy $\hat{h} = p/\rho + \hat{u}$ is introduced to obtain the final form

$$-\left[\left[\boldsymbol{q}\cdot\boldsymbol{n}^{\Sigma}\right]\right] + \dot{m}\left[\left[\hat{h}\right]\right] = 0. \tag{2.56}$$

In the course of this work either a model for material interfaces is employed, in which case

$$-\left[\left[\boldsymbol{q}\cdot\boldsymbol{n}^{\Sigma}\right]\right] = 0, \tag{2.57a}$$
$$\left[\left[T\right]\right] = 0, \tag{2.57b}$$

or a simple evaporation model, with a constant saturation temperature from either bulk phase at the interface:

$$\left[\left[\hat{h}\right]\right] = \hat{h}_{vap}, \tag{2.58a}$$
$$T = T_{sat}. \tag{2.58b}$$

This model is motivated by considering equilibrium thermodynamics, were it is assumed, that liquids and their vapor are in mechanical, thermal (and chemical) equilibrium at the interface. More involved models take into account the pressure dependency of the local saturation temperature, which in turn depends on the local curvature (Kelvin effect), interfacial thermal and kinetic resistances (Schrage molecular-kinetic theory of evaporation), molecular forces (disjoining pressure), especially at the contact line and other microscopic effects that may be relevant, see e.g. (Marengo and Coninck, 2022; Rednikov and Colinet, 2013; Rednikov and Colinet, 2019, p. 133ff.).

2.5.3 Line behavior

At last the line behavior needs to be specified. By assuming a negligible line density

$$\rho^{L} = 0, \tag{2.59}$$

together with mass-less interfaces, the left-hand side (LHS) of the jump mass balance on common lines Eq. (2.22) vanishes identically. By using Eq. (2.51) and assuming a non-existing line stress tensor

$$\mathbf{T}^{L} = \mathbf{0}, \tag{2.60}$$

the jump momentum balance on common lines Eq. (2.30) immediately transforms to

$$\left(\left(\sigma\boldsymbol{n}^{L}\right)\right) = \mathbf{0}. \tag{2.61}$$

Finally, it is assumed that no energy transfer takes place along the common lines, in which case Eq. (2.40) gives

$$\left(\left(\sigma(\boldsymbol{u}^{\Sigma} - \boldsymbol{u}^{L})\cdot\boldsymbol{n}^{L}\right)\right) = 0, \tag{2.62}$$

which reduces to Eq. (2.61), when assuming $\left(\left(\boldsymbol{u}^{\Sigma}\cdot\boldsymbol{n}^{L}\right)\right) = 0$. Throughout the remainder of this work not three separate fluid phases are considered, but usually two fluids that may both be in contact with a solid body. Furthermore, this solid is often times very rigid, and it may be helpful to consider it non-deformable. In that special case one usually neglects the force balance normal to

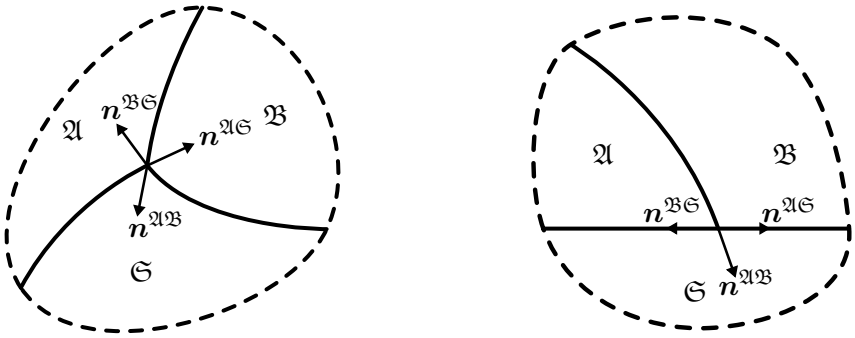

Figure 2.2: Left: Depiction of the Neumann triangle (Slattery et al., 2007, p. 127), i.e. Eq. (2.61), for the section through the normal plane of a general three-phase contact line.
Right: A fluid-fluid interface intersecting a rigid solid. This situation is described by Young's equation (2.65).

the fluid-solid interfaces and restricts it to the solid-fluid interface tangential plane at the contact line:

$$\mathbf{P}^{\mathfrak{S}}\left(\left(\sigma \boldsymbol{n}^{L}\right)\right) = \mathbf{0}. \tag{2.63}$$

This situation is depicted in Fig. 2.2. Here, $\mathfrak{A}$ and $\mathfrak{B}$ describe the fluid phases and $\mathfrak{S}$ the solid. Using the respective interfacial energies and normal vectors as shown in the figure Eq. (2.63) reduced to

$$\left(\sigma^{\mathfrak{AB}}\boldsymbol{n}^{\mathfrak{AB}} + \sigma^{\mathfrak{AS}}\boldsymbol{n}^{\mathfrak{AS}} + \sigma^{\mathfrak{BS}}\boldsymbol{n}^{\mathfrak{BS}}\right) \cdot \boldsymbol{n}^{\mathfrak{AS}} = 0, \tag{2.64}$$

$$\sigma^{\mathfrak{AB}}\cos(\theta_{\text{stat}}) + \sigma^{\mathfrak{AS}} - \sigma^{\mathfrak{BS}} = 0, \tag{2.65}$$

known as Young's equation (Marengo and Coninck, 2022, p. 6). Thus, in a model with this exact three phases it is sufficient to prescribe the fluid-fluid surface tension $\sigma = \sigma^{\mathfrak{AB}}$ and static contact-angle

$$\theta_{\text{stat}} = \cos\left(-\frac{\sigma^{\mathfrak{AS}} - \sigma^{\mathfrak{BS}}}{\sigma}\right)^{-1}. \tag{2.66}$$

2.6 Systems of equations

With the description of multiphase flows established up to this point we can specify the complete form of the systems of equations we want to solve, using the numerical method described later in Chapter 4. Even though this section might be a bit repetitive we want to take the time to write the complete set of differential equations, interfacial jump conditions and boundary conditions used for the different kinds of multiphase flows investigated in this work. To shorten the notation it is not explicitly distinguished which phase a variable belongs to, in other words, $\boldsymbol{u}$ denotes the bulk velocity in any phase, based on location $\boldsymbol{x}$. Throughout the actual simulations performed in this work usually exactly two fluid phases are considered. In that case $\mathfrak{A}$ and $\mathfrak{B}$ are used to denote the respective partial domains, cf. Fig. 2.2.

2.6.1 Material incompressible multiphase flow

The first type of flow to be considered is based on the modeling described in the section before. However, the energy equation is not included in the final system and the phases are assumed to not exchange mass, i.e., $\dot{m} = 0$ on Σ and therefore

$$\boldsymbol{u}^{\Sigma} \cdot \boldsymbol{n}^{\Sigma} = \boldsymbol{u} \cdot \boldsymbol{n}^{\Sigma}. \tag{2.67}$$

With this we are prepared to state the complete system of equations for the incompressible mutliphase flow without masstransfer.

Definition 2.8 (Bulk equations). *The governing bulk equations valid in each phase separated by sharp dividing interfaces are*

$$\nabla \cdot (\boldsymbol{u}) = 0, \tag{2.68a}$$

$$\rho \left(\frac{\partial \boldsymbol{u}}{\partial t} + \boldsymbol{u} \cdot \nabla \boldsymbol{u} \right) = -\nabla p + \mu \nabla \cdot \left(\nabla \boldsymbol{u} + \nabla \boldsymbol{u}^T \right) + \rho \boldsymbol{g}. \tag{2.68b}$$

Each phase defines its own variables $\boldsymbol{u}$ and p as well as material parameters ρ and μ.

Definition 2.9 (Interface equations). *On the interface the jump conditions are reduced to*

$$\left[\!\left[\boldsymbol{u} \cdot \boldsymbol{n}^{\Sigma} \right]\!\right] = 0, \tag{2.69a}$$

$$\left[\!\left[\mathbf{T} \cdot \boldsymbol{n}^{\Sigma} \right]\!\right] = -\sigma \kappa \boldsymbol{n}^{\Sigma} + \nabla_{\Sigma} \sigma. \tag{2.69b}$$

With the no-slip closure condition (Slattery et al., 2007, p. 160)

$$\left[\!\left[\mathbf{P}^{\Sigma} \boldsymbol{u} \right]\!\right] = \mathbf{0}. \tag{2.70}$$

Definition 2.10 (Boundary conditions). *Finally, it is necessary to prescribe appropriate boundary condition (BC)s. This is done here by Robin type boundary conditions, in somewhat unconventional notation, splitting the boundary condition in a normal and tangential part, using the projection tensor $\mathbf{P}^{\partial\Omega} = \mathbf{I} - \boldsymbol{n}^{\partial\Omega} \otimes \boldsymbol{n}^{\partial\Omega}$:*

$$\mathbf{P}^{\partial\Omega} \left(\left(-p\mathbf{I} + \mu \left(\nabla \boldsymbol{u} + \nabla \boldsymbol{u}^T \right) \right) \boldsymbol{n}^{\partial\Omega} - \boldsymbol{\tau}_{\partial\Omega} \right) = -\beta \mathbf{P}^{\partial\Omega} \left(\boldsymbol{u} - \boldsymbol{s} \right), \tag{2.71a}$$

$$\boldsymbol{n}^{\partial\Omega} \cdot \left(\left(-p\mathbf{I} + \mu \left(\nabla \boldsymbol{u} + \nabla \boldsymbol{u}^T \right) \right) \boldsymbol{n}^{\partial\Omega} - \boldsymbol{\tau}_{\partial\Omega} \right) = -\beta_N \boldsymbol{n}^{\partial\Omega} \cdot \left(\boldsymbol{u} - \boldsymbol{s} \right). \tag{2.71b}$$

This formulation allows to switch between a no-slip wall for $\beta \to \infty$ (resembling a Dirichlet type BC), a prescribed shear stress $\beta = 0$ (resembling a Neumann type BC) or a Navier-slip boundary condition (Robin type) else[4][5]. In boundary normal direction the same condition is given. However, usually either $\beta_N \to \infty$ for an impermeable wall or $\beta_N = 0$ for an outlet is used. Equation (2.65) *stated Young's equation, as a result from the contact line momentum balance at an idealized rigid solid. In this work the following condition, commonly referred to as generalized Navier boundary condition, cf.*

[4] The boundary stress is always assumed to be $\boldsymbol{\tau}_{\partial\Omega} = \mathbf{0}$ in case of a Robin boundary condition.

[5] The tangential slip boundary condition in the solver is always combined with a Dirichlet boundary condition in boundary normal direction.

Gerbeau and Lelièvre (2009) and Smuda and Kummer (2021), is set as a boundary condition for the interface:

$$\sigma(cos(\theta_{stat}) - cos(\theta)) = \beta_L(\boldsymbol{u}^\Sigma - \boldsymbol{s}) \cdot \hat{\boldsymbol{n}}^L. \tag{2.72}$$

The formulation introducing the contact line friction parameter β_L enables us to either consider an immobile contact line $\beta \to \infty$, disregarding the static contact angle completely, or a freely moving contact line $\beta = 0$, always ensuring the dynamic contact angle follows the equilibrium value. The augmented normal $\hat{\boldsymbol{n}}^L$ is normal to the contact line, and tangential to the rigid solid, i.e., $\boldsymbol{n}^{\mathfrak{AS}}$ in the right image of Fig. 2.2.

2.6.2 Incompressible multiphase flow with evaporation

Next, multiphase flow with mass transfer, due to evaporation, is considered. The systems in question are still single component in the fluid phases. Now, the energy equation is included and in general $\dot{m} \neq 0$. Therefore, the interface normal velocity evaluated from either phase is

$$\boldsymbol{u}^\Sigma \cdot \boldsymbol{n}^\Sigma = \boldsymbol{u} \cdot \boldsymbol{n}^\Sigma - \frac{\dot{m}}{\rho}. \tag{2.73}$$

Definition 2.11 (Bulk equations). *For the incompressible multiphase flow with evaporation the bulk equations are*

$$\nabla \cdot (\boldsymbol{u}) = 0, \tag{2.74a}$$

$$\rho\left(\frac{\partial \boldsymbol{u}}{\partial t} + \boldsymbol{u} \cdot \nabla \boldsymbol{u}\right) = -\nabla p + \mu \nabla \cdot \left(\nabla \boldsymbol{u} + \nabla \boldsymbol{u}^T\right) + \rho \boldsymbol{g}, \tag{2.74b}$$

$$\rho \hat{c}\left(\frac{\partial T}{\partial t} + \boldsymbol{u} \cdot \nabla T\right) = \hat{k} \nabla \cdot (\nabla T)\,. \tag{2.74c}$$

Each phase defines its own variables $\boldsymbol{u}, p$ and T as well as material parameters $\rho, \mu, \hat{c}$ and $\hat{k}$. By omitting the momentum and mass balance it is possible to include a solid phase in which only the conjugate heat transfer is calculated.

Definition 2.12 (Interface equations). *Taking into account the mass flux, the jump equations on the interface are*

$$\left[\!\left[\boldsymbol{u} \cdot \boldsymbol{n}^\Sigma\right]\!\right] = \dot{m} \left[\!\left[\frac{1}{\rho}\right]\!\right], \tag{2.75a}$$

$$-\dot{m} \left[\!\left[\boldsymbol{u}\right]\!\right] + \left[\!\left[\mathbf{T} \cdot \boldsymbol{n}^\Sigma\right]\!\right] = -\sigma\kappa \boldsymbol{n}^\Sigma + \nabla_\Sigma \sigma, \tag{2.75b}$$

$$\left[\!\left[\boldsymbol{q} \cdot \boldsymbol{n}^\Sigma\right]\!\right] = \dot{m} \hat{h}_{vap}. \tag{2.75c}$$

With the closure conditions

$$\left[\!\left[\mathbf{P}^\Sigma \boldsymbol{u}\right]\!\right] = \mathbf{0}, \tag{2.76a}$$

$$T = T_{sat}. \tag{2.76b}$$

The last condition enforces saturation temperature on the interface, on which evaporation takes place. On all other interfaces the jump condition

$$[\![\boldsymbol{q} \cdot \boldsymbol{n}^{\Sigma}]\!] = -Q^{\Sigma}, \tag{2.77a}$$

taking into account a possible heat source on the interface and closure

$$[\![T]\!] = 0 \tag{2.77b}$$

are employed instead.

Definition 2.13 (Boundary conditions). *At last the boundary conditions have to be specified. These follow the same considerations as in Section 2.6.1, but extended by the appropriate boundary condition for the temperature:*

$$\mathbf{P}^{\partial\Omega}\left(\left(-p\mathbf{I} + \mu\left(\nabla\boldsymbol{u} + \nabla\boldsymbol{u}^{T}\right)\right)\boldsymbol{n}^{\partial\Omega} - \boldsymbol{\tau}_{\partial\Omega}\right) = -\beta\mathbf{P}^{\partial\Omega}\left(\boldsymbol{u} - \boldsymbol{s}\right), \tag{2.78a}$$

$$\boldsymbol{n}^{\partial\Omega} \cdot \left(\left(-p\mathbf{I} + \mu\left(\nabla\boldsymbol{u} + \nabla\boldsymbol{u}^{T}\right)\right)\boldsymbol{n}^{\partial\Omega} - \boldsymbol{\tau}_{\partial\Omega}\right) = -\beta_N\boldsymbol{n}^{\partial\Omega} \cdot \left(\boldsymbol{u} - \boldsymbol{s}\right), \tag{2.78b}$$

$$\left(\hat{k}\nabla T \cdot \boldsymbol{n}^{\partial\Omega} - q_{\partial\Omega}\right) = -\beta_T\left(T - T_{\partial\Omega}\right). \tag{2.78c}$$

The parameter β_T can be thought of as a thermal resistance of the boundary, switching between a prescribed boundary temperature or heat flux [6]. The boundary condition for the interface remains unchanged:

$$\sigma(cos(\theta_{stat}) - cos(\theta)) = \beta_L(\boldsymbol{u}^{\Sigma} - \boldsymbol{s}) \cdot \hat{\boldsymbol{n}}^{L}. \tag{2.79}$$

2.6.3 Free surface flows

In Section 7.1 the modeling of the boundary condition for the dynamic contact angle will be investigated. To this end a free surface flow is considered. This is a special case of the system presented in Section 2.6.1, where only one “active” phase exists. This means the opposing phase at the dividing interface has no influence on the “active” phase and the jump conditions are exchanged for boundary conditions on the interface. Additionally, the flow equations are solved quasi-stationary and are non-dimensionalized, introducing the Reynolds *Re*, Weber *We* and Froude *Fr* numbers

$$Re = \frac{\rho U L}{\mu}, \tag{2.80}$$

$$We = \frac{\rho U^2 L}{\sigma}, \tag{2.81}$$

$$Fr = \frac{U^2}{|\boldsymbol{g}|L}. \tag{2.82}$$

For completeness we state again the whole system of equations and boundary conditions.

[6] The heat flux is always assumed to be $\boldsymbol{q} = \mathbf{0}$ in case of a Robin boundary condition.

Definition 2.14 (Bulk equations). *For the bulk equations of the single phase flow with moving boundary we find*[7]

$$\nabla \cdot (\boldsymbol{u}) = 0, \tag{2.83a}$$

$$-\nabla p + \frac{1}{Re}\nabla \cdot (\mu \nabla \boldsymbol{u}) + \frac{\boldsymbol{g}}{Fr} = 0. \tag{2.83b}$$

Definition 2.15 (Interface equations). *On the interface the jump conditions are exchanged for boundary conditions*

$$\mathbf{P}^{\Sigma}\left(\left(-p\mathbf{I} + \frac{\mu}{Re}\nabla \boldsymbol{u}\right)\boldsymbol{n}^{\Sigma}\right) = \frac{1}{We}\nabla_{\Sigma}\sigma, \tag{2.84a}$$

$$\left(\left(-p\mathbf{I} + \frac{\mu}{Re}\nabla \boldsymbol{u}\right)\boldsymbol{n}^{\Sigma}\right)\cdot \boldsymbol{n}^{\Sigma} - \frac{\sigma}{We}\kappa = \beta_{\Sigma}\boldsymbol{u}\cdot\boldsymbol{n}^{\Sigma}, \tag{2.84b}$$

describing a fixed, immobile interface for $\beta_{\Sigma} \to \infty$ or a movable interface and constant pressure environment when $\beta_{\Sigma} = 0$

Definition 2.16 (Boundary conditions). *On the boundary the same boundary conditions as before are considered:*

$$\mathbf{P}^{\partial\Omega}\left(\left(-p\mathbf{I} + \frac{\mu}{Re}\nabla \boldsymbol{u}\right)\boldsymbol{n}^{\partial\Omega} - \boldsymbol{\tau}_{\partial\Omega}\right) = -\beta\mathbf{P}^{\partial\Omega}\left(\boldsymbol{u} - \boldsymbol{s}\right), \tag{2.85a}$$

$$\boldsymbol{n}^{\partial\Omega}\cdot\left(\left(-p\mathbf{I} + \frac{\mu}{Re}\nabla \boldsymbol{u}\right)\boldsymbol{n}^{\partial\Omega} - \boldsymbol{\tau}_{\partial\Omega}\right) = -\beta_{N}\boldsymbol{n}^{\partial\Omega}\cdot\left(\boldsymbol{u} - \boldsymbol{s}\right). \tag{2.85b}$$

As we wish to investigate the influence of the modeling for the dynamic contact angle with this system, the condition for this angle is not fully specified yet, but merely given in implicit form:

$$f(\boldsymbol{u}, \boldsymbol{s}, \theta, \theta_{stat}) = 0. \tag{2.86}$$

[7] Here, the viscosity, surface tension and gravitational direction vector $\boldsymbol{g}$ are non-dimensional parameters of $\mathcal{O}(1)$ to capture spatial variations in magnitude (and direction).

3 Fundamentals of the extended discontinuous Galerkin method

In Chapter 2, sets of partial differential equations describing multiphase flows are introduced. To make predictions of the behavior of real fluids, one needs to find a strategy to solve these equations for the dependent variables. In practice, it is rare to find a closed-form solution for these equations, although possible in individual cases, cf. (Slattery et al., 2007). It is therefore practicable to search for numerical schemes to obtain approximate solutions. The method of choice for this work is the discontinuous Galerkin (DG) method. In context of the multiphase flows investigated in this work, an extension of the DG method working on unfitted meshes, called extended discontinuous Galerkin (XDG) method, is used. In the following sections, the main ideas and principles behind the DG and XDG method will be presented. The presentation of the DG method is heavily influenced by the works of Arnold et al. (2002), Di Pietro and Ern (2012), and Dolejší and Feistauer (2015).

3.1 Discontinuous Galerkin essentials

To motivate the discussion of the DG method, consider the following example: The task at hand is to calculate the movement of a droplet sitting on a flat plate (Fig. 3.1). The way one would proceed is to first make an abstraction in selecting only a part of the real problem to be computed. This selection is called the computational domain Ω and the task at hand is to solve the equations discussed in Chapter 2 on this domain. Three questions one may ask are:

1. How to represent the sought-after variables?
2. How to calculate a specific solution for this representation?
3. How accurate is the prediction obtained in this way?

How to represent the sought-after variables? Now, to answer the first question two natural choices arise. One could imagine to only compute a solution at discrete points, kind of in the way a printer creates a document by depositing small droplets of ink that in their entirety give a complete picture. Or one could try to represent the solution by computing functions defined over the whole domain, the way a painter creates a picture with many continuous strokes. Before continuing to answer the questions above it is therefore practical to introduce some formal definitions for the function spaces, from which the solution functions are taken. The overall goal is then to find a solution in some vector space, solving a weak (integral) form of the original partial differential equation (PDE).

Definition 3.1 (Inner product and induced norms). *The L^p-norm of a function $f : \boldsymbol{x} \in \Omega \subset \mathbb{R}^D \to \mathbb{R}$ is defined as (Di Pietro and Ern, 2012; Dolejší and Feistauer, 2015)*

$$\|f\|_{L^p(\Omega)} = \left(\int_\Omega |f|^p \ dV \right)^{\frac{1}{p}}. \tag{3.1}$$

Of special significance is the L^2-norm, which is induced by the inner product

$$\langle f, f \rangle_{L^2(\Omega)} = \int_\Omega f \cdot f \ dV = \|f\|^2_{L^2(\Omega)}. \tag{3.2}$$

The Sobolev norm and seminorm are defined as

$$\|f\|_{W^{m,p}(\Omega)} = \left(\sum_{\alpha \in A^m_D} \|\partial^\alpha f\|^p_{L^p(\Omega)} \right)^{\frac{1}{p}}, \tag{3.3a}$$

$$|f|_{W^{m,p}(\Omega)} = \left(\sum_{\alpha \in \overline{A}^m_D} \|\partial^\alpha f\|^p_{L^p(\Omega)} \right)^{\frac{1}{p}}, \tag{3.3b}$$

where the degree of the derivatives is controled by multi-index α:

$$A^m_D := \left\{ \alpha \in \mathbb{N}^D \mid \sum_i |\alpha_i| \leq m \right\}, \tag{3.4a}$$

$$\overline{A}^m_D := \left\{ \alpha \in \mathbb{N}^D \mid \sum_i |\alpha_i| = m \right\}. \tag{3.4b}$$

Note the special cases

$$\|f\|_{W^{0,p}(\Omega)} = \|f\|_{L^p(\Omega)}, \tag{3.5a}$$

$$\|f\|_{H^m(\Omega)} = \|f\|_{W^{m,2}(\Omega)}. \tag{3.5b}$$

Definition 3.2 (Lebesgue spaces). *The Lebesgue space $L^p(\Omega)$ is the space that contains all functions that are Lebesgue measurable:*

$$L^p(\Omega) := \left\{ f : \Omega \to \mathbb{R} \mid \|f\|_{L^p(\Omega)} < \infty \right\}. \tag{3.6}$$

When equipped with the inner product inducing the L^2-norm, $L^2(\Omega)$ is a Hilbert space (a special form of a metric space) (Di Pietro and Ern, 2012). In this sense the L^2-norm defines the length of a function (over some domain Ω) in the same way the euclidean norm defines the length of a vector in $\mathbb{R}^D$. In the later analysis, we will not rely on these spaces too much, but for completeness we shall also give the definition of Sobolev spaces.

Definition 3.3 (Sobolev spaces). *The $W^{m,p}$ Sobolev space not only makes demands on the integrability of a function, but also its derivatives. It consists of those functions that are part of $L^p(\Omega)$ and whose derivatives up to degree m are also part of $L^p(\Omega)$:*

$$W^{m,p}(\Omega) := \left\{ f \in L^p(\Omega) \mid \forall \alpha \in A^m_D, \partial^\alpha f \in L^p(\Omega) \right\}. \tag{3.7}$$

Commonly used are the special cases

$$H^1(\Omega) := W^{1,2}(\Omega), \tag{3.8a}$$
$$H^2(\Omega) := W^{2,2}(\Omega). \tag{3.8b}$$

The DG method proceeds then by dividing the computational domain in many disjunct subdomains, called cells, and representing the sought-after solution in each of these cells as a linear combination of a set of smooth, differentiable (usually polynomial) functions. In this sense the solution is an element of one of the above vector spaces defined over the set of all cells, called the mesh. This procedure is sketched in Fig. 3.1, assuming already a two-phase problem.

Definition 3.4 (Computational Mesh). *Given a computational domain*

$$\Omega \in \mathbb{R}^D, \tag{3.9}$$

a numerical mesh divides this domain into a non-overlapping set of cells that covers the complete domain:

$$\mathfrak{K}_h := \{K_1, \dots, K_{N_K}\}, \quad K_i \cap K_j = \emptyset \, for \, i \neq j, \quad \overline{\Omega} = \bigcup_i \overline{K}_i. \tag{3.10}$$

In many circumstances, e.g. when Ω is polygonal and simply connected the mesh covers the domain exactly. The set of all edges in the mesh is defined by the union of cell boundaries, which can be distinguished by inner Γ_{int} and boundary edges Γ_{out}:

$$\Gamma := \bigcup_i \partial K_i = \Gamma_{int} \cup \Gamma_{out} = \{\Gamma_1, \dots, \Gamma_{N_\Gamma}\}, \quad \Gamma_{int} = \Gamma \setminus \partial\Omega. \tag{3.11}$$

For piecewise continuous functions $f \in C^1(\mathfrak{K}_h \setminus \Gamma)$ and $\boldsymbol{f} \in \left(C^1(\mathfrak{K}_h \setminus \Gamma)\right)^D$ the broken gradient and divergence operators are denoted by $\nabla_h f$ and $\nabla_h \cdot (\boldsymbol{f})$, such that they return exactly the usual gradient and divergence on each cell, i.e., $\mathfrak{K}_h \setminus \Gamma$. Furthermore, a normal field is defined on Γ, complying with the definitions of Section 2.1, see also Fig. 2.1. Finally, to shorten the later notation the integration over the whole computational mesh and set of edges describes the following operations

$$\int_{\mathfrak{K}_h} f \; dV = \sum_{i=1}^{N_K} \int_{K_i} f \; dV, \tag{3.12a}$$
$$\int_{\Gamma} f \; dS = \sum_{i=1}^{N_\Gamma} \int_{\Gamma_i} f \, dS, \tag{3.12b}$$

in the same fashion the L^p-norm over the whole mesh follows

$$\|f\|_{L^p(\mathfrak{K}_h)} = \left(\sum_{i=1}^{N_K} \|f\|^p_{L^p(K_i)} \right)^{\frac{1}{p}}. \tag{3.13}$$

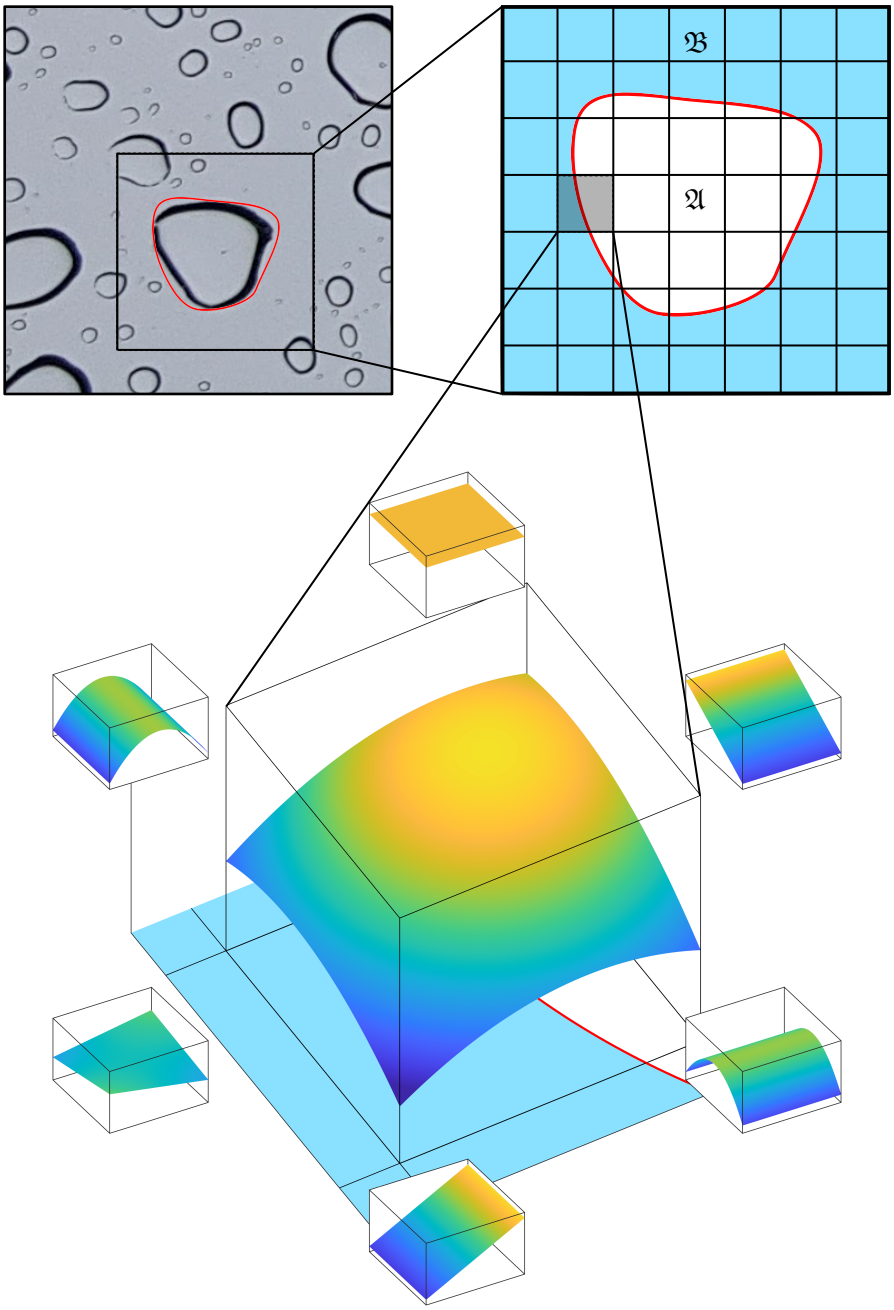

Figure 3.1: Rough sketch of the discretization procedure. From a physical process, here a few droplets sitting on a plate (Newbry, 2017), some subdomain considering a single droplet (and excluding all others) is selected. Then a mesh is defined on this subdomain. The interface is highlighted in red, the liquid domain $\mathfrak{A}$ in white and the vapor (gas/air) domain $\mathfrak{B}$ in blue. In each background cell of the mesh a set of functions as the basis for the DG solution is defined (lower picture small plots), which can be superposed to obtain the cell-local solution (lower picture central large plot). For the XDG method these functions are subsequently restricted to their respective phase using the interface position (not shown in the picture).

Definition 3.5 (Jump and average operators). *In analogy to Definition 2.1 we define the jump and average operators for an arbitrary function f on the edges of the mesh as*

$$[\![f]\!] = \begin{cases} f^- - f^+ \text{ on } \Gamma_{int} \\ f^- \text{ on } \Gamma_{out} \end{cases}, \tag{3.14a}$$

$$\{\{f\}\} = \begin{cases} \frac{1}{2}\left(f^- + f^+\right) \text{ on } \Gamma_{int} \\ f^- \text{ on } \Gamma_{out} \end{cases}. \tag{3.14b}$$

The inner f^- and outer f^+ values are defined w.r.t. to the normal on the edge

$$f^- := \lim_{\epsilon \to 0} f(\boldsymbol{x} - \epsilon \boldsymbol{n}^\Gamma) \quad \text{for } \boldsymbol{x} \in \Gamma, \tag{3.15a}$$

$$f^+ := \lim_{\epsilon \to 0} f(\boldsymbol{x} + \epsilon \boldsymbol{n}^\Gamma) \quad \text{for } \boldsymbol{x} \in \Gamma_{int}. \tag{3.15b}$$

Note that especially for $\Gamma_k = \partial K^- \cap \partial K^+$ we find

$$\int_{\partial K^- \cap \partial K^+} \boldsymbol{f}^- \cdot \boldsymbol{n}_{\partial K^-} + \boldsymbol{f}^+ \cdot \boldsymbol{n}_{\partial K^+} \, dS = \int_{\Gamma_k} [\![\boldsymbol{f} \cdot \boldsymbol{n}_{\Gamma_k}]\!] \, dS, \tag{3.16a}$$

$$\int_{\partial K^- \cap \partial K^+} \frac{1}{2}\left(\boldsymbol{f}^- + \boldsymbol{f}^+\right) \, dS = \int_{\Gamma_k} \{\{\boldsymbol{f}\}\} \, dS. \tag{3.16b}$$

For the DG method, in each cell of the mesh a dependent variable is represented by a linear combination of a set of basis functions. Each of these basis functions is weighted by a coefficient, called a degree of freedom (DOF). In principle the choice of basis is completely free. In most cases, also in this work, the space of polynomials of a certain degree is chosen.

Definition 3.6 (Polynomial spaces). *The polynomial space $\mathbb{P}_k^C(\Omega)$ contains all polynomials up to total degree k:*

$$\mathbb{P}_k^C(\Omega) := \left\{ f \in L^2(\Omega) \mid f \text{ is polynomial with } \deg(f) \leq k \right\}. \tag{3.17}$$

The adjective “discontinuous” in the DG method describes, that a variable can have discontinuities at the edges between cells. This motivates the definition of broken polynomial spaces as a space of piecewise polynomial functions.

Definition 3.7 (Broken polynomial spaces). *The broken polynomial space $\mathbb{P}_k(\mathfrak{K}_h)$ contains all elements of the piece-wise polynomial spaces over all cells and is defined as*

$$\mathbb{P}_k(\mathfrak{K}_h) := \left\{ f \in L^2(\Omega) \mid f|_K \in \mathbb{P}_k^C(K), \quad \forall K \in \mathfrak{K}_h \right\}. \tag{3.18}$$

Finally, a specific basis can be chosen for these finite dimensional spaces:

$$\text{basis}(\mathbb{P}_k^C(K_i)) := \boldsymbol{\Phi_i} = (\Phi_{i,1}, \ldots, \Phi_{i,N_k})^T, \tag{3.19a}$$

$$\text{basis}(\mathbb{P}_k(\mathfrak{K}_h)) := \boldsymbol{\Phi} = (\boldsymbol{\Phi_1}, \ldots, \boldsymbol{\Phi_{N_K}})^T, \tag{3.19b}$$

taking into account the number of basis polynomials $N_k = (k+D)!/(k!D!)$ (Di Pietro and Ern, 2012). There is an infinite number of specific bases that may be chosen. In practice, often either

a modal or nodal basis is used, where in this work a modal basis is employed. For the first kind the basis polynomials satisfy

$$\langle \Phi_{i,n}, \Phi_{i,m} \rangle_{L^2(K_i)} = \delta_{nm} = \begin{cases} 1, & n = m \\ 0, & n \neq m \end{cases}, \tag{3.20}$$

whereas a nodal basis is defined by

$$\Phi_{i,n}(\boldsymbol{x}_{i,m}) = \delta_{nm} = \begin{cases} 1, & n = m \\ 0, & n \neq m \end{cases}, \tag{3.21}$$

at a set of distinct points $\boldsymbol{x}_{i,m} \in K_i$ (Marsden et al., 2008).

In Fig. 3.1, the following steps to represent a specific variable in the DG space are outlined. First, a computational domain is selected as a subdomain of the complete environment. Next, a mesh is defined on this domain. Finally, on each cell a set of basis functions is specified, here exemplary done for one cell. A discrete representation of a variable (e.g. fluid velocity) $f_h \in \mathbb{P}_k(\mathfrak{K}_h)$ is then given by the scalar product of a time-dependent DOF vector $\hat{\boldsymbol{f}} \in \mathbb{R}^{N_K \times N_k}$ and the basis functions:

$$f_h(t, \boldsymbol{x}) = \hat{\boldsymbol{f}}(t) \cdot \boldsymbol{\Phi}(\boldsymbol{x}) = \sum_{i=1}^{N_K} \hat{\boldsymbol{f}}_i(t) \cdot \boldsymbol{\Phi}_i(\boldsymbol{x}) = \sum_{i=1}^{N_K} \sum_{j=1}^{N_k} \hat{f}_{i,j}(t) \Phi_{i,j}(\boldsymbol{x}). \tag{3.22}$$

How to calculate a specific solution for this representation? Now, that it is defined how a variable can be represented on the domain, it must be determined how a specific solution based on a PDE can be computed. Before considering a PDE, first consider the optimal approximation inside a given broken polynomial space of any function $f \in L^2(\Omega)$ by $f_I \in \mathbb{P}_k(\mathfrak{K}_h)$. This optimality condition can be interpreted as minimizing the distance between f and f_I. Which means

$$\min_{f_I \in \mathbb{P}_k(\mathfrak{K}_h)} \quad \frac{1}{2} \| f - f_I \|_{L^2(\mathfrak{K}_h)}, \tag{3.23}$$

when choosing the L^2-norm to compute this distance. It is immediately clear, that this distance is minimal iff the deviation $f - f_I$ is orthogonal to the ansatz space $\mathbb{P}_k(\mathfrak{K}_h)$:

$$\langle f - f_I, v \rangle_{L^2(\mathfrak{K}_h)} = 0, \quad \forall v \in \mathbb{P}_k(\mathfrak{K}_h). \tag{3.24}$$

The heuristic approach to DG is to now apply this projection to the residual of some initial value problem governed by a PDE. I.e. given a PDE

$$\mathcal{L}(f) = 0 \tag{3.25}$$

the goal is to minimize the residual w.r.t. the ansatz space of the approximate solution $f_h \in \mathbb{P}_k(\mathfrak{K}_h)$:

$$\langle \mathcal{L}(f) - \mathcal{L}(f_h), v \rangle_{L^2(\mathfrak{K}_h)} = \langle -\mathcal{L}(f_h), v \rangle_{L^2(\mathfrak{K}_h)} = 0, \quad \forall v \in \mathbb{P}_k(\mathfrak{K}_h). \tag{3.26}$$

Of course this is not the complete truth but this sketch outlines the idea behind DG very well. To actually apply a DG method a few more steps are necessary. This includes the introduction of numerical fluxes in order to couple the cell-wise solutions and ensure certain properties of the discrete forms. Also it is still undefined how boundary conditions are enforced. An example for the DG discretization of Poisson's equation is given towards the end of this section.

How accurate is the prediction obtained in this way? The last question is, how good this method actually works. There are two different approaches to answer this question. As a first option, a-priori error analysis (Di Pietro and Ern, 2012; Dolejší and Feistauer, 2015) aims to give an upper bound of the error before computing a solution. As such it only depends on properties of the (unknown) exact solution to the problem and the discretization, e.g.

$$\|f - f_h\|_{L^2(\mathfrak{K}_h)} \leq \mathcal{F}\left(\mathfrak{K}_h, k, f\right). \tag{3.27}$$

A-posteriori error analysis (Di Pietro and Ern, 2012) does the opposite and tries to give upper and lower bounds of the error after a numerical solution has been found. Its predictions depend on properties of the numerical solution, discretization and potentially the source terms g:

$$\|f - f_h\|_{L^2(\mathfrak{K}_h)} \leq \mathcal{E}\left(\mathfrak{K}_h, k, g, f_h\right) \leq C\|f - f_h\|_{L^2(\mathfrak{K}_h)}. \tag{3.28}$$

Usually, there exists a cell-local expression for the error estimator $\mathcal{E}$, such that it can be used to locally refine the mesh or polynomial degree to ensure a certain error threshold. In this work, no posterior estimates are used and we focus on the a-priori estimates to highlight a few properties of the DG method. The analysis for these kind of estimates is very complex and depends on many details, e.g. what kind of mesh is used (triangles, hexahedrals etc.), how does the PDE look like (linear/non-linear) or which fluxes are used. Therefore, it is beyond the scope of this work to answer this question to full extend. However, to underline one key advantage one hopes to achieve in employing a high-order method like DG, we want to discuss an elemental result of functional analysis regarding polynomial approximations.

Definition 3.8 (Bramble-Hilbert Lemma). *The Lemma of Bramble-Hilbert, see e.g. (Dolejší and Feistauer, 2015, Theorem 2.18), gives a bound for the projection error (on convex domains), when $f_I \in \mathbb{P}_k^C(K)$ is the projection of f and $k \leq n-1$:*

$$|f - f_I|_{W^{m,p}(K)} \leq Ch^{n-m}|f|_{W^{n,p}(K)}, \tag{3.29}$$

the measure h denotes the diameter of the cell. For the special case $n = k+1$ this becomes

$$|f - f_I|_{W^{m,p}(K)} \leq Ch^{k+1-m}|f|_{W^{k+1,p}(K)}, \tag{3.30a}$$

and when choosing $m = 0$

$$\|f - f_I\|_{L^p(K)} \leq Ch^{k+1}|f|_{W^{k+1,p}(K)}, \tag{3.30b}$$

or $p = 2$

$$|f - f_I|_{H^m(K)} \leq Ch^{k+1-m}|f|_{H^{k+1}(K)}. \tag{3.30c}$$

Assuming a uniform diameter for all cells in the grid, it follows from Definition 3.8 and Eq. (3.13) that for the projection (3.24)

$$\|f - f_I\|_{L^2(\mathfrak{K}_h)} \leq Ch^{k+1}|f|_{H^{k+1}(\mathfrak{K}_h)}. \tag{3.31}$$

This result may seem abstract at first, but gives quite a few insights into the expected performance of the DG method. First, it should be clear that the error between numerical and exact solution cannot be better than the projection error of the exact solution onto the approximation space. In that regard an a-priori analysis is called optimal if it gives a similar upper bound of the error in terms of the factor h^{k+1}. Second, this scaling factor predicts the convergence slopes

we expect when the method performs optimal. Higher approximation degrees mean a higher convergence order under refinement of the mesh, which makes DG methods very efficient w.r.t. to the achievable accuracy in relation to the total number of degrees of freedom (DOFs). Third, the highest guaranteed convergence order depends on the regularity of the (usually unknown) exact solution. In this work often times $f \in H^2(\Omega)$, as the PDEs in focus are of second order, compare Section 2.6. We will see later in Section 6.3 that it is not immediately clear how smooth a solution is which heavily depends on the prescribed boundary conditions.
To estimate the actually obtained convergence order in practice, a simulation may be repeated on different grids to estimate the errors. By computing the regression of the errors as a function of grid size the convergence order can be calculated. If available, the exact solution to the problem is used. However, often an exact solution is not known. In that case, the result computed on the finest grid is used to compute the error estimates on all other grids, in which case the experimental order of convergence (EOC) is measured.

A brief example - SIP To give more insight how the DG discretization for the equations in Section 2.6 can be obtained, we want to give a brief example on how the DG method solves the Poisson problem

$$-\nabla \cdot (\mu \nabla u) = g \quad \text{on} \quad \Omega, \tag{3.32a}$$

$$u = u_D \quad \text{on} \quad \partial\Omega_D, \tag{3.32b}$$

$$\mu \nabla u \cdot \boldsymbol{n}^{\partial\Omega} = u_N \quad \text{on} \quad \partial\Omega_N. \tag{3.32c}$$

The assumption of a continuous right-hand side (RHS) $g \in C^0(\Omega)$, sufficiently smooth and differentiable boundary values u_D, u_N and parameter $\mu \in C^1(\Omega)$ implies, that we are looking for a at least two times continuously differentiable solution $u \in C^2(\Omega)$. First, Eq. (3.32) is multiplied by a test-function $v \in H^1(\Omega)$ and integrated over the whole domain, to obtain the variational form, sometimes called strong-weak form,

$$\int_\Omega -\nabla \cdot (\mu \nabla u)\, v \ \mathrm{d}V = \int_\Omega g v \ \mathrm{d}V \quad \forall v \in H^1(\Omega). \tag{3.33}$$

Note, how this step softens the requirements of the solution, as Eq. (3.33) does not need to be fulfilled at every point but only in an integral sense, i.e., $u \in H^2(\Omega)$ can be assumed. Next, integration by parts is applied to obtain the continuous weak formulation

$$\int_\Omega \mu \nabla u \cdot \nabla v \ \mathrm{d}V + \int_{\partial\Omega} -\mu \nabla u \cdot \boldsymbol{n}^{\partial\Omega} v \ \mathrm{d}S = \int_\Omega g v \ \mathrm{d}V \quad \forall v \in H^1(\Omega), \tag{3.34}$$

weakening the solution requirements even further to $u \in H^1(\Omega)$. The boundary conditions can now be incorporated by directly replacing the flux on the boundary with the correct Neumann value, while weakly enforcing the Dirichlet boundary condition through a penalty (Arnold et al., 2002)

$$\int_\Omega \mu \nabla u \cdot \nabla v \ \mathrm{d}V + \int_{\partial\Omega_N} -u_N v \ \mathrm{d}S + \int_{\partial\Omega_D} \eta (u - u_D) v \ \mathrm{d}S = \int_\Omega g v \ \mathrm{d}V \quad \forall v \in H^1(\Omega). \tag{3.35}$$

Now, we switch to the discrete setting by introducing a mesh for the domain and consider the piecewise continuous functions $u, v \in H^2(\mathfrak{K}_h)$, defined by

$$H^2(\mathfrak{K}_h) := \left\{ f \in L^2(\Omega) \mid u|_K \in H^2(K) \, \forall K \in \mathfrak{K}_h \right\}. \tag{3.36}$$

As is customary for a Galerkin method, in this work these ansatz and test functions are elements of the same space, though more generally they may be chosen from different spaces which is then commonly referred to as a Petrov-Galerkin method. Then the integration by-parts formula introduces cell boundary contributions, that can be collected by applying Eq. (3.16a), so that the discrete weak-formulation becomes

$$\int_{\mathfrak{K}_h} \mu \nabla u \cdot \nabla v \ \mathrm{d}V + \int_{\Gamma} \left[\!\left[-\mu \nabla u \cdot \boldsymbol{n}^{\partial\Omega} v \right]\!\right] \ \mathrm{d}S = \int_{\mathfrak{K}_h} g v \ \mathrm{d}V \quad \forall v \in H^2(\mathfrak{K}_h). \tag{3.37}$$

However, Eq. (3.37) is not well-posed, as it does not possess a unique solution. For example a solution may be shifted by an arbitrary constant in an inner cell and still be a valid solution to Eq. (3.37), one can think of the cells not being coupled together yet. To ensure well-posedness, i.e., the problem possesses a unique solution that changes continuously w.r.t. initial and boundary conditions, the crucial step in a DG scheme is to replace the second term on the LHS in Eq. (3.37) by a suitable numerical flux. A popular choice for this example, and also employed in this work for the Laplacian term, is the symmetric interior penalty (SIP) flux, see Arnold et al. (2002), Di Pietro and Ern (2012), and Dolejší and Feistauer (2015):

$$\begin{aligned} &\int_{\mathfrak{K}_h} \mu \nabla u \cdot \nabla v \ \mathrm{d}V + \int_{\Gamma \setminus \partial\Omega_N} -\left\{\!\left\{ \mu \nabla u \cdot \boldsymbol{n}^{\Gamma} \right\}\!\right\} \left[\!\left[v \right]\!\right] - \left\{\!\left\{ \mu \nabla v \cdot \boldsymbol{n}^{\Gamma} \right\}\!\right\} \left[\!\left[u \right]\!\right] + \eta \left[\!\left[u \right]\!\right] \left[\!\left[v \right]\!\right] \ \mathrm{d}S \\ &= \int_{\mathfrak{K}_h} g v \ \mathrm{d}V + \int_{\partial\Omega_D} -\left(\mu \nabla v \cdot \boldsymbol{n}^{\Gamma} \right) u_D + \eta u_D v \ \mathrm{d}S + \int_{\partial\Omega_N} u_N v \ \mathrm{d}S \quad \forall v \in H^2(\mathfrak{K}_h). \end{aligned} \tag{3.38}$$

By collecting the RHS in a bilinear form Eq. (3.38) can be rewritten:

$$a_{sip}(u, v) = s(v). \tag{3.39}$$

The motivation of this specific choice of flux is multifold. The consistency term $\left\{\!\left\{ \mu \nabla u \cdot \boldsymbol{n}^{\Gamma} \right\}\!\right\} \left[\!\left[v \right]\!\right]$ ensures that a solution to Eq. (3.32) is also a solution of Eq. (3.38). The symmetry term $\left\{\!\left\{ \mu \nabla v \cdot \boldsymbol{n}^{\Gamma} \right\}\!\right\} \left[\!\left[u \right]\!\right]$ preserves the identity $a_{sip}(u, v) = a_{sip}(v, u)$, which can be used to show a property of the bilinear form called adjoint consistency. In analogy to how the Dirichlet boundary conditions are incorporated, the penalization $\eta \left[\!\left[u \right]\!\right] \left[\!\left[v \right]\!\right]$ of jumps on the edges weakly enforces continuity of the solution. For the right choice of penalty parameter, usually scaling inversely with the mesh width, boundedness and coercivity of $a_{sip}(u, v)$ can be proven. These specific features (adjoint consistency, boundedness, coercivity) are mandatory to prove solvability, error estimates and stability of the method (Arnold et al., 2002; Di Pietro and Ern, 2012; Dolejší and Feistauer, 2015). At last, the specific DG ansatz can be inserted. By choosing u_h acccording to Eq. (3.22), i.e., searching for a solution vector $\hat{\boldsymbol{u}}_h$ for the DOFs, and calculating the integrals for every basis function $v_h \in \mathbb{P}_k(\mathfrak{K}_h)$ a system of linear equations can be constructed:

$$\mathbf{A} \hat{\boldsymbol{u}}_h = \boldsymbol{b}. \tag{3.40}$$

Each column in the operator matrix $\mathbf{A}$ corresponds to a DOF in the ansatz and each row to a basis function spanning the space $\mathbb{P}_k(\mathfrak{K}_h)$. Every row of the RHS vector $\boldsymbol{b}$ is given by evaluating the RHS of Eq. (3.39) for a single test function.

3.2 Unfitted methods

In Section 3.1, we introduced the principles of the conventional DG method, which is suitable to solve single phase equations. However, the problems regarded in this work often contain more than

a single phase. Therefore, the discretization scheme has to be extended to take multiple phases, their dividing interfaces and common lines into account. To this end, two major adjustments are necessary. First, the representation of variables has to take the phase wise nature of the multiphase problem into account. Second, the coupling through fluxes at the dividing interfaces has to consider the interfacial equations defined in Section 2.6. To achieve these goals, we utilize the XDG method proposed by Kummer (2017) and Smuda and Kummer (2021), following the ideas presented by Mos et al. (1999) and Bastian and Engwer (2009). To consider all present distinct phases these methods cut the static background mesh into parts, based on the interface position. As thereby cells of arbitrary shape and size can occur a method of this type is called "unfitted" or in our case "extended". In this section the necessary adaptions to the mesh and solution spaces are presented, and the extension to the DG method is applied to the Poisson problem.

Extended approximation spaces As before, the first task is to define a representation for the solution variables, which respects the existing phases.

Definition 3.9 (Phase-cells and cut-cell mesh). *As defined by Kummer (2017) the domain of the problem under investigation may be divided into several (potentially time-dependent) sub-domains* $\mathfrak{s}(t) = \left\{\Omega^{(1)}(t), \dots, \Omega^{(N_\Omega)}(t)\right\}$ *called phases or species. These subdomains are disjunct and their union forms the original domain. Each cell of the numerical mesh* $\mathfrak{K}_h$ *from Definition 3.4 is then divided into several time-dependent phase-cells*

$$K^X_{i,\Omega^{(j)}}(t) := K_i \cap \Omega^{(j)}(t). \tag{3.41}$$

The union of all these phase-cells defines the cut-cell mesh

$$\mathfrak{K}^X_h(t) := \left\{K^X_{1,\Omega^{(1)}}(t), \dots, K^X_{1,\Omega^{(N_\Omega)}}(t), \dots, K^X_{N_K,\Omega^{(1)}}(t), \dots, K^X_{N_K,\Omega^{(N_\Omega)}}(t)\right\}. \tag{3.42}$$

A phase-cell may be empty in which case the corresponding species is not present in the respective background cell. If a background cell contains more than one species it is called a cut-cell, otherwise the background cell is equal to the only present phase-cell, i.e.,

$$K^X_{i,\Omega^{(j)}}(t) = K_i \quad \text{if} \quad K^X_{i,\Omega^{(k)}}(t) = \emptyset,\ \forall \Omega^{(k)} \in \mathfrak{s} \setminus \Omega^{(j)}. \tag{3.43}$$

Now, cell boundaries occur not only between cells of the background mesh, but also between phase-cells within a cut-cell. This means the set of all inner edges is now understood to contain as well the separating interfaces between phases.

With the definition of the cut-cell mesh at hand, the approximation spaces can be extended as well.

Definition 3.10 (Broken cut-polynomial Spaces). *In principle the XDG method is a DG method defined on this cut-cell mesh. Thus, a natural definition for the broken cut-polynomial space used as the extended approximation space is*

$$\mathbb{P}^X_k(\mathfrak{K}^X_h(t)) := \left\{f \in L^2(\Omega) \mid f|_K \in \mathbb{P}^C_k(K), \quad \forall K \in \mathfrak{K}^X_h(t)\right\}. \tag{3.44}$$

Note the theoretical maximum number of DOFs is $\dim(\mathbb{P}^X_k(\mathfrak{K}^X_h(t))) = N_\Omega * N_K * N_k$*, which can be reduced in the application of the method by disregarding empty phase-cells.*

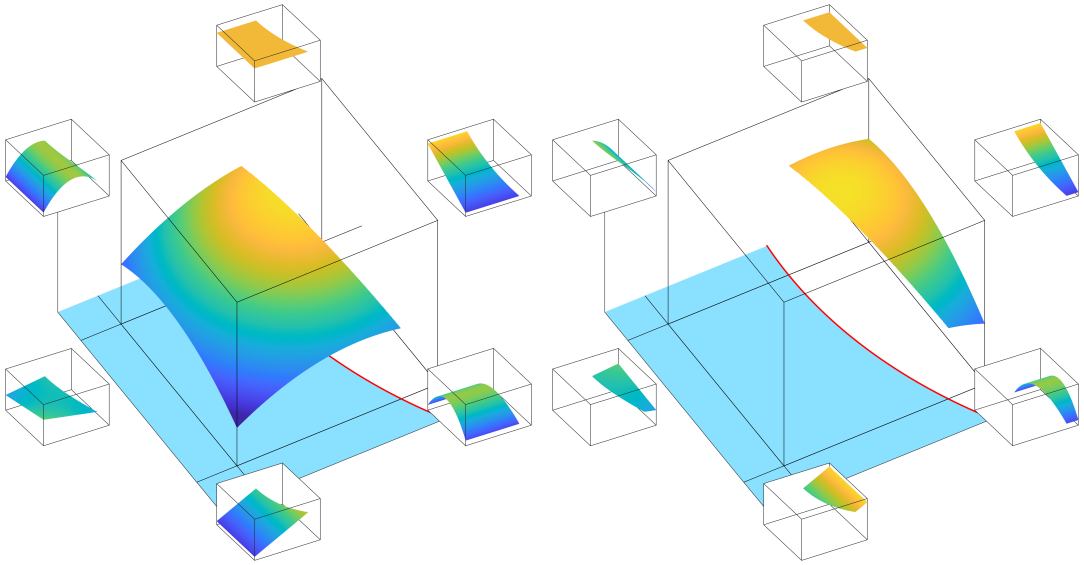

Figure 3.2: Separation of the basis displayed in Fig. 3.1 into two phase-wise bases along the interface, visible as a red line. On the left the basis for the gaseous phase is displayed and on the right for the liquid phase.

To conclude the considerations of these extended approximation spaces, we present how to choose a basis for these broken cut-polynomial spaces. Making use of the basis on the uncut mesh (3.19a) and by restricting the basis to the respective phase we find:

$$\text{basis}(\mathbb{P}_k^{\mathrm{X}}(\mathfrak{K}_h^{\mathrm{X}}(t))) = \boldsymbol{\Phi}^{\mathrm{X}} = \left(\boldsymbol{\Phi}^{\mathrm{X}}_{\mathbf{1},\boldsymbol{\Omega}^{(1)}}, \dots, \boldsymbol{\Phi}^{\mathrm{X}}_{\mathbf{1},\boldsymbol{\Omega}^{(n)}}, \dots, \boldsymbol{\Phi}^{\mathrm{X}}_{\boldsymbol{N_K},\boldsymbol{\Omega}^{(1)}}, \dots, \boldsymbol{\Phi}^{\mathrm{X}}_{\boldsymbol{N_K},\boldsymbol{\Omega}^{(n)}}\right)^T, \tag{3.45a}$$

$$\boldsymbol{\Phi}^{\mathrm{X}}_{\boldsymbol{i},\boldsymbol{\Omega}^{(j)}} = \boldsymbol{\Phi}_{\boldsymbol{i}} X_{i,\Omega^{(j)}}(t,\boldsymbol{x}), \tag{3.45b}$$

$$X_{i,\Omega^{(j)}}(t,\boldsymbol{x}) = \begin{cases} 1, & \boldsymbol{x} \in K^{\mathrm{X}}_{i,\Omega^{(j)}}(t) \\ 0, & \text{else} \end{cases}. \tag{3.45c}$$

A visual example for such a cut-cell basis is displayed in Fig. 3.2.

The extension to XDG - SIP Apart from the formal extension from the DG to XDG spaces, it is also necessary to adapt the discretization at the interfaces. In order to give an example for this we reconsider the Poisson problem (3.32) in the context of multiple phases. The parameter μ may change discontinuously across phase boundaries. In addition, it may not be desirable to enforce continuity in the variable and flux at the interfaces but jump conditions in the following form (Rieckmann et al., 2023e), compare also the jump conditions given in Section 2.6:

$$[\![u]\!] = f_1, \tag{3.46a}$$

$$[\![\mu \nabla u \cdot \boldsymbol{n}^{\Sigma}]\!] = f_2. \tag{3.46b}$$

The question is then, how can these be incorporated? To show a heuristic derivation of the necessary extensions, integration by parts is applied again to Eq. (3.38):

$$\begin{aligned}
&\int_{\mathfrak{K}_h} -\nabla\cdot(\mu\nabla u)\,\nabla v \;\mathrm{d}V \\
+\int_{\Gamma\setminus\partial\Omega_N} &-\{\{\mu\nabla u\cdot\boldsymbol{n}^\Gamma\}\}\;[\![v]\!] - \{\{\mu\nabla v\cdot\boldsymbol{n}^\Gamma\}\}\;[\![u]\!] + \eta\,[\![u]\!]\;[\![v]\!] \;\mathrm{d}S + \int_\Gamma [\![\mu\nabla u\cdot\boldsymbol{n}^\Gamma v]\!] \;\mathrm{d}S \\
&= \int_{\mathfrak{K}_h} gv \;\mathrm{d}V + \int_{\partial\Omega_D} -\left(\mu\nabla v\cdot\boldsymbol{n}^\Gamma\right)u_D + \eta u_D v \;\mathrm{d}S + \int_{\partial\Omega_N} u_N v \;\mathrm{d}S.
\end{aligned} \tag{3.47}$$

After summarizing terms and sorting after separate edges, we obtain

$$\begin{aligned}
&\underbrace{\int_{\mathfrak{K}_h} -\nabla\cdot(\mu\nabla u)\,\nabla v \;\mathrm{d}V}_{(1)} + \underbrace{\int_{\partial\Omega_D} -\left(\mu\nabla v\cdot\boldsymbol{n}^\Gamma\right)u + \eta uv \;\mathrm{d}S}_{(2)} + \underbrace{\int_{\partial\Omega_N} \mu\nabla u\cdot\boldsymbol{n}^\Gamma v \;\mathrm{d}S}_{(3)} \\
&\quad + \underbrace{\int_{\Gamma_{\text{int}}\setminus\Sigma} [\![\mu\nabla u\cdot\boldsymbol{n}^\Gamma]\!]\;\{\{v\}\} - \{\{\mu\nabla v\cdot\boldsymbol{n}^\Gamma\}\}\;[\![u]\!] + \eta\,[\![u]\!]\;[\![v]\!] \;\mathrm{d}S}_{(4)} \\
&\quad + \underbrace{\int_{\Sigma} [\![\mu\nabla u\cdot\boldsymbol{n}^\Gamma]\!]\;\{\{v\}\} - \{\{\mu\nabla v\cdot\boldsymbol{n}^\Gamma\}\}\;[\![u]\!] + \eta\,[\![u]\!]\;[\![v]\!] \;\mathrm{d}S}_{(5)} \\
&= \underbrace{\int_{\mathfrak{K}_h} gv \;\mathrm{d}V}_{(1)} + \underbrace{\int_{\partial\Omega_D} -\left(\mu\nabla v\cdot\boldsymbol{n}^\Gamma\right)u_D + \eta u_D v \;\mathrm{d}S}_{(2)} + \underbrace{\int_{\partial\Omega_N} u_N v \;\mathrm{d}S}_{(3)}.
\end{aligned} \tag{3.48}$$

The goal is to obtain a consistent final discretization, in the context of this example this means that a solution to Eqs. (3.32) and (3.46) also solves the discrete form (3.48) exactly. By inserting such a solution into Eq. (3.48), the (1)-terms vanish as the bulk equation is fulfilled, the same applies to the (2) and (3) terms as the solution abides to the boundary conditions. Due to the continuity of the solution, the jumps on inner edges, excluding the interfaces, equate to zero and the (4)-term vanishes as well. Thereby, only the (5)-term is left and it becomes visible which correction to the RHS is necessary to obtain a consistent discretization:

$$\begin{aligned}
&\int_\Sigma [\![\mu\nabla u\cdot\boldsymbol{n}^\Gamma]\!]\;\{\{v\}\} - \{\{\mu\nabla v\cdot\boldsymbol{n}^\Gamma\}\}\;[\![u]\!] + \eta\,[\![u]\!]\;[\![v]\!]\;dS \\
&\quad = \int_\Sigma f_2\,\{\{v\}\} - \{\{\mu\nabla v\cdot\boldsymbol{n}^\Gamma\}\}\,f_1 + \eta f_1\,[\![v]\!]\;dS.
\end{aligned} \tag{3.49}$$

The same consideration is followed in the next chapter to obtain the XDG discretization for the combinations of bulk equations and jump conditions presented in Section 2.6.

3.3 Summary of the XDG method

To summarize briefly, the XDG method is very similar to the conventional DG method. However, in the design of the method two important differences arise. First, the method finds solutions

on the unfitted cut-cell mesh. Second, the fluxes on the phase interfaces have to be adapted to account for the physically motivated jump conditions, not necessarily preserving continuity in the solution variables.
To conclude this presentation we want to emphasize the main reasons that motivate the pursuit of this high order XDG method. First, the expected high convergence order proportional to h^{k+1} makes it possible to the same or higher accuracy with less DOFs than in a low order method. Less DOFs means smaller systems and computationally more affordable solutions. Secondly, the discontinuities between cells allow for a relatively easy parallelization of the method when compared with continuous Galerkin methods. Also as no globally continuous basis has to be constructed mesh refinement and local adaption of polynomial degree are straight-forward. However, these topics are not further discussed within this work. Thirdly, the usage of the cut-cell structure with the XDG bases conforming to the interface position makes it possible to obtain a polynomial approximation of the solution right up to the interface. Thereby, solution variables and their derivatives are obtained at the interface without the need for additional reconstruction. The evaluation of these quantities is necessary to conform to the physical jump conditions.

4 Numerical solution of conservation laws with the extended discontinuous Galerkin method

In Chapter 3 the operation principle and fundamentals of the spatial DG and XDG discretization are introduced. However, these methods only build up the core of a complete numerical scheme designed to obtain solutions for the PDEs presented in Section 2.6. To obtain a complete solver, additional auxiliary algorithms and methods are needed, which are described in this chapter. The representation of the numerical scheme at this point extends that from Rieckmann et al. (2023e). In Section 4.1 the abstract spatial discretization of the systems presented in Section 2.6 is introduced. The methods to evaluate the integrals arising in this abstract discretization are then established in Section 4.2. In addition to the discretization of the fluid equations, a description for the interface is needed. This is handled by the level set method, which is presented together with the scheme to evolve the level set in time in Section 4.3. To finally obtain a completely discretized system the temporal derivatives need also to be discretized. The methods used for this purpose and also the coupling between level set and fluid solution are presented in Section 4.4. After all these steps, one is left with a non-linear or linear system of equations, for which the solution methods are presented in Section 4.5.

4.1 Spatial discretization

In Chapter 3 the fundamentals of the XDG discretization are presented. There the notion of a bilinear form and retrieval of a linear algebraic system for a Poisson problem is discussed. In this section this procedure is applied to the systems of equations presented in Section 2.6, by specifying the appropriate solution spaces and a complete representation of the spatially discrete problem in terms of linear, bilinear, trilinear and non-linear forms.
In Section 2.6 BCs are introduced in a mixed form, able to represent the limiting cases of Dirichlet, Neumann and Robin BCs (e.g. Definition 2.13). Numerically these have to be treated differently, which is why the boundary is distinguished by different parts, depending on the value of the respective “slip” parameter β:

$$\partial\Omega = \begin{cases} \partial\Omega_D & \beta \to \infty \\ \partial\Omega_N & \beta = 0 \\ \partial\Omega_R & \text{else} \end{cases} . \tag{4.1}$$

In Section 3.2 the subscript “h” was used to mark an approximate solution. For simplicity, this subscript is dropped from here on, with the understanding that such approximate solutions and corresponding test functions are implied.

4.1.1 Material incompressible multiphase flow

The first considered system of equations is that of incompressible multiphase flow with material interfaces Section 2.6.1, i.e., without evaporation. In that case, we want to find a solution

$$(\boldsymbol{u}, p) \in \mathbb{V}_{k,1}^{\mathrm{X}} := \left(\mathbb{P}_k^{\mathrm{X}}(\mathfrak{K}_h^{\mathrm{X}}(t))^D \times \mathbb{P}_{k-1}^{\mathrm{X}}(\mathfrak{K}_h^{\mathrm{X}}(t))\right) \tag{4.2}$$

such that

$$\begin{aligned} &\underbrace{m(\boldsymbol{u}, \boldsymbol{v})}_{\rho\frac{\partial \boldsymbol{u}}{\partial t}} + \underbrace{c(\boldsymbol{u}, \boldsymbol{u}, \boldsymbol{v})}_{\rho \boldsymbol{u}\cdot\nabla\boldsymbol{u}} + \underbrace{b(p, \boldsymbol{v})}_{\nabla p} \\ &\underbrace{-b(q, \boldsymbol{u})}_{-\nabla\cdot(\boldsymbol{u})} + \underbrace{a(\boldsymbol{u}, \boldsymbol{v})}_{-\mu\nabla\cdot(\nabla\boldsymbol{u}+\nabla\boldsymbol{u}^{\mathrm{T}})} \\ &= \underbrace{s(\boldsymbol{v}, q)}_{\rho\boldsymbol{g},\, \nabla_\Sigma\cdot(\sigma\mathbf{P}^\Sigma)} \qquad \forall\, (\boldsymbol{v}, q) \in \mathbb{V}_{k,1}^{\mathrm{X}}. \end{aligned} \tag{4.3}$$

The terms in the underbraces in Eq. (4.3) show which component from the orginal PDE is discretized in which form, and a complete expansion in integral form is given in Appendix A.1. The designations of m as temporal, c convective, b pressure gradient and velocity divergence, a as viscous or diffusive and s as source and boundary term for the individual forms can be found in this classification. The polynomial order for the pressure is chosen of one order lower than for the velocity as described in Eq. (4.2). This mixed-order discretization is chosen to stabilize the scheme and follows along the lines of the well-known Checker-Board instability, see (Di Pietro and Ern, 2012, p. 266ff.).
The discretization of the surface tension diplayed in is obtained by applying the surface divergence theorem (Definition 2.6) to the divergence of the surface stress tensor (weighted by the test functions):

$$\oint_\Sigma \nabla_\Sigma \cdot \left(\sigma\mathbf{P}^\Sigma\right) \cdot \{\{\boldsymbol{v}\}\} \;\mathrm{d}S = \oint_\Sigma -\sigma\mathbf{P}^\Sigma : \{\{\nabla_\Sigma \boldsymbol{v}\}\} \;\mathrm{d}S + \oint_{\Sigma\cap(\Gamma)} \sigma\left\{\{\boldsymbol{t}^\Sigma\}\right\} \cdot [\![\{\{\boldsymbol{v}\}\}]\!], \tag{4.4}$$

on the intersection of the interface with edges of the mesh a central flux is applied for the coupling between parts of the interface located in neighboring cells. The averages of the test function ($\{\{\boldsymbol{v}\}\}$ and $\{\{\nabla_\Sigma \boldsymbol{v}\}\}$) are taken over the interface (from both phases), while all other jumps and averages denote the cell-wise jumps/averages. The vector $\boldsymbol{t}^\Sigma$ is defined in Eq. (A.15).

4.1.2 Incompressible multiphase flow with evaporation

In the second considered system of equations from Section 2.6.2, evaporation and the energy balance are considered. Thereby, the temperature is included in the sought-after solution variables. For the new solution space we define

$$(\boldsymbol{u}, p, T) \in \mathbb{V}_{k,2}^{\mathrm{X}} := \left(\mathbb{P}_k^{\mathrm{X}}(\mathfrak{K}_h^{\mathrm{X}}(t))^D \times \mathbb{P}_{k-1}^{\mathrm{X}}(\mathfrak{K}_h^{\mathrm{X}}(t)) \times \mathbb{P}_k^{\mathrm{X}}(\mathfrak{K}_h^{\mathrm{X}}(t))\right) \tag{4.5}$$

such that

$$\begin{aligned} &m((\boldsymbol{u}, T), (\boldsymbol{v}, r)) + c(\boldsymbol{u}, (\boldsymbol{u}, T), (\boldsymbol{v}, r)) + b((p, T), \boldsymbol{v}) \\ &-b(q, (\boldsymbol{u}, T)) + a((\boldsymbol{u}, T), (\boldsymbol{v}, r)) + d(T, \boldsymbol{v}) \\ &= s(\boldsymbol{v}, q, r) \quad \forall\, (\boldsymbol{v}, q, r) \in \mathbb{V}_{k,2}^{\mathrm{X}}. \end{aligned} \tag{4.6}$$

As the inclusion of evaporation means the interfaces may no longer be material and jumps in interface normal velocity can occur, most fluxes on the interface have to be modified. The expanded integral forms and necessary modifications from the implementation for material flows are shown in Appendix A.1. In Eq. (4.5) the same order for the velocity and temperature solution is chosen. In Section 6.3 a case study is considered, which implies this equal order approach to be sub-optimal. Nevertheless, the finding requires verification through additional tests and was obtained after the simulations for this work had already been conducted.
Compared with Eq. (4.3) one additional term, $d(T, \boldsymbol{v})$, arises in Eq. (4.6). This term discretizes the recoil pressure, see Eq. (2.75), which is physically connected to convection at the interface, but numerically (partially owed to the employed splitting scheme Section 4.4) not treated in the other forms.

4.1.3 Free surface flow

The difference of the last model in focus, the free surface flow from Section 2.6.3, to the material incompressible multiphase flow is very nuanced. First, a simplified system is considered, in which the temporal and convective terms are omitted. Secondly, the definition of the solution spaces differs, as now a solution is sought in one phase only, i.e., on the augmented mesh

$$\bar{\mathfrak{K}_h}^{\mathrm{X}}(t) = \left\{ K^{\mathrm{X}}_{1,\Omega^{(1)}}(t), \ldots, K^{\mathrm{X}}_{N_K,\Omega^{(1)}}(t) \right\}, \tag{4.7}$$

containing only the phase-cells of one phase. Thirdly, the boundary conditions of the interface are altered, as an opposing phase is missing. Finally solutions

$$(\boldsymbol{u}, p) \in \mathbb{V}^{\mathrm{X}}_{k,3} := \left(\mathbb{P}^{\mathrm{X}}_k(\bar{\mathfrak{K}_h}^{\mathrm{X}}(t))^D \times \mathbb{P}^{\mathrm{X}}_{k-1}(\bar{\mathfrak{K}_h}^{\mathrm{X}}(t)) \right) \tag{4.8}$$

to the discrete system

$$\begin{aligned} & b(p, \boldsymbol{v}) - b(q, \boldsymbol{u}) + a(\boldsymbol{u}, \boldsymbol{v}) \\ =& s(\boldsymbol{v}, q) \quad \forall\, (\boldsymbol{v}, q) \in \mathbb{V}^{\mathrm{X}}_{k,3} \end{aligned} \tag{4.9}$$

are sought.

For completeness, the expansion in integral form is given in Appendix A.1. To shorten and unify the notation there with the implementation of the other two systems of equations, the dimensionless numbers are not explicitly mentioned.

4.2 Integrand evaluation

In Section 4.1 the solution of the flow equations of Section 2.6 is presented in a spatially discrete form as a sequence of integrals. In the implementation of the method, these integrals over volumes, surfaces and lines must be evaluated numerically. This evaluation is done with respect to a mapping from any cell of the grid to a reference cell.

4.2.1 Transformations

For each cell in the mesh a transformation from a reference element $K^* := \left\{\boldsymbol{\xi} \in [-1,1]^D\right\}$ (Kummer and Müller, 2021), to the physical cell K_i is defined as

$$\boldsymbol{T}_i : K^* \to K_i, \quad \boldsymbol{x} = \boldsymbol{T}_i(\boldsymbol{\xi}). \tag{4.10}$$

The Jacobian of this transformation is

$$\mathbf{J}_i = \frac{\partial \boldsymbol{T}_i}{\partial \boldsymbol{\xi}}, \tag{4.11}$$

and can be used to transform volume integrals

$$\int_{K_i} f(\boldsymbol{x}) \ \mathrm{d}V = \int_{K^*} f(\boldsymbol{T}_i(\boldsymbol{\xi})) \det(\mathbf{J}_i)(\boldsymbol{\xi}) \ \mathrm{d}V^*, \tag{4.12}$$

and gradients, with $\nabla^* = \partial(.)/\partial\boldsymbol{\xi}$:

$$\nabla f(\boldsymbol{x}) = \mathbf{J}_i^{-1} \nabla^* f(\boldsymbol{T}_i(\boldsymbol{\xi})). \tag{4.13}$$

Surface integrals can be transformed by introducing additional face transformations from a reference face $F^* := \left\{\boldsymbol{\eta} \in [-1,1]^{D-1}\right\}$ to the respective face of the reference cell:

$$\boldsymbol{T}_F : F^* \to \partial K^*, \quad \boldsymbol{\xi} = \boldsymbol{T}_F(\boldsymbol{\eta}). \tag{4.14a}$$

This allows to construct the metric

$$g = \det\left(\frac{\partial \boldsymbol{T}_F}{\partial \boldsymbol{\eta}}^T \mathbf{J}_i^T \mathbf{J}_i \frac{\partial \boldsymbol{T}_F}{\partial \boldsymbol{\eta}}\right), \tag{4.15}$$

and finally transform surface integrals:

$$\int_{\partial K_i} f(\boldsymbol{x}) \ \mathrm{d}S = \int_{F^*} f(\boldsymbol{T}_i(\boldsymbol{T}_F(\boldsymbol{\eta})))g \ \mathrm{d}S^*. \tag{4.16}$$

In this work, basis functions that are orthonormal in the physical cell are used exclusively, and can be retrieved through a linear combination of orthonormal reference basis functions:

$$\Phi_{i,n} = \Phi_s^* B_{i,ns}. \tag{4.17}$$

The orthonormalization matrix $\mathbf{B}$ is obtained by performing the Cholesky factorization of an intermediate mass matrix (Kummer and Müller, 2021):

$$\begin{aligned} \delta_{nm} = \int_{K_i} \Phi_{i,n}\Phi_{j,n} \ \mathrm{d}V &= \int_{K^*} \Phi_s^* B_{i,sn} \Phi_t^* B_{i,tm} \det(\mathbf{J}_i)(\boldsymbol{\xi}) \ \mathrm{d}V^* \\ &= \underbrace{B_{i,sn}}_{\mathbf{B}_i^T} \underbrace{\int_{K^*} \Phi_s^* \Phi_t^* \det(\mathbf{J}_i)(\boldsymbol{\xi}) \ \mathrm{d}V^*}_{\mathbf{M}_i^*} \underbrace{B_{i,tm}}_{\mathbf{B}_i}, \end{aligned} \tag{4.18a}$$

$$\mathbf{M}_i^* = \mathbf{Q}_i^T \mathbf{Q}_i, \tag{4.18b}$$

$$\mathbf{B}_i = \mathbf{Q}_i^{-1}. \tag{4.18c}$$

In case of a purely linear transformation, the determinant of the Jacobian matrix is constant and $\mathbf{B}_i = \mathbf{I}/\sqrt{\det(\mathbf{J}_i)}$. In this way, all integral and DG field evaluations can be pulled back to an evaluation of the reference basis on the reference element and appropriate transformation to the physical cell.

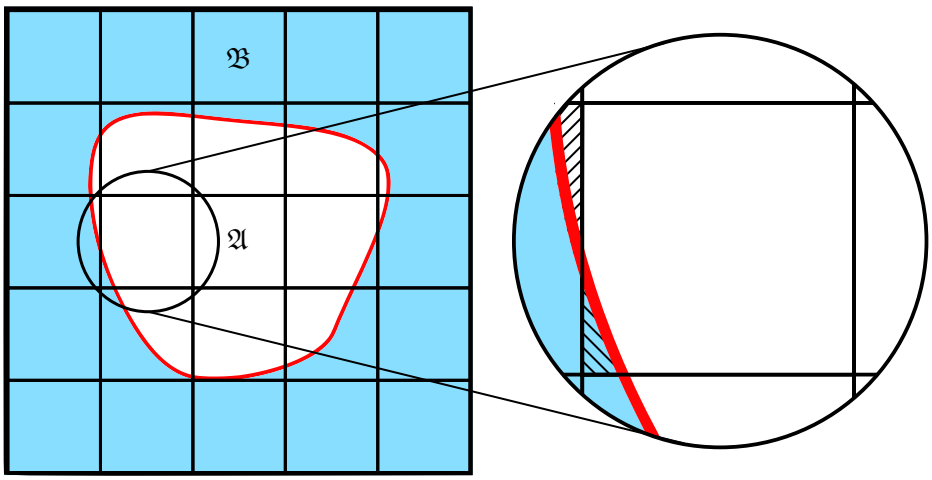

Figure 4.1: Visualization of the cut-cell mesh. The domain from Fig. 3.1 is discretized by a fixed background mesh. The interface divides cells containing both phases into two phase-cells. The two hatched cells exemplify small phase-cells, which need to be agglomerated to an appropriate neighbor.

4.2.2 Quadrature and cut-cell quadrature

For the construction of the discrete system, it is necessary to evaluate the forms in Section 4.1 on the cut-cell mesh, shown e.g. in Fig. 4.1. This can be done by constructing appropriate quadrature rules on the individual cut-cells, which discretize the evaluation of volume, surface and line integrals using a set of quadrature nodes $\boldsymbol{\xi}_i$ and weights w_i, i.e.,

$$\int_{K^*} f(\boldsymbol{\xi}) \ \mathrm{d}V^* \approx \sum_i f(\boldsymbol{\xi}_i) w_i. \tag{4.19}$$

This numeric evaluation of the integrals is performed on the reference elements by the procedure described in the previous section. On affine linear uncut cells of the background mesh, the common Gauss-Legendre quadrature rules are employed, with order $3k$ if convection is involved and $2k$ else. For curved cells the order of the transformation must be taken into account as well. For the cut-cells augmented quadrature rules, taking into account the interface position, have to be constructed for each contained phase-cell. In this work, the procedure suggested by Saye (2015) is employed. The basic idea behind that scheme is, analogous to the transformation from reference to background cell, to construct a transformation from a reference to the phase-cell by expressing the interface as a graph over a cell face. This may require a recursive subdivision of the cut-cell. Finally, the so-found transformation for each of the subdivided parts is applied to a standard Gauss-Legendre quadrature rule defined on the reference cell. Details of the implementation, as well as an extension for handling of cut-cells that are divided by multiple level sets can be found in the work of Beck and Kummer (2023). It should be noted that at the time of this writing the handling of curved cut-cells is not yet implemented in the code.

4.2.3 Handling of small phase-cells

In the handling of the cut-cell mesh a problem arises when phase-cells become very small, as displayed in Fig. 4.1. In such cases, the discrete system may be poorly conditioned, which impairs its solvability. To remedy this problem a cell agglomeration is performed, merging small phase-cells, indicated by the the volume fraction $\alpha_{j,\Omega^{(i)}} = \text{Vol}(K^{\text{X}}_{j,\Omega^{(i)}})/\text{Vol}(K_j)$, to a suitable neighbor cell. For all simulations in this work agglomeration is performed for phase-cells where $\alpha_{j,\Omega^{(i)}} < 0.1$. Additional details on the implementation of this procedure can be found in (Smuda, 2021) and (Toprak et al., 2024). In essence, cell agglomeration is a change of approximation basis. Such changes of basis are employed multiple times during the solution procedure to achieve a better condition of the discrete system, like here and in Section 4.5, or to handle the time evolution of the interface and possible changes in cut-mesh topology, see Section 4.4.1.

4.2.4 Operator evaluation

Using the so-defined process of numerical integration it is possible to evaluate the abstract operators defined in Section 4.1 for a specific solution guess and a single test function. As such a guess does not usually solve the discrete problem, the residual is obtained. For Eq. (4.3) this becomes

$$r(\boldsymbol{u}, p) = m(\boldsymbol{u}, \boldsymbol{v}) + c(\boldsymbol{u}, \boldsymbol{u}, \boldsymbol{v}) + b(p, \boldsymbol{v}) - b(q, \boldsymbol{u}) + a(\boldsymbol{u}, \boldsymbol{v}) - s(\boldsymbol{v}, q). \tag{4.20}$$

The residual for the other systems introduced in Section 4.1 follows analogously. By repeating this evaluation for all test functions, i.e., all basis polynomials according to Eq. (3.45), $\Phi^{\text{X}}_i \in \text{basis}(\mathbb{P}^{\text{X}}_k(\mathfrak{K}^{\text{X}}_h(t))^D)$ and $\Psi^{\text{X}}_i \in \text{basis}(\mathbb{P}^{\text{X}}_{k-1}(\mathfrak{K}^{\text{X}}_h(t)))$, and expanding the solution in terms of the DOF vectors $\hat{\boldsymbol{u}}$ and $\hat{\boldsymbol{p}}$, see Eq. (3.22), the residual vector can be expressed as

$$\boldsymbol{r}(t, \hat{\boldsymbol{u}}, \hat{\boldsymbol{p}}) = \begin{pmatrix} \mathbf{M}_{\boldsymbol{u}}(t) & 0 \\ 0 & 0 \end{pmatrix} \frac{\partial}{\partial t} \begin{pmatrix} \hat{\boldsymbol{u}} \\ \hat{\boldsymbol{p}} \end{pmatrix} + \boldsymbol{op}\,(t, \hat{\boldsymbol{u}}, \hat{\boldsymbol{p}}) + \boldsymbol{af}(t). \tag{4.21}$$

In Eq. (4.21) three contributions can be identified. The temporal term is linear with respect to the DOFs, which is why they can be pulled out of the integral to obtain the mass matrix

$$\mathbf{M}_{\boldsymbol{u}} := M_{\boldsymbol{u},i,j} = m(\Phi^{\text{X}}_j, \Phi^{\text{X}}_i). \tag{4.22}$$

The XDG basis functions are generally time-dependent. However, owing to the splitting scheme the interface is assumed fixed during a time-step of the flow solution, which is why the time derivative of the XDG basis is neglected, cf. Section 4.4.1. The operator vector bundles all other terms, excluding their affine contributions (that is the constant parts, not depending on the solution coordinates):

$$\boldsymbol{op} = \begin{pmatrix} \boldsymbol{op}_{\boldsymbol{u}} \\ \boldsymbol{op}_p \end{pmatrix}, \tag{4.23a}$$

$$\begin{aligned} \boldsymbol{op}_{\boldsymbol{u}} := op_{\boldsymbol{u},i} = &\left(c(\Phi^{\text{X}}_j \hat{\boldsymbol{u}}_j, \Phi^{\text{X}}_j \hat{\boldsymbol{u}}_j, \Phi^{\text{X}}_i) - c(0, 0, \Phi^{\text{X}}_i)\right) + \left(b(\Psi^{\text{X}}_j \hat{p}_j, \Phi^{\text{X}}_i) - b(0, \Phi^{\text{X}}_i)\right) \\ &+ \left(a(\Phi^{\text{X}}_j \hat{\boldsymbol{u}}_j, \Phi^{\text{X}}_i) - a(0, \Phi^{\text{X}}_i)\right), \end{aligned} \tag{4.23b}$$

$$\boldsymbol{op}_p := op_{p,i} = -\left(b(\Psi^{\text{X}}_i, \Phi^{\text{X}}_j \hat{\boldsymbol{u}}_j) - b(\Psi^{\text{X}}_i, 0)\right). \tag{4.23c}$$

Finally, the affine vector contains all contributions that are independent from the coordinates of the DOF vectors. However, it may still depend on the time coordinate. The affine vector is defined as

$$\boldsymbol{af} = \begin{pmatrix} \boldsymbol{af}_{\boldsymbol{u}} \\ \boldsymbol{af}_{p} \end{pmatrix}, \tag{4.24a}$$

$$\boldsymbol{af}_{\boldsymbol{u}} := af_{\boldsymbol{u},i} = -s(\Phi_i, 0) + c(0, 0, \Phi_i^{\mathrm{X}}) + b(0, \Phi_i^{\mathrm{X}}) + a(0, \Phi_i^{\mathrm{X}}), \tag{4.24b}$$

$$\boldsymbol{af}_{p} := af_{p,i} = -s(0, \Psi_i^{\mathrm{X}}) - b(\Psi_i^{\mathrm{X}}, 0). \tag{4.24c}$$

By introducing a general vector, bundling the DOFs for all solution variables, $\boldsymbol{z} = (\hat{\boldsymbol{u}}, \hat{\boldsymbol{p}})$, the residual Eq. (4.21) can be written as

$$\boldsymbol{r}(t, \boldsymbol{z}) = \mathbf{M}(t)\frac{\partial \boldsymbol{z}}{\partial t} + \boldsymbol{op}(t, \boldsymbol{z}) + \boldsymbol{af}(t). \tag{4.25}$$

Thus, it is possible to evaluate the residual of the method at a given time and for a specific solution guess. The task of the solver is to find a solution for which the residual Eq. (4.25) vanishes. In this case, Eqs. (4.21) and (4.25) give an ordinary differential equation (ODE) system for the DOF vector. Owing to the structure of this system, notice how the time derivative of the pressure is disregarded in Eq. (4.21), this is a special form of ODE called an Index-2 differential-algebraic equation (DAE) system, cf. Hairer and Wanner (1996). The incompressibility acts as an algebraic constraint, making the system very stiff and sensitive to deviations violating the incompressibility. To solve such systems, an ODE solver must be able to handle these specific systems. The analysis of DAE systems is very extensive and goes beyond the scope of this work, we instead refer to the books of Hairer et al. (1993) and Hairer and Wanner (1996). In Section 4.4 the discretization of the time derivative will be further specified and in Section 4.5 the process to obtain a solution for which this residual vanishes will be discussed. Before proceeding with the description of the flow solution, it is essential to explain the treatment of the interface.

4.3 Interface and phase representation - level sets

Up to this point, it was assumed that the separation of the domain into multiple phases and dividing interfaces is known. In this section the representation of phase domains and associated interfaces is discussed. As mentioned in Section 1.2.2 several approaches exist to represent the interfaces and the level set method is used in this work to accomplish this task. In this work exactly two phases are considered (with the exception of Section 7.3.3), hence the description of the interface representation is restricted to this case.

Definition 4.1 (Level set field). *We define a level set field $\varphi(\boldsymbol{x}, t) \in C^0(\Omega)$, whose zero set determines the interface*

$$\Sigma := \{\boldsymbol{x} \in \Omega \mid \varphi(\boldsymbol{x}, t) = 0\}. \tag{4.26a}$$

The phase domains separated by this interface, which we will call $\mathfrak{A}$ and $\mathfrak{B}$, are given by

$$\mathfrak{A} := \{\boldsymbol{x} \in \Omega \mid \varphi(\boldsymbol{x}, t) < 0\}, \tag{4.26b}$$

$$\mathfrak{B} := \{\boldsymbol{x} \in \Omega \mid \varphi(\boldsymbol{x}, t) > 0\}. \tag{4.26c}$$

The normals belonging to the respective interface are given as

$$\boldsymbol{n}^{\Sigma} = \frac{\nabla\varphi}{|\nabla\varphi|}, \tag{4.27}$$

assuming non-vanishing gradients of the level set field at the zero set.

In general it is possible to extend this definition for extra phases and interfaces by introducing additional level sets. In this way a third solid phase is considered in Section 7.3.3 by using a second level set. The level set dividing the fluid phases is then only active on the fluid side of this fluid-solid level set. Through the introduction of even more level sets and a level set hierarchy it is then possible to treat arbitrary many phases.

4.3.1 Interface advection

Whenever the interface is considered to be moving in time, an auxiliary problem is solved to obtain a temporal solution for the level set. In this section two possible methods to accomplish this task are presented. Hinting on the characteristics of the methods these will be introduced as "scalar advection" and "phase field" method.

Scalar advection method For the first method, the pure advection of the scalar level set field according to a globally defined advection velocity is considered. In differential form this results in the following PDE:

$$\frac{\partial\varphi}{\partial t} + \boldsymbol{u}_{\text{ext}}\nabla\varphi = 0. \tag{4.28}$$

In general, this advection velocity $\boldsymbol{u}_{\text{ext}}$ differs from the velocities defined in the bulk of the phases. However, at the zero set, the normal component of this advection velocity should be equal to interface velocity

$$\boldsymbol{u}_{\text{ext}} \cdot \boldsymbol{n}^{\Sigma} = \boldsymbol{u}^{\Sigma} \cdot \boldsymbol{n}^{\Sigma} \quad \forall \boldsymbol{x} \in \Sigma, \tag{4.29}$$

so the correct shape evolution of the interface is preserved. Equation (4.28) can also be rewritten:

$$\frac{\partial\varphi}{\partial t} + \nabla \cdot (\boldsymbol{u}_{\text{ext}}\varphi) - \varphi\nabla \cdot (\boldsymbol{u}_{\text{ext}}) = 0. \tag{4.30}$$

If the velocity is solenoidal, the velocity divergence term vanishes and the level set advection equation is given in conservative form:

$$\frac{\partial\varphi}{\partial t} + \nabla \cdot (\boldsymbol{u}_{\text{ext}}\varphi) = 0. \tag{4.31}$$

For such conservation laws, a variety of stable DG discretizations exists. Here, a standard upwind DG scheme is employed, which can be found in any DG textbook, such as Di Pietro and Ern (2012). As a result, the quality of the level set field is maintained for many time-steps and fewer reinitializations are necessary compared to the marching scheme which was used in the work of Smuda and Kummer (2022) or a discretization using a divergent extension velocity. However, due to the treatment of the (inflow) boundary conditions, only considering the inner values, it is important that the level set field is monotonous w.r.t. the distance from the interface. Otherwise, it would be possible for new unphysical interfaces to spawn at the (inflow) boundaries. Therefore,

occasional reinitialization is still necessary to maintain this monotonicity. The reinitialization procedure is explained towards the end of this section in Section 4.3.4.

For completeness, we finally state the spatial discretization for the level set advection with Eq. (4.30), used to find a solution $\varphi \in \mathbb{P}_k^{\mathrm{X}}(\mathfrak{K}_h(t))$:

$$\begin{aligned} &\int_{\mathfrak{K}_h} \frac{\partial \varphi}{\partial t} v \ \mathrm{d}V - \int_{\mathfrak{K}_h} \varphi \boldsymbol{u}_{\text{ext}} \cdot \nabla_h v + \varphi \nabla_h \cdot (\boldsymbol{u}_{\text{ext}})\, v \ \mathrm{d}V \\ &+ \sum_{\Gamma} \int_{\Gamma} \hat{f}(\varphi^-, \boldsymbol{u}_{\text{ext}}^-, \varphi^+, \boldsymbol{u}_{\text{ext}}^+, \boldsymbol{n}^\Gamma) v \, dS = 0 \quad \forall \quad v \in \mathbb{P}_k^{\mathrm{X}}(\mathfrak{K}_h), \end{aligned} \tag{4.32a}$$

$$\hat{f}(\varphi^-, \boldsymbol{u}_{\text{ext}}^-, \varphi^+, \boldsymbol{u}_{\text{ext}}^+, \boldsymbol{n}^\Gamma) = \begin{cases} \varphi^- \boldsymbol{u}_{\text{ext}}^- \cdot \boldsymbol{n}^\Gamma & , \frac{\boldsymbol{u}_{\text{ext}}^- + \boldsymbol{u}_{\text{ext}}^+}{2} \cdot \boldsymbol{n}^\Gamma \geq 0 \\ \varphi^+ \boldsymbol{u}_{\text{ext}}^+ \cdot \boldsymbol{n}^\Gamma & , \frac{\boldsymbol{u}_{\text{ext}}^- + \boldsymbol{u}_{\text{ext}}^+}{2} \cdot \boldsymbol{n}^\Gamma < 0 \\ \varphi^- \boldsymbol{u}_{\text{ext}}^- \cdot \boldsymbol{n}^\Gamma & , \boldsymbol{x} \in \partial\Omega \end{cases}. \tag{4.32b}$$

Herein, the velocity divergence is still included as a source term. In most simulations in this work, the advection velocity is divergence free (in the weak sense), Eq. (4.31) is used and this term neglected. For temporal integration of the level set equation (4.32) the total variation diminishing (TVD) 3 scheme proposed by Gottlieb and Shu (1998) is employed. If not stated otherwise, this "scalar advection" method is employed to evolve the level set throughout this work.

Phase field method The idea behind the second method stems from diffuse interface modeling. Originally the Cahn-Hilliard equations were devised by the name giving authors in Cahn and Hilliard (1958), Cahn (1959), and Cahn and Hilliard (1959) to describe the free energy in a non-uniform system. In the context of diffuse interface models, the idea is developed to combine the description of the phase transition through the so-called order parameter in the Cahn-Hilliard with e.g. (but not necessarily) the Navier-Stokes equations, e.g. (Caginalp, 1986; Seppecher, 1996; Badalassi et al., 2003; Yue et al., 2010). Implementations of these kind of models in the context of DG methods are already investigated in e.g. (Wells et al., 2006; Xia et al., 2007; Kay et al., 2009; Feng et al., 2016; Liu and Riviere, 2018; Manzanero et al., 2020). In original diffuse interface modeling, the order parameter is then used in the Navier-Stokes equations to introduce an additional stress (basically the surface tension) in the transition region between the phases. Furthermore, material parameters are functions of this order parameter to mark the transition from one phase to another, while only using one system of equations for both phases. This coupling is omitted here, instead the sharp interface models, deploying separate systems for each phase coupled at the sharp interface, described in Section 2.6 are used. Therefore, the order parameter is identified only as the level set and used to obtain the interface position. Compared to the scalar advection equation, Eq. (4.28) is modified with a non-linear RHS. The Cahn-Hilliard equation, see (Kay et al., 2009) reads as

$$\frac{\partial \varphi}{\partial t} + \boldsymbol{u}_{\text{ext}} \nabla \varphi = \nabla \cdot (M \nabla \gamma), \tag{4.33a}$$

$$\gamma = \varphi^3 - \varphi - \xi^2 \Delta \varphi, \tag{4.33b}$$

using the same extension velocity as for the "scalar advection" method. The additional variables/parameters are called the chemical potential γ, mobility M and gradient energy coefficient

ξ. The Cahn-Hilliard method basically aims to minimize the free-energy functional, e.g. Yue et al. (2010),

$$F(\varphi) = \int_\Omega \frac{1}{2}\left(\varphi^2 - 1\right)^2 + \frac{\xi^2}{2}|\nabla\varphi|^2 \ \mathrm{d}V. \tag{4.34}$$

The first contribution, modeled here in the form of a double-well potential, is called the local energy and the second the gradient energy (Cahn, 1959). Equation (4.34) is minimal when the double-well potential is minimized, forcing the order parameter towards the limiting values ± 1, while simultaneously minimizing the gradient energy, i.e., the length and thickness of phase boundaries. The balance between these contributions is influenced by the gradient energy coefficient ξ, determining the equilibrium thickness of the transition region. The RHS of Eq. (4.33a) therefore "pulls" the transition region back to its equilibrium shape, which for a plane interface is given by

$$\varphi\left(\boldsymbol{x}, t\right) = \tanh\left(\frac{\boldsymbol{x} - \boldsymbol{x}_\Sigma(t)}{\sqrt{2}\xi}\right). \tag{4.35}$$

If the profile of φ becomes too steep, the gradient energy contribution grows and the minimization of the free energy pushes the transition region apart again. On the other hand if the profile is too shallow, the local energy is not minimized and causes the transition region to be pulled together, approaching a step profile. The mobility or diffusion parameter M controls the amount of these regularizing effects. However, too large M leads to an artificial smoothing of sharp curvatures in the interface, e.g. filaments arising in rising bubble simulations. Finally, the boundary conditions used to close Eq. (4.33a) need to be specified. Here, we limit the consideration of possible boundary conditions to impenetrable walls in which case

$$\nabla\varphi \cdot \boldsymbol{n}^{\partial\Omega} = -\frac{\cos(\theta_{\text{stat}})}{\sqrt{2}\xi}\left(1 - \varphi^2\right) \quad \text{on } \boldsymbol{x} \in \partial\Omega, \tag{4.36a}$$

$$\gamma = 0 \quad \text{on } \boldsymbol{x} \in \partial\Omega. \tag{4.36b}$$

The Neumann type boundary condition for φ takes into account the equilibrium contact-angle (Yue et al., 2010). The numerical solution for the level set is found by solving Eq. (4.33a) as a system of two coupled second order equations, employing the method introduced in Section 3.1. For temporal discretization a singly diagonal implicit Runge Kutta (SDIRK) scheme, e.g. implicit euler or SDIRK22 (Kennedy and Carpenter, 2016), is employed, in conjunction with a Newton solver to treat the nonlinearity of the system. The implementation of Eq. (4.33a) follows along the lines of the implementation for the fluid equations, cf. Section 4.1, Appendix A.1, and Eq. (4.32), using an upwind scheme for the convective flux and the SIP method for the Laplacian terms. Aspects on the choice of parameters and also why this method was ultimately not further pursued as a level set evolution technique are discussed later in Section 6.2.

4.3.2 Advection velocity

To evolve the interface in time, knowledge of the normal component of the interface velocity is required. For the three different systems presented in Section 2.6 varying expressions can be found, which are presented here. The first step is to determine the velocity of the interface, which in case of non-vanishing mass fluxes differs from the bulk phase velocities. After the velocity at the interface is known, it has to be extended to the whole domain in a suitable manner to solve the level set equations presented in Section 4.3.1

Interface velocity In case of the material multiphase flow described in Section 2.6.1, Eq. (2.67) is found, meaning the normal components of the interface velocity and velocities of either phase are equal. As the tangential interface velocity has no influence on the shape evolution of the interface it can be freely chosen. Furthermore, the interface velocity can be evaluated from either phase as they lead to the same result. Therefore, every weighted average is also a valid expression. The final expression

$$\boldsymbol{u}^{\Sigma} = \frac{\{\{\rho \boldsymbol{u}\}\}}{\{\{\rho\}\}} \tag{4.37}$$

follows from a density averaging of the interface velocity, while neglecting the restriction to the normal components. It is evident from Eq. (4.29) that only the normal component of the interface velocity is ultimately used. However, the choice of interface velocity in Eq. (4.37) is due to the implementation, where it is favorable to not project the normal component $\boldsymbol{u}^{\Sigma} \cdot \boldsymbol{n}^{\Sigma}$ on an auxiliary field. For the case of multiphase flows with evaporation (Section 2.6.2), the mass flux appears in the expression for the interface velocity, Eq. (2.73). By employing the jump condition for the energy equation and otherwise following the same steps as for material flows, the expression

$$\boldsymbol{u}^{\Sigma} = \frac{\{\{\rho \boldsymbol{u}\}\} - \frac{[\![-k\nabla T]\!]}{\hat{h}_{vap}}}{\{\{\rho\}\}} \tag{4.38}$$

is found for the interface velocity with evaporation. The most convenient case is that of the free surface flow (Section 2.6.3), which is also assumed to be material. Here no opposing phase exists and therefore, the interface and fluid velocities coincide:

$$\boldsymbol{u}^{\Sigma} = \boldsymbol{u} \tag{4.39}$$

Velocity extension over the domain Now, that the interface velocity at the interface is known by Eqs. (4.37) to (4.39), it is still necessary to extend it over the whole domain, to obtain a globally defined velocity field for the level set advection by Eq. (4.28) or Eq. (4.33a). In Smuda (2021) and Smuda and Kummer (2022) the presented method employs a marching scheme for computing the extension velocity in a narrow band around the interface. For most calculations in this work, a different approach is chosen, which was first presented in Rieckmann et al. (2023e). To obtain the velocity extension on the whole domain, the following system is solved:

$$\nabla \cdot (\boldsymbol{u}_{\text{ext}}) = 0, \quad \boldsymbol{x} \in \Omega, \tag{4.40a}$$

$$-\nabla p_{\text{ext}} + \Delta \boldsymbol{u}_{\text{ext}} = \boldsymbol{0}, \quad \boldsymbol{x} \in \Omega, \tag{4.40b}$$

$$(-p_{\text{ext}}\mathbf{I} + \nabla \boldsymbol{u}_{\text{ext}}) \cdot \boldsymbol{n}^{\partial\Omega} = \boldsymbol{0}, \quad \boldsymbol{x} \in \partial\Omega, \tag{4.40c}$$

$$\boldsymbol{u}_{\text{ext}} \cdot \boldsymbol{n}^{\Sigma} = \boldsymbol{u}^{\Sigma} \cdot \boldsymbol{n}^{\Sigma}, \quad \boldsymbol{x} \in \Sigma. \tag{4.40d}$$

Homogeneous Neumann boundary conditions are applied on all outer domain boundaries, while a Dirichlet-type condition is imposed on the interface to ensure the correct advection velocity (using only the normal component). In general, these boundary conditions differ from those employed during the flow solution. The similarity of Eq. (4.40) to the Stokes equations is evident. The auxiliary variable p_{ext} represents an artificial pressure (without direct physical meaning) that is necessary to obtain a solenoidal extension velocity $\boldsymbol{u}_{\text{ext}}$. The discretiziation of this system follows the same procedure as of the fluid system described in Section 4.1. The divergence, gradient and Laplacian are discretized in the same way as the corresponding operators in the flow

solution described. However, it is fully single-phase, supplemented with an additional penalty term enforcing the Dirichlet condition for the velocity at the interface. Finally, the resulting discrete problem is to find $(\boldsymbol{u}_{\text{ext}}, p_{ext}) \in \left(\mathbb{P}_k^{\text{X}}(\mathfrak{K}_h(t))^D \times \mathbb{P}_{k-1}^{\text{X}}(\mathfrak{K}_h)\right)$, such that

$$\begin{aligned}
&\int_{\mathfrak{K}_h} \nabla_h \cdot (\boldsymbol{u}_{\text{ext}})\, q \;\mathrm{d}V + \sum_{\Gamma} \int_{\Gamma} -[\![\boldsymbol{u}_{\text{ext}}]\!] \cdot \boldsymbol{n}^{\Gamma}\, \{\{q\}\}\; dS = 0 \\
&\int_{\mathfrak{K}_h} -\nabla_h \cdot (\boldsymbol{v})\, p_{\text{ext}} \;\mathrm{d}V + \sum_{\Gamma} \int_{\Gamma} [\![\boldsymbol{v}]\!] \cdot \boldsymbol{n}^{\Gamma}\, \{\{p_{\text{ext}}\}\}\; dS + \int_{\mathfrak{K}_h} \nabla_h \boldsymbol{u}_{\text{ext}} : \nabla_h \boldsymbol{v} \;\mathrm{d}V \\
&+ \sum_{\Gamma} \int_{\Gamma} -\left\{\left\{\nabla_h \boldsymbol{u}_{\text{ext}} \cdot \boldsymbol{n}^{\Gamma}\right\}\right\} \cdot [\![\boldsymbol{v}]\!] - \left\{\left\{\nabla_h \boldsymbol{v} \cdot \boldsymbol{n}^{\Gamma}\right\}\right\} \cdot [\![\boldsymbol{u}_{\text{ext}}]\!] + \eta\, [\![\boldsymbol{u}_{\text{ext}}]\!] \cdot [\![\boldsymbol{v}]\!]\; dS \\
&+ \int_{\Sigma} \eta(\boldsymbol{u}_{\text{ext}} - \boldsymbol{u}^{\Sigma}) \cdot \boldsymbol{n}^{\Sigma} (\boldsymbol{v} \cdot \boldsymbol{n}^{\Sigma}) \;\mathrm{d}S = 0 \quad \forall \quad (\boldsymbol{v}, q) \in \left(\mathbb{P}_k^{\text{X}}(\mathfrak{K}_h)^D \times \mathbb{P}_{k-1}^{\text{X}}(\mathfrak{K}_h)\right).
\end{aligned} \tag{4.41}$$

The penalty parameter η is chosen according to Shahbazi (2005), i.e., on each edge as the maximum penalty for the neighboring cells i and j with an arbitrarily chosen safety factor of 4:

$$\begin{aligned}
\eta &= \max(\eta_i, \eta_j), \\
\eta_i &= 4(k+1)^2 \frac{\text{Vol}(\partial K_i)}{\text{Vol}(K_i)}.
\end{aligned} \tag{4.42}$$

The Vol$(\cdot)$ operator denotes the measure (D dimensional volume) of the cell or its surface ($D-1$ dimensional volume). The details of the boundary treatment are omitted for brevity. Two choices are implemented, for the former all boundaries are homogeneous Neumann boundaries, as in Eq. (4.40). In the latter boundaries that are impermeable in the flow solver are impermeable during the level set evolution as well. The former approach allows more flexibility, when interface and fluid velocity are different, as common in problems involving evaporation. In the test cases involving evaporation the area enclosed by domain boundaries and the interface is not conserved. Therefore, a solenoidal extension velocity needs to allow an in- or outflow at the domain boundaries. After inserting the DG ansatz from Eq. (3.22) and solving the system, the extension velocity $\boldsymbol{u}_{\text{ext}}$ can finally be obtained. Owing to the form of the system, this approach is called the Stokes extension.
As an alternative also the Fast Marching method from Smuda and Kummer (2022) can be employed. If not stated otherwise all calculations with a moving interface are done using the Stokes extension with all around homogeneous Neumann boundaries. This approach also allows an augmented scheme, omitting the velocity divergence and artificial pressure. Then, only a Laplace problem is solved, which motivates the description as Laplace extension. However, in this case the advection velocity is no longer solenoidal and an additional source term appears in the advection equation, see Eq. (4.30). This approach is not used for results displayed in this work and therefore not presented in detail.

4.3.3 Projection onto a continuous field

As defined in Definition 4.1 the level set has to be a continuous field, such that the interfaces are compact submanifolds without any holes. However, for DG solutions of Eq. (4.28) this is not guaranteed. The situation is more likely to resemble what is shown in Fig. 4.2. From the figure, it is evident that the cell faces for neither the white nor blue phase-cells align in neighboring

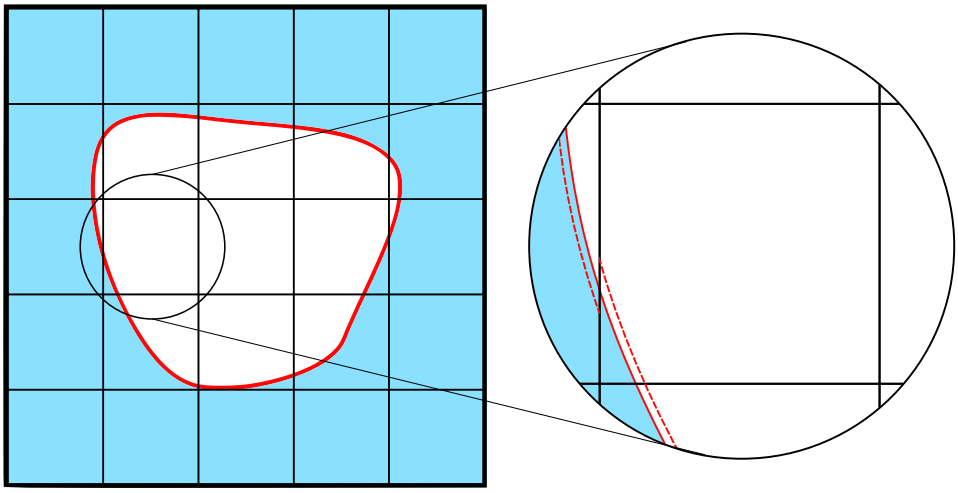

Figure 4.2: The cut-cell mesh from Fig. 4.1 is depicted. In the magnification a possible situation of an initially discontinuous interface (dashed red) and a continuous representation of the same interface (solid red) is shown.

cells. This is caused by a discontinuity of the initial interface representation shown by the dashed red line. The necessary integrals over cell faces occuring in the discretization, e.g. Eq. (4.28), are thus no longer uniquely defined. To the best of our knowledge, there is no way to devise a well-posed method in this case. Therefore, these faces need to align from either cell. This is achieved by computing a continuous representation of the level set field φ_c in a narrow band of cells $\mathfrak{K}_{\text{nb}}$ around the zero-set, which will then subsequently be used during the flow solution to obtain the division of the domain into the different phases. The continuous representation is shown in the figure as the solid red line. To compute this continuous interface, the following quadratic optimization problem is solved (Smuda, 2021):

$$\min \quad \|\varphi - \varphi_c\|^2_{L^2(\mathfrak{K}_{\text{nb}})}, \quad \mathfrak{K}_{\text{nb}} \subset \mathfrak{K}_h, \tag{4.43a}$$

$$\text{s.t.} \quad \varphi_{c,j_{in}}|_{\Gamma_i} = \varphi_{c,j_{out}}|_{\Gamma_i}, \quad \forall \Gamma_i \in \mathfrak{K}_{\text{nb}}. \tag{4.43b}$$

4.3.4 Reinitialization

The reinitialization procedure is partially motivated by the need to enforce non-diminishing gradients and monotonicity of the level set field w.r.t. the distance from the interface. In relevant literature, this is usually done by using a signed-distance level set, see e.g. Mirjalili et al. (2017) or Owkes and Desjardins (2013). The signed-distance property is generally not preserved during the advection step. Therefore, starting from the current interface, the reinitialization seeks to restore this property. Several procedures are proposed in the literature, for which a good overview is given in Basting and Kuzmin (2013). For this work, a variation of the elliptic reinitialization proposed in Basting and Kuzmin (2013) is used. Details on the implementation can be found in the work of Utz et al. (2017). In our method the level set is not required to be an exact signed-distance field, as this property is not leveraged. Consequently, it is not necessary to perform the reinitialization on every time-step. In case of the phase field level set, the RHS terms of Eq. (4.33a) serve to contract the transition region around the interface, while forcing the level set values to the bounds

of ± 1 elsewhere. Therefore, there is no need to reinitialize the level set in that method, which is one of its main advantages.

4.4 Temporal discretization

In Sections 4.1 to 4.3 the components of the spatial discretization for the flow solution and interface representation are introduced. To obtain a working numerical method, these components need to be combined to allow a temporal evolution of the flow and interface solutions. In this section first the interplay between interface and flow solution is presented and the schemes used to discretize the temporal terms, i.e., the partial time derivatives in Eq. (4.21), are described.

4.4.1 Interface flow coupling

Even though the equations describing the fluid flow are solved in a monolithic system (i.e. velocity, pressure and temperature are solved simultaneously) the solution to the interface evolution is excluded from this monolithic block. Therefore, the method basically acts as a series of DG and XDG schemes strung together. For a single time-step, the solver proceed as follows, splitting the complete problem into three parts:

1. Using the current flow solution, compute the extension velocity $\boldsymbol{u}_{ext}$, as described in Section 4.3.2
2. Solve the level set evolution, as described in Section 4.3.1
3. Solve the flow equations, Sections 4.1, 4.2, 4.4 and 4.5

Lie splitting The basic idea of the splitting approach is to solve coupled systems sequentially instead of simultaneously. To illustrate this, consider the ODE system

$$\frac{\partial f}{\partial t} = H_1(t, f, g), \tag{4.44a}$$

$$\frac{\partial g}{\partial t} = H_2(t, f, g). \tag{4.44b}$$

In the present method, the first equation could be thought of as the level set evolution problem, which depends not only on the level set but also the solution of the second equation, representing the flow problem. The flow problem in turn also depends on the level set, namely the interface position, in a non-trivial way. During the splitting procedure these equations are decoupled and solved sequentially. First the interface evolution problem is solved, using the initial flow solution:

$$\frac{\partial f^{n+1}}{\partial t} = H_1(t^{n+1}, f^{n+1}, g^n). \tag{4.45}$$

Then, the flow solution is updated, using the new interface position:

$$\frac{\partial g^{n+1}}{\partial t} = H_2(t^{n+1}, f^{n+1}, g^{n+1}). \tag{4.46}$$

This simple, first order accurate, splitting procedure is called Lie-Splitting (or Lie-Trotter Splitting) (Holden et al., 2010). As the interface is assumed fixed during one step of the flow solution, the mass matrices stay constant during one time-step, as mentioned already in Section 4.2. However, the new flow solution is dependent on the old one (through the approximation of the time derivative), which is given with respect to the old interface position. Therefore, a method is needed to extrapolate the old solution from the old onto the new cut-cell mesh. An alternative to this splitting procedure is the moving interface approach presented by Kummer et al. (2018). However, the discretization for that approach is more involved and not explored in this work. Compared to the splitting approach , the advantage is that higher temporal convergence orders can be achieved and the extrapolation procedure becomes obsolete.

Extrapolation In each cell K_j the solution for a single phase $\mathfrak{s}$ is given in terms of a coordinate vector $\boldsymbol{z}_{j,\mathfrak{s}}$, Eq. (4.25), and a basis for the broken cut-polynomial space $\mathbb{V}^{\mathrm{X}}_{\boldsymbol{k}}$, see e.g. Eq. (4.2). These cut-cell bases are constructed as displayed in Eq. (3.45). To transfer the old solution to the new cut-mesh two different situations have to be distinguished: In the first instance, the interface stays within the same cell, i.e., the species $\mathfrak{s}$ exists in cell K_j at the current as well as all required previous time-steps, e.g., $K^{\mathrm{X}}_{j,\mathfrak{s}}(t) \neq \emptyset, \quad t = \{t_n, t_{n-1}\}$. In this case the transformation is done by projecting the previous solution onto the current basis. Concretely, the solution coordinates are reused and the characteristic function from Eq. (3.45) is updated to the current time:

$$\boldsymbol{z}_{j,\mathfrak{s}}(t_{n-1})^T \boldsymbol{\Phi}_j(\boldsymbol{x}) X_{j,\mathfrak{s}}(\boldsymbol{x}, t_{n-1}) \rightarrow \boldsymbol{z}_{j,\mathfrak{s}}(t_{n-1})^T \boldsymbol{\Phi}_j(\boldsymbol{x}) X_{j,\mathfrak{s}}(\boldsymbol{x}, t_n). \tag{4.47}$$

In the second instance, the interface moves across the boundary between cells, i.e., K_j is a newly formed cut-cell, e.g., $K^{\mathrm{X}}_{j,\mathfrak{s}}(t_n) \neq \emptyset$ but $K^{\mathrm{X}}_{j,\mathfrak{s}}(t_{n-1}) = \emptyset$. In this case, no solution-coordinates exist for K_j that can be reused. Instead, solution coordinates $\hat{\boldsymbol{z}}_{j,\mathfrak{s}}(t_{n-1})$ are obtained by extrapolating the solution from a neighbor cell with $K^{\mathrm{X}}_{i,\mathfrak{s}}(t_{n-1}) \neq \emptyset$. This situation and the extrapolation procedure is illustrated in Fig. 4.3. The two cells are then agglomerated together and a combined basis is formed by extending the basis $\boldsymbol{\Phi}_i$, i.e.,

$$\boldsymbol{\Phi}^{Agg} = \boldsymbol{\Phi}_i X_{K_i \cup K_j} = \boldsymbol{\Phi}_i X_{K_i} + \boldsymbol{\Phi}_i X_{K_j} = \boldsymbol{\Phi}_i X_{K_i} + \mathbf{M} \boldsymbol{\Phi}_j X_{K_j}. \tag{4.48}$$

The transformation matrix $\mathbf{M}$ to convert $\boldsymbol{\Phi}_j$ to $\boldsymbol{\Phi}_i$ is obtained by solving the projection

$$\left\langle \boldsymbol{\Phi}_j^T, \boldsymbol{\Phi}_j \right\rangle_{K_j} \mathbf{M} = \left\langle \boldsymbol{\Phi}_j^T, \boldsymbol{\Phi}_i \right\rangle_{K_j}. \tag{4.49}$$

Finally, by expressing the solution on the agglomerated cell

$$\begin{aligned} \boldsymbol{z}^{Agg}_{\mathfrak{s}}(t_{n-1}, \boldsymbol{x}) &= \boldsymbol{z}_{i,\mathfrak{s}}(t_{n-1})^T \boldsymbol{\Phi}_i(\boldsymbol{x}) X_{K_i \cup K_j} \\ &= \boldsymbol{z}_{i,\mathfrak{s}}(t_{n-1})^T \boldsymbol{\Phi}_i(\boldsymbol{x}) X_{K_i} + \boldsymbol{z}_{i,\mathfrak{s}}(t_{n-1})^T \mathbf{M} \boldsymbol{\Phi}_j(\boldsymbol{x}) X_{K_j} \\ &= \boldsymbol{z}_{i,\mathfrak{s}}(t_{n-1})^T \boldsymbol{\Phi}_i(\boldsymbol{x}) X_{K_i} + \boldsymbol{z}_{j,\mathfrak{s}}(t_{n-1})^T \boldsymbol{\Phi}_j(\boldsymbol{x}) X_{K_j}, \end{aligned} \tag{4.50}$$

we obtain the required solution coordinates

$$\boldsymbol{z}_{j,\mathfrak{s}}(t_{n-1})^T = \boldsymbol{z}_{i,\mathfrak{s}}(t_{n-1})^T \mathbf{M}. \tag{4.51}$$

Once again applying Eq. (4.47) completes the procedure. Note that this whole process is basically a cell agglomeration as done in Section 4.2.3, but performed in the opposite direction.

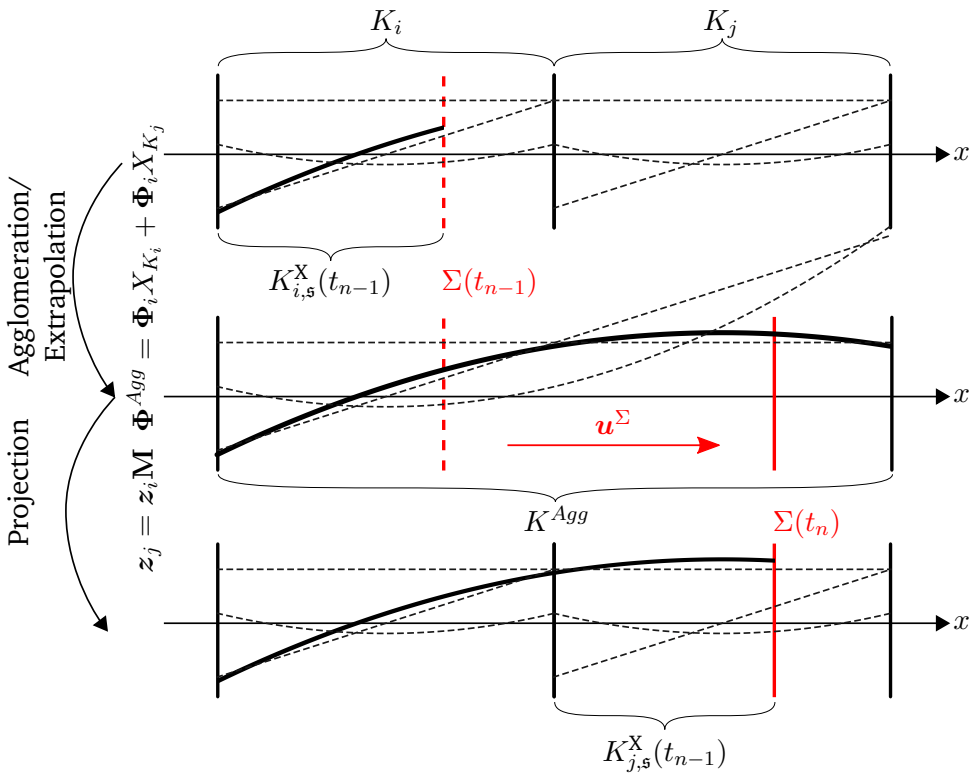

Figure 4.3: Extrapolation procedure of a solution onto a newly formed cut-cell. Dashed lines indicate the basis functions in each cell.
Top: At the previous time-step the solution (solid black line) in the left phase is only known in the cell $K^{\mathrm{X}}_{i,\mathfrak{s}}$ with respect to the old interface position (dashed red line).
Middle: The cells K_i and K_j are agglomerated together to form the cell K^{Agg}. By reusing the basis and coefficients of the solution from cell K_i for K^{Agg} the solution is extrapolated. Additionally, the transformation between the basis of K_j and that of K^{Agg} is computed.
Bottom: Finally the basis transformation is reused to obtain the solution in the newly formed cell $K^{\mathrm{X}}_{j,\mathfrak{s}}$ (solid red line).

4.4.2 Timestepping schemes

In Section 4.2 it is described how the abstractly discretized systems from Section 4.1 can be brought in the form of a DAE system. To solve these systems, two different methods are implemented and available in the solver. These are the SDIRK and backward differentiation formula (BDF) schemes (Hairer and Wanner, 1996). Given the equation (4.25) for the residual and demanding this residual to vanish, the goal is to find a solution for the next time-step $\boldsymbol{z}^{(n+1)} = \boldsymbol{z}(t^{(n)} + \Delta t^{(n)}) = \boldsymbol{z}(t^{(n+1)})$. In this section it will be shown how the solver accomplishes this task, following closely the actual implementation of the mentioned schemes.

Runge Kutta methods Runge Kutta (RK) methods are single-step methods, but using multiple intermediate stages (Hairer et al., 1993; Hairer and Wanner, 1996). An s-stage method is

Table 4.1: Butcher tableaus for Runge-Kutta methods employed in this work (Gottlieb and Shu, 1998; Kennedy and Carpenter, 2016)

Scheme	$\mathbf{a}$	$\boldsymbol{b}$	$\boldsymbol{c}$
Implicit Euler	$\begin{pmatrix}1\end{pmatrix}$	$\begin{pmatrix}1\end{pmatrix}$	$\begin{pmatrix}1\end{pmatrix}$
SDIRK22	$\begin{pmatrix}1-\sqrt{2}/2 & \\ \sqrt{2}/2 & 1-\sqrt{2}/2\end{pmatrix}$	$\begin{pmatrix}\sqrt{2}/2 & 1-\sqrt{2}/2\end{pmatrix}$	$\begin{pmatrix}1-\sqrt{2}/2 & 1\end{pmatrix}$
TVD3	$\begin{pmatrix}0 & & \\ 1 & 0 & \\ 0.25 & 0.5 & 0\end{pmatrix}$	$\begin{pmatrix}1/6 & 1/6 & 2/3\end{pmatrix}$	$\begin{pmatrix}0 & 1 & 0.5\end{pmatrix}$

characterized by three sets of coefficients, $\mathbf{a} \in \mathbb{R}^{s\times s}$, and $\boldsymbol{b}, \boldsymbol{c} \in \mathbb{R}^s$. Here, we limit our presentation to those methods, whose coefficient matrix $\mathbf{a}$ is of lower triangular shape, in case of an explicit scheme even strictly lower triangular. The intermediate solution vector $\boldsymbol{z}^{(i,n)}$ for the i-th RK stage (here counting starts at 1) in the n-th time-step is then obtained by solving

$$\frac{1}{\Delta t^{(n)}}\mathbf{M}\boldsymbol{z}^{(i,n)} + a_{i,i}\boldsymbol{op}(t^{(n)} + c_i\Delta t^{(n)}, \boldsymbol{z}^{(i,n)}) = \frac{1}{\Delta t^{(n)}}\mathbf{M}\boldsymbol{z}^{(n)} - \sum_{j=1}^{i-1} a_{i,j}\boldsymbol{k}_j - a_{i,i}\boldsymbol{af}(t^{(n)} + c_i\Delta t^{(n)}). \tag{4.52}$$

For an explicit stage, the diagonal coefficient vanishes, $a_{i,i} = 0$. The values for the change-rate are defined as

$$\boldsymbol{k}_j = \boldsymbol{op}(t^{(n)} + c_j\Delta t^{(n)}, \boldsymbol{z}^{(j,n)}) + \boldsymbol{af}(t^{(n)} + c_j\Delta t^{(n)}). \tag{4.53}$$

If the scheme is stiffly accurate (Hairer and Wanner, 1996; Kennedy and Carpenter, 2016), i.e. $c_s = 1$ and $a_{s,i} = b_i$, the intermediate solution for the final stage is the solution for the next time-step:

$$\boldsymbol{z}^{(n+1)} = \boldsymbol{z}^{(s,n)}. \tag{4.54}$$

Otherwise, the value for the new time-step is found by performing a last explicit step:

$$\frac{1}{\Delta t^{(n)}}\mathbf{M}\boldsymbol{z}^{(n+1)} = \frac{1}{\Delta t^{(n)}}\mathbf{M}\boldsymbol{z}^{(n)} - \sum_{j=1}^{s} b_j\boldsymbol{k}_j. \tag{4.55}$$

Usually, the RK schemes are classified with an abbreviation, hinting on the characteristics of the scheme, e.g. SDIRK or TVD and two numbers indicating the number of stages and order of the scheme. The Butcher tableaus for the methods used within this work are displayed in Table 4.1.

Backwards differentiation formulas The BDF schemes are so-called multi-step methods, which means the solution at the next time-step can depend on multiple past steps (Hairer and Wanner, 1996). In the current solver this method is implemented as

$$\frac{1}{\Delta t}\mathbf{M}\boldsymbol{z}^{(n+1)} + \Theta\boldsymbol{op}(t^{(n+1)}, \boldsymbol{z}^{(n+1)}) = \sum_{i=0}^{K-1} \theta_i \frac{1}{\Delta t}\mathbf{M}\boldsymbol{z}^{(n-i)} - \Theta\boldsymbol{af}(t^{(n+1)}), \tag{4.56}$$

using a fixed time-step size $\Delta t^{(n)} = \Delta t$ and BDF order K. In Table 4.2 the coefficients for the BDF methods up to order 3 are displayed.

Table 4.2: Coefficients for BDF1 - BDF3

Scheme	Θ	$\boldsymbol{\theta}$
Implicit Euler (BDF1)	1	(1)
BDF2	$2/3$	$(4/3, -1/3)$
BDF3	$6/11$	$(18/11, -9/11, 2/11)$

Unification of timestepping methods Looking at Eqs. (4.52) and (4.56) it can be observed that both schemes possess a similar structure. The LHS of Eqs. (4.52) and (4.56) depends on the unknown solution vector, while the RHS solely depends on already known quantities. This motivates the following reformulation in a solution dependent LHS and an independent RHS vector:

$$\boldsymbol{F}(\boldsymbol{y}) = \boldsymbol{lhs}(\boldsymbol{y}) - \boldsymbol{rhs} = \boldsymbol{0}. \tag{4.57}$$

In case of the BDF method, $\boldsymbol{y}$ would mean the solution at the next time-step $\boldsymbol{z}^{(n+1)}$, while the meaning for a RK scheme is the intermediate solution value for the current stage $\boldsymbol{z}_i$. Compared with the BDF method the implicit RK methods allow an uncomplicated implementation of adaptive time-steps. Additionally, there are stable high-order methods available, while BDF is unstable from BDF6 onward. On the other hand, the BDF method is computationally more efficient, as only a single step is solved.

4.4.3 Selection of time-step size

In Eqs. (4.52) and (4.56) the time-step size $\Delta t^{(n)}$ appears as a parameter in the temporal discretization. For the evolution of the interface, Section 4.3.1, the same time-step size is used. Some caution must be exercised in choosing $\Delta t^{(n)}$. If $\Delta t^{(n)}$ is chosen too large, the interface may skip a whole cell which is fatal for the solver, because then it is unclear how the solution can be extrapolated onto the newly formed cut-cells. However, in most cases the scalar level set advection equation is used and solved using the explicit TVD3 scheme, Table 4.1. In that case a Courant-Friedrichs-Lewy (CFL) condition must be respected, limiting the maximum admissible time-step

$$\Delta t_{\boldsymbol{u}} \leq \frac{\min(h)}{\max(\boldsymbol{u}_{\text{ext}})(2k+1)}, \tag{4.58}$$

depending on the maximum velocity $\max(\boldsymbol{u}_{\text{ext}})$, minimum grid size $\min(h)$ and polynomial degree k of the level set field. In most setups the (static) capillary time-step restriction[1] (Denner and van Wachem, 2015)

$$\Delta t \leq \sqrt{\frac{\{\{\rho\}\}\left(\frac{\min(h)}{k+1}\right)^3}{\pi\sigma}} \tag{4.59}$$

is even more severe, as it scales super-linearly with $\min(h)$. Recent works suggest that this super-linear (w.r.t. the grid size) restriction can be circumvented by a fully implicit method (Denner et al., 2022). However, in this work, an explicit splitting between interface and flow solution is

[1] For the more precise dynamic restriction the fluid velocity parallel to the interface is also taken into account (Denner and van Wachem, 2015), this velocity is usually not known a-priori, which is why we use the static restriction.

employed and the restriction is binding. In Section 6.1 the derivation of Eq. (4.59) is displayed, followed by an analysis on the severity of this restriction.

4.5 Nonlinear solution

After introducing the temporal discretization in Section 4.4, we are left with the root-finding problem of Eq. (4.57). The $\boldsymbol{lhs}$-term may depend non-linearly on the solution vector $\boldsymbol{y}$. In this case, a non-linear solver has to be employed. In the numerical scheme in this work two different approaches are implemented. Both resemble a fixed point iteration, one using an approximation of the Jacobian of $\boldsymbol{F}$ and the other one being Newton's method with the exact Jacobian.

4.5.1 Linearization

Both implemented fixpoint iterations aim to obtain a correction $\Delta\boldsymbol{y}_n$ to the current solution guess $\boldsymbol{y}_n$ by solving

$$\mathbf{J}(\boldsymbol{y}^*)\Delta\boldsymbol{y}_n = -\boldsymbol{F}(\boldsymbol{y}_n). \tag{4.60}$$

The matrix $\mathbf{J}$ is an approximation of the Jacobian of $\boldsymbol{F}$ at the linearization point $\boldsymbol{y}^* = \boldsymbol{y}_n$. The next solution iterate is obtained by inserting the calculated correction in the iteration rule

$$\boldsymbol{y}_{n+1} = g(\boldsymbol{y}_n, \Delta\boldsymbol{y}_n). \tag{4.61}$$

The solver repeats this procedure of solving Eq. (4.60) and evaluating Eq. (4.61) until a specified termination criterion

$$\|\boldsymbol{F}(\boldsymbol{y}_n)\| < \epsilon(1 + \|\boldsymbol{F}(\boldsymbol{y}_0)\|) \quad \epsilon > 0, \tag{4.62}$$

or a maximum number of iterations is reached. As a starting guess for the non-linear solver usually the last time-step is used $\boldsymbol{y}_0 = \boldsymbol{z}^n$.

Fixpoint iteration The first approach approximates the non-linear problem as a fixed point iteration around some linearization point $\boldsymbol{y}^*$

$$\boldsymbol{F}(\boldsymbol{y}) \approx \tilde{\boldsymbol{F}}(\boldsymbol{y}) = \tilde{\mathbf{J}}(\boldsymbol{y}^*)\boldsymbol{y} - \boldsymbol{rhs}, \tag{4.63}$$

such that $\boldsymbol{F}(\boldsymbol{y}^*) = \tilde{\boldsymbol{F}}(\boldsymbol{y}^*)$. In this case the approximate Jacobian of the system is given as

$$\mathbf{J}(\boldsymbol{y}^*) = \frac{\partial\tilde{\boldsymbol{F}}}{\partial\boldsymbol{y}}|_{\boldsymbol{y}=\boldsymbol{y}^*} = \tilde{\mathbf{J}}(\boldsymbol{y}^*). \tag{4.64}$$

For this method, the linearization has to be implemented in the abstract operator manually, which is not shown explicitly in the integral forms shown in Appendix A.1. The iteration rule for the fixed-point iteration is implemented as a simple under-relaxation:

$$g(\boldsymbol{y}_n, \Delta\boldsymbol{y}_n) = \boldsymbol{y}_n + \lambda\Delta\boldsymbol{y}_n \quad \lambda \in (0, 1]. \tag{4.65}$$

Newton method The second approach employs a Taylor expansion around the current linearization point $\boldsymbol{y}^*$:

$$\boldsymbol{F}(\boldsymbol{y}) \approx \tilde{\boldsymbol{F}}(\boldsymbol{y}) = \boldsymbol{F}(\boldsymbol{y}^*) + \frac{\partial \boldsymbol{lhs}}{\partial \boldsymbol{y}}|_{\boldsymbol{y}=\boldsymbol{y}^*} (\boldsymbol{y} - \boldsymbol{y}^*), \tag{4.66}$$

This approach is therefore a true Newton method and the Jacobian is the exact one of Eq. (4.57):

$$\mathbf{J}(\boldsymbol{y}^*) = \frac{\partial \boldsymbol{F}}{\partial \boldsymbol{y}}|_{\boldsymbol{y}^*} = \frac{\partial \boldsymbol{lhs}}{\partial \boldsymbol{y}}|_{\boldsymbol{y}=\boldsymbol{y}^*}. \tag{4.67}$$

In the solver the Jacobian can either be implemented explicitly or, which is done in this work, is obtained by a forward finite difference scheme based on the forms as given in the appendix Appendix A.1, i.e., it is calculated by

$$J_{-,i}(\boldsymbol{y}^*) \approx \frac{\boldsymbol{lhs}(\boldsymbol{y}^* + \delta y_i \boldsymbol{e}_i) - \boldsymbol{lhs}(\boldsymbol{y}^*)}{\delta y_i}. \tag{4.68}$$

For the iteration rule, the dogleg method, also known as trust-region method, is employed (Pawlowski et al., 2006).

4.6 Linear solution

After performing the spatial and temporal discretization with respect to the current linearization point in each non-linear solver iteration (for a completely linear system the linearization and non-linear solver iteration can be skipped), a linear system of the form of Eq. (4.60) has to be solved using a linear solver. Equation (4.60) can be expressed in the more common form

$$\mathbf{A}\boldsymbol{x} = \boldsymbol{b}, \tag{4.69}$$

using a general coefficient matrix $\mathbf{A}$, unknown vector $\boldsymbol{x}$ and RHS vector $\boldsymbol{b}$. Methods for solving such linear systems of equations can be classified in two branches. Direct solvers obtain an exact solution to the linear problem, while iterative solvers search for an approximate solution by employing an inexpensive iteration rule. In this work solely direct solvers, MUMPS (Amestoy et al., 2001; Amestoy et al., 2006) and PARDISO (Schenk and Gärtner, 2006), are deployed. However, the direct solution of Eq. (4.60) can be challenging if the condition number of the matrix $\mathbf{A}$ is very high. Therefore, the performance of the solver and quality of numerical solution can be improved by employing a suitable preconditioning.

4.6.1 Preconditioning

A preconditioning of the linear system can be performed using left $\mathbf{L}$ and right $\mathbf{R}$ preconditioning matrices, like so

$$\mathbf{LAR}\tilde{\boldsymbol{x}} = \mathbf{L}\boldsymbol{b}, \tag{4.70a}$$

$$\boldsymbol{x} = \mathbf{R}\tilde{\boldsymbol{x}}. \tag{4.70b}$$

The interpretation of this procedure can be purely numerical, to change some characteristic of the system, e.g. the condition number, but also of geometric nature. The left preconditioning

can be read as a change of basis of the test function space, while the same is true for the right preconditioning and the space of ansatz functions. The first such manipulation is the small cell agglomeration mentioned in Section 4.2.3. Afterwards, also the zero rows and columns, corresponding to empty phase-cells, are filtered out, which can also be interpreted as a preconditioning. Additionally, depending on the boundary conditions, the system may be underdetermined. This occurs when only Dirichlet boundary conditions are used for the velocity. In that case, the pressure is only unique up to an arbitrary constant. Therefore, the average pressure in an arbitrary cell (usually the cell with lowest index that has a minimum distance to a cut-cell) is set to zero, i.e., the first DG coordinate for the pressure in the selected cell. Given the global index for that coordinate i the corresponding entries in $A_{-,i}$, $A_{i,-}$ and b_i are set to zero and a single unit entry is set on the diagonal $A_{i,i} = 1$.
Finally, the preconditioning is applied to the system, to improve its condition number. One reason for a poor condition of the system can be the discrepancy in scales between the discretized equations, e.g. $\hat{c}\rho \gg \rho$, or across the phases, e.g. $\rho_{\mathfrak{A}} \gg \rho_{\mathfrak{B}}$ or a poorly conditioned mass matrix block in a cut-cell. In the solver different methods for the preconditioning of the system are available in the form of block preconditioners. These act locally on the matrix and RHS entries corresponding to a single cell, and even single variable. To understand their procedure, it is necessary to keep in mind that the coefficient matrix in the solver has two contributions, the mass matrix and the operator matrix (stemming from the linearization of the operator)

$$\mathbf{A} = \mathbf{M} + \mathbf{Op}. \tag{4.71}$$

Throughout this work three preconditioners are applied. In the following presentation it is understood, that the matrices denote a single block, corresponding to only one cell, species and variable. The first preconditioner is basically a re-orthonormalization along the lines of Eq. (4.18), using a (modified) Cholesky/LDL decomposition, such that

$$\mathbf{Q}^T\mathbf{M}\mathbf{Q} = \mathbf{D}, \tag{4.72a}$$
$$\mathbf{R} = \mathbf{Q}, \tag{4.72b}$$
$$\mathbf{L} = \mathbf{R}^T, \tag{4.72c}$$

$\mathbf{D}$ being a diagonal matrix. This procedure basically only affects cut-cells, as in all other cells the mass matrix is already diagonal by design. In the actual implementation in unique cases the mass matrix in a cut-cell may become indefinite, in that case $\mathbf{D}$ can contain zero entries on its diagonal. These indefinite parts are detected by the solver and skipped during the preconditioning. This preconditioner is applied for the contributions corresponding to the discrete continuity equation. The second preconditioner uses a similar procedure, but applied to the symmetric part of the operator matrix:

$$\mathbf{Q}^T\frac{1}{2}\left(\mathbf{Op} + \mathbf{Op}^T\right)\mathbf{Q} = \mathbf{D}, \tag{4.73a}$$
$$\mathbf{R} = \mathbf{Q}, \tag{4.73b}$$
$$\mathbf{L} = \mathbf{R}^T. \tag{4.73c}$$

In the solver this procedure is applied for the momentum equation and temperature equation (only in Section 7.2). For all other simulations carried out as part of this work a third preconditioner is employed for the temperature equation. Here, the left and right preconditioning matrices are

constructed as

$$\mathbf{R} = \mathbf{I}, \tag{4.74a}$$

$$\mathbf{L} = \mathbf{O}\mathbf{p}^{-1}. \tag{4.74b}$$

During various simple test cases, where the condition number is investigated in dependence of the grid resolution, this method gave the best results. However, more recent extended tests indicate that the second preconditioner is the most suitable method to precondition the discretized heat equation. In Kummer (2017) the influence these matrix manipulations (small cell agglomeration and preconditioning) can have on the condition of the system is discussed in more detail.

5 Results for single-phase flows

The first chapter displaying results of the solver described in Chapter 4 deals with pure single-phase flows. Basis is the system of equations stated in Section 2.6.1, restricted to a single domain, without the occurrence of phase interfaces or contact lines. In addition, the temporal and convective terms are omitted and the pure Stokes problem is considered. The chapter contains two sections which originated as part of the present thesis. Both are concerned with the flow of a fluid through the nip between two cylinders. Because of the technical relevance in gravure printing this nip will be called the printing nip. Section 5.1 focuses on the position of stagnation points in the printing nip in dependence of the inhomogeneous boundary conditions. In Section 5.2 the focus is then shifted towards homogeneous solutions of the Stokes problem. Analytical results are presented and compared with a numerical investigation of the predicted viscous eddies in the printing nip.

5.1 Numerical investigation of printing nip hydrodynamics

This sections is largely identical in terms of text, equations and figures to the publication of the author of this thesis (Rieckmann et al., 2023c). In the cited publication the contributing authors combined analytical, numerical and experimental methods to obtain insights into the hydrodynamics of the printing nip. The following section focuses on the numerical results, which have emerged from this work and were written by the author of this thesis. With the exception of individual corrections and minor textual adjustments to fit within the scope of this thesis, this section is a direct quote from the publication mentioned. For better readability, additional indentation has been omitted.
Special attention is paid towards the position and pressure gradients at stagnation points, as an estimate of the meniscus position, in the printing nip. To provide an introduction into the topic and a literature overview, the introduction from Rieckmann et al. (2023c), originally written mostly by H. M. Sauer, is repeated here, emphasized by an indentation.

> The first aim of this section is to show how the extreme conditions in fluid flow in the printing nip can be made accessible to numerical simulation, in spite of the fact that pressure and shear singularities are associated with partly ill-defined boundary conditions.
> The hydrodynamics of the printing nip comprises different aspects. The ink filling and emptying of gravure cells, the formation of liquid filaments between the diverging cylinder surfaces have been intensively studied by Dodds, Carvalho & Kumar (Dodds et al., 2009; Dodds et al., 2011b; Dodds et al., 2011a; Dodds et al., 2012), Hoda & Kumar (Hoda and Kumar, 2008), Huang et al. (Huang et al., 2008), and Huang, Carvalho & Kumar (Huang et al., 2016), who employ numerical models, Cen et al.

(Cen et al., 2014), Khandavalli et al. (Khandavalli et al., 2015). Khandavalli & Rothstein (Khandavalli and Rothstein, 2017) also include fluids with complex rheology. All these studies apply to the flow problem in succession of passing the nip, excluding the singularity. In our former work (Sauer et al., 2018), some of the authors have argued that a distinction of fluid splitting into an early and a late phase is useful here. According to this distinction, liquid-air interface dynamics and filament formation counts as a late phenomenon. In contrast, the early phase of ink splitting refers to the hydrodynamics prior to the contact with the compressible gas phase. Pressure and liquid shear exceed the late phase, where air entrainments are present, by orders of magnitude. We also emphasize the effects of ink rheology and of the printing substrate material. Usually, printing ink viscosity is shear-thinning. This feature was also recognized in our emperiments, and has been studied by Wu, Carvalho & Kumar (Wu et al., 2019b; Wu et al., 2019a). The important case of paper web has been studied by Elsayad (Elsayad et al., 2002), who identified the most relevant ink and surface parameters. The specific features of paper porosity has been studied by Yang (Yang, 2013).

Principal insight into rotative printing nip flows date back to the studies on gravure coating technology by Gaskell et al. (Gaskell et al., 1998), Coyle et al. (Coyle et al., 1990), and Benkreira (Benkreira and Cohu, 1998), making the analogy to the retracting liquid meniscus in the cuvette experiment of Saffman and Taylor (Saffman and Taylor, 1958) evident. Similar phenomena have also been observed in models using alternative geometries. E.g., Voss (Voß, 2002) considered ink splitting in an opening wedge geometry, with solid half planes, where a viscous finger instability occurs as well. A stability analysis based on lubrication-models was presented by Carvalho & Scriven (Carvalho and Scriven, 1997) who also discuss the effect of surface elasticity. The particular effect of the gravure raster on film formation on the substrate has been studied by Schwarz (Schwartz, 2002) using lubrication models. The crucial point here is that a closed liquid film persists in the nip even under very high mechanical pressure. The gravure printing studies of Bornemann et al. (Bornemann et al., 2011) use, quite different from industrial custom, rigid surfaces for both cylinder and substrate. This excluded that extra space could form due to surface compressibility. Sauer et al. (Sauer et al., 2015), and Brumm et al. (Brumm et al., 2019) have proposed a lubrication model for the ink flow close to the center of the nip. This access differs from the model of Carvalho & Scriven by the feature that nip width is not considered as fixed parameter. Rather, the view of Casademunt (Casademunt, 2004) is adopted, and the nip width is scaling with elastic and hydrodynamical forces, and steady-state operation appears as a fixed point of a highly non-linear, self-stabilizing dynamical system. Being developed for elastic printing cylinders, where no nip singularity appears, the gravure printing case can formally be obtained by setting the elastic moduli of the surfaces to infinity. However, this requires to renormalize the hydrodynamical fields to avoid a singularity, and to have them floating with the arbitrary residual nip width. We have implemented here a concept based on the renormalization group ideas of Stueckelberg & Petermann (Stückelberg and Petermann, 1953), and of Gell-Mann & Low (Gell-Mann and Low, 1954). We use this to identify the invariant, macroscopically controlled features of the nip flow.

A somewhat complementary view on ink splitting in the gravure press has been

pursued by Hübner (Hübner, 1991). Remarkable here is the predicted transition phenomenon between point and lamella splitting which has been reported to exist in practical experience and in countless studies. The existence of a transition regime has been stated by Brumm et al. (Brumm et al., 2021) and a classification scheme for point splitting, lamella splitting and transition regime has been presented. Point splitting means that each gravure cell deposits an individual ink drop on the substrate, without drop coalescence to occur. Lamella splitting, however, is characterized by the development of a continuous liquid meniscus across the complete nip width. Capillary forces retain an excess of ink in the nip, which is also the origin of the viscous fingering instability, known to the printer as ribbing effect. Finally, one must admit that all these studies on gravure contribute well to a closed macroscopic understanding, but could not resolve the question about the nature of singular ink flow in the nip.

Current progress in this question came from the direct high-speed video observations of nip dynamics by Schäfer (Schäfer et al., 2019), who could resolve some of the hydrodynamic boundary conditions of the nip flow by pinching down the residual gap ((Schäfer, 2020), subsection 6.2.3) on rigid surfaces using a mechanical pressure of order of 10 MPa. In view of this, and also regarding the complex cell flow profiles observed by Yin & Kumar (Yin and Kumar, 2006), one begins to understand that Hübner's distinction of regimes is an essentially macroscopic one. On the microscopic scale, however, a delicate dynamics evolves, and the principal distinction of point and lamella becomes vague. Instead, fluid splitting appears to be related to the extreme pressure and ink shear in the nip, initialized milliseconds in advance of the actual process of ink splitting, i.e., of the creation of the liquid-air interface. The physics of a complex coupled system of hydrodynamic, elastic, and surface related degrees of freedom is revealed here, and appears as the key to proper understanding. It has up to now remained open whether vapor bubble cavitation, breakdown of liquid-solid adhesion, elastic deformation of even hardened metal surfaces are the weak point in this multiply interdependent system which finally smooths the apparent singularity into physically reasonable limits.

As a part of this program the simulation of the fluid flows in the nip in the early phase, we present here our recent progress in setting up a numerical simulation on the fluid flow, which can deal with the singular situation. As the nature of the printing nip geometry and its singular geometry is 2D, we restrict simulation strategy to the 2D boundary-value problem. This approximation already captures the full strength of divergence of pressure and shear in the nip. Simulation algorithm, mesh definition and features of algorithmic convergence can be transferred to the full 3D problem. We also benchmark the simulation with analytic lubrication results (Sauer et al., 2015), which handle the divergent features in an apparently correct manner, at least to linear order in the velocities. We emphasize that one can simulate aspects of the early, but not of the late ink splitting phase in 2D as the, e.g., viscous finger instabilities and liquid filament dynamics are essential 3D phenomena.

For numerical studies the printing nip offers principal challenges in various respect. The Stokes boundary-value in the printing nip involves both macroscopic and microscopic length scales between 100 nm and few mm. This large ratio of relevant scales requires particular strategies in simulation mesh definition. The second challenge is due to the feature of the Stokes or Navier-Stokes models that they sensitively depend on the boundary conditions at singular positions such as three-phase wetting contact

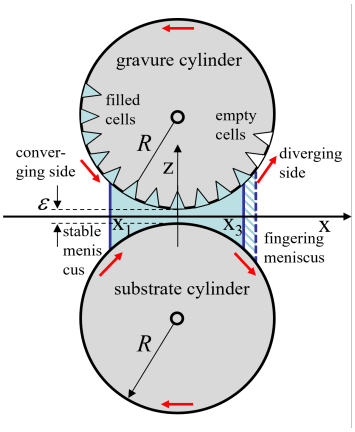

Figure 5.1: Geometry of printing nip with gravure and substrate cylinder, fluid volume, converging and diverging menisci, residual gap ε, and gravure cells. Cell size is vastly exaggerated compared to the other dimensions.

lines or the nip. When approaching these points liquid velocity, pressure, or their gradients tend to grow without obvious upper bound. Small variations, due either to inevitable imperfections of surfaces or process control, or deliberately seeded by ever-changing printing patterns and subjects, cause large fluctuations in liquid pressure and shear.

A typical question concerning the gravure printing press is on the shear rate in the nip. Actually, this question is an ill-defined one. Our access to the nip relies on a small but finite additional length, the residual gap height ε between cylinder and substrate. We shall not make the attempt to eludicate the physical origin of this microscopic length, and admit that the gap is not more than a virtual one. We compare situations which are distinct in ε, and identify the asymptotic scaling of the divergent hydrodynamical parameters. This does not only yield the actually finite and useful parameters, but also yields the corresponding scaling exponents of divergent quantities like pressure and shear. The simulated results are related to analytical and a selection of experimental ones.

Simulation codes and original data from printing experiments are available for further use, see (Rieckmann et al., 2023a).

5.1.1 Hydrodynamic model of the nip

We model the nip hydrodynamics by using the following strategy. First, we define the 2D-restricted hydrodynamic boundary value problem of a liquid between two synchronously rotating cylinders or disks, and present an appropriate coordinate system for the simulation mesh in the highly distorted liquid domain. Before doing so, we take a lubrication theory preview on the velocity and pressure profiles and on the particular singularities to be expected in the nip center, quantified by the scaling exponents of the hydrodynamic quantities, which depend on the height ε between the disks. With this image in mind, we apply a specific Discontinuous Galerkin algorithm, and compare simulated with approximate numerical results. We consider an incompressible Stokes fluid between rigid disks of radius R, synchronously rotating with revolution velocity V_W. The

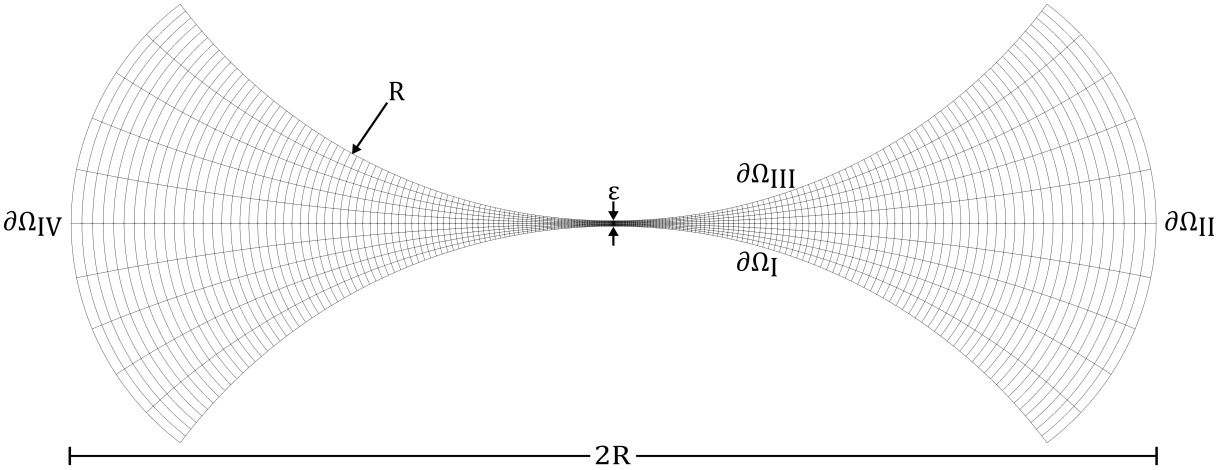

Figure 5.2: Grid used for the numerical simulation. The cells are aligned in a bipolar coordinate system.

mutual distance $\varepsilon \ll R$ is considered small compared to all other physical dimensions. The boundary value problem of cylinder and plate is depicted in Fig. 5.1. Note that our model does not explicitly take account of the gravure cells of the printing cylinder and of the fluid flow therein. The actual cell depth on the printing cylinder is of microscopic size, with a depth of few µm and thus comparable to the residual gap height ε. There are cylinders with larger cells as well. However, typical gravure cells have a rather shallow profile. The ratio of depth and width is smaller than unity. We thus assume that their effect on pressure and shear in the nip is well captured by our scaling proceedure. In order to calculate pressure and shear in the close vicinity of a cell one could simply rescale these quantities by augmenting ε by the cell depth. Note that this is applicable for a one-phase flow only, but should not be adequate for cell filling and emptying flows at the menisci.
While we stay with standard Cartesian coordinates in the lubrication model, an adapted curved coordinate setup is used for mesh definition as depicted in Fig. 5.2. The simulation grid is extended horizontally by $2R$, with this value fixed to $R = 0.1$ m if not stated otherwise. The grid cells are aligned in a bipolar coordinate system (ξ, η), with the vertical grid lines representing constant ξ and the horizontal lines constant η. The transformation from these bipolar to Cartesian coordinates (x, y) is given by

$$x(\xi,\eta) = -\frac{c\sin(\xi)}{\cosh(\eta)-\cos(\xi)}, \quad y(\xi,\eta) = \frac{c\sinh(\eta)}{\cosh(\eta)-\cos(\xi)}, \tag{5.1}$$

and the parameter $c = |R\sinh(\mathrm{acosh}(1+\frac{\varepsilon}{R}))|$. Consequently, the distance between the opposing cylinder surfaces at point x is

$$H(x) \;=\; \varepsilon + \frac{x^2}{2r_n} + O\left(\frac{x}{2r_n}\right)^4, \tag{5.2}$$

where $r_n = R/2$ is the total curvature radius of substrate of an printing cylinder.
For the first series of simulations the Stokes equations are considered, the nip width varies

between $\varepsilon \in [10^{-3}\ \mathrm{m}, 10^{-6}\ \mathrm{m}]$ and the boundary conditions are set as the impermeability and no slip condition on substrate and gravure cylinder respectively, Eq. (5.3a), and fixed stress on the other two boundaries, Eq. (5.3b).

$$\boldsymbol{u} \cdot \boldsymbol{n}^{\partial\Omega} = 0, \quad \boldsymbol{u} \cdot \boldsymbol{t} = V_W \quad \boldsymbol{x} \in \partial\Omega_I \cup \partial\Omega_{III}, \tag{5.3a}$$

$$\left(-p\mathbf{1} + \mu\left(\nabla\boldsymbol{u} + (\nabla\boldsymbol{u})^T\right)\right) \cdot \boldsymbol{n}^{\partial\Omega} = \boldsymbol{\tau}_{\text{in/out}}, \quad \boldsymbol{\tau}_{\text{in/out}} = \begin{cases} -\Delta p \boldsymbol{n}^{\partial\Omega}, & \boldsymbol{x} \in \partial\Omega_{II} \\ \Delta p \boldsymbol{n}^{\partial\Omega}, & \boldsymbol{x} \in \partial\Omega_{IV} \end{cases}, \tag{5.3b}$$

where $\boldsymbol{u}$ is the flow velocity, p the pressure, and μ is the viscosity.

5.1.2 Discussion of numerical procedure

The question arises how a simple numerical solution of the Stokes equations that is obviously not suitable to portray any instability or capillarity effect observed experimentally can be compared to a real gravure printing process. To this end we shall perform a parameter study where we vary the boundary conditions given by Eq. (5.3a) and Eq. (5.3b) as well as the nip width ε. Our attention will then be focused on the positions of stagnating flow and the pressure gradients measured there, which can be compared to experimentally obtained results. As we shall show in this section, these pressure gradients are independent of the nip width — if chosen sufficiently small. Therefore, the exact choice of nip width does not matter. For all simulations the radii of both cylinders are fixed to $R = 0.1$ m and the viscosity of the fluid is $\mu = 0.0395$ Pa s. Before presenting the final parameter study, we discuss how the stagnation points depend on the boundary conditions, and how the flow behaves in the limit of $\varepsilon \to 0$.

Flow properties in dependence of nip width First, we set a homogenous boundary condition for the pressure $\Delta p = 0$ Pa and vary the surface velocity of the cylinders $V_W \in [0.1, 10]$ m/s and $\varepsilon \in [10^{-6}, 10^{-3}]$ m. For brevity we refer to this setup as case A. Then, we swap the role of the boundary conditions, set $V_W = 0$ m/s, and vary $\Delta p \in [10^2, 10^{10}]$Pa and $\varepsilon \in [10^{-6}, 10^{-3}]$ m, which we will denote case B.
We first investigate how the following set of properties behave as the nip widths tends towards zero:

- Maximum pressure range Δp_{max}
- Maximum velocity in ξ-direction u_{max}
- Mass flux through the nip $\dot{m}$
- Pressure gradient in x-direction in symmetry plane in the nip $\left.\frac{\partial p}{\partial x}\right|_{\text{nip}}$
- Shear rate on either cylinder in the nip $\gamma_{\partial\Omega_I}$
- Shear force acting on either cylinder $F_{\partial\Omega_I}$, viscous stress integrated over whole boundary $\partial\Omega_I$
- Position of stagnating flow x_{stag}, point where $u_x(x_{\text{stag}}) = 0$

Table 5.1: Exponents of measured quantities in dependence of nip width

	Δp_{max}	u_{max}	$\dot{m}$	$\left.\frac{\partial p}{\partial x}\right\|_{\text{nip}}$	$\gamma_{\partial\Omega_I}$	$F_{\partial\Omega_I}$	x_{stag}	x_{sync}	ϵ
Case A	-1.498	-0.001	1.0	-2.001	-1.002	-0.527	0.5	0.499	-0.526
Case B	0.0	1.5	2.5	-0.5	0.5	1.0	—	—	2.5

- Position of synchronous flow x_{sync}, point where $u_x(x_{\text{sync}}) = V_W$
- Total viscous dissipation ϵ, viscous dissipation integrated over the whole numerical domain Ω

Table 5.1 shows the measured exponents of the aforementioned flow properties for cases A and B. Each measurement includes 35 simulations, i.e., five different values for the boundary conditions ranging from $V_W \in [0.1, 10]$ m/s in case A and $\Delta p \in [10^2, 10^{10}]$ Pa in case B, and seven data points for the nip width $\varepsilon \in [10^{-6}, 10^{-3}]$ m. For each data line a linear regression in log-log space is performed, and the values displayed in Table 5.1 are the ensemble averages. A graphical representation of these relations is given in Fig. 5.3 for the maximum velocities and the pressure gradients in the nip in Fig. 5.4. The results for case A are shown on the left, whereas the results for case B are shown on the right. As a reference the predicted slopes from lubrication theory Section 5.1.1[1] are also included. It is immediately visible that these results match very well.
Next, we consider the pressure and axidirectional velocity profiles along the ξ-axis. These are

[1]The presentation of the lubrication theory is shortened in the present work, the complete discussion is available in the original publication (Rieckmann et al., 2023c).

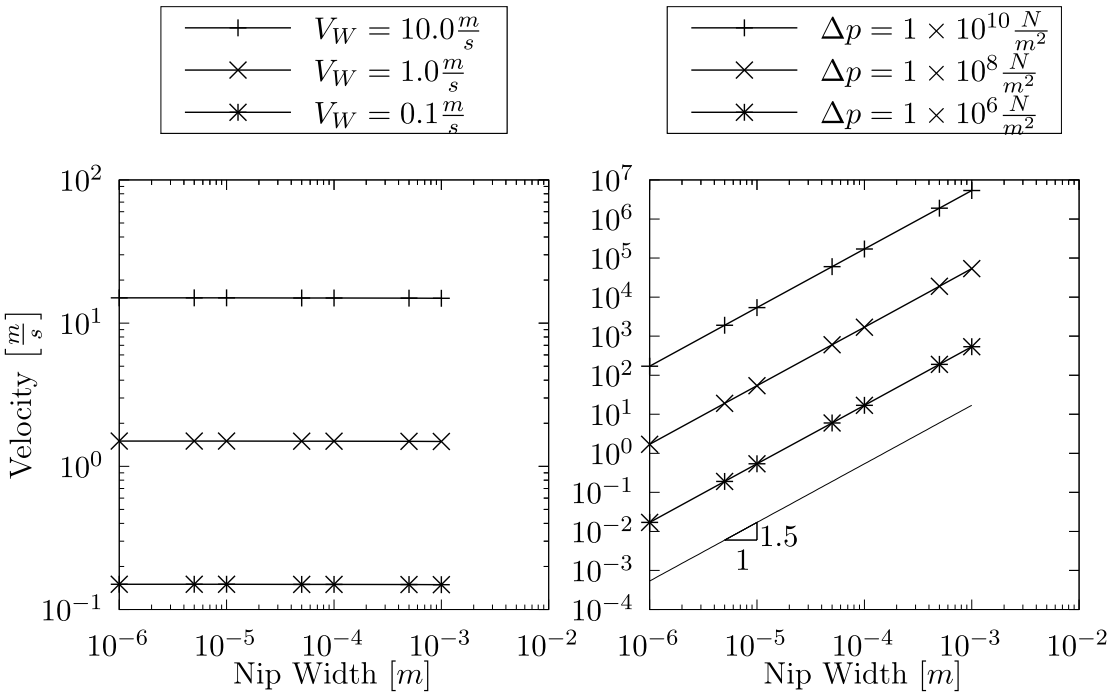

Figure 5.3: Maximum velocity in the nip. Results for case A are displayed on the left, for case B on the right. The slopes predicted by lubrication theory are included for reference.

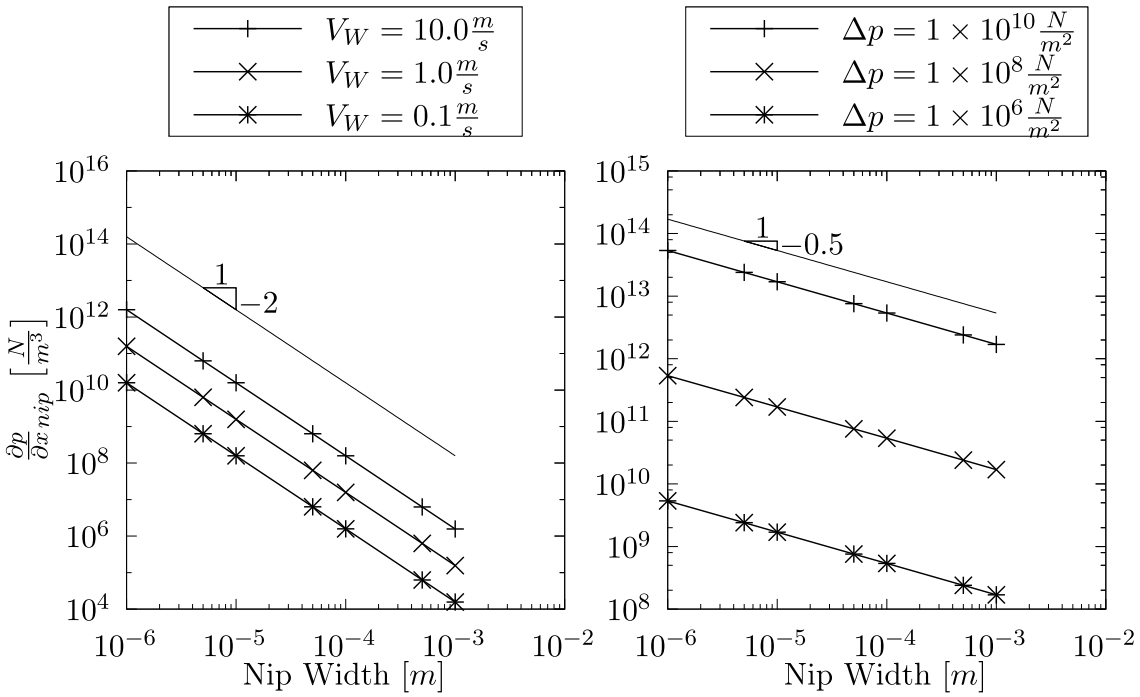

Figure 5.4: Axidirectional pressure gradient in the nip. Results for case A are displayed on the left, for case B on the right. The slopes predicted by lubrication theory are included for reference.

displayed for cases A and B as solid lines in Fig. 5.5 and Fig. 5.6. The nip width for all displayed lines is $\varepsilon = 10^{-4}$ m, in Fig. 5.5 the velocity is $V_W = 1$ m/s and for Fig. 5.6 the pressure difference is $\Delta p = 10^5$ Pa.

For case A the pressure is an uneven function around the printing nip, asymptotically tending towards zero. Furthermore, the pressure possesses two extremas at the positions of synchronous flow. In case B the pressure is an uneven function as well, however without extremes and approaching the set pressure in the outer regions of the printing nip. For both cases the velocity profiles are even functions around the nip. The most notable difference is that in case B the profile of the velocity does not become zero at any point. Therefore no stagnation points are present.

Due to the linear nature of the Stokes system solutions can be superpositioned. How this influences pressure and velocity can be seen in Fig. 5.5 as well as in Fig. 5.6. Starting from case A or B respectively, we superpose the boundary condition of the opposite case, with increasingly strong influence. It is notable in Fig. 5.5 that the stagnation points shift outwards when increasing the pressure difference. However, to effect a significant outwards shift, this pressure difference quickly dominates the shape of the pressure profile. On the other hand, it is visible from Fig. 5.6 that with increasing velocity the stagnation points move inward. For higher velocity the pressure extremes originating from the case A solution are clearly visible. Using these results we obtain the expressions Eq. (5.4a) and Eq. (5.4b), showing how the pressure difference has to be chosen

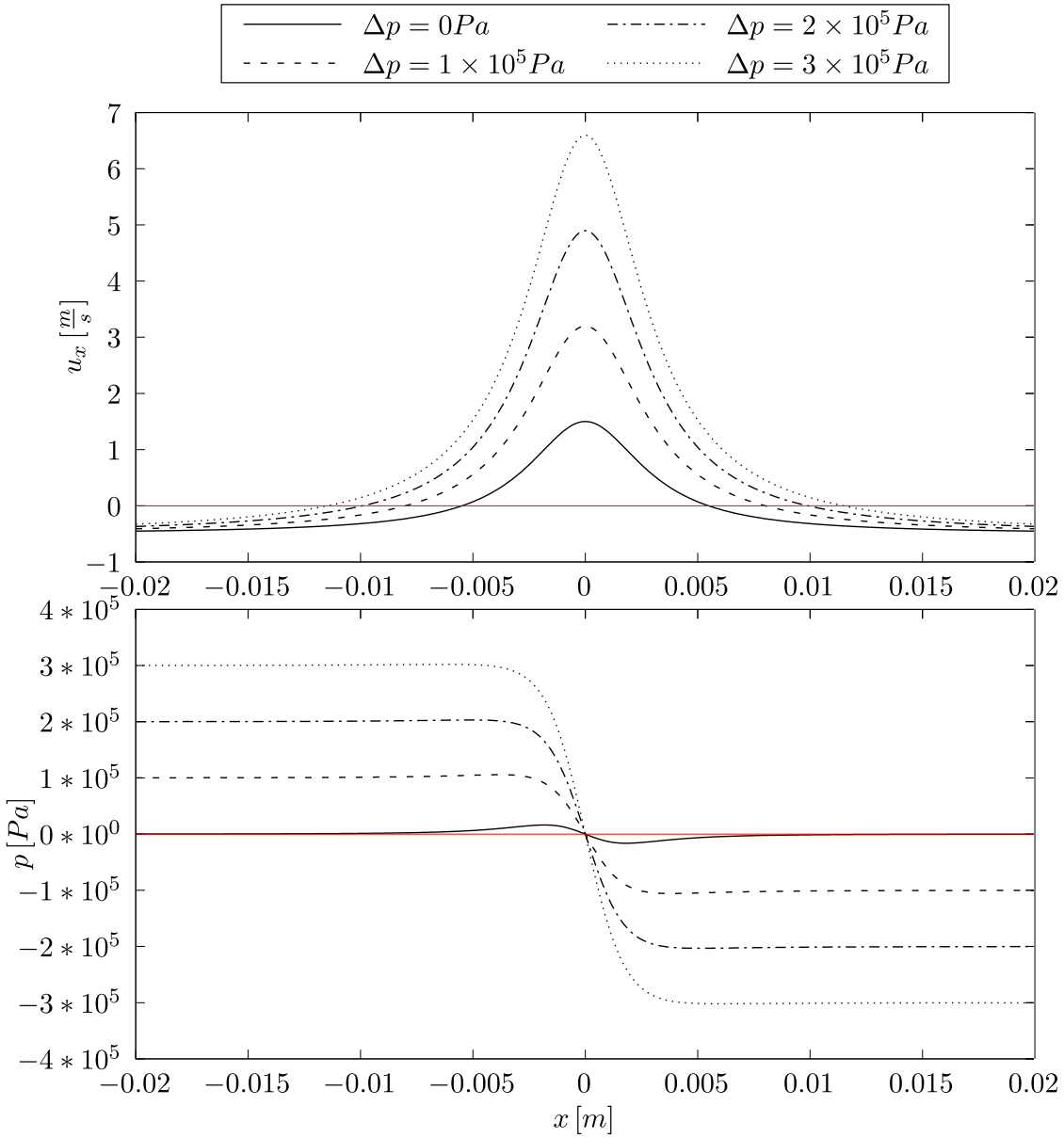

Figure 5.5: The upper figure shows the axidirectional velocity along the center of the printing nip. The lower figure displays the respective pressure profile. Starting from the setup $\varepsilon = 10^{-4}$ m, $V_W = 1$ m/s, $\Delta p = 0$ Pa visible as the solid line, the pressure is increased and the resulting profiles are superimposed.

in order to shift the stagnation points to a specific location:

$$u(x, V_W, \Delta p, \varepsilon) = \frac{V_W}{V_{W,0}} u_A\left(x\sqrt{\frac{\varepsilon_0}{\varepsilon}}\right) + \frac{\Delta p}{\Delta p_0}\left(\frac{\varepsilon}{\varepsilon_0}\right)^{1.5} u_B\left(x\sqrt{\frac{\varepsilon_0}{\varepsilon}}\right), \tag{5.4a}$$

$$\Delta p(x_{\text{stag}}, V_W, \varepsilon) = -\,\Delta p_0\left(\frac{\varepsilon_0}{\varepsilon}\right)^{1.5} \frac{V_W}{V_{W,0}} \frac{u_A\left(x_{\text{stag}}\sqrt{\frac{\varepsilon_0}{\varepsilon}}\right)}{u_B\left(x_{\text{stag}}\sqrt{\frac{\varepsilon_0}{\varepsilon}}\right)}. \tag{5.4b}$$

Here, u_A and u_B denote the profiles along the symmetry plane evaluated from some reference

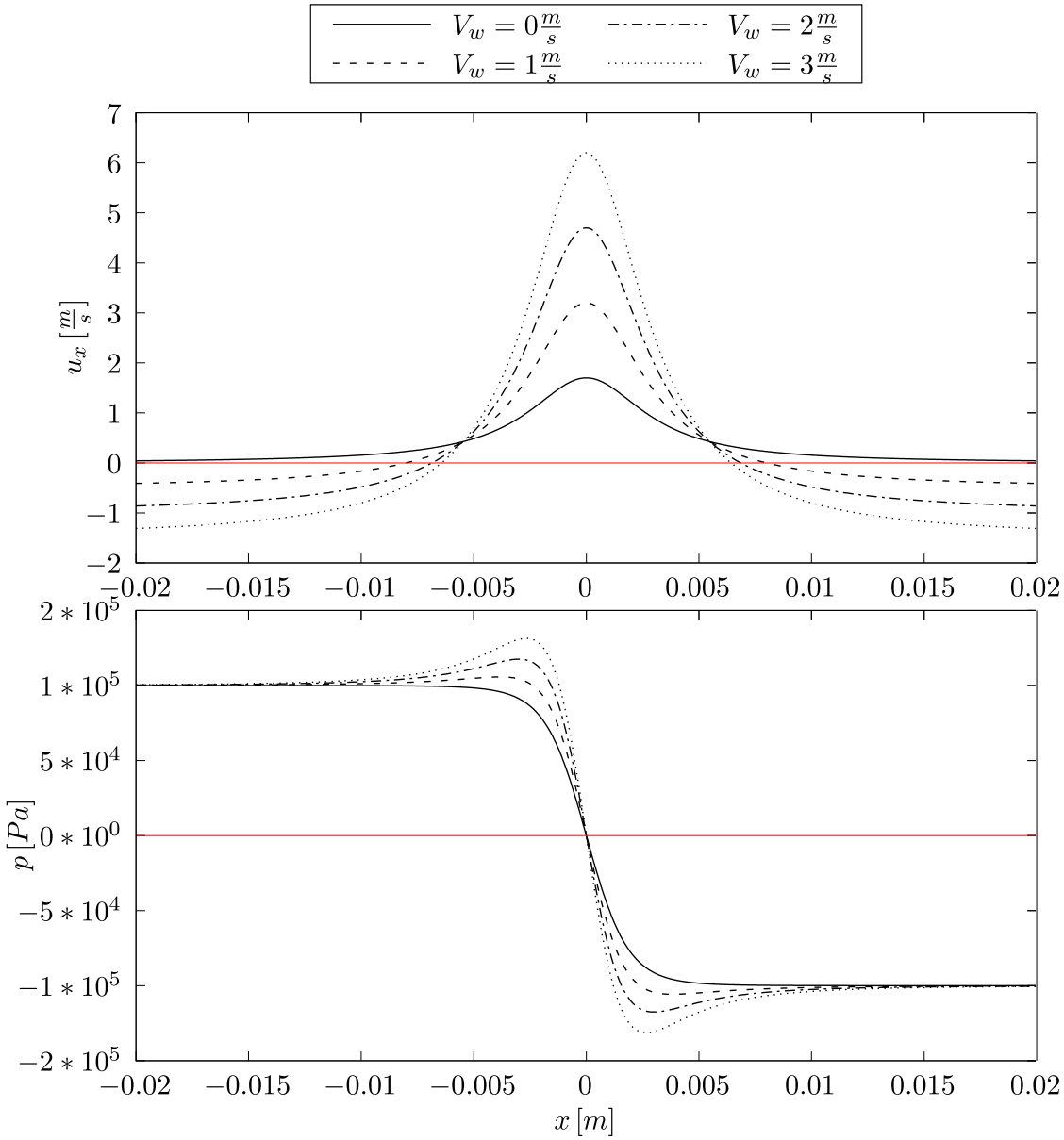

Figure 5.6: The upper figure shows the axidirectional velocity along the center of the printing nip. The lower figure displays the respective pressure profile. Starting from the setup $\varepsilon = 10^{-4}$ m, $V_W = 0$ m/s, $\Delta p = 10^5$ Pa visible as the solid line, the velocity is increased and the resulting profiles are superimposed.

simulations of case A using $V_{W,0}, \varepsilon_0$ and case B with $\Delta p_0, \varepsilon_0$. The rest of the construction follows from the proportionalities found above.

Flow properties at constant stagnation point Using Eq. (5.4b) we are now able to predict the necessary pressure difference to tune the position of the stagnating flow. Therefore, we continue by setting $x_{\text{stag}} = 0.01$ m. First, we verify that the procedure suggested above does give the right prediction. Indeed, in Fig. 5.7 it is immediately visible, that the stagnation point, while

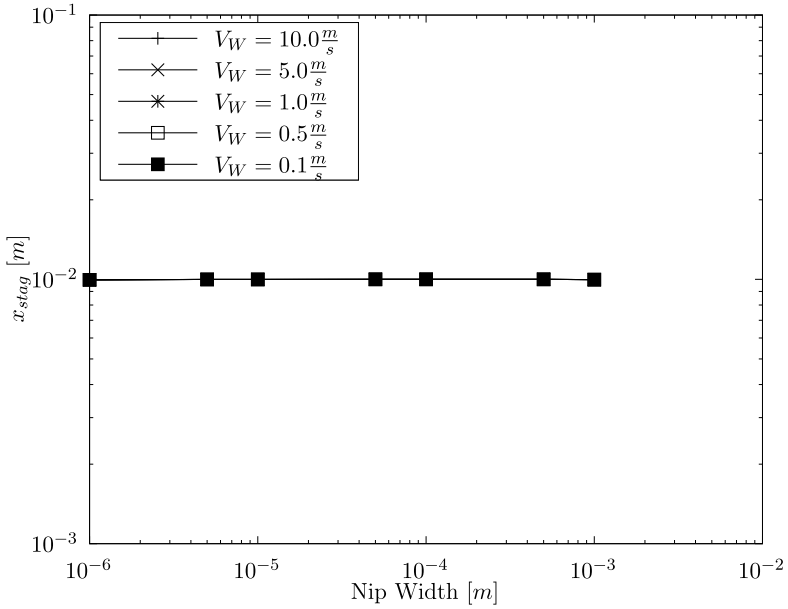

Figure 5.7: Position of stagnation point. All data series are lying on top of each other.

choosing the pressure boundary in accordance to Eq. (5.4b), is not a function of V_W or ε any more, as this dependency is included in the pressure boundary condition. Now, the property we are interested in is the pressure gradient in x-direction at the stagnation points. Our hypothesis is that this measure is independent of the nip width, while fixing the stagnation point. This is a crucial property, as the nip width cannot be measured experimentally and is therefore unknown to us. If the pressure gradient at the stagnation point is not dependant on nip width, we can choose an arbitrary ε in the simulation. In Fig. 5.8 the pressure gradient is plotted over the nip width. Clearly, while $x_{\text{stag}} \approx \sqrt{\varepsilon}$, there is a dependence between pressure gradient and nip width. However, in the limit $\lim \varepsilon \to 0$ it can be assumed that the pressure gradient is independent of the nip width. Therefore, the specific choice of ε is arbitrary when measuring these pressure gradients.

In Fig. 5.9 we give an impression of the flow conditions in the printing nip. As the pressure is almost constant over the nip-width, which verifies the justification for the usage of lubrication approximation in Section 5.1.1, we skip its display here. Instead we choose to plot the shear rate and axidirectional velocity in the printing nip. This properties nicely illustrates the high dissipation and forces at work in the nip. The upper pictures illustrates the results for an exemplary case A simulation ($\varepsilon = 10^{-5}$ m, $V_W = 1$ m/s, $\Delta p = 0$ Pa), the middle for case B ($\varepsilon = 10^{-5}$ m, $V_W = 0$ m/s, $\Delta p = 10^6$ Pa) and the lower pictures for a simulation with fixed stagnation point ($\varepsilon = 10^{-5}$ m, $V_W = 1$ m/s, $x_{\text{stag}} = 0.01$ m). To enhance the visibility of the flow features, the domain is scaled in y-direction by a factor of 100. Subsequently, we cut out a circle of radius 0.015 m around the origin before elevating the plots by the respective variable itself. To give a reference, the streamlines crossing through the origin are illustrated as well. Probably, the most interesting region, apart from the origin itself, is the point of synchronous flow present in the upper and lower pictures. Here, the velocity is constant across the nip and matches the printing velocity. At these points we note how the velocity profile is turned over and the shear rate exhibits a clear minimum.

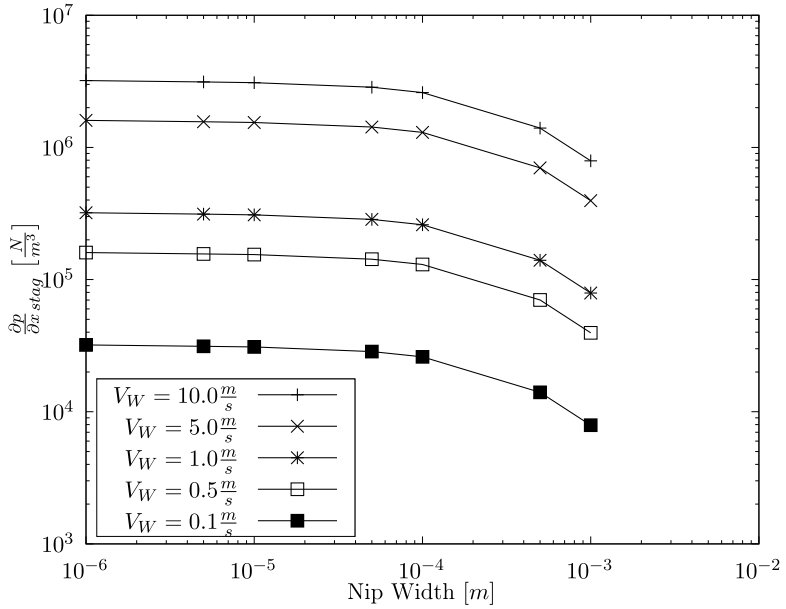

Figure 5.8: Axidirectional pressure gradient at the stagnation point.

Comparison to experimental results Finally, we can draw a comparison to the experimental results. In the experiment samples were printed using different printing speeds and patterns of gravure cups on the cylinders, while staying in the lamella splitting regime. The samples were then digitalized and by Fast Fourier Transformation (FFT) finger frequencies were determined. These frequencies are related to the pressure gradient at the diverging ink meniscus according to

$$n_F^2 = \frac{1}{16\sigma} \left.\frac{\partial p}{\partial x}\right|_{x_m} . \tag{5.5}$$

Approximating the flow in the printing nip as a channel flow relates the pressure gradient to printing velocity and meniscus height (i.e. the height of the nip at the meniscus position):

$$V_W = -\frac{H_m^2}{8\mu} \left.\frac{\partial p}{\partial x}\right|_{x_m} . \tag{5.6}$$

Finally, using Eq. (5.2) an estimate for the position of the meniscus can be obtained to be

$$x_m = \sqrt{2r_n(H_m - \varepsilon)} \approx \sqrt{2r_n H_m}. \tag{5.7}$$

This predicted meniscus position is then used as an input for the simulation to place the stagnation points accordingly ($x_{\text{stag}} = x_m$). The experimental procedure is described in more detail in Rieckmann et al. (2023c). Using Eq. (5.4b) and the result that the pressure gradients at the stagnation points are independent of the chosen nip width, we set $\varepsilon = 10^{-5}$ m and perform a parameter study with varying x_{stag} and V_W. As a result, we measure the pressure gradient in x-direction at the stagnation points, i. e., their absolute values. Due to the symmetries explained in Fig. 5.5 and Fig. 5.6 it does not matter whether we choose the stagnation point before or after the nip. With this at hand, we can draw a surface plot in Fig. 5.10. Using the procedure described in the next section, we can also obtain these three quantities experimentally. This has been done, and the experimental results are superimposed in Fig. 5.10 as blue squares. As can be

seen these lie exactly on the surface of the numerically obtained results. This is a direct result of the approximate applicability of Darcy's law, i.e., the assumption of the flow in the nip as a Poisseuille flow, in the printing nip with $\varepsilon \ll R$.
Therefore, the scaling of pressure gradients at the stagnation point as a function of printing velocity, displayed in Fig. 5.11, which we found numerically and experimentally, is unsurprisingly identical. To conclude this section we give here the exponents α of $\partial p/\partial x|_{\text{stag}} \propto V_W^{\alpha}$ as measured in the experiments for different raster densities:

- 60 lines/cm : $\alpha = 0.479 \pm 0.03613$
- 70 lines/cm : $\alpha = 0.683 \pm 0.0767$
- 80 lines/cm : $\alpha = 0.60834 \pm 0.082$

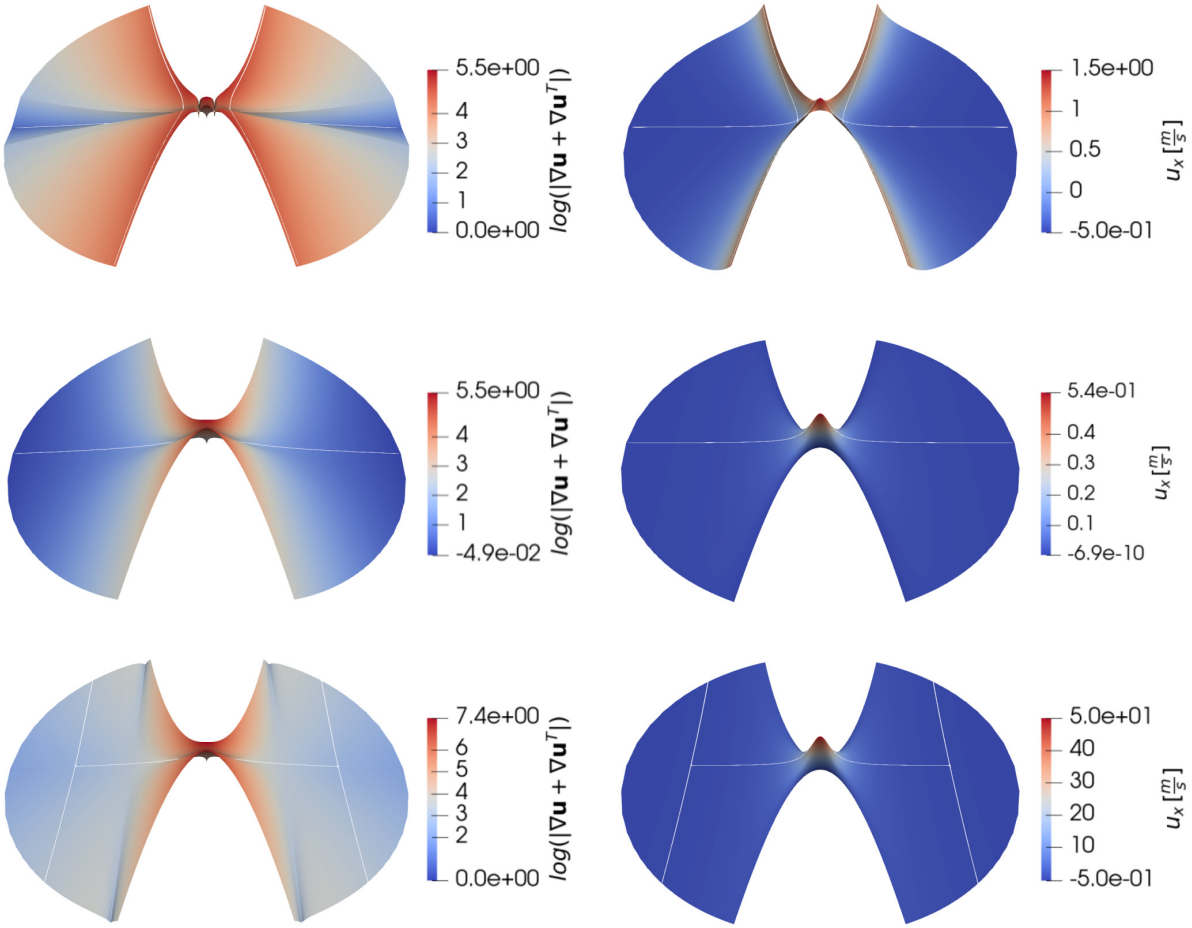

Figure 5.9: Display of the shear rate (left) and x-directional velocity in the printing nip (right). Streamlines through the origin are represented as white lines. The domain is stretched by a factor of 100 in y-direction and we display a cutout of radius 0.015 m around the origin. Upper pictures : $\varepsilon = 10^{-5}$ m, $V_W = 1$ m/s, $\Delta p = 0$ Pa , middle pictures : $\varepsilon = 10^{-5}$ m, $V_W = 0$ m/s, $\Delta p = 10^6$ Pa, lower pictures : $\varepsilon = 10^{-5}$ m, $V_W = 1$ m/s, $x_{\text{stag}} = 0.01$ m

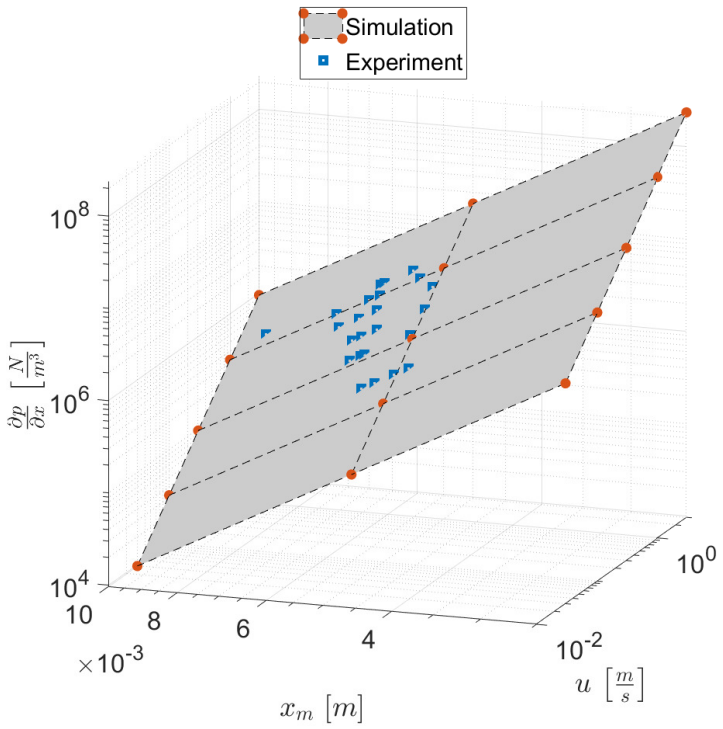

Figure 5.10: Pressure gradients predicted from experiments, using Eq. (5.2), Eq. (5.5) and Eq. (5.7) overlayed with simulated pressure gradients for different printing velocities and stagnation point positions. All axes use a logarithmic scale.

- 100 lines/cm : $\alpha = 0.732 \pm 0.072138$

The raster size references the geometry of the gravure cylinder, indicating how many lines of cups are imprinted on the surface of the cylinder per length. The error is given as the standard error in the coefficient, when fitting the mean values from the measurements to a power law. For the smallest raster size the data point for the highest velocity was excluded.

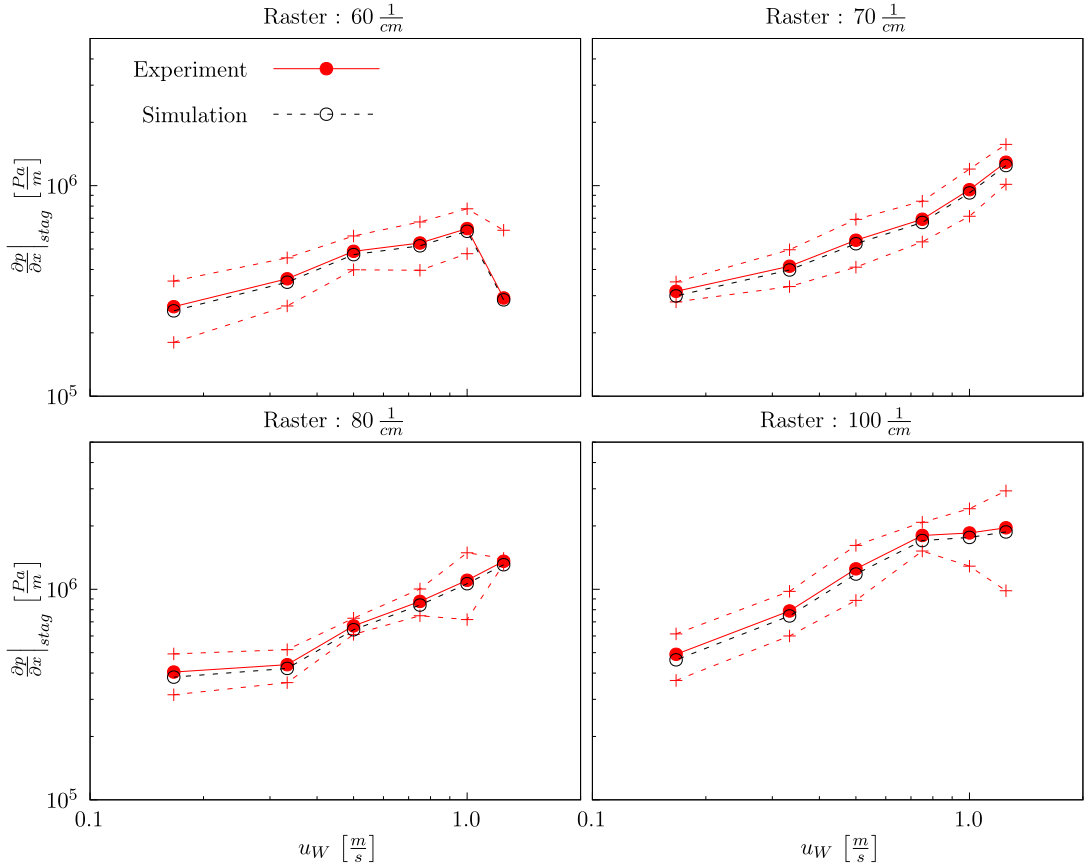

Figure 5.11: Comparison of experimental and simulation results. Each picture shows the experimentally predicted pressure gradient for a certain cylinder geometry and different printing velocities. These results are overlayed with the simulated pressure gradients, using the experimentally obtained stagnation point as input. Red dashed lines denote the standard deviation of the experimental measurements.

5.2 Occurence of viscous vortices in the printing nip

In Section 5.1 the solution of the Stokes flow in the printing nip using inhomogeneous boundary conditions is considered. In this section the consideration of the Stokes problem in the printing nip is extended to homogeneous solutions. The analytic results presented in this section were generated as part of the bachelor's thesis of Anton Erbach, which the author supervised. In addition numerical simulations are performed to verify the occurrence of the analytically predicted viscous vortices in the nip.

5.2.1 Introduction

The two-roller printing problem deals with the two-dimensional Stokes flow in the nip of two counter-rotating rollers. The term "printing" comes from the possible application of this flow in the nip of two printing rollers. In the, at the time of this writing unpublished, work on which this section is based on, the Stokes equation for this flow is solved completely with both

inhomogeneous and homogeneous boundary conditions (BC). However, in this section we will focus on the homogeneous solutions only. These describe highly complex flow patterns, which form the core of the present section. In contrast to the analytical approach chosen in Section 5.1, where the lubrication theory was deployed, in this section the Stokes problem is solved in bipolar coordinates.
Jeffery (1922) transforms the Stokes equation into a bipolar coordinate system, probably for the first time, which allows the two cylinder surfaces to be represented as coordinate lines. He also constructed the first solutions to the inhomogeneous problem. Another specific solution for the problem at hand has also been published in German by Müller (1942). However, this work is limited to rollers with the same rotational speeds. Pitts and Greiller (1961) analyzed the flow between two cylinders partially immersed in liquid experimentally and then theoretically, neglecting the inertia term. A specific solution for the Stokes flow in bipolar coordinates is also given by Wakiya (1975b) in the second part of his three-part work. In it, he first provides a general solution for the behavior of the Stokes flow in the vicinity of two cylinders. He starts from the solution of the biharmonic equation in the bipolar coordinate system given in (Jeffery, 1922). He further assumes that the cylinders cannot rotate independently, i.e., at different speeds.
A more general approach to the problem is taken by Dorrepaal and O'Neill (1979), who solve the biharmonic equation of the stream function using 'matched asymptotic expansions'. In the following works, the Stokes flow is also considered in the bipolar coordinate system, but with different boundary conditions. In the first part of (Wakiya, 1975a) he deals with the 'flow along a plane with a projection or a depression'. And in the third part (Wakiya, 1978) the Stokes flow within a cylinder in which another cylinder is placed eccentrically, not unlike a hydrodynamic bearing, is considered. The latter setup is also investigated by Kazakova (2020).
The solution of the problem with homogeneous boundary conditions leads to an eigenvalue problem for the assumed stream function, which can only be solved numerically. The resulting eigenvalues generate various associated flow patterns, which are characterized by a chain of counter-rotating vortices in the printing nip. A very well-known phenomenon of viscous vortex formation, and related to the present flow, is that in a corner with a moving wall, which was described by Moffatt (1964). Moffat shows that a cascade of increasingly smaller counter-rotating vortices forms between two rigid walls at an opening angle of less than 146° within the corner.
In this section, the mathematical model of Section 2.6.1 for a single phase and without temporal and convective terms, namely the stationary Stokes equation is considered. The Stokes equation is reformulated to the biharmonic equation in terms of a stream function and solved in a bipolar coordinate (BPC) system. By using the BPC system, the boundary conditions on the surfaces of the rollers are defined by constant coordinate lines. By means of a further transformation, see e.g. (Bluman and Gregory, 1985), the biharmonic equation for the stream function is converted into a linear differential equation with constant coefficients in the BPC system. Using a general solution for the problem formulated in the BPC, the series of homogeneous solutions are constructed and investigated. Due to the linearity of the probleme these homogeneous solutions can be superposed at will, also with solutions to the inhomogeneous boundary value problem. For the inhomogeneous boundary conditions, the speeds at the two roller surfaces are specified independently of each other. Since the correct physical boundary conditions are already solved by the inhomogeneous problem, the rollers are "virtually" at rest for the homogeneous boundary conditions. For both cases, the roller surfaces are considered as impenetrable walls. In this sections solutions to the inhomogeneous problem are not discussed.

5.2.2 2D Stokes equation in bipolar coordinates

First, this subsection introduces the BPC and presents the transformation of Stokes' equation into these coordinates. At last the boundary conditions for the homogeneous solution are defined.

Bipolar coordinates Contrary to an often used definition, see Happel and Brenner (1981, p. 498) or Moon and Spencer (1971, p. 89), the BPC are rotated by $90°$ in this work to uphold a main flow direction in the horizontal plane. In complex notation the transformation from BPC to cartesian coordinates is

$$z = x + \mathrm{i}y = -c \cot\left(\frac{1}{2}(\xi + \mathrm{i}\eta)\right) = -c \cot\left(\frac{1}{2}(\zeta)\right), \tag{5.8}$$

c controls the position of so-called focal points and is described in Eq. (5.14) below. Here, $z = x + \mathrm{i}y$ describes the cartesian and $\zeta = \xi + \mathrm{i}\eta$ the bipolar coordinates. The BPC has the following limits to map to the entire plan, $-\infty < \eta < \infty$ and $0 \leq \xi < 2\pi$. At $(x, y) = (0, c)$ and $(x, y) = (0, -c)$ constant ξ-lines meet, simultaneously these focal points denote values of $\eta = \infty$ in the upper and $\eta = -\infty$ in the lower half-plane. Resolving Eq. (5.8) into imaginary and real part explicit expressions for the coordinate transformation can be found, this is also the form used in Eq. (5.1):

$$x = \frac{-c\ \sin\xi}{\cosh\eta - \cos\xi}, \quad y = \frac{c\ \sinh\eta}{\cosh\eta - \cos\xi}. \tag{5.9}$$

The Jacobi determinant J (Bluman and Gregory, 1985) is an important metric factor for this transformation and will be used intensively throughout this section

$$J = \left|\frac{dz}{d\zeta}\right| = \frac{c}{\cosh\eta - \cos\xi}. \tag{5.10}$$

Half the nip width h and the radius of the rollers R serve as the specified length scales, see Fig. 5.12. The center of the rollers is $y_{\mathrm{RC}} = \pm h + R$ and the surfaces of the two rollers are each described by constant η coordinate lines, where η_0 stands for the upper roller and η_1 for the lower roller. This can subsequently be used to define the boundary conditions on constant η coordinate lines, i.e., on the roller surfaces, which allows a comparatively simple solution construction. According to Happel and Brenner (1981, p. 498), the center and the roller radius are related to constant η coordinate lines by

$$y_{\mathrm{RC}} = c\coth(\eta) = h + R, \tag{5.11}$$

and

$$R = \frac{c}{|\sinh(\eta)|}. \tag{5.12}$$

From Eqs. (5.11) and (5.12) the constant η_0 for the surface of the upper rollers as a function of the dimensionless gap ratio h/R can be determined to

$$\eta_0 = \cosh^{-1}\left(\frac{h}{R} + 1\right). \tag{5.13}$$

Inserting this relationship into equation Eq. (5.12) results in the pre-factor c of the BPC as a function of h/R:

$$c = R\sinh\left[\cosh^{-1}\left(\frac{h}{R} + 1\right)\right]. \tag{5.14}$$

This prefactor can also be understood as the limiting point of the constant ξ lines: At the points $(x, y) = (0, \pm c)$ all arcs of the constant ξ-lines begin or end, (Happel and Brenner, 1981, p. 499).

In this section upper and lower rollers have the same radius R and are placed in a distance of $2h$, which results in

$$\eta_1 = -\eta_0. \tag{5.15}$$

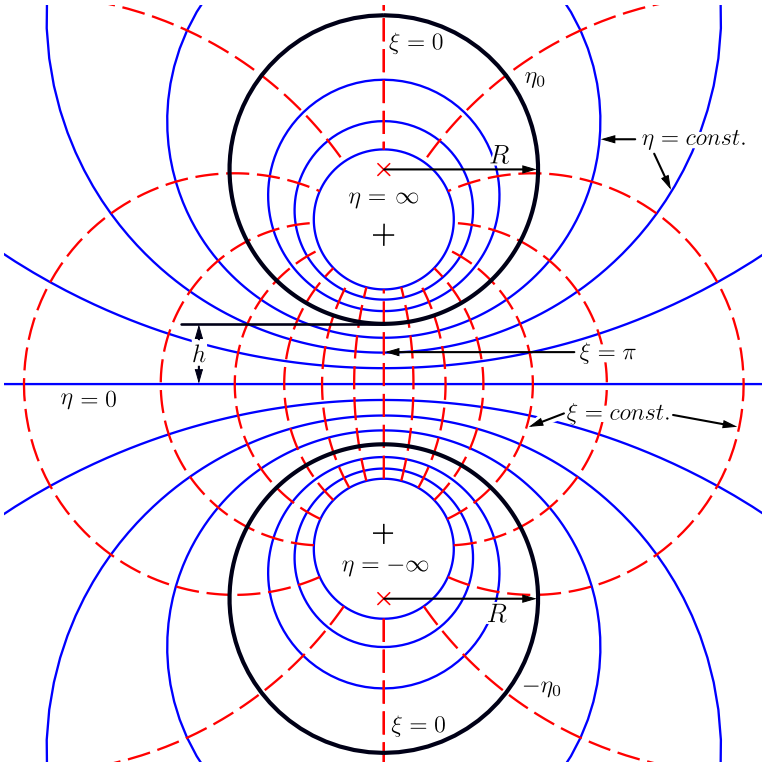

Figure 5.12: Coordinate lines of the bipolar coordinate system for $c = \text{const.}$. The blue lines represent the constant η lines. The red dashed lines represent the constant ξ lines with $\frac{\pi}{8}$ spacing in each case. In the black crosses at $(x, y) = (0, c)$ and $(x, y) = (0, -c)$ all constant ξ-lines meet, at the same time it also represents the points $\eta = \infty$ in the upper half and $\eta = -\infty$ in the lower half. The red vertical dashed lines above and below the black crosses are $\xi = 0$, while $\xi = \pi$ lies between the black crosses. As an example, the rollers with radius R and half the gap width h are shown with a thick black line. The center points (x) and the contour lines η_0 and $-\eta_0$ result from the given h and R.

Transformation of the Stokes stream function equation to bipolar coordinates The 2D Stokes equation in dimensionless variables,

$$\nabla p = \Delta \boldsymbol{u}, \tag{5.16}$$

can also be written as the biharmonic equation for a newly introduced stream function, see (Happel and Brenner, 1981, p. 60). To this end the velocities are defined in terms of the stream function as

$$u_x = \frac{\partial \psi}{\partial y}, \quad u_y = -\frac{\partial \psi}{\partial x}, \tag{5.17}$$

Table 5.2: General solutions for Eq. (5.23)

I.	$P = E\ \cosh(\alpha\xi) + F\ \sinh(\alpha\xi)$ $Q = A\ \cosh\eta\cos(\alpha\eta) + B\ \cosh\eta\sin(\alpha\eta) + C\ \sinh\eta\cos(\alpha\eta) + D\ \sinh\eta\sin(\alpha\eta)$
II.	$P = E\ \cos(\alpha\xi) + F\ \sin(\alpha\xi)$ $Q = A\ \cosh(\alpha+1)\eta + B\ \sinh(\alpha+1)\eta + C\ \cosh(\alpha-1)\eta + D\ \sinh(\alpha-1)\eta$
III.	$P = E\ \cos(\beta-1)\xi + F\ \sin(\beta-1)\xi + G\ \cos(\beta+1)\xi + H\ \sin(\beta+1)\xi$ $Q = A\ \cosh(\beta\eta) + B\ \sinh(\beta\eta)$
IV.	$P = E\ \cosh(\beta\xi)\cos\xi + F\ \sinh(\beta\xi)\cos\xi + G\ \cosh(\beta\xi)\sin\xi + H\ \sinh(\beta\xi)\sin\xi$ $Q = A\ \cos(\beta\eta) + B\ \sin(\beta\eta)$

in Eq. (5.16). By taking the curl of Eq. (5.16), imagining a third coordinate, we obtain

$$\Delta^2\psi = 0. \tag{5.18}$$

Using the BPC the velocity components in coordinate unit vector direction become

$$u_\xi = \frac{1}{J}\frac{\partial\psi}{\partial\eta}, \quad u_\eta = -\frac{1}{J}\frac{\partial\psi}{\partial\xi}. \tag{5.19}$$

Similar to Wakiya (1975a), the pressure gradient can be extracted from Eq. (5.16):

$$\frac{\partial p}{\partial\xi} = \frac{\partial(\Delta\psi)}{\partial\eta}, \quad \frac{\partial p}{\partial\eta} = -\frac{\partial(\Delta\psi)}{\partial\xi}. \tag{5.20}$$

According to Bluman and Gregory (1985) the biharmonic equation in the BPC can be transformed to a linear PDE with constant coefficients by modifying the stream function

$$\psi(\xi,\eta) = J\Phi(\xi,\eta). \tag{5.21}$$

Explicitly expanding the Laplacian in BPC gives

$$\Delta = \frac{\partial^2}{\partial x^2} + \frac{\partial^2}{\partial y^2} = \frac{1}{J^2}\left(\frac{\partial^2}{\partial\xi^2} + \frac{\partial^2}{\partial\eta^2}\right). \tag{5.22}$$

And by inserting Eq. (5.21) into Eq. (5.18) the desired form of the equation is obtained:

$$\Delta^2\psi(\xi,\eta) = \frac{1}{J^3}\left[\left(\frac{\partial^2}{\partial\xi^2} + \frac{\partial^2}{\partial\eta^2}\right)^2 + 2\left(\frac{\partial^2}{\partial\xi^2} - \frac{\partial^2}{\partial\eta^2}\right) + 1\right]\Phi(\xi,\eta) = 0. \tag{5.23}$$

For Eq. (5.23) the solutions displayed in Table 5.2 can be found by inserting a generic product ansatz

$$\psi(\xi,\eta) = J\Phi(\xi,\eta) = JP(\xi)Q(\eta). \tag{5.24}$$

Table 5.3: Summary of the constants to the homogeneous Stokes problem

	asymmetric flow (**a**)	symmetric flow (**s**)
odd stream function (**o**)	$C = -\frac{\cosh((\alpha+1)\eta_0)}{\cosh((\alpha-1)\eta_0)}\ A$ $B = D = 0$ $F = -\cot(\pi\alpha)E$	$A = C = 0$ $D = -\frac{\sinh((\alpha+1)\eta_0)}{\sinh((\alpha-1)\eta_0)}\ B$ $F = -\cot(\pi\alpha)E$
even stream function (**e**)	$C = -\frac{\cosh((\alpha+1)\eta_0)}{\cosh((\alpha-1)\eta_0)}\ A$ $B = D = 0$ $F = \tan(\pi\alpha)E$	$A = C = 0$ $D = -\frac{\sinh((\alpha+1)\eta_0)}{\sinh((\alpha-1)\eta_0)}\ B$ $F = \tan(\pi\alpha)E$

Formulation of boundary conditions To identify the solution constants in Table 5.2 the solution is demanded to fulfill a set of boundary conditions. Here, we focus solely on homogeneous BC. As in the BPC is constant η coordinate lines meet at $\xi = 0$ and $\xi = 2\pi$ a continuity condition on ψ and p or u_ξ and u_η is enforced:

$$\left.\begin{aligned} \psi(\xi = 0, \eta) &= \psi(\xi = 2\pi, \eta), \quad & p(\xi = 0, \eta) &= p(\xi = 2\pi, \eta) \\ u_\xi(\xi = 0, \eta) &= u_\xi(\xi = 2\pi, \eta), \quad & u_\eta(\xi = 0, \eta) &= u_\eta(\xi = 2\pi, \eta) \end{aligned}\right\}. \tag{5.25}$$

It should already be pointed out here that this continuity condition can only be fulfilled for two of the mentioned field quantities at the same time. For the other two field quantities, there are discontinuities that increase with the distance to the roller. This gives rise to two distinct forms of the stream function, being either odd or even in ξ around $\xi = \pi$. Further the rollers are impermeable:

$$u_\eta(\xi, \eta = \eta_0) = u_\eta(\xi, \eta = -\eta_0) = 0. \tag{5.26}$$

And for homogeneous solutions at rest:

$$u_\xi(\xi, \eta = \eta_0) = u_\xi(\xi, \eta = -\eta_0) = 0. \tag{5.27}$$

5.2.3 Solution of the homogeneous Stokes problem, eigenvalues and vortex solutions

When searching for solutions of the type presented in Table 5.2 fulfilling the homogeneous BC, Eqs. (5.25) to (5.27), it can be shown that the paths I and II collapse and III and IV only give trivial solutions. Thus, solutions can be sought for the following unified stream function:

$$\begin{aligned} \psi(\xi, \eta; \alpha) = &\frac{c}{\cosh(\eta) - \cos(\xi)} \big[E\cos(\alpha\xi) + F\sin(\alpha\xi)\big] \big[A\cosh((\alpha+1)\eta) \\ &+\ B\sinh((\alpha+1)\eta) +\ C\cosh((\alpha-1)\eta) + D\sinh((\alpha-1)\eta)\big]. \end{aligned} \tag{5.28}$$

For the still to be determined eigenvalues $\alpha \in \mathbb{C} \setminus \{-\mathrm{i}, -1, 0, 1, \mathrm{i}\}$ applies. The excluded values are used for the construction of particular solutions, which is not shown here. Over the course of inserting the boundary condition a total of 4 different solution paths arise. These are either asymmetric (**a**) or symmetric (**s**) around $\eta = 0$ and even (**e**) or odd (**o**) in relation to $\xi = \pi$. Therefore, we distinguish the resulting stream functions like so:

$$\Psi_{\mathrm{e/o,a/s}}. \tag{5.29}$$

Table 5.4: Numerically calculated eigenvalues

		$h/R = 0.01$	$h/R = 0.005$	$h/R = 0.0025$
asym. (**a**)	α_1	8.0152 + 14.896i	11.294 + 21.064i	15.944 + 29.788i
	α_2	11.028 + 37.902i	15.556 + 53.582i	21.971 + 75.763i
	α_3	12.613 + 60.411i	17.796 + 85.4i	25.139 + 120.75i
sym. (**s**)	α_1	9.8456 + 26.525i	13.884 + 37.5i	19.606 + 53.025i
	α_2	11.909 + 49.181i	16.802 + 69.526i	23.733 + 98.306i
	α_3	13.199 + 71.611i	18.625 + 101.23i	26.309 + 143.14i

The solution constants for each of these branches are displayed in Table 5.3. Furthermore, Table 5.4 shows the first three eigenvalues for different relations h/R, and Fig. 5.13 the position of the eigenvalues in the complex plane when assuming $\alpha = p + \mathrm{i}q$. Note that the stream functions are scaled by a constant factor when the real part of α switches sign, while they are indifferent to sign changes in the imaginary part. Thus it suffices to consider the eigenvalues in the first quadrant. Four possible flow patterns can be derived from these results. They are the combinations of asymmetric, symmetric flow and odd, even stream function around $\xi = \pi$. The different flow patterns are discussed in the following paragraphs. The upcoming Figs. 5.14 to 5.19c show constant streamlines of the real part of the stream function of the respective flow with a given eigenvalue α_n and nip width to radius ratio h/R. The streamlines have a distance of a power of ten to each other and the thick lines denote zero sets of the stream function. The blue and red colors indicate counter-rotating flow directions dictated by the stream function.

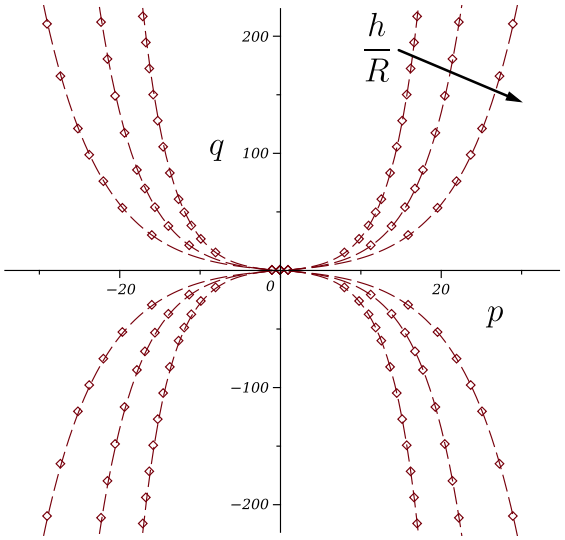

Figure 5.13: Numerically calculated eigenvalues in the complex plane: $\alpha_n, -\alpha_n, \overline{\alpha}_n, -\overline{\alpha}_n$ for three different nip ratios $h/R = 0.005, 0.01, 0.02$. The arrow indicates a decreasing nip ratio.

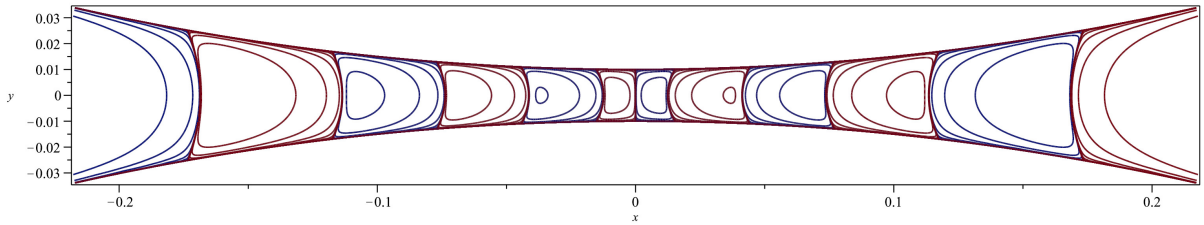

(a) $\alpha_1 = 8.0152 + 14.896\mathrm{i}$

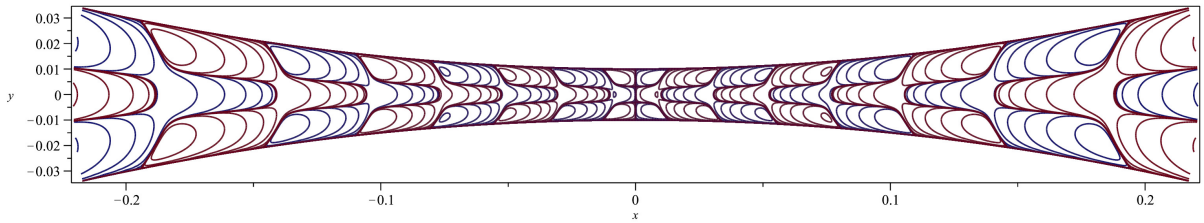

(b) $\alpha_2 = 11.028 + 37.902\mathrm{i}$

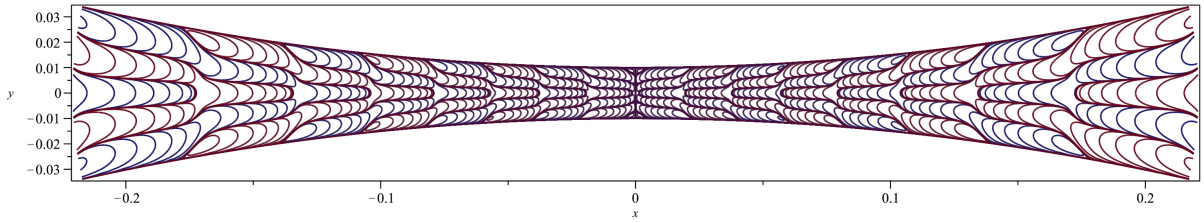

(c) $\alpha_3 = 12.613 + 60.411\mathrm{i}$

Figure 5.14: Constant stream lines of $\Psi_{\mathbf{o},\mathbf{a}}$ around $\xi = \pi$ for increasing α_n with $h/R = 0.01$. The blue and red streamlines indicate clockwise and counterclockwise flow directions.

Solution for the asymmetric flow and odd stream function For asymmetric flow and odd stream function the solution has the form

$$\begin{aligned}\Psi_{\mathbf{o},\mathbf{a}}(\xi,\eta;\alpha_n) =& AE\,\frac{c}{\cosh(\eta)-\cos(\xi)}\left[\cos(\alpha_n\xi)-\cot(\pi\alpha_n)\sin(\alpha_n\xi)\right] \\ &\times\left[\cosh((\alpha_n+1)\eta)-\frac{\cosh((\alpha_n+1)\eta_0)}{\cosh((\alpha_n-1)\eta_0)}\cosh((\alpha_n-1)\eta)\right].\end{aligned} \tag{5.30}$$

The diagrams in Fig. 5.14 show the constant streamlines of the first three eigenvalues. A vertical dividing line forms between the left and right halves. In addition, vortices form with alternating direction of rotation. The magnitude of the stream function decreases towards the center of the gap and increases again after passing the narrowest point. Stagnation points only form at the walls and in the center of the vortices. For the second eigenvalue (Fig. 5.14b) two co-rotating vortices are formed on the walls, enveloped by a larger vortex, that extends as a “finger-like” structure along the axis of the printing nip. This is shown enlarged in Fig. 5.15 for the center of the nip, but the same pattern can be observed for all vortices. In addition, the vortex density, i.e. the number of vortices per unit length, increases compared to the first eigenvalue. At the narrowest point of the nip, two additional free stagnation points are formed in the flow, at the position of intersection zero stream lines, see Fig. 5.15.
With the third eigenvalue (Fig. 5.14c) it can be seen that the tendency to develop “finger-like”

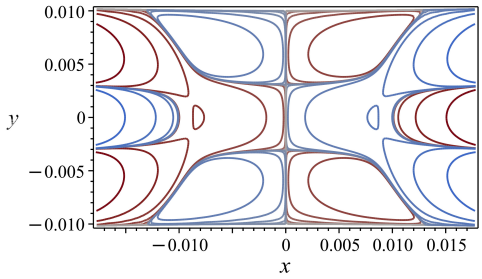

Figure 5.15: Magnification of $\Psi_{\mathbf{o,a}}$ around $\xi = \pi$ for $\alpha_2 = 11.028 + 37.902\text{i}$, $\frac{h}{R} = 0.01$

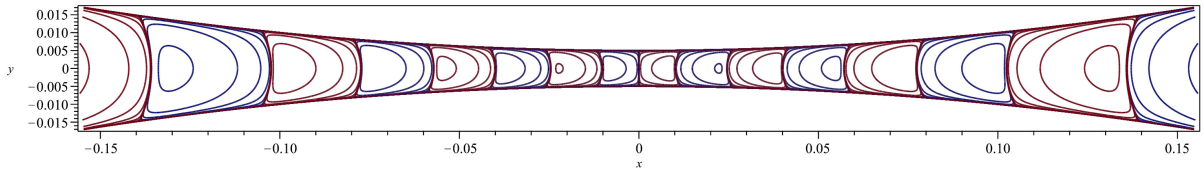

(a) $\alpha_1 = 11.294 + 21.064\text{i}$, $\frac{h}{R} = 0.005$

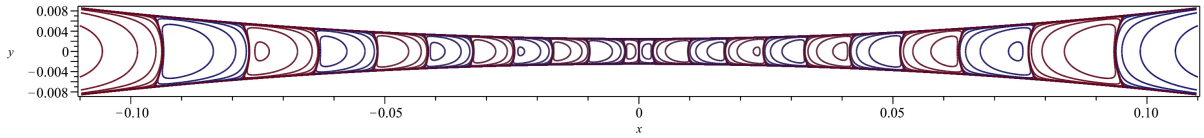

(b) $\alpha_1 = 15.944 + 29.788\text{i}$, $\frac{h}{R} = 0.0025$

Figure 5.16: Constant stream lines of $\Psi_{\mathbf{o,a}}$ around $\xi = \pi$ for varying h/R

elongated flow patterns continues. As with the second eigenvalue, vortices form at the both boundaries with the same direction of rotation. These vortex patterns are elongated and staggered in a step-like profile along the axis forming even more pronounced “finger-like” structures. The vortex density continues to increase with growing eigenvalue. At the narrowest point, four free stagnation points form in the flow. In Fig. 5.16 constant streamlines of the first eigenvalues of the nip ratios $h/R = 0.005, 0.0025$ are plotted. It can be seen that the overall structure of the vortices remains unchanged at lower nip ratios.

Solution for the asymmetric flow and even stream function For asymmetric flow and even stream function around $\xi = \pi$ the solution has the form

$$\begin{aligned}\Psi_{\mathbf{e,a}}(\xi,\eta;\alpha_n) =& AE\,\frac{c}{\cosh(\eta)-\cos(\xi)}\left[\cos(\alpha_n\xi)+\tan(\pi\alpha_n)\sin(\alpha_n\xi)\right]\\ &\times\left[\cosh((\alpha_n+1)\eta)-\frac{\cosh((\alpha_n+1)\eta_0)}{\cosh((\alpha_n-1)\eta_0)}\cosh((\alpha_n-1)\eta)\right].\end{aligned} \tag{5.31}$$

Figure 5.17a,b shows constant streamlines of the even stream function from equation Eq. (5.31) for the first two eigenvalues. Compared to the odd stream function around $\xi = \pi$, the even stream function has no vertical dividing line in the center of the nip. As can be seen in Fig. 5.17b, this means that no free stagnation points occur for higher eigenvalues. In the center of the nip, the first vortices on both sides join together to form a vortex structure. Outside the nip center, the

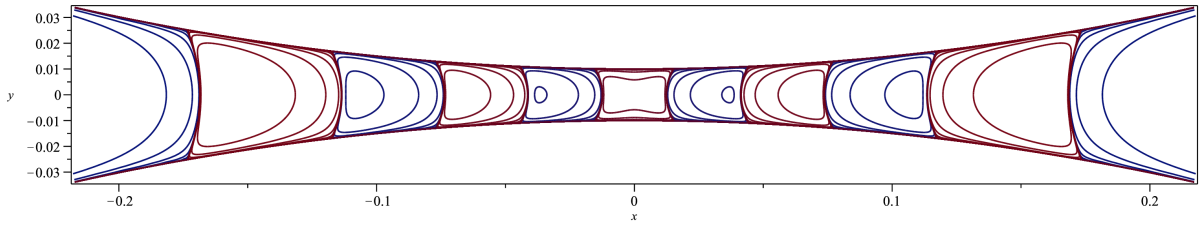

(a) $\alpha_1 = 8.0152 + 14.896\text{i}$, $\frac{h}{R} = 0.01$

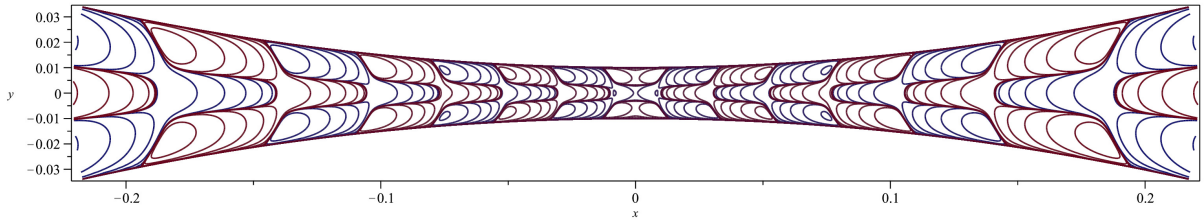

(b) $\alpha_2 = 11.028 + 37.902\text{i}$, $\frac{h}{R} = 0.01$

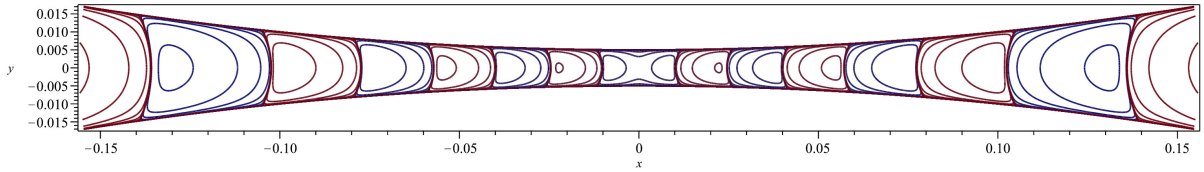

(c) $\alpha_1 = 11.294 + 21.064\text{i}$, $\frac{h}{R} = 0.005$

Figure 5.17: Constant stream lines of $\Psi_{\mathbf{e,a}}$ around $\xi = \pi$

structure remains unchanged in relation to the odd stream function, while the direction of rotation of the vortices in the right half is reversed. The stream function also decreases in magnitude towards the center of the nip, as it is the case for the odd stream function. Another parallel is the increasing vortex density for decreasing nip ratios, as can be seen by comparing Fig. 5.17a and Fig. 5.17c.

Solution for the symmetric flow and odd stream function For symmetric flow and odd stream function the solution has the form

$$\begin{aligned}\Psi_{\mathbf{o,s}}(\xi,\eta;\alpha_n) =& BE\,\frac{c}{\cosh(\eta)-\cos(\xi)}\left[\cos(\alpha_n\xi)-\cot(\pi\alpha_n)\sin(\alpha_n\xi)\right]\\ &\times\left[\sinh((\alpha_n+1)\eta)-\frac{\sinh((\alpha_n+1)\eta_0)}{\sinh((\alpha_n-1)\eta_0)}\sinh((\alpha_n-1)\eta)\right].\end{aligned} \tag{5.32}$$

Figure 5.18a,b shows constant streamlines of this stream function for the first two eigenvalues. First of all, it can be seen that there is a horizontal dividing line in the flow. This means that there are several free stagnation points in the flow along the horizontal dividing line. There is also a vertical separation line in the center of the gap, which leads to free stagnation points along this axis at higher eigenvalues. Above and below the horizontal dividing line, vortices form with alternating direction of rotation. The magnitude of the stream function decreases towards the center of the nip.
For higher eigenvalues, a “finger-like” flow results, similar to the asymmetric flow, whereby, in

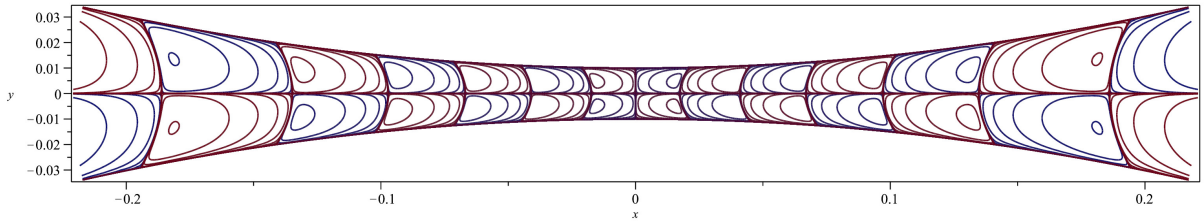

(a) $\alpha_1 = 9.8456 + 26.525\text{i}$, $\frac{h}{R} = 0.01$

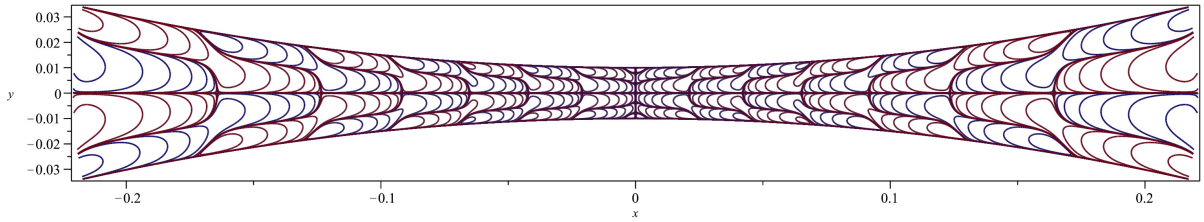

(b) $\alpha_2 = 11.909 + 49.181\text{i}$, $\frac{h}{R} = 0.01$

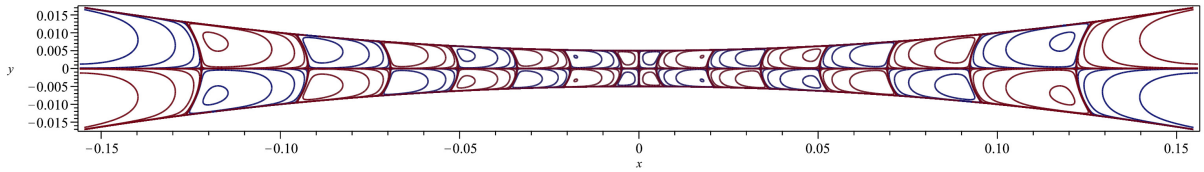

(c) $\alpha_1 = 13.884 + 37.5\text{i}$, $\frac{h}{R} = 0.005$

Figure 5.18: Constant stream lines of $\Psi_{\mathbf{o,s}}$ around $\xi = \pi$

contrast to the asymmetric flow, no central vortex forms on the horizontal axis of symmetry. The vortex density increases for further increasing eigenvalues.
Figure 5.18c shows the first eigenvalue for the nip ratio $h/R = 0.005$. It can be seen that the vortex density increases as the nip ratio decreases. The arrangement of the vortices in relation to each other remains unchanged.

Solution for the symmetric flow and even stream function For symmetric flow and even stream function the solution has the form

$$\begin{aligned}\Psi_{\mathbf{e,s}}(\xi,\eta;\alpha_n) =& BE\,\frac{c}{\cosh(\eta)-\cos(\xi)}\left[\cos(\alpha_n\xi)+\tan(\pi\alpha_n)\sin(\alpha_n\xi)\right]\\ &\times\left[\sinh((\alpha_n+1)\eta)-\frac{\sinh((\alpha_n+1)\eta_0)}{\sinh((\alpha_n-1)\eta_0)}\sinh((\alpha_n-1)\eta)\right].\end{aligned} \tag{5.33}$$

Figure 5.19a,b shows constant streamlines of the first two eigenvalues of the even stream function. Compared to the odd flow, the vertical separation line is omitted, but the horizontal separation line still exists. The position of the vortices that are not in the direct vicinity of the center of the nip remains unchanged, while the direction of rotation of the vortices in the right half is reversed. The upper and lower vortices converge in the center of the nip.
Figure 5.19c shows constant streamlines of the first eigenvalue of the even current function for $h/R = 0.005$. The arrangement of the vortices remains unchanged, but the vortex density increases.

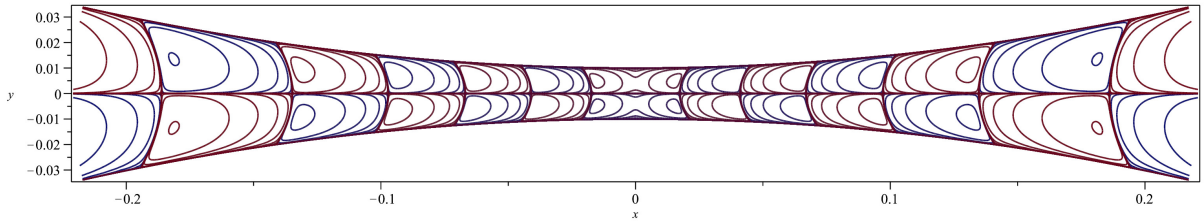

(a) $\alpha_1 = 9.8456 + 26.525\text{i}$, $\frac{h}{R} = 0.01$

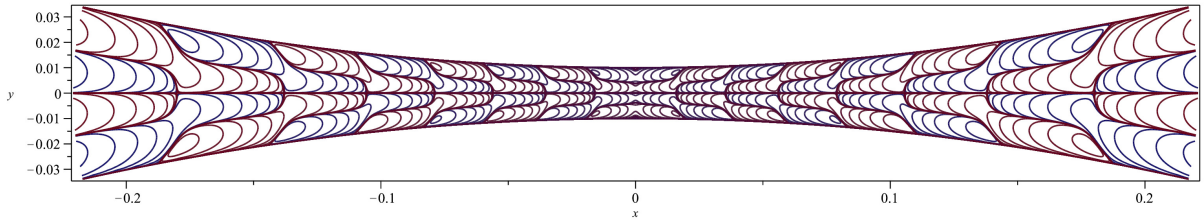

(b) $\alpha_2 = 11.909 + 49.181\text{i}$, $\frac{h}{R} = 0.01$

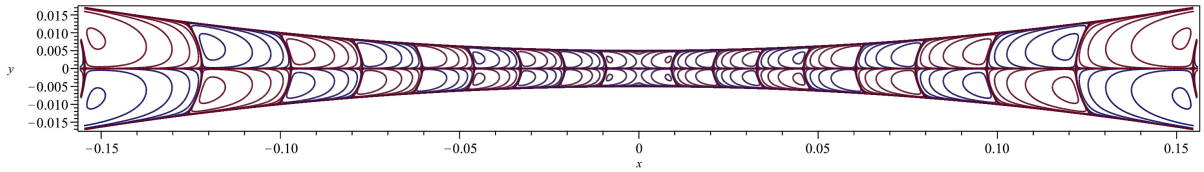

(c) $\alpha_1 = 13.884 + 37.5\text{i}$, $\frac{h}{R} = 0.005$

Figure 5.19: Constant stream lines of $\Psi_{\mathbf{e,s}}$ around $\xi = \pi$

5.2.4 Numerical simulation of viscous eddies in the printing nip

To combine the analytical results presented in the previous section numerical simulations of these viscous vortex structures are performed. The setup is similar to that presented in Fig. 5.2. The radius is chosen to be $R = 1$, the nip width $\varepsilon = 2h = 0.02$, such that the nip ratio is $h/R = 0.01$. On $\partial\Omega_I$ and $\partial\Omega_{III}$ impermeable slip walls are prescribed, while the velocity on $\partial\Omega_{II}$ and $\partial\Omega_{IV}$ is prescribed according to the investigated stream function, i.e. using Eq. (5.19). The polynomial degree for velocity is $k = 5$ and the grid is meshed with 200×10 cells in ξ and η direction. The ξ limits are set such the extend of the domain in x-direction is $-0.25R < x < 0.25R$.
For the simulation, limited to finite precision arithmetic, it proved to be more robust to rewrite the ξ depend factors determining if the stream function is odd or even in the following form:

$$[\cos(\alpha_n\xi) - \cot(\pi\alpha_n)\sin(\alpha_n\xi)] = -\frac{\sin(\alpha_n(\xi-\pi))}{\sin(\alpha_n\pi)}, \tag{5.34a}$$

$$[\cos(\alpha_n\xi) + \tan(\pi\alpha_n)\sin(\alpha_n\xi)] = \frac{\cos(\alpha_n(\xi-\pi))}{\cos(\alpha_n\pi)}. \tag{5.34b}$$

Thereby, the summation/substraction of the potentially extremely large factors (e.g. $\cos(\alpha_n\xi) \propto e^{\Im(\alpha_n)|\xi-\pi|}$) is replaced by a division, which can be evaluated with higher precision. This form also helps to illustrate the role of the imaginary and real part of the eigenvalues. The real part controls the periodicity, i.e. the vortex density, while the imaginary part is responsible to the decay behavior of the stream function towards the nip center.

In Figs. 5.20 to 5.23 the streamlines for the numerical simulations are plotted for each of the four solution branches and the first two eigenvalues. The shape and position of the numerically found vortices agrees well with the analytical prediction (Figs. 5.14 to 5.19) thus validating that the so-found solution are real solution to the Stokes problem. Due to the fast decay of the flow towards the nip center the simulation is not able to obtain significant results over the whole nip.

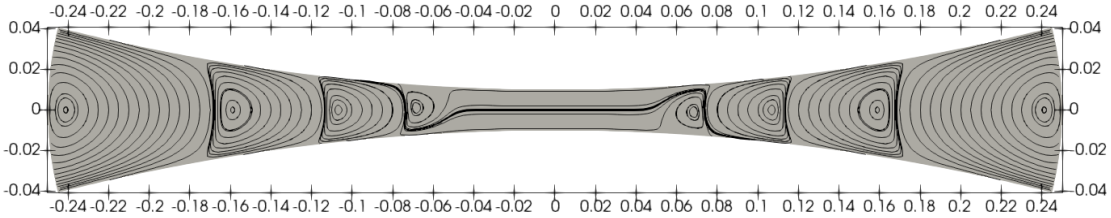

(a) $\alpha_1 = 8.0152 + 14.896\text{i}$, $\frac{h}{R} = 0.01$

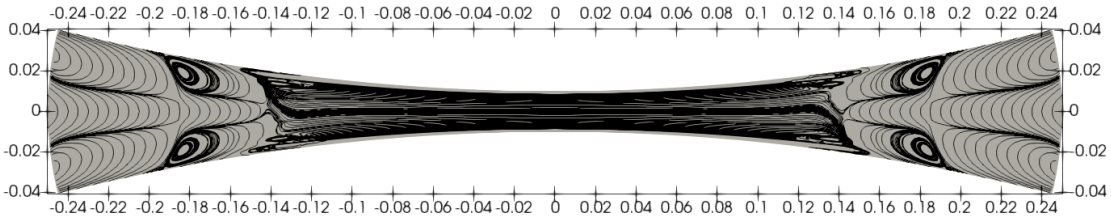

(b) $\alpha_2 = 11.028 + 37.902\text{i}$, $\frac{h}{R} = 0.01$

Figure 5.20: Constant stream lines of $\Psi_{\mathbf{o,a}}$ around $\xi = \pi$

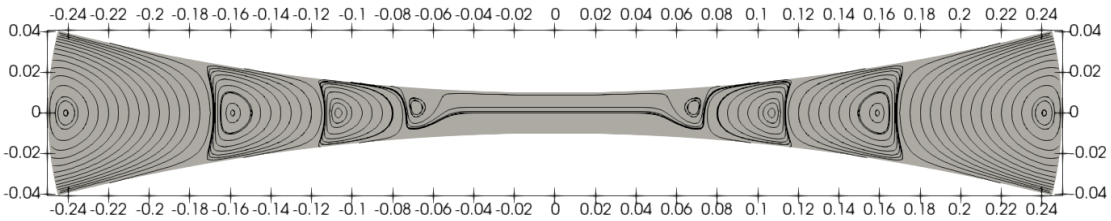

(a) $\alpha_1 = 8.0152 + 14.896\text{i}$, $\frac{h}{R} = 0.01$

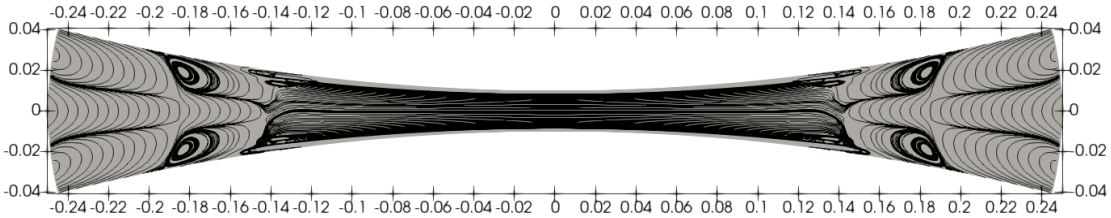

(b) $\alpha_2 = 11.028 + 37.902\text{i}$, $\frac{h}{R} = 0.01$

Figure 5.21: Constant stream lines of $\Psi_{\mathbf{e,a}}$ around $\xi = \pi$

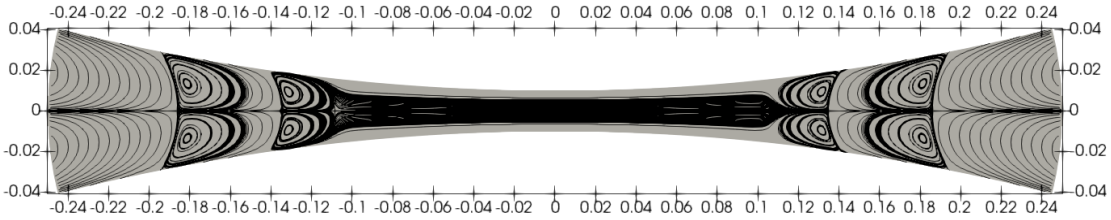

(a) $\alpha_1 = 9.8456 + 26.525\text{i}$, $\frac{h}{R} = 0.01$

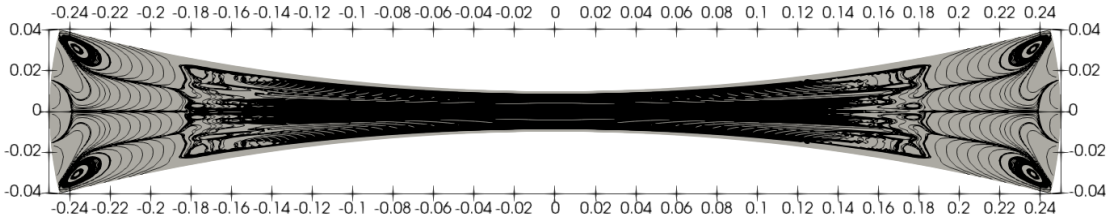

(b) $\alpha_2 = 11.909 + 49.181\text{i}$, $\frac{h}{R} = 0.01$

Figure 5.22: Constant stream lines of $\Psi_{\mathbf{o,s}}$ around $\xi = \pi$

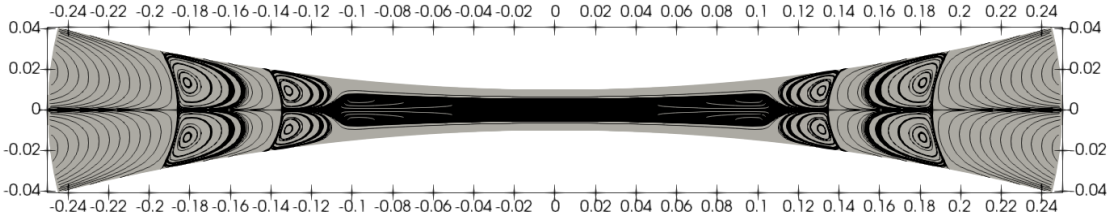

(a) $\alpha_1 = 9.8456 + 26.525\text{i}$, $\frac{h}{R} = 0.01$

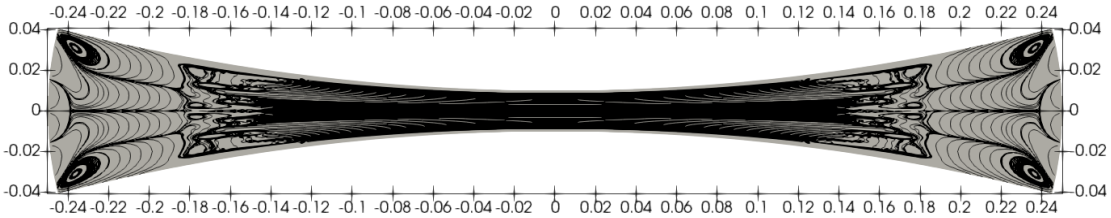

(b) $\alpha_2 = 11.909 + 49.181\text{i}$, $\frac{h}{R} = 0.01$

Figure 5.23: Constant stream lines of $\Psi_{\mathbf{e,s}}$ around $\xi = \pi$

5.3 Conclusion

Two studies were conducted in this chapter. Both dealt with the flow through the nip between two printing cylinders. In Section 5.1 the focus was on finding solutions to the inhomogeneous problem under a variation of printing velocity and a prescribed pressure difference before and after the nip. Special attention was then paid to the behavior of the flow quantities as the nip width tends towards zero. For this the simulation was able to confirm the analytically, using lubrication theory, predicted behavior. In a second step, the boundary conditions in the simulation were used to create free stagnation points at precise locations in the printing nip. These can be seen as an approximation for the meniscus position without actually computing a two-phase problem. The pressure gradients at these stagnation points were then measured and compared to values extracted from experimental results, which agreed well. The pressure gradient in turn indicates the emergence of an instability at the diverging meniscus, responsible for the formation of finger-like structures in real printing. Thus, an accurate prediction of the pressure gradients allows to navigate the printing regime between point- and lamella-splitting, i.e., with or without these finger-like structures, better.

The second study, Section 5.2, focused on homogeneous solutions to Stokes' problem in the printing nip. By using the BPC we were able to find analytical solutions to this problem. Four distinct solution paths were identified, differing by their behavior in the ξ and η coordinates. In each of these solution branches an infinite number of modes, characterized by a complex eigenvalue, can be superposed to construct the final solution. In addition to the flow patterns arising for each of the solution branches, the influence of the nip width to cylinder radius ratio and the effect of choosing a higher mode were investigated. Higher modes lead to more complex structures and a faster decay of the flow towards the nip center. A reduction in nip ratio effects an increase in vortex density, i.e., amount of vortices per unit length. Depending of the solution

branch and observed mode free stagnation point may emerge from the flow. The section finally presents numerical simulations of these structures for the first two modes. The simulation was able to confirm the analytical findings, however due to the fast decay of the flow the arising structures could not be simulated over the whole extend of the printing nip.

6 Results for two-phase flows without contact lines

In this chapter we proceed to investigate two-phase problems with and without evaporation. With a single exception these simulations do not yet contain a three phase contact line.
The discussion starts with a detailed look into the capillary time-step restriction in Section 6.1. We analyze the origin and cause of this restriction and try to determine its severity in actual simulations. To this end a precisely defined capillary wave is propagated in an isolated setup and we intentionally breach the restriction to see if this leads to a failure of the simulation.
Afterwards, in Section 6.2 the phase field level set method presented in Section 4.3.1 is investigated. Two test cases are considered. With the well established rising bubble benchmark we illustrate the influence of the mobility parameter, adjusting the amount of diffusion in the phase field equation, on the interface evolution. To demonstrate the handling of contact lines, we consider a droplet sitting on a flat plate. Theoretically, the droplet should remain completely stationary, which for the phase field level set is only true in the sharp interface limit. Thus a conflict between phase field and flow solution arises in this hybrid method. The section concludes with a comparison of the presented level sets methods and justifies the choice made for the subsequent simulations.
In Section 6.3 the sensitivity to the EOC of the method to appropriate boundary conditions is investigated. In addition we establish a simple test case in order to find out which coupling of approximation orders between temperature and velocity is optimal.
Finally, Section 6.4 presents the verification of the XDG method for two-phase flows with evaporation. For this purpose a series of well established 1D, 2D and 3D test cases is computed and the findings are compared to results from literature and analytical solutions. The contents of this section are published in (Rieckmann et al., 2023e). Section 6.5 concludes the chapter summarizing the findings of the sections mentioned.

6.1 Selection of stable time-step sizes

When simulating two-phase flows with a moving interface using the method presented in Chapter 4, an upper bound for the time-step size arises. In this section some context is provided, where this time-step restriction originates and also some results are presented illustrating the severity of this restriction.

Capillary waves - Dispersion relation and time-step restriction Capillary waves are surface waves occurring at dividing interfaces, whose driving mechanism are capillary forces. For a flat two-phase interface in an inviscid ($\mu \approx 0$) setting and without external forces a dispersion relation

for these capillary waves can be derived. It is obtained by means of linear stability analysis, using a normal mode ansatz, cf. (Chandrasekhar, 1961, p 428ff.). This dispersion relation

$$\omega(\alpha) = \sqrt{\frac{\sigma\alpha^3}{\rho_{\mathfrak{A}} + \rho_{\mathfrak{B}}}} \tag{6.1}$$

describes the angular frequency of the capillary waves as a function of the wavenumber (or wavelength) $\alpha = 2\pi/\lambda$. It can be utilized to obtain the phase velocity

$$c(\alpha) = \frac{\omega(\alpha)}{\alpha} = \sqrt{\frac{\sigma\alpha}{\rho_{\mathfrak{A}} + \rho_{\mathfrak{B}}}} \tag{6.2}$$

of these waves. Using the phase velocity, it is possible to identify the time δt the crest in a wave with a certain wavelength needs to propagate a distance δx as

$$\delta t = \frac{\delta x}{c(\lambda)} = \sqrt{\frac{(\rho_{\mathfrak{A}} + \rho_{\mathfrak{B}})\,\delta x^2 \lambda}{2\pi\sigma}}. \tag{6.3}$$

The last step in the analysis is to identify the smallest resolved wavelengths and the assumed propagation distance with the resolution of the method

$$\lambda = \delta x \approx \Delta x \approx \frac{h_{min}}{2k+1}, \tag{6.4}$$

where k is the polynomial degree of the level set field and h_{min} the diameter of the smallest cell in the mesh. The dependence on h and k is chosen in analogy to the CFL condition in explicit compressible DG methods, e.g. (Cockburn and Shu, 2001). Owing to the explicit coupling between interface movement and flow solution described in Section 4.4, the numerical time-step Δt has to be smaller than δt, which is very similar to a common CFL condition. Thereby, the capillary time-step restriction

$$\Delta t \leq \sqrt{\frac{(\rho_{\mathfrak{A}} + \rho_{\mathfrak{B}}) \left(\frac{h_{min}}{2k+1}\right)^3}{2\pi\sigma}} \tag{6.5}$$

arises, see also (Denner and van Wachem, 2015). Note, that other sources, e.g. Smuda (2021), give a slightly different expression (which is used e.g. in Section 6.4, replacing $2k+1$ with $k+1$), deviating by a constant factor, which in practice accounts to a different safety factor. Equation (6.5) should not be used as an exact limit, but more as a guideline. However, it is important to observe that the permissible time step decreases super-linearly with the refinement of the polynomial order and the grid. In addition, it should be noted that this restriction applies to the case, where no additional fluid motion is considered. If such a movement is present, Denner and van Wachem (2015) propose to take into account both the phase velocity of the capillary waves and the additional interfacial velocity when calculating the appropriate time-step size. As in this work usually fixed time-steps are used and the interface velocity is not always known beforehand, only the static restriction is used.

Severity of a breach in capillary time-step restriction To gain an insight into how severe this time-step restriction is in actual simulations, a numerical experiment is performed. In the setup a standing capillary wave is set as initial condition by the level set field

$$\varphi(x, y) = y - \frac{\hat{y}}{j} \sin(\alpha_j x) \tag{6.6}$$

in an otherwise undisturbed domain, as shown in Fig. 6.1 on the left. The material parameters are set to be $\rho_{\mathfrak{A}} = \rho_{\mathfrak{B}} = 1$, $\mu_{\mathfrak{A}} = \mu_{\mathfrak{B}} = 0.0001$ and $\sigma = 1$, such that the approximation for capillary waves derived in the last section is applicable. For the amplitude $\hat{y} = 0.01$ is chosen and the wave number is varied as

$$\alpha_j = 2\pi j, \quad j = 1 \dots 4. \tag{6.7}$$

The grid is constructed to accurately resolve the capillary wave, with minimum cell size $h_{min} \approx 0.074$. The left and right boundaries are periodic, while the upper and lower ones are homogeneous Neumann boundaries. The simulations are performed with approximation order $k = 2 \dots 4$ for the velocity and level set field. For this specific capillary wave, the prediction for the maximum admissible time-step is

$$\Delta t_{max} = \frac{h_{min}}{2k+1} \sqrt{\frac{\rho_{\mathfrak{A}} + \rho_{\mathfrak{B}}}{\alpha_j \sigma}}. \tag{6.8}$$

Equation (6.8) is based on Eq. (6.3), with the distinction compared with Eq. (6.5) that $\delta x \approx \Delta x$, while for the wavelength the relation $\lambda = 2\pi/\alpha_j$ is used. We now want to compute one oscillation period $t_{end} = 1/(cj)$ in the evolution of this oscillating interface with different time-steps,

$$\Delta t_i = \frac{5}{5+i} \Delta t_{max}, \quad i = 0 \dots 5, \tag{6.9}$$

exactly on and slightly below the predicted maximum time-step size Δt_{max} (Eq. (6.8)). Figure 6.1 shows the progression of a simulation, which failed after 12 time-steps. The first few time-steps seem inconspicuous. However, by the eighth time-step some raggedness becomes visible in the interface and the simulation degrades quickly afterwards. To circumvent this instability a time-step

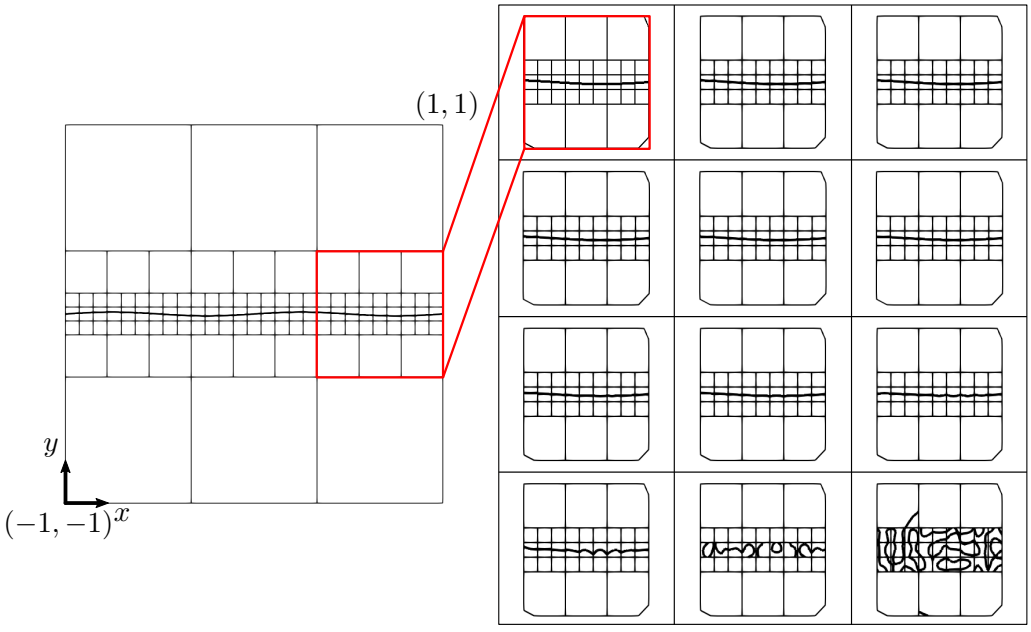

Figure 6.1: Failed simulation for $j = 1$, $i = 0$, $k = 2$. The initial interface and the grid is displayed on the left. The right images show the interface evolution, from top left to bottom right $t^{(1)} \dots t^{(12)}$, for the red cutout. Some raggedness in the interface can be seen with the naked eye by the eighth time-step at the latest. The simulation then deteriorates quickly and irreversibly fails at time-step $t^{(12)}$.

Table 6.1: Success of capillary time-step simulations

	$i=0$			$i=1$			$i=2$			$i=3$			$i=4$			$i=5$		
k	2	3	4	2	3	4	2	3	4	2	3	4	2	3	4	2	3	4
$j=1$																		
$j=2$																		
$j=3$																		
$j=4$																		

sufficiently below the predicted capillary time-step must be chosen.
The results for all tested waves, approximation degrees and time-step sizes are displayed in Table 6.1. Simulations that finished are marked in green, while those marked red ended prematurely. The overall trend is very clear, smaller time-steps perform better. The estimation for the time-step size fits better for smaller approximation order. And when the wavenumber is higher, which corresponds also to a smaller time-step and shorter oscillation period, the simulation is more likely to finish. We therefore conclude that abiding to this restriction is extremely important and violating it can lead to a solver crash very fast.
Also in contrast to this setup, in real simulations the occurring capillary wavelengths are not known a-priori. This means the restriction must be selected according to the estimate for the smallest resolved wavelength. It should be noted, that this setup can also fail when simulating for an extended duration, especially for the higher polynomial orders. Long term stability is a sensitive topic and requires a careful selection of material parameters, grid and time-step size and additional schemes like reinitialization.
A recent work by Denner et al. (2022) suggests, that this time-step limit can be breached by employing a fully implicit method. However, due to the explicit splitting between interface and flow solver, the capillary time-step restriction must be adhered to in this work.

6.2 Phase field level set results

In this section some results for two phase flows, under usage of the phase field level set method introduced in Section 4.3, are presented. Two problems will be considered. These test cases serve to emphasize the influence the phase field parameters (mobility M and gradient energy coefficient ξ, Eq. (4.33a)) have on the observed physical behavior.
First, a rising bubble simulation, cf. (Smuda, 2021; Hysing et al., 2009), is performed with different choices for the mobility parameter. Secondly, a static droplet on a plane surface is simulated. For this setup the contact angle boundary condition for the phase field equation and the influence of the gradient energy coefficient are examined.
The section will conclude with a brief comparison of the phase field and scalar advection method and motivate the choice of interface evolution for the remainder of this work. For the computation of the extension velocity according to Section 4.3.2 the impermeability boundary condition is used for those boundaries that are impermeable for the flow solver as well.

6.2.1 Influence of the mobility parameter

The setup for the rising bubble benchmark case from Hysing et al. (2009) is displayed in Fig. 6.2. Only the test case 2 will be considered, with non-dimensional parameters $\rho_{\mathfrak{A}} = 1$, $\rho_{\mathfrak{B}} = 1000$, $\mu_{\mathfrak{A}} = 0.1$, $\mu_{\mathfrak{B}} = 10$, $\sigma = 1.96$ and $g = 0.98$. The domain of size $\Omega = [0, 1] \times [0, 2]$ is meshed with cells of size $h = 0.1$, two levels ($l = 2$) of adaptive mesh refinement (AMR) are performed at the interface and an approximation degree of $k = 2$ is chosen. The bubble of radius $r = 0.25$ is initialized at $(x_c, y_c) = (0.5, 0.5)$ with the phase field

$$\varphi(\boldsymbol{x}) = \tanh\left(\frac{\sqrt{(x - x_c)^2 + (y - y_c^2)} - r}{\sqrt{2}\xi}\right). \tag{6.10}$$

Due to the buoyancy force acting on the bubble in the gravitational field, it will move upwards and assume at first an oblique shape. Due to the drag along the upper contour of the bubble, it starts to develop filaments at its lower side. In this test case the surface tension is too low to inhibit the development of these filaments and enforce a convex shape of the bubble. The simulated interface shapes at different times, for mobility parameter

$$M = 10^i, \quad i = -4 \dots 0, \tag{6.11}$$

are displayed in Fig. 6.3. For all simulations the transition length (cf. Eq. (4.33a)) is set to

$$\xi = \frac{4h}{(2k + 1)2^l}, \tag{6.12}$$

and the SDIRK22 scheme, Table 4.1, is used for timestepping with non-dimensional time-step $\Delta t = 0.001$. For higher mobility parameters the trailing edges of the filaments are smoothed away by the additional diffusion, observable at $t = 2$. This additional smoothing is so strong that full development of filaments and the emergence of satellite bubbles only occurs for the lowest mobility parameter, as can be seen at $t = 3$. At the second lowest value, satellite bubbles are also split off, but the filaments recede afterwards. For the two highest mobility values, the bubble shape is so strongly influenced that the rise velocity of the bubble differs considerably. At the highest value, the bubble even retains an ellipsoidal shape at all times. In the original benchmark by Hysing et al. (2009) several benchmark quantities are introduced to compare the results of different methods. However, for the means to discuss the qualitative influence of the mobility parameter, the visual analysis suffices.

6.2.2 Influence of the phase field contact line boundary condition

The second test case does not fit completely into this chapter, as a contact line is considered already. However, it serves to evaluate the phase field level set method and justify a decision on which evolution algorithm to use before moving on to more complex simulations. A droplet of radius $r = 0.5$ is placed in a box of size $\Omega = [-1, 1] \times [0, 1]$. Its center is shifted from the origin, such that different contact angles,

$$\theta_i = \frac{\pi}{4} + i\frac{\pi}{12}, \quad i = 0 \dots 3, \tag{6.13a}$$

$$y_i = r\cos(\theta_i), \tag{6.13b}$$

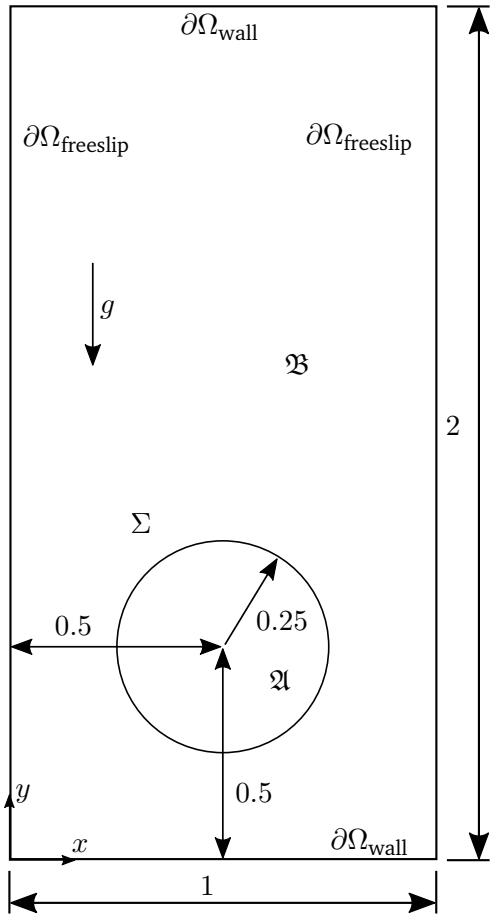

Figure 6.2: Setup for the rising bubble test case, image source (Smuda, 2021)

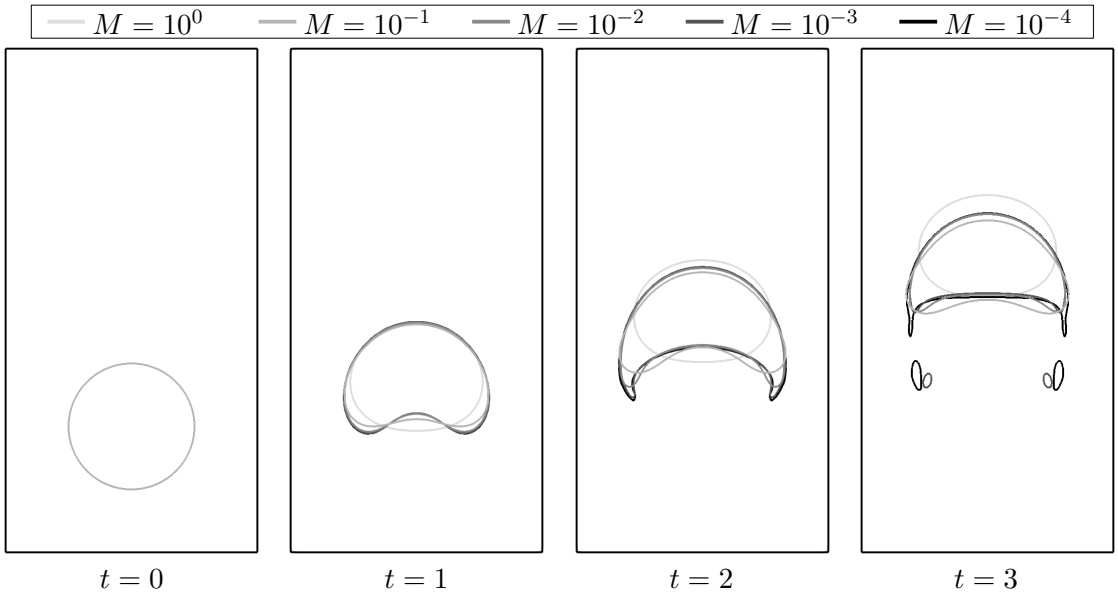

Figure 6.3: Interface shape at different times, for different mobility parameters.

are prescribed at the contact points between interface and wall, see Fig. 6.4. The non-dimensional material parameters are chosen arbitrarily to $\rho_{\mathfrak{A}} = 1000$, $\rho_{\mathfrak{B}} = 1000$, $\mu_{\mathfrak{A}} = 1$, $\mu_{\mathfrak{B}} = 1$, $\sigma = 1$. The static contact angle is deliberately chosen as $\theta_{\text{stat}} = \theta_i$ to match the geometrically prescribed angle in each test case. The domain is meshed with cells of size $h = 0.1$ and three levels ($l = 3$) of AMR at the interface. The approximation degree is chosen as $k = 2$. The droplet is initialized with the phase field

$$\varphi(x, y) = \tanh\left(\frac{\sqrt{(x)^2 + (y - y_i^2)} - r}{\sqrt{2}\xi_j}\right). \tag{6.14}$$

The transition length is varied with

$$\xi_j = \frac{(4 - j)4h}{(2k + 1)2^l}, \quad j = 0 \dots 3, \tag{6.15}$$

while the mobility is chosen as $M = 1$. With the different transition lengths the result in the sharp interface limit $\xi \to 0$ can be investigated. The high value of the mobility exaggerates the effect of the phase field boundary condition for the contact angle Eq. (4.36a), which as we will see clashes with the contact angle boundary condition employed during the flow solution Eq. (2.72). For both the flow and phase field solution, the implicit Euler scheme is used and 1000 time-steps of size $\Delta t = 0.001$ are performed.
In principle, the prescribed initial state is in equilibrium already, therefore the contact angle and contact point position should not change. Also the kinetic energy should be very small, i.e., only non-zero due to parasitic currents originating from inaccuracies of the surface tension computation at the interface.
In Fig. 6.5 the deviation of the contact angle and position from the prescribed equilibrium value and kinetic energy is displayed for the different transition lengths over the simulation time. As a reference the same simulation performed with the scalar advection evolution (Section 4.3.1) is displayed (initial interface shape according to Eq. (6.14) with $j = 0$).
From the contact angle plot it is visible that larger transition lengths (triangles and squares) lead to larger deviations in the observed contact angle. This effect is especially pronounced when the contact angle is sharper (red and green lines). In the sharp interface limit, as $\xi \to 0$ (i.e. for increasing j), the deviation in contact angle diminishes for all test cases, apart from one outlier (blue diamonds). Furthermore, a few abrupt changes in the contact angle are visible. These are usually related to time-steps, in which the contact line enters a new cell.
The contact point position, displayed below the contact angle, is influenced by two effects. For one, the initial phase field profile is not the exact equilibrium one, which causes the zero set to move. The tanh profile (Eq. (6.15)) is only a good approximation to the true equilibrium profile as $\xi \ll 1/\kappa$. The second effect is the induced contact line velocity, due to the deviation in contact angle.
This effect becomes even more visible in the plot for the kinetic energy. The kinetic energy, which should vanish in this test case, does not disappear, as the phase field evolution computes an equilibrium contact angle significantly differing from the prescribed static one. This causes the contact line to move and slightly distorts the interface causing a flow due to unbalanced capillary forces. From the reference simulations using the scalar advection, it is visible that the movement of the contact point and the kinetic energy approximately disappear. However, depending on the contact angle a small deviation is still observed, which can be attributed to the projection of the tanh profile. This shape was chosen to ensure the comparability and highlight the effects

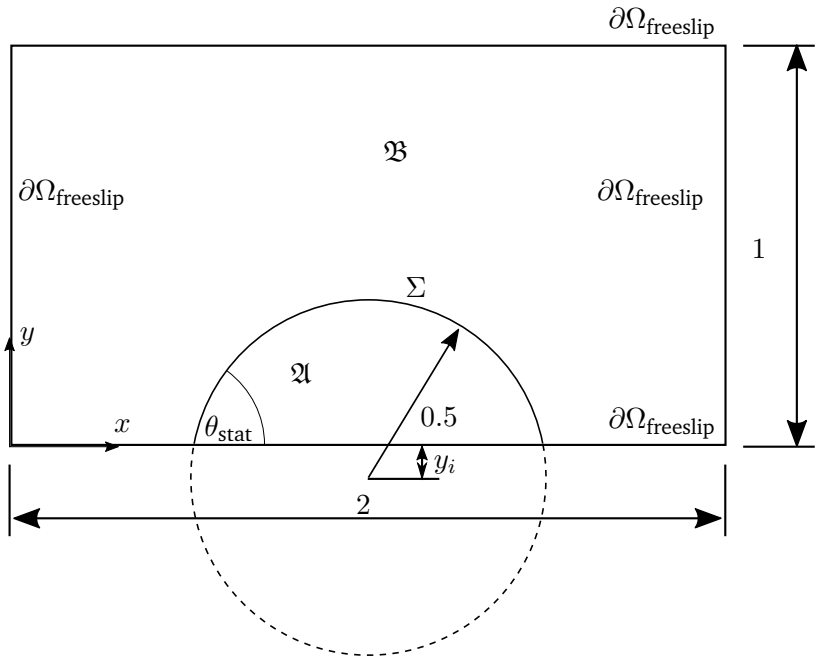

Figure 6.4: Setup for the static droplet test case

attributable to the phase field. In more complex simulations a different profile would be used, e.g. a signed-distance profile.

6.2.3 Discussion of phase field level set findings

Even though the Cahn-Hilliard equation is conservative w.r.t the order parameter, i.e., the scalar level set variable, it does not conserve the mass enclosed by its zero set. In addition, the diffusive terms introduce an artificial smoothing of sharp contours, whose dominance scales with the mobility parameter. However, choosing the mobility parameter too low basically results in the scalar advection equation, and the advantages of the phase field level set method are lost. Therefore, the mobility parameter must be chosen so that there is enough diffusion to contract or expand the interface in its normal direction towards its equilibrium shape, while limiting the unwanted tangential diffusion.
The results for the static droplet show that the boundary condition for the contact angle in the phase field only results in the equilibrium contact angle at the zero set in the sharp interface limit. In practice this means that the two contact angle boundary conditions in the level set and fluid equations do not match and an artificial movement of the contact line is introduced.
The main advantage of the phase field level set is its robustness. The diffusive terms work to hold the transition of the order parameter in the tanh shape normal to the interface. Furthermore, there are also indications that the additional diffusion in the phase field level set method serves to go beyond the capillary time-step limit. However, this is not further explored in this work. In contrast to this stand the disadvantages of the method. Due to the fourth order nature of the non-linear Cahn-Hilliard equation, an implicit timestepping with a non-linear solver has to

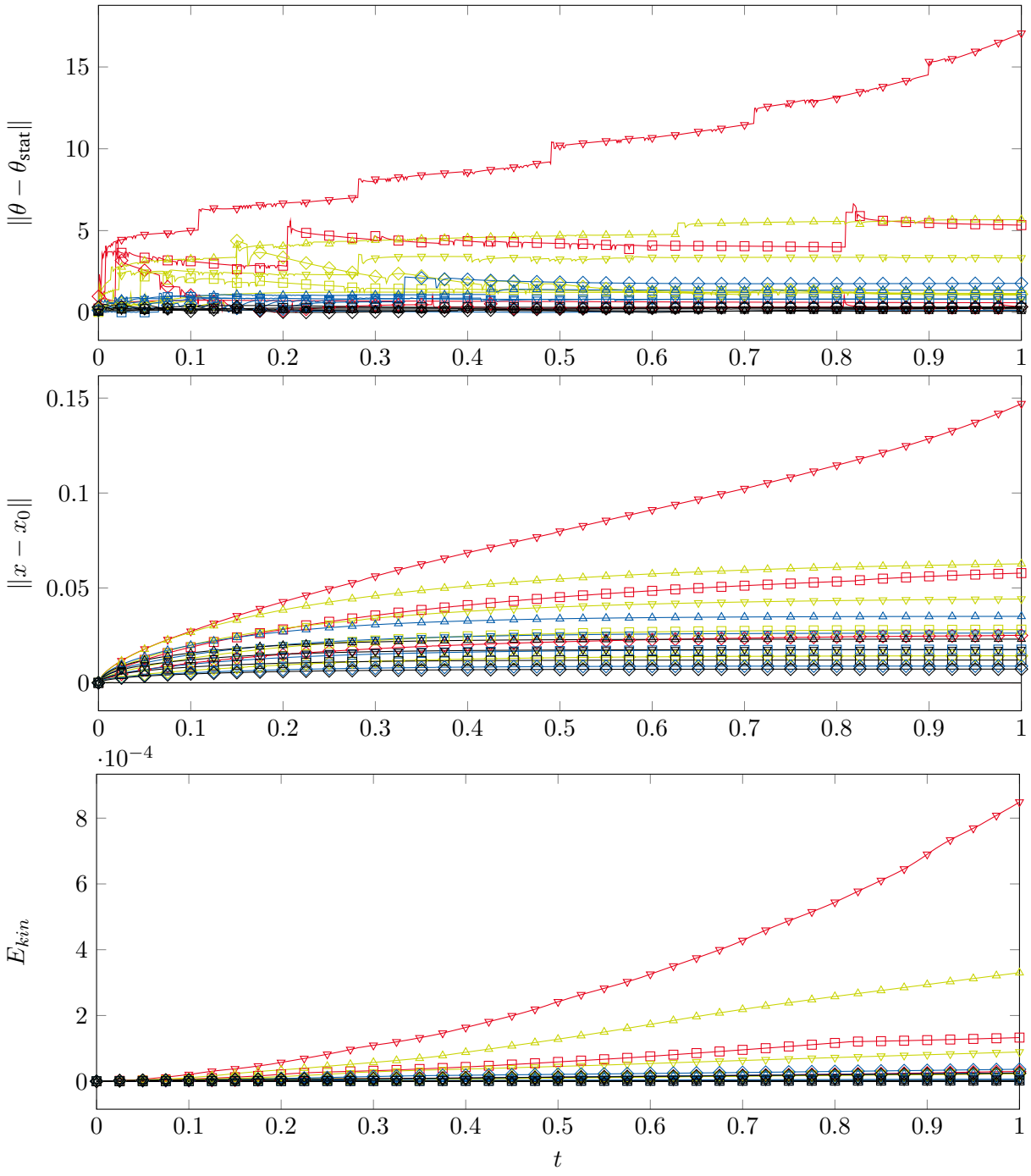

Figure 6.5: Deviation of the measured contact angle and position and kinetic energy from the prescribed equilibrium values in the static droplet test. Colors decode the prescribed angle θ_0, θ_1, θ_2, θ_3, markers the transition length $\triangle$ ξ_0, $\triangledown$ ξ_1, $\square$ ξ_2, $\diamond$ ξ_3 and the reference case is displayed without markers.

be employed to solve the phase field evolution. This is much more expensive than the explicit timestepping used for the scalar advection equation. Furthermore, the choice of the additional parameters is not straightforward and significantly influences or even distorts the results. Summarizing all this, we conclude that the downsides of the hybrid diffuse-sharp interface phase field level set method outweigh its advantages and the scalar advection is chosen as the primary interface evolution method for the remainder of this work.

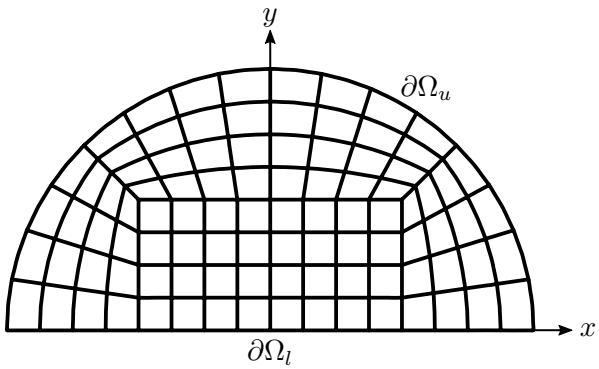

Figure 6.6: 16×8 O-Grid, meshed with biquadratic cells. 8×4 cells are used for the center section of size $R \times R/2$ and another 4 cells in the radial direction of the outer ring.

6.3 Consideration of DG convergence in dependence of boundary conditions

In this section a few small convergence studies are collected. Two investigations are performed. In the first investigation the steady heat equation (basically Poisson's problem) is solved on a semi-circular domain. It will be shown that even smooth boundary values can result in a suboptimal convergence order for the temperature. The second investigation considers a free floating evaporating liquid drop and compares the convergence orders for velocity and pressure in dependence of the convergence order for the temperature. The results serve to justify the choice of equal approximation order for the velocity and temperature fields, as determined in Section 4.1.

6.3.1 Sensitivity to non-obvious non-smooth solutions

The purpose of the first presented investigation is to underline the importance of carefully selected temperature boundary conditions, especially in the context of contact line problems, when high order convergence is to be achieved. The setup is chosen to resemble a semi-circular 2D droplet of radius $R = 0.8$, in which the temperature distribution is to be solved. In this investigation the scope is limited to pure single phase flow and the droplet is meshed using an O-Grid, as displayed in Fig. 6.6. On this mesh the steady heat equation, Eq. (2.74c) $\rho\hat{c} = 0$ and $\hat{k} = 1$, is solved. The boundary of the droplet is split in two parts, the upper half $\partial\Omega_u$, representing the fluid-fluid interface and the flat lower part $\partial\Omega_l$, representing the fluid-solid interface. Over the course of the study the boundary conditions, as well as the polynomial order for the temperature are changed.

Table 6.2: EOC $\|T - T_{ref}\|_{L^2(\Omega)}$, for the steady heat equation

$\partial\Omega_u$	$\partial\Omega_l$	$k=2$	$k=3$	$k=4$	$k=5$
$T = \sin(x)e^y$	$T = \sin(x)e^y$	3.27	4.15	5.04	6.15
$T = \ln(r_0)$	$T = \ln(r_0)$	0.84	0.91	0.90	0.91
$T = \ln(r_{0.01})$	$T = \ln(r_{0.01})$	1.34	1.62	1.81	1.89
$T = \ln(r_{0.1})$	$T = \ln(r_{0.1})$	2.26	2.86	3.46	4.13
$T = \ln(r_1)$	$T = \ln(r_1)$	3.24	4.17	4.88	5.89
$T = 0$	$T = \sin(\pi(x-R)/(R))$	2.94	3.35	3.30	3.19
$T = 0$	Eq. (A.28)	3.02	3.90	4.70	4.88

The EOC, which is determined using five different grids of size $4\times 2, 8\times 4, 16\times 8, 32\times 16, 64\times 32$, is displayed in Table 6.2.
The first row of Table 6.2 uses a smooth, exact, non-polynomial solution to Poisson's problem and serves as a baseline, verifying the optimal EOC of $k+1$ of the method. Afterwards a solution to the problem in polar coordinates is used, exhibiting a singularity at $r_a = \sqrt{x^2 + (y+a)^2} = 0$. The results clearly show the loss of optimal convergence for this low regularity solution. Subsequently, the center point of this solution is shifted outside the domain and it is visible that the EOC recovers, the further the singularity is moved outside of the computational domain. We then shift to a setting resembling the evaporation setup, where the upper fluid-fluid interface is held at saturation temperature $T = 0$ and the lower wall is heated. However, the results show a decrease in EOC even though the boundary conditions are smooth.
For the last row an exact solution, based on the procedure described by Polyanin (2015, p. 788), is used for the boundary conditions. From Fig. 6.7 it is visible that the BC chosen in this way differs only slightly from the sine BC. Even though these conditions look very similar, Table 6.2 clearly shows an increase in EOC for the carefully crafted BC, approaching the optimal order again, up to $k = 4$. When increasing the approximation order to $k = 5$, again a stagnation in EOC is visible. It is not clear what is causing this diminution.

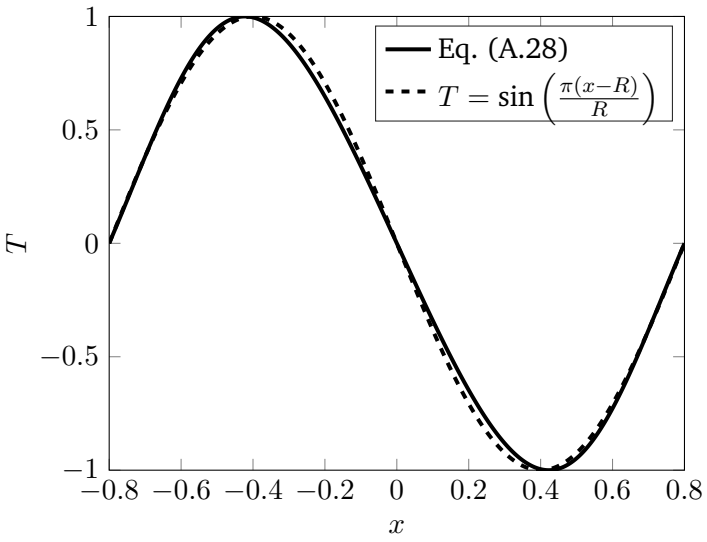

Figure 6.7: Comparison of the boundary condition on $\partial\Omega_l$ of Eq. (A.28) and a sine function

6.3.2 Temperature velocity coupling

In Eq. (4.5) the same approximation order is chosen for the temperature and velocity solution. In this section a test case is presented, whose purpose is to investigate the justification of this choice. To this end, consider the setup depicted in Fig. 6.8. A droplet of radius $R = 0.8$ is placed in a closed box of size $\Omega = [-1.5, -1.5] \times [1.5, 1.5]$, using the level set field

$$\varphi(x, y) = \left(\frac{x}{R}\right)^2 + \left(\frac{y}{R}\right)^2 - 1. \tag{6.16}$$

The walls of the box employ the freeslip boundary condition for velocity/pressure (Eq. (2.78) with $\beta, \beta_N = 0$) and Dirichlet boundaries for the temperature with three different choices:

$$T_0(x, y) = x, \tag{6.17a}$$
$$T_1(x, y) = xy, \tag{6.17b}$$
$$T_2(x, y) = \sin\left(\frac{\pi x}{3}\right) \sin\left(\frac{\pi y}{3}\right). \tag{6.17c}$$

The steady state solution is computed, neglecting convective terms, with arbitrarily chosen material parameters as $\rho_{\mathfrak{A}} = 1$, $\rho_{\mathfrak{B}} = 0.1$, $\mu_{\mathfrak{A}} = 0.5$, $\mu_{\mathfrak{B}} = 0.05$, $\hat{k}_{\mathfrak{A}} = 1$, $\hat{k}_{\mathfrak{B}} = 0.1$. Surface tension is neglected ($\sigma = 0$) to avoid flow due to capillarity and focus on the flow due to evaporation. The thermal parameters for the interface are chosen as $T_{sat} = 0$ and $\hat{h}_{vap} = 1000$. As in prior investigations the EOC, using a series of grids with $8 \times 8, 16 \times 16, 32 \times 32, 64 \times 64, 128 \times 128$ cells, for the solution variables is investigated.
In Table 6.3 the results for different pairings of temperature and velocity degree are shown. It is not suprising that the EOC for pressure/velocity depends on the approximation order for the temperature, as the test case is designed in such a way that the flow is only generated by evaporation. Therefore, the solution of velocity and pressure should be heavily influenced by the quality of the temperature solution at the interface. From Eq. (2.75) it is visible that the jump in velocity at the interface is proportional to the jump in temperature gradients. Hence, the

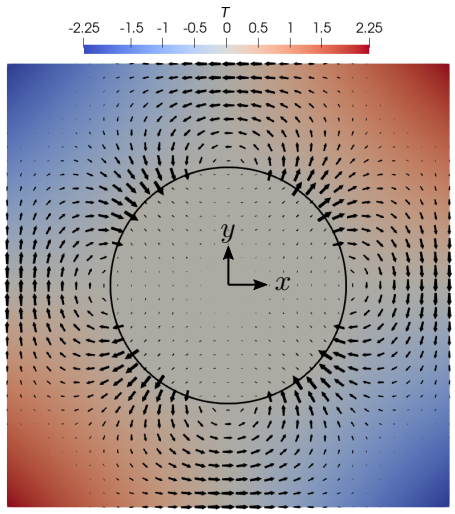

Figure 6.8: Temperature and velocity field for T_1, i.e. Eq. (6.17b), in a free floating evaporating droplet

Table 6.3: EOC, for the temperature velocity coupling

$k_{\boldsymbol{u}} \mid k_p$	2 | 1				3 | 2				4 | 3			
k_T	1	2	3	4	2	3	4	5	3	4	5	6
$\|p - p_{ref}\|$												
T_0	-.02	1.06	1.87	2.09	1.08	1.85	2.98	2.99	1.53	3.06	3.40	2.46
T_1	0.14	0.92	1.78	2.47	0.81	1.64	2.94	2.85	1.32	2.89	3.22	2.44
T_2	0.20	0.95	1.77	2.48	0.85	1.59	2.88	2.72	1.27	2.90	3.05	2.42
$\|\boldsymbol{u} - \boldsymbol{u}_{ref}\|$												
T_0	0.76	2.10	3.21	3.40	2.10	2.88	4.03	4.06	2.85	4.12	4.88	3.63
T_1	0.99	2.09	3.13	2.90	2.12	3.20	3.98	3.71	3.22	4.21	4.97	3.93
T_2	0.93	2.08	3.14	2.85	2.11	3.21	3.92	3.59	3.24	4.17	4.81	3.97
$\|T - T_{ref}\|$												
T_0	1.41	3.43	3.88	4.96	3.43	3.88	4.96	5.76	3.88	4.96	5.76	5.39
T_1	1.44	3.36	3.96	4.91	3.36	3.96	4.91	5.79	3.96	4.91	5.79	6.29
T_2	1.18	3.15	3.35	3.12	3.15	3.35	3.12	3.05	3.35	3.12	3.05	3.01

hypothesis to test is whether the temperature order should be chosen one degree higher than the velocity order. From looking at the first entry of every multicolumn in Table 6.3 it becomes evident that the temperature order should not be chosen smaller than that of the velocity. Even for the same approximation order, the EOC for velocity/pressure seem reduced compared to the expected optimum. When chosen of one order higher the EOC finally reaches the optimal value. A further increase in approximation order for the temperature seems to have a negative impact on the convergence of velocity and pressure. It is Interesting to note that this overall behavior does not change even when the global EOC for the temperature solution is reduced, as is the case for the BC T_2 from Eq. (6.17c). The findings support the hypothesis that the polynomial order for the temperature should be chosen one degree higher than that of the velocity. However, these results were obtained towards the end of this work, which is why equal approximation orders are used for the evaporation calculations carried out as part of this thesis. Additionally, the short investigation presented here does not deal with the coupling in the convective terms and overall stability of the method. Further investigations into this matter are required in order to reach a final conclusion.

6.4 Verification of the evaporation solver

The following section is an excerpt of the publication of the author of this thesis (Rieckmann et al., 2023e) on the implementation of evaporation in the XDG method. With the exception of individual corrections and minor textual adjustments to fit within the scope of this thesis, this section is a direct quote from the publication mentioned. For better readability, additional indentation has been omitted. This publication originated as part of this thesis and presented the XDG evaporation solver to solve the system described in Section 2.6.2 for the first time. The details of the method are discussed in more depth in Chapter 4. To conclude this chapter a variety of well established evaporation test cases, not involving contact lines, are computed. The results of these simulations in $1-3$ dimensions serve to validate the method. First, two 1D test cases,

known as the Stefan & Sucking problem, see e.g. (Welch and Wilson, 2000; Gibou et al., 2007; Sato and Ničeno, 2013; Bureš and Sato, 2021a), are considered. Next, a 2D film boiling, similar to (Son and Dhir, 1998; Welch and Wilson, 2000; Gibou et al., 2007), is simulated. And finally the growth of a vapor bubble in superheated liquid, as known from (Scriven, 1959; Sato and Ničeno, 2013; Bureš and Sato, 2021a), serves as a 3D test case.[1,2]

6.4.1 1D: Stefan problem & Sucking problem

Setup The first two test cases are known as the Stefan and Sucking problem. For completeness, we repeat their problem statement and material properties used here, following Bureš and Sato (2021a). Both cases have a similar setup, which is displayed in Fig. 6.9: a linear cavity of total length L (closed on its left side) contains a vapor adjacent to its liquid. The right boundary is open, allowing liquid to enter or exit the domain. However, in addition to the different initial conditions and size of the cavity, the test cases differ in the way heat is supplied to the system to cause evaporation at the vapor-liquid interface. Both cases use water and its vapor at the conditions given in Table 6.4. In the Stefan problem, the left wall is kept at a temperature higher than the saturation temperature, resulting in a heat flux from the wall towards the interface through the vapor. In the Sucking problem, the liquid is initially superheated, resulting in a heat flow from the liquid bulk towards the interface.
For these test cases, an analytical solution for the interface position over time is known:

$$\begin{aligned} x_\Sigma(t) &= 2\beta_v\sqrt{\alpha_v t}, \\ \alpha_v &= \frac{\hat{k}_v}{\rho_v \hat{c}_{p,v}}, \\ \epsilon &= 1 - \frac{\rho_v}{\rho_l}. \end{aligned} \tag{6.18}$$

The velocity is constant throughout the phases, with a discontinuity at the interface. Of particular interest is the temperature profile in the active phase (i.e. the vapor phase in the Stefan problem

[1]The software used to obtain the presented results is open source and available from (Kummer et al., 2023)
[2]The data sets containing the results of the numerical simulations are available online (Rieckmann et al., 2023b)

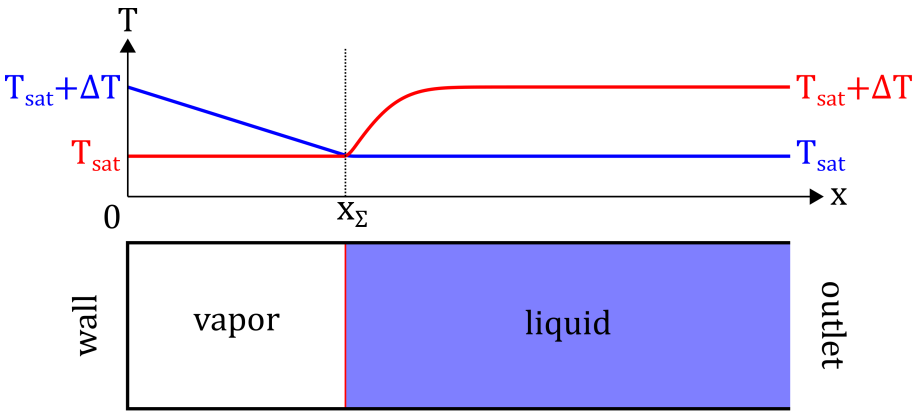

Figure 6.9: Stefan & Sucking problem setup. The simulation setup for the 1D test cases is sketched. The qualitative temperature profiles for the Stefan problem (in blue) and Sucking problem (in red) are plotted in the upper image.

Table 6.4: Material properties of water at saturation for atmospheric pressure

	Density ρ [kg/m^3]	Heat capacity $\hat{c}_p$ [J/(kg K)]	Thermal conductivity $\hat{k}$ [W/(m K)]	Dyn. viscosity μ [Pa s]
Liquid	958.4	4216	0.679	2.8×10^{-4}
Vapor	0.597	2030	0.025	1.26×10^{-5}

Latent heat $\hat{h}_{vap}$ [J/kg] $= 2.258 \times 10^6$, Surface tension σ [N/m] $= 0.059$,
Saturation temperature T_{sat} [K] $= 373.15$

Table 6.5: Parameters for the Stefan and Sucking problem

	ΔT [K]	β_v [−]	t_0 [s]	$x_\Sigma(t_0)$ [mm]	L [mm]
Stefan	10	0.0669	0.03	0.0105	1
Sucking	5	0.7677	0.1	2.21	10

and the liquid phase in the Sucking problem). Solutions for velocity and temperature can be found in the work of Welch and Wilson (2000). The specific parameters used in the simulations are listed in Table 6.5. Both test cases are initialized at a time $t_0 > 0$ such that $x_\Sigma(t_0) > 0$.
For both simulations, we investigate the solutions under refinement of the grid and polynomial degree. The grid sequence includes grids with $n = [8, 16, 32, 64]$ equal-sized cells, and the polynomial order varies within $k = [1, 2, 3]$ Eq. (4.5). Both test cases use the fields defined by the analytical solution as initial values for velocity and temperature. Although the surface tension does not play a role in the analytical solution, it limits the stable time-step size of our numerical method, according to Eq. (6.5). To obtain a practical step size, we reduce the surface tension by a factor of 10^6 for the Stefan problem and 10^3 for the Sucking problem, resulting in $\sigma = 0.059 \times 10^{-6}$ N/m and $\sigma = 0.059 \times 10^{-3}$ N/m, respectively. For both cases, we simulate until $t_E = 0.6$ s with a constant time-step of $\Delta t = 1.4 \times 10^{-4}$ s in all runs. Furthermore, the temperature is rescaled to $\Theta = (T - T_{sat})/\Delta T$.

Results With the setup established, we provide a brief discussion of the results. Simulations using the same polynomial degree are grouped together, and the interface position in time is considered. The results for the Stefan problem are shown in Fig. 6.10, and those for the Sucking problem are shown in Fig. 6.11.
In case of the Stefan problem, Fig. 6.10, all plot lines are nearly identical, indicating that the numerical solution reproduces the analytical one very well. Only when substantially magnifying, as shown int the cutouts in Fig. 6.10, some differences become visible. For simulations using the lowest polynomial order, a convergence towards a slightly offset solution compared to the analytical one is apparent. For simulations with polynomial order $k = 2$ and $k = 3$, the numerical solution does not vary noticeable when refining the grid. In all three cases, there exist a deviation from the analytical solution that does not vanishing with hk-refinement and remains nearly constant. This is most likely due to the temporal error arising through the first order coupling between flow solution and interface movement.
Proceeding to the Sucking problem, the results shown in Fig. 6.11 are more interesting, as the temperature profile is more complex. Overall, there is a convergence towards the analytical solution for all polynomial degrees. Even the simulations using the coarsest grid and a thereby under-resolved temperature profile, are able to reproduce the qualitative behavior of the interface

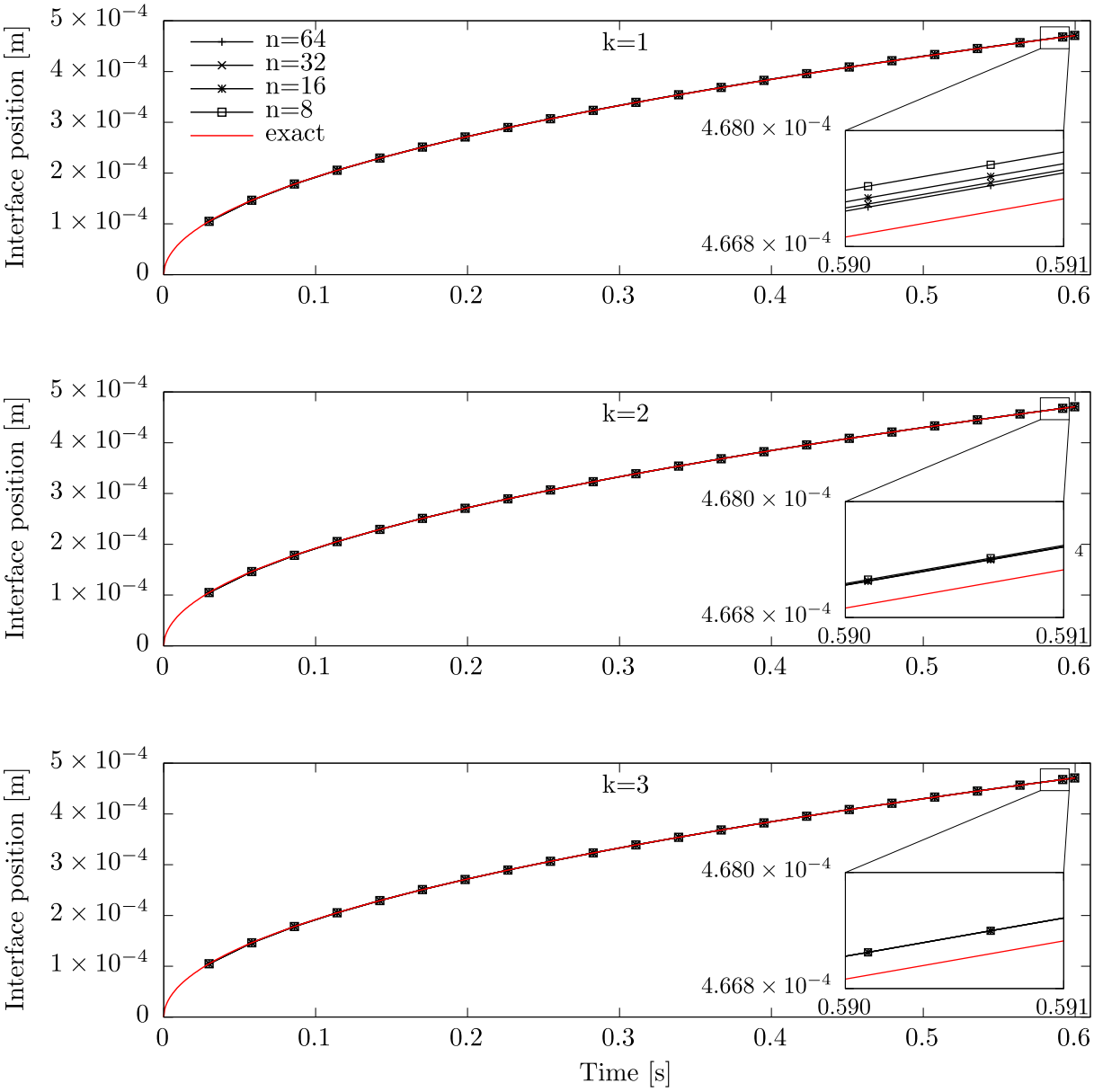

Figure 6.10: Stefan problem results. The interface position for simulations of the Stefan problem with different polynomial degree $k = [1, 2, 3]$ under grid refinement with $n = [8, 16, 32, 64]$ cells is displayed, the exact solution Eq. (6.18) is given in red.

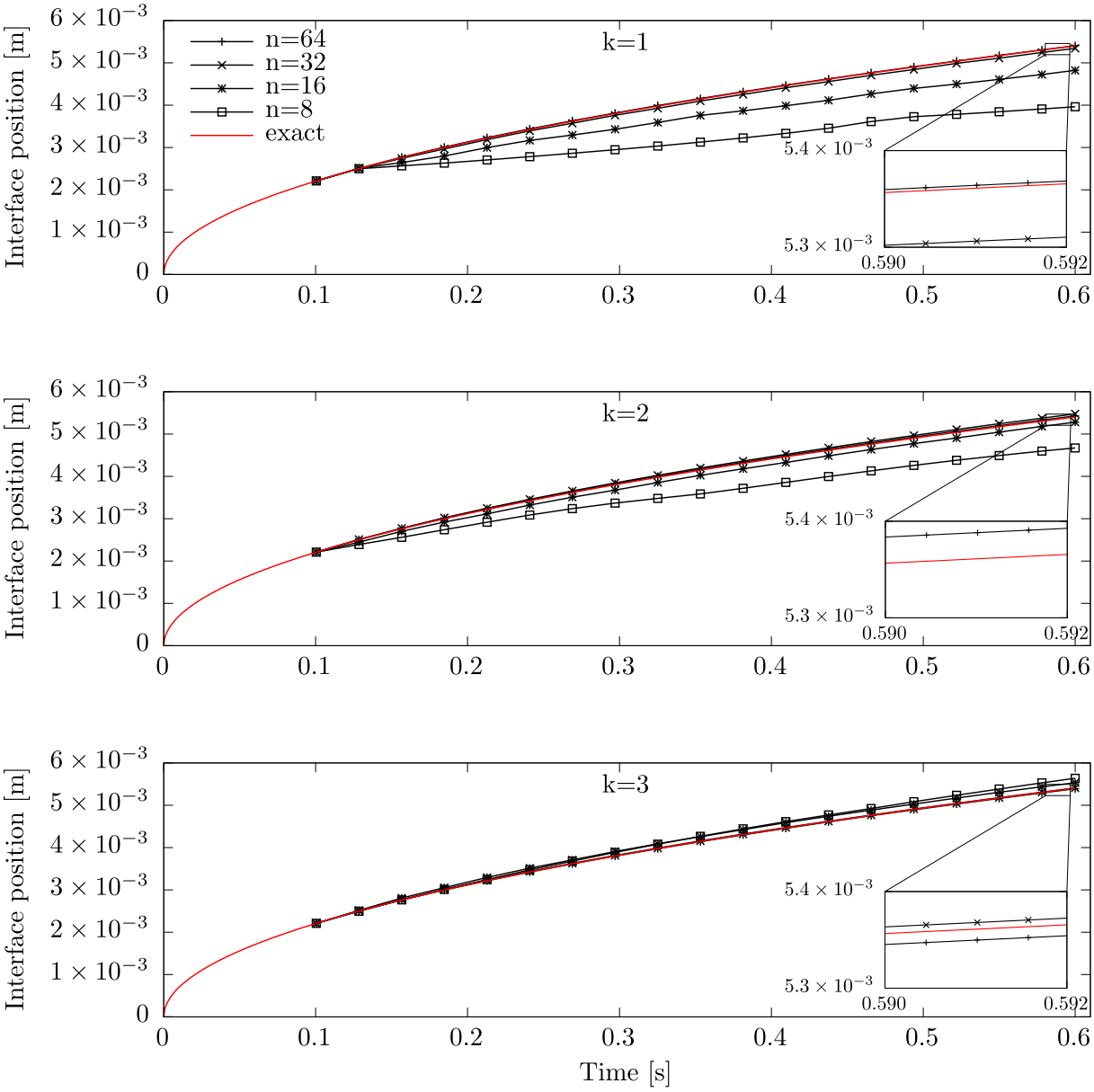

Figure 6.11: Sucking problem results. The interface position for simulations of the Sucking problem with different polynomial degree $k = [1, 2, 3]$ under grid refinement with $n = [8, 16, 32, 64]$ cells is displayed, the exact solution Eq. (6.18) is given in red.

movement. The magnifications also reveal some noteworthy findings. The best solution is obtained for $k = 1, n = 64$, whereas one would expect the best result for $k = 3, n = 64$. A detailed investigation of this observation is beyond the scope of this paper, but we can offer a short explanation for this phenomenon.
From the results in Fig. 6.10, where the error in interface position is mainly attributable to the temporal error, we can deduce that the temporal discretization overestimates the movement of the interface. On the other hand, from the simulations in Fig. 6.11 using coarse meshes, it is apparent that the spatial discretization tends to underestimate the interface speed. Together, these two error components can lead to an annihilation, leading to the observed phenomenon.
To relate these results to alternative methods, Fig. 6.12 shows the l^1-mean value of the relative error in interface position, i.e.,

$$\bar{E}_1 = \frac{1}{N} \sum_i \left| \frac{x_{\Sigma,i}}{x_{\Sigma,theor}(t_i)} - 1 \right|, \tag{6.19}$$

in comparison to the results obtained by Bureš and Sato (2021a). The formula Eq. (6.19) is slightly modified, taking into account the fixed time-step size and total number of time-steps N in our simulations. On the abscissa the inverse of number of cells per domain length is displayed, normalized by the coarsest grid level. The normalization constant is $n = 8$ in both our simulations for the Stefan and Sucking problems, whereas it differs in the reference between $n = 50$ and $n = 400$. For the Stefan problem the simulations for all polynomial degrees converge towards the same residual error, without displaying a clear order of convergence. This suggests that the flow solution is approximated well even for $k = 1$ and the majority of the error arises from the time discretization and coupling between flow solution and interface movement. For the Sucking problem all simulations display a similar, approximately first order convergence. For the simulations with $k = 3$ similar relative errors as by Bureš and Sato (2021a) are achieved. This is particularly significant when taking into account the total number of DOFs. Looking at

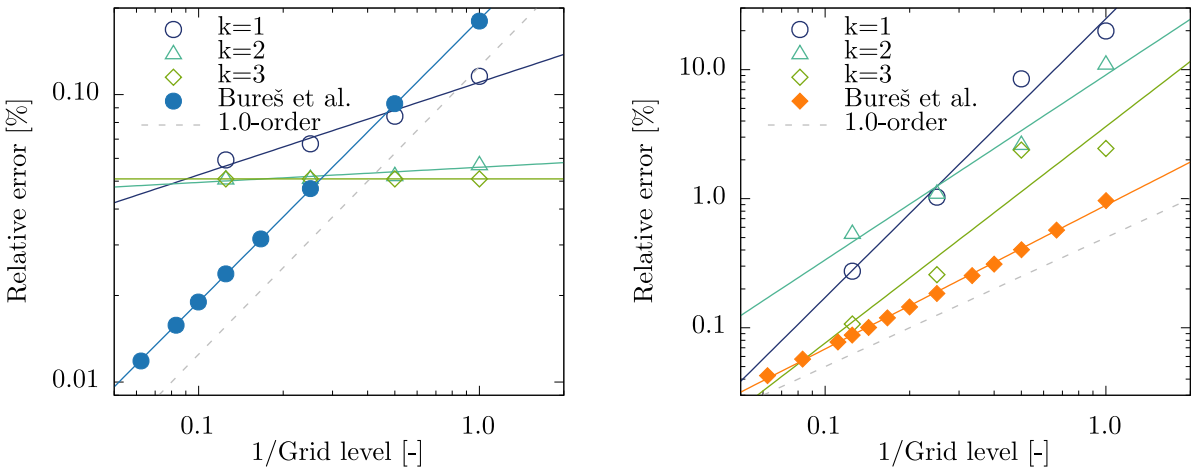

(a) Stefan problem

(b) Sucking problem

Figure 6.12: Relative error in interface position, Eq. (6.19), in comparison to the results of Bureš and Sato (2021a). The abscissa shows the inverse cell length scale normalized for the coarsest grid $n = 8$ (different values for Bureš and Sato (2021a) a) $n = 50$, b) $n = 400$). As in the reference the dashed lines show power-law fits of the data points. A different scaling for the ordinate was chosen for the two test cases.

Table 6.6: Material properties for the 2D film boiling

	Density ρ [kg/m^3]	Heat capacity $\hat{c}_p$ [J/(kg K)]	Thermal conductivity $\hat{k}$ [W/(m K)]	Dyn. viscosity μ [Pa s]
Liquid	200	400	40	0.1
Vapor	5	200	1	0.005

Latent heat $\hat{h}_{vap}$ [J/kg] $= 10^4$, Surface tension σ [N/m] $= 0.1$,
Saturation temperature T_{sat} [K] $= 500$

the data points at grid level 8 we have 2340 DOFs in our simulation whereas Bureš and Sato (2021a) use $\sim 400 \times 8 \times 4 = 12800$ DOFs. Thereby, it is possible to achieve the same accuracy with only a fraction of the DOFs in our method. It is important to note that for DG methods, usual convergence theorems hold for integral properties on fixed domains. However, the interface position in time is no such integral property, instead depending only on values evaluated at the exact interface position, on a time dependent domain. Therefore, high-order convergence for the interface position is not guaranteed.

6.4.2 2D: Film boiling

Setup In the second test case, we consider the 2D film boiling problem proposed in Welch and Wilson (2000) and also studied in Gibou et al. (2007). We focus solely on the setup with wall superheat $\Delta T = 5$ K. The physical parameters for the test case are given in Table 6.6. The level set is initialized according to

$$\begin{aligned} \varphi(\vec{x}, 0) &= \frac{\lambda}{128}\left(4 + \cos\left(2\pi\frac{x}{\lambda}\right)\right) - y, \\ \lambda &= 2\pi\sqrt{\frac{3\sigma}{g\,|\rho_l - \rho_v|}}, \end{aligned} \tag{6.20}$$

using the most unstable wavelength λ of the developing Rayleigh-Taylor instability. The temperature profile is set to resemble a linear profile assuming T_{sat} at the interface and $T_{sat} + \Delta T$ at the wall. The domain size is chosen as $[-\lambda/2, \lambda/2] \times [0, \lambda]$. The lower boundary is a wall held at constant temperature, while the upper boundary employs a homogeneous Neumann boundary condition $(-p\mathbf{1} + \mu(\nabla \boldsymbol{u} + \nabla \boldsymbol{u}^T))\boldsymbol{n} = \mathbf{0}$, the left and right boundaries are periodic.
All simulations use a base grid of 4×4 equal-sized cells ($n = 2/(\lambda/2)$). However, different levels $l = 2...4$ of AMR are employed. Each level corresponds to a division of the refined cell in its center, meaning for $l = 1$ one cell is divided into four and so on. The refinement is applied to all cut-cells and their neighbor cells. The polynomial degrees used are $k = 2$ and $k = 3$, and the time-step used in all simulations is $\Delta T = 4.867 \times 10^{-5}$ s.

Results As the main result the interface shape under polynomial and grid refinement is regarded. For comparison the bubble shape from Gibou et al. (2007) is included at time $t = 0.425$ s. In Fig. 6.13 the final interface shape for the $k = 2$ simulations is shown. Under increasing AMR they converge towards a similar shape as in the reference, but without reaching the identical shape. The simulation on the coarsest mesh stands out, in that it gives a significantly different result,

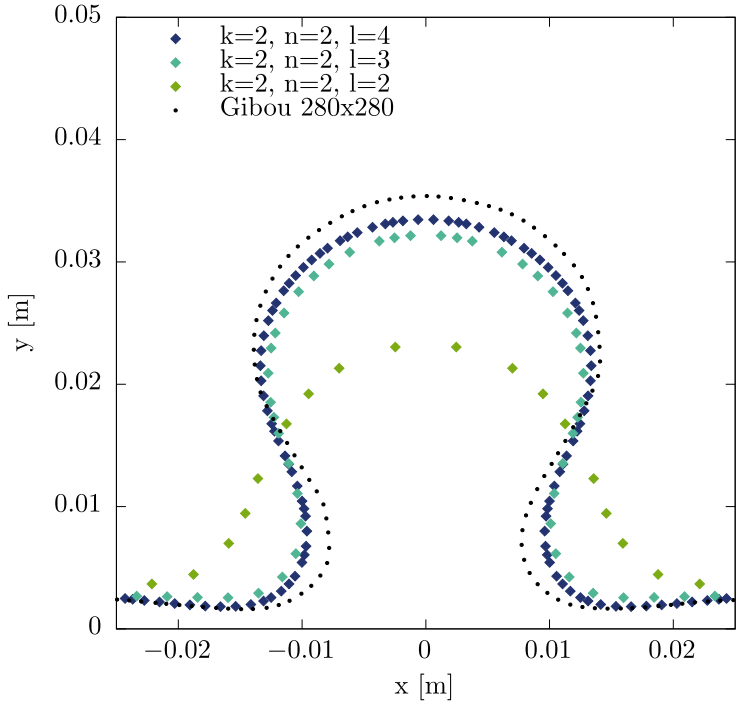

Figure 6.13: Film boiling results for $k = 2$, comparing the bubble shapes at $t = 0.425$ s for $k = 2$, $n = 2$ and different levels of AMR $l = [2, 3, 4]$

where the bubble that is forming is still in an earlier stage of development.
For the $k = 3$ simulations, shown in Fig. 6.14, an identical result is found, however this time the coarsest simulation does not deviate that far and the two other results are practically lying on top of each other.
Under polynomial refinement the same trend is visible, see Fig. 6.15. Here, the interface shape again seems to converge toward the reference, although not quite reaching it.
It is interesting to note the direction of convergence here. In both cases ($k = 2$ and $k = 3$) the bubble becomes larger under refinement. In the reference the direction is exactly inversed, with the bubble becoming smaller under refinement. By this observation our method and the one employed in Gibou et al. (2007) converge towards the same solution, although from a different direction. A very similar effect, regarding the direction of convergence, was noticed in the comparative work on capillary rise by Gründing et al. (2020), where a similar version of our solver was compared to finite volume based schemes. There the direction of convergence between the finite volume methods and the XDG method was also inversed.
To gain more insight into this phenomenon the temporal evolution of the interface for $k = 2, l = 2$ and $k = 2, l = 4$ is compared in Fig. 6.16. At the beginning of both simulations, there is no notable difference, with the interface almost uniformly moving upwards until $t = 0.167$ s. However, as soon as the instability starts to form, the two simulations begin to diverge, visible at $t = 0.333$ s. In the low resolution simulation the development of the instability is delayed compared to the fine resolution. Our interpretation is the presence of additional numerical diffusion in the coarse simulation. This slows down the formation of the instability, leading to a different final state at $t = 0.5$ s.

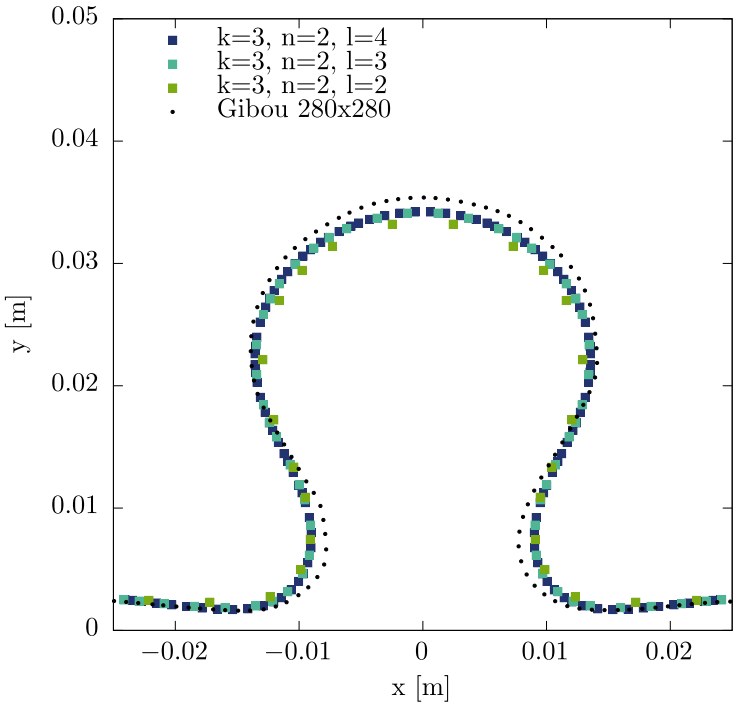

Figure 6.14: Film boiling results for $k = 3$, comparing the bubble shapes at $t = 0.425$ s for $k = 3$, $n = 2$ and different levels of AMR $l = [2, 3, 4]$

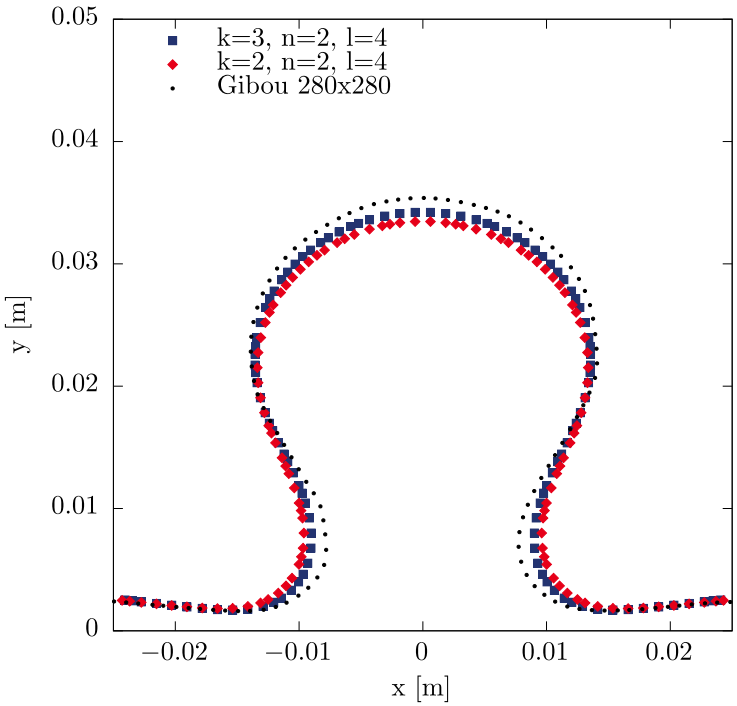

Figure 6.15: Comparison of film boiling results for $k = 2$ and $k = 3$ at $t = 0.425$ s for different polynomial degrees $k = [2, 3]$, $n = 2$ and $l = 4$

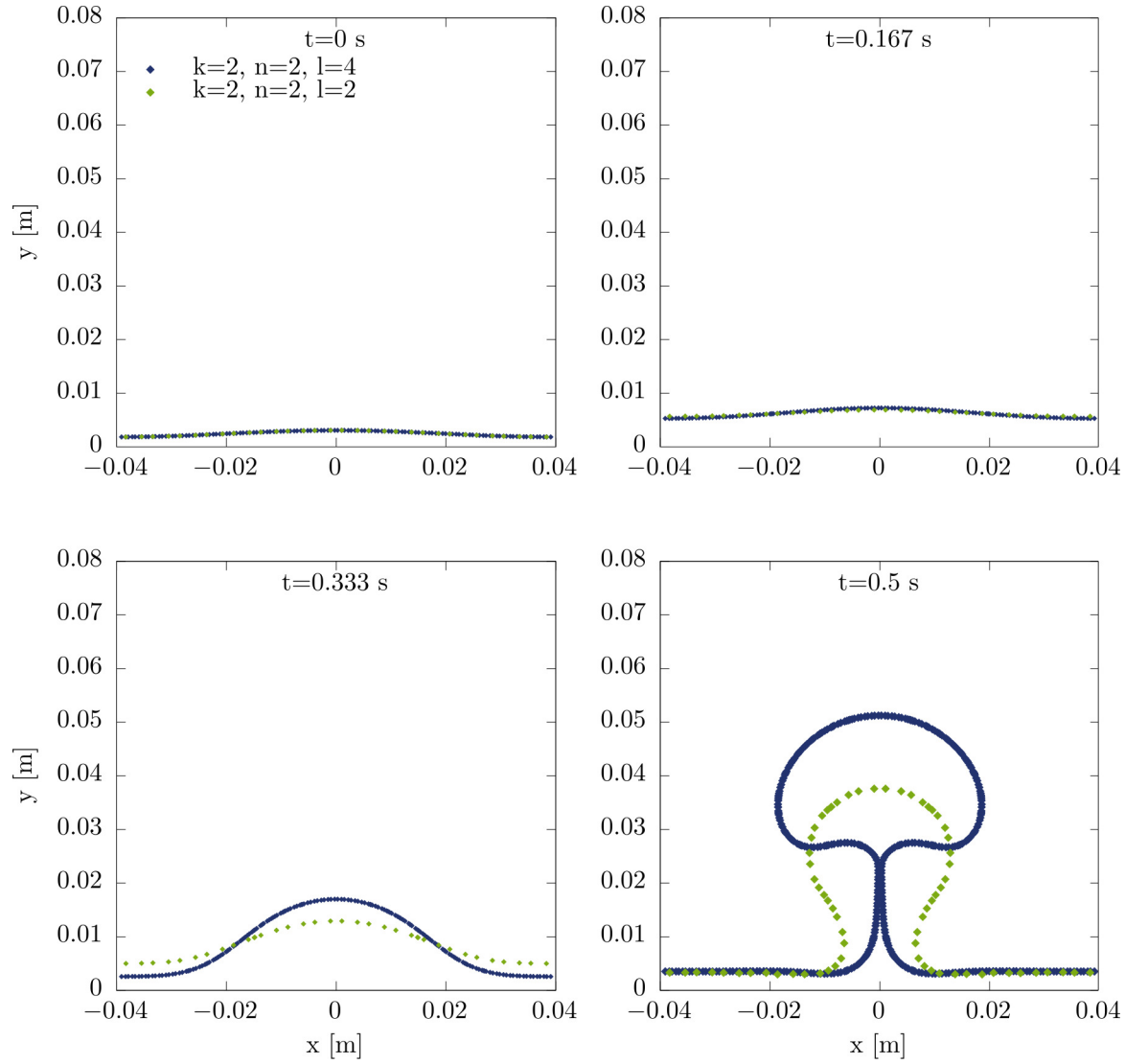

Figure 6.16: Evolution of the interface shape during the film boiling simulations with $k = 2$, $n = 2$, and different levels of AMR, $l = 2$ and $l = 4$. The formation of the instability is significantly delayed for the simulation with less AMR.

6.4.3 3D: Scriven test case

Setup The final test case presented in this work is the 3D growth of a vapor bubble in superheated liquid, commonly referred to as the Scriven test case, see e.g. Sato and Ničeno (2013) and Bureš and Sato (2021a). As in the 1D test cases, the material properties from Table 6.4 are used. The interface position over time is given by Eq. (6.18), where x_Σ represents the bubble radius r_Σ. When expressed in a spherical coordinate system all solution fields are only dependent on the radial coordinate. In such a coordinate system this test case is therefore very similar to the 1D test cases. However, here a cartesian coordinate system is used, for which no such dimensional reduction can be made. The computational domain is a cube with edge length L, containing 1/8-th of the vapor bubble. The additional parameters for superheat, start time and length scale are summarized in Table 6.7.

Table 6.7: Parameters for the Scriven test case

ΔT [K]	β_v [−]	t_0 [s]	$r_\Sigma(t_0)$ [mm]	L [mm]
1.25	4.063	0.000225	0.05	0.1875

The exact solutions for the radial-velocity and temperature are expressed in terms of the radial coordinate, given by $r = \sqrt{x^2 + y^2 + z^2}$, cf. Scriven (1959) or Sato and Ničeno (2013). The initial conditions are projected from these solutions, as shown in the top of Fig. 6.17. Symmetry boundary conditions are employed on the boundaries intersecting with the interface, while homogeneous Neumann boundary conditions are used on the three other boundaries. Although this is a small deviation from the expected analytical solution, we do not expect it to significantly influence the overall solution in terms of the interface position.
Similar to the film boiling case discussed in Section 6.4.2, we investigate the vapor bubble growth for different levels of AMR $l = 0...2$. The base grid consists $8 \times 8 \times 8$ equal-sized cells, denoted as $n = 8$. In all simulations, the polynomial degree is $k = 2$. The final time is chosen such that the analytical result gives double the initial radius, i.e. $r_\Sigma(t_E) = 2r_\Sigma(t_0)$. As in Section 6.4.1, the surface tension is rescaled by a factor of 5×10^4 ($\sigma = 0.0118 \times 10^{-4}$ N/m) to obtain a larger stable time-step, without influencing the growth behavior in this particular case. The temperature is

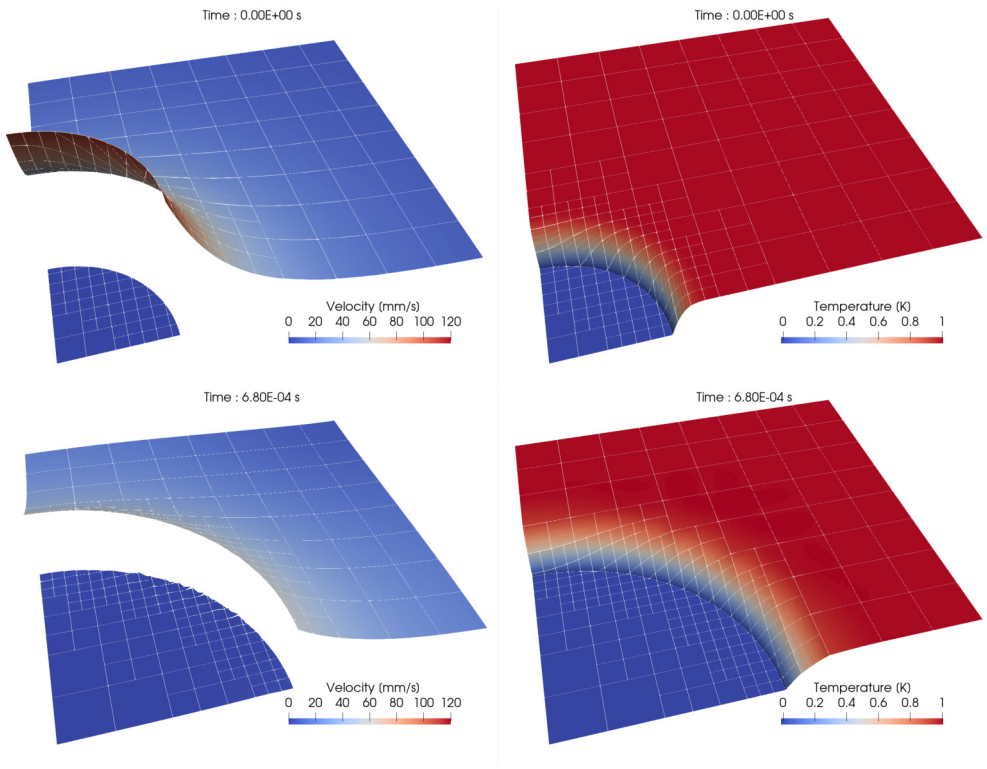

Figure 6.17: Scriven test case initial and final states. The section of the velocity (left) and temperature (right) fields with the x-y-plane is plotted. The projection of initial values (top) is compared to the final state (bottom). The white grid shows the section of the computational mesh. The interface can be seen by the position of the discontinuities.

rescaled according to $\Theta = (T - T_{sat})/\Delta T$. The time-step size used is then $\Delta T = 5.488 \times 10^{-6}$ s. To investigate the effect of the time-step size, we perform the simulations with original and half time-step size $\Delta T, \Delta T/2$.

Results The growth of the bubble radius over time is shown in Fig. 6.18. As the level of AMR is increased, the numerical solution converges towards the analytical one. All simulations use the same time-step, so this increase in accuracy is solely attributable to the spatial refinement. To investigate the role of the time-step in this particular test case, the simulation using AMR level $l = 1$ is repeated with half the time-step size. The result is shown in the lower image of Fig. 6.18. There is no significant increase in accuracy under temporal refinement. Only when magnified a difference between the lines for $\Delta T/2$ and ΔT becomes visible.
Figure 6.19 shows the initial temperature field in the x-y-plane for the $l = 2$ and $l = 0$ simulations. The initial values for the coarse simulation differ substantially from the exact solution (note the pronounced discontinuities), including the solution at the interface. Despite this, even the coarse simulation can reproduce the qualitative behavior of the bubble growth without employing any reconstruction or filtering of the values at the interface.
Finally, the results obtained with our method are compared to the findings of Bureš and Sato (2021a). Figure 6.20 displays the l^1-mean value of the relative error in interface position, Eq. (6.19), plotted over the inverse cell length scale, normalized by the length scale on the coarsest grid, with $n = 8$ for our data and $n = 24$ for the reference. The power-law fit of our

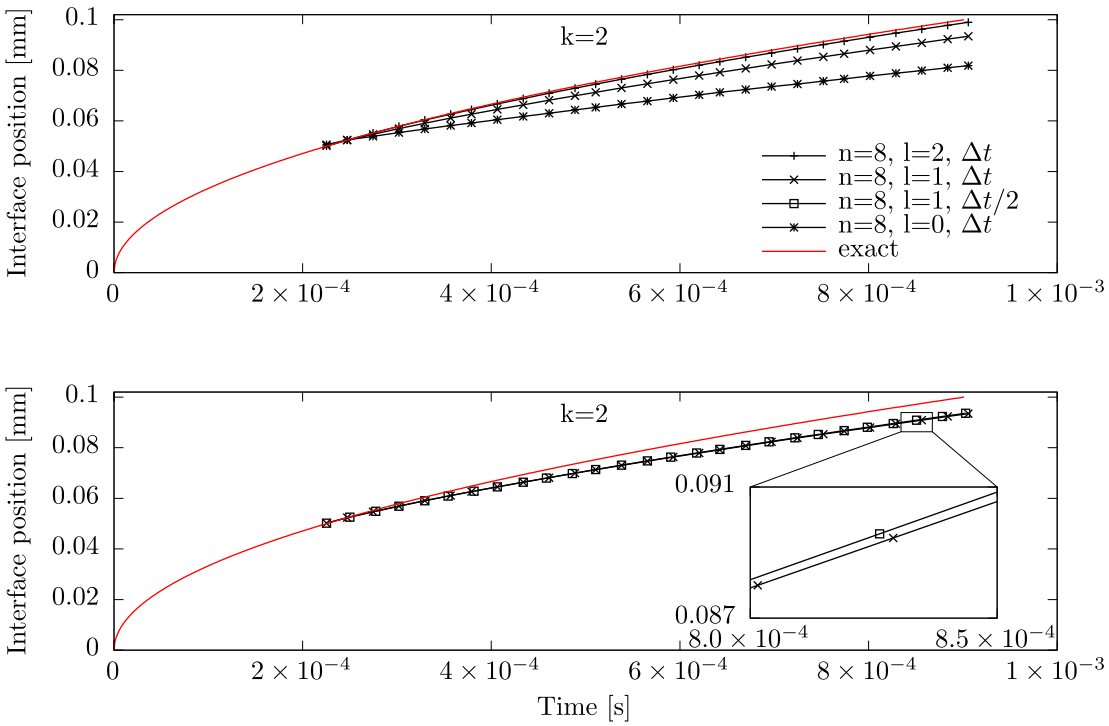

Figure 6.18: Scriven test case results. The radius of the vapor bubble over time is displayed, using $k = 2$, $n = 8$ and different levels of AMR $l = [0, 1, 2]$. The upper picture shows the solution under AMR. The lower plot compares the $l = 1$ simulation with original and halved time-step size.

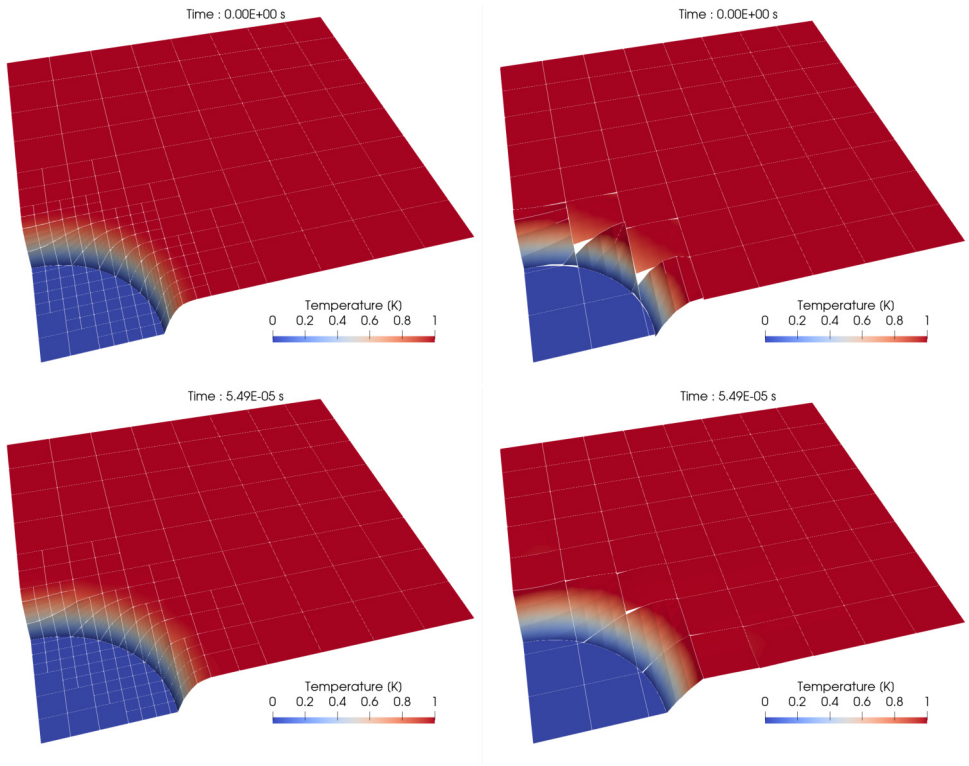

Figure 6.19: Scriven test case comparison of refinement level. The section of the temperature field with the x-y-plane is plotted for (from left to right) $l = 2$ and $l = 0$ after the projection of initial values (top) and after 10 time-steps (bottom).

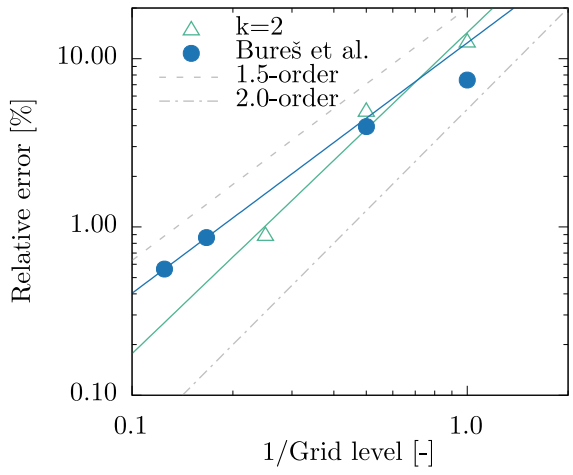

Figure 6.20: Relative error in interface position, Eq. (6.19), in comparison to the results of Bureš and Sato (2021a). The abscissa shows the inverse cell length scale normalized for the coarsest grid $n = 8$ (different value for Bureš and Sato (2021a) $n = 24$, “Cartesian case”). As in the reference the dashed lines show power-law fits of the data points.

data shows approximately second order convergence under grid refinement. To be able to classify these results, two important differences must be mentioned. First, our simulations use interface based AMR instead of uniform refinement over the whole domain. This reduces the number of DOF used in the simulations. E.g., For the data points at grid level 0.25 we used ~ 17612 DOF (varying with number of refined cell), whereas the reference used $\sim 24^3 \times 4^3 \times 4 = 3538944$ DOF. Again, the results show that with only a fraction of the DOF the same level of accuracy can be achieved. A large part of this reduction can be attributed to the refinement. Second, the end time is smaller than in the reference (~ 0.9 ms to ~ 1.5 ms). This means that a certain discrepancy in the absolute values of the measured errors is to be expected.

6.5 Conclusion

Over the course of this chapter several results obtained with the solver described in Chapter 4 are presented. With one exception they are all limited to flows not involving a contact line. Two variants of the solver are employed, without and with evaporation, see Sections 2.6.1 and 2.6.2. In the beginning, Section 6.1, the dynamics of capillary waves and their relevance in determining a suitable time-step size for the numerical method are reviewed. We were able to confirm the findings of other authors that owing to the explicit coupling between interface and flow solution, a rigid restriction to the time-step arises. This restriction is based on the propagation speed of the resolved capillary waves.

This analysis is followed by an investigation of the phase field level set method combining the ideas of diffuse and sharp interface methods, in Section 6.2. In this approach the phase field, as used in diffuse interface methods, is utilized as the level set field, describing the interface location for the otherwise sharp interface method. The additional diffusion in the phase field equation is a double-edged sword. On the one hand, it serves to stabilize the method in that it pulls the interface towards an equilibrium shape, eliminating the need for reinitialization. On the other hand, it smooths out sharp curvatures, serving as a kind of low-pass filter for capillary waves. This behavior has the advantage of relaxing the time-step restriction, even though this was not reviewed in detail. However, it also hides interface shapes or movements one would be interested in. Finally, there is also the question of computational cost. The phase field method, which requires an implicit time-stepping scheme and a non-linear solver, is considerably more expensive than the explicit scalar advection approach. Due to the uncertainty in how to choose the values for the parameters in this hybrid approach, namely the mobility and gradient energy coefficients, the distortion of the interface behavior by the phase field solution and the higher computational cost, the method was ultimately not further pursued.

In Section 6.3 two convergence studies are carried out. The first focuses on the impact the choice of boundary conditions has on the overall convergence of the method. This is investigated using the steady heat equation. It is found that the convergence order can be very sensitive to “hidden” irregularities. The observed EOC is reduced in simulations where the BC are described such that a singularity lies outside of the domain, and the solution inside is supposed to be smooth. Further, it is recognized that describing arbitrary but smooth BC can also yield reduced EOC. These results underline the importance of carefully choosing appropriate BCs when high order convergence is to be achieved. It is not always possible to sense if the chosen conditions are suitable to accomplish this task, especially on domains involving complex shapes. This is particularly relevant when considering evaporation at any interface.

The second convergence study examines the optimal order for the coupling between the approximation orders of the velocity and temperature fields. To this end, several combinations of velocity and temperature degree are tested. The hypothesis is inspected that optimal results can be achieved, when the temperature is one order higher than the velocity. The findings seem to confirm this hypothesis, returning optimal convergence orders in velocity and pressure for that case. A further increase does not seem to have a positive impact on the EOC. This behavior is even observed when an unfit boundary condition is used for the temperature, such that the EOC for the temperature is reduced. However, the analysis is limited to steady flow without convective terms, i.e., a one way coupling between temperature and velocity solution. To come to a conclusive result, further research into the matter is necessary. Also these results are obtained too late to impact the calculations in this thesis, for which equal approximation orders are used.

In the last section of this chapter, Section 6.4, the solver, Chapter 4, including evaporation, Section 2.6.2, is validated. It is based on the publication by Rieckmann et al. (2023e), which was created as part of this thesis. There the solver, as described in Chapter 4, was first presented. This newly devised method provides a direct coupling of mass, momentum and energy transport. The solution is available in both phases using independent high-order ansatz functions. Thereby, jumps and kinks arising at the interface can be sharply represented without any reconstruction of temperature and velocity gradients. Instead the higher-order ansatz functions are evaluated at the interface position to obtain the required (gradient) values. For a sharp representation of the interface itself, the level set method using the scalar advection approach from Section 4.3 is employed. From the level set the cut-cell quadrature is constructed and crucial in discretizing the interfacial jump conditions at the exact location of the interface, see Section 4.2.
The method is verified using a variety of well known evaporation test cases in 1, 2 and 3 dimensions. Convergence towards analytical or other numerical solutions under refinement of grid and polynomial degree is observed. The XDG based method was able to obtain results displaying the same accuracy as finite volume simulations but using only a fraction of the number of degrees of freedom. Even on very coarse grids the method was able to qualitatively predict the behavior of the interface.

As the results for the temperature velocity coupling and capillary time-step show, there is further potential for improvement in the coupling between interface and flow solution. The current splitting approach is limited to first order accuracy, restricted to the capillary time-step size and the results of Section 6.3 indicate that the equal order approximation might be sub optimal. These topics, aiming for a tighter coupling and higher convergence orders, can be revisited in future works.

7 Results for two-phase flows with contact lines

Over the course of this chapter several computations involving two-phase (or even three-phase) flows with contact lines are collected. The discussion starts with a review of singularities occurring at the contact line, in Section 7.1, while evaporation is excluded. Several models for the dynamic contact angle are introduced and the influence of the contact angle condition and wall boundary condition on the velocity and pressure behavior towards the contact line is investigated. A few test cases are presented to illustrate the capability of the method to implement different models for the dynamic contact angle as well as take into account more complex behavior like contact angle hysteresis.
Afterwards, the implemented evaporation model is examined in Section 7.2. We find that there exists a conflict between the no-slip condition on the interface and the impermeability of the wall at the contact line. The severity of this conflict is investigated by determining the EOC with and without this conflict present in a carefully selected setup. As a possible remedy the introduction of slip on the interface is considered.
To conclude the section a test case from the super ordinate project of this work is simulated. Section 7.3 begins with a discussion of the technical limitations of the method to simulate large real experimental problems. Motivated by this limitations a drastically simplified setup is proposed, simulated and analyzed. The section concludes with a showcase, which includes conjugate heat transfer in the solid phase. The evaporative heat flux is heavily influenced by the temperature boundary conditions chosen and drastically changes when heat transport is also computed in the solid phase. The findings of these three sections are summarized in Section 7.4.

7.1 Review of contact line dynamics

First, Section 7.1.1 focuses on either the movement of a material contact line or the pressure/velocities at this particular line. To this end, the free surface problem, Section 2.6.3, is solved using the solver described in Chapter 4. The first part of this section focuses on the pressure and velocity fields close to the contact line. Depending on the employed model for boundary conditions, contact angle and viscosity, singularities of various severity are observed at the contact line. In these simulations the temporal evolution of the interface is omitted. The second part (Section 7.1.2) then moves on to investigate different conditions for the dynamic contact angle, Eq. (2.86), namely of the form

$$f(\boldsymbol{u}, \boldsymbol{s}, \theta, \theta_{\text{stat}}) = \sigma(\cos(\theta_{\text{stat}}) - \cos(\theta)) - \operatorname{sgn}\left(\left(\boldsymbol{u}^{\Sigma} - \boldsymbol{s}\right) \cdot \hat{\boldsymbol{n}}^{L}\right) \beta_L \left|\left(\boldsymbol{u}^{\Sigma} - \boldsymbol{s}\right) \cdot \hat{\boldsymbol{n}}^{L}\right|^{\alpha} = 0, \quad (7.1)$$

and contact angle hysteresis. This describes the situation where the contact line pins, i.e. remains stationary, when the measured contact angle is between the advancing (θ_{adv}) and receding (θ_{rec})

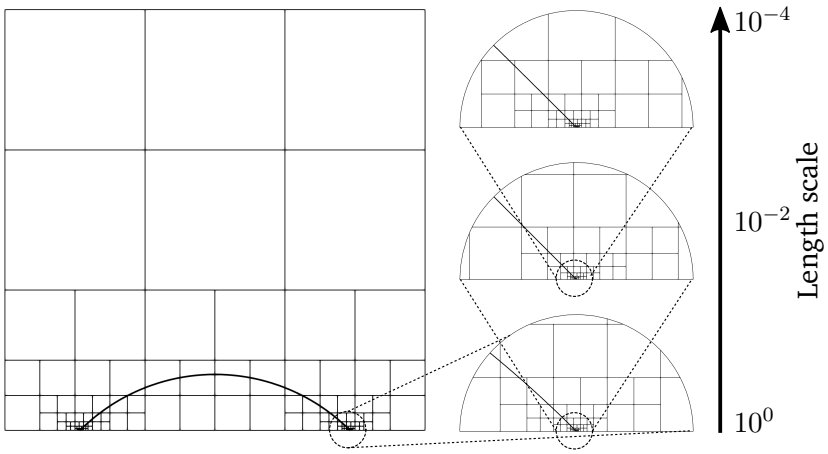

Figure 7.1: Setup to test the pressure and velocity behavior towards the contact line. A freesurface droplet with $R = 10$ sits on a slip wall. At the contact line very fine scales are resolved.

contact angle. In this case the contact line velocity is enforced to be

$$U_L = (\boldsymbol{u}^\Sigma - \boldsymbol{s}) \cdot \hat{\boldsymbol{n}}^L = 0 \quad \text{if} \quad \theta_{rec} < \theta < \theta_{adv}, \tag{7.2}$$

while Eq. (7.1) is used otherwise.

7.1.1 Pressure and velocity singularities towards the contact line

Influence of the wall boundary condition In the works of Sprittles and Shikhmurzaev (2011) and Fricke et al. (2019) the Stokes flow in the corner between an impermeable free slip wall dragged over another impermeable wall is investigated. When slip is enforced on the lower wall according to Eq. (2.85) with

$$\beta = \beta_0 \tilde{x}^{\gamma-2}, \tag{7.3}$$

stream functions of the form

$$\Psi = \tilde{x}^\lambda F(\psi) \tag{7.4}$$

can be assumed. Here $\tilde{x}$ and ψ denote the radial and angular coordinates of a polar coordinate system, whose origin is placed on the contact line. From the stream function the leading order behavior of the pressure and velocities as the radial coordinate approaches zero, hence $\tilde{x} \to 0$, can be derived as

$$\boldsymbol{u} \propto \tilde{x}^{\gamma-1}, \tag{7.5a}$$

$$p \propto \int \tilde{x}^{\gamma-3}, \tag{7.5b}$$

by inserting Eq. (7.4) into the slip boundary condition written in polar coordinates

$$\frac{1}{\tilde{x}^2}\frac{\partial^2 \Psi}{\partial \psi^2} + \beta_0 \tilde{x}^{\gamma-2}\left(V_{wall} - \frac{1}{\tilde{x}}\frac{\partial \Psi}{\partial \psi}\right) \quad \text{for} \quad \tilde{x} > 0, \psi = 0. \tag{7.6}$$

This case is tested in the setup depicted in Fig. 7.1. A circular 2D droplet of radius $R = 10$ is placed on a flat surface, such that the contact angle is $\theta = \pi/4$. The boundary condition on the lower wall is varied according to Eq. (7.3), with $\gamma = [1, 2, 3]$. This covers the three cases, where β either becomes singular, constant or vanishes at the contact line, corresponding to no-slip, slip and free-slip at the contact line. Surface tension is switched off in Eq. (2.84), i.e. $1/We = 0$ and we set $1/Re = 1$. The domain is set to $\Omega = [-1.1R, 0] \times [1.1R, 2.2R]$ and meshed with 4×4 cells with 20 levels of mesh refinement at the contact points, giving a minimum cell size $h_{min} = 2.623 \times 10^{-6}$. The velocity of the lower wall is set to $\boldsymbol{s} = (-1, 0)^T$ and the approximation order for the velocity is set to $k = 5$. For each simulation, applying one of the three functions for the slip coefficient, the velocity and pressure are evaluated using

$$\tilde{f}(\tilde{x}) = |f(x_0 - \tilde{x}, 0) - f(0, 0)|\,, \tag{7.7a}$$

when rational (e.g. $1/\tilde{x}$) scaling is expected. When polynomial or logarithmic scalings are expected the value at the contact point is subtracted

$$\tilde{f}(\tilde{x}) = |f(x_0 - \tilde{x}, 0) - f(x_0, 0)|\,. \tag{7.7b}$$

The results for these augmented pressure and velocity profiles at the right contact point are displayed in Fig. 7.2. In the log-log or semi-logarithmic representations the behavior as expected from Eq. (7.5) is confirmed. The plots demonstrate the capability of the high-order XDG method to even reproduce the logarithmic or rational behavior as the contact line is approached. However, it is not possible to completely resolve the singularity itself using polynomial approximations.

Influence of the contact line boundary condition In the next step, the setup is maintained with two adjustments. Firstly, surface tension is included by setting $1/We = 1$ and the interface is not enforced to be impermeable, i.e., it can move now if a time-stepping scheme for the level set is employed. Secondly, the wall velocity is switched off with $\boldsymbol{s} = \boldsymbol{0}$ and instead the equilibrium contact angle is set to $\theta_{\text{stat}} = 0$, such that the contact line is not in equilibrium in the initial setup. The slip coefficient on the lower wall is varied again as before, Eq. (7.3) with $\gamma = [1, 2, 3]$. Additionally, Eq. (7.1) is employed with $\beta_L = 0, \alpha = 1$ and $\beta_L = 1, \alpha = 1$. Therefore, either a quasi-stationary contact angle, trying to always enforce the equilibrium angle, or a dynamic contact angle, using a linear relation between the contact line (slip) velocity and deviation in contact angle, is enforced.
The results for these calculations are displayed in Fig. 7.3. The first row shows the situation where the wall boundary condition behaves as no-slip at the contact line. This immediately poses a problem, as the contact angle boundary condition forces the contact line to move to regain the equilibrium angle, while the wall boundary condition inhibits this movement. From the plot this contradiction becomes visible as a singular behavior in both pressure $\tilde{p} \propto \tilde{x}^{-2}$ and velocity $\tilde{u}_x \propto \tilde{x}^{-1}$. There is no noticeable difference in whether the quasi-stationary or dynamic contact angle condition is applied. The results in the second and third row do not contain the contradiction between the two boundary conditions. However, still they display singular behavior in both fields as $\tilde{p} \propto \tilde{x}^{-1}$ and $\tilde{u}_x \propto \ln(\tilde{x})$. To explain how this behavior arises it is helpful to consider the Stokeslet problem. This describes the introduction of a (bounded) point force in the Stokes equation, which is similar to the effect of the contact angle boundary condition, which introduces a line force. For a 3D point force introduced in the Stokes equation, i.e.

$$\nabla \cdot (\boldsymbol{u}) = 0, \tag{7.8a}$$

$$-\nabla p + \mu \Delta \boldsymbol{u} = \boldsymbol{F}\delta(\tilde{\boldsymbol{x}}), \tag{7.8b}$$

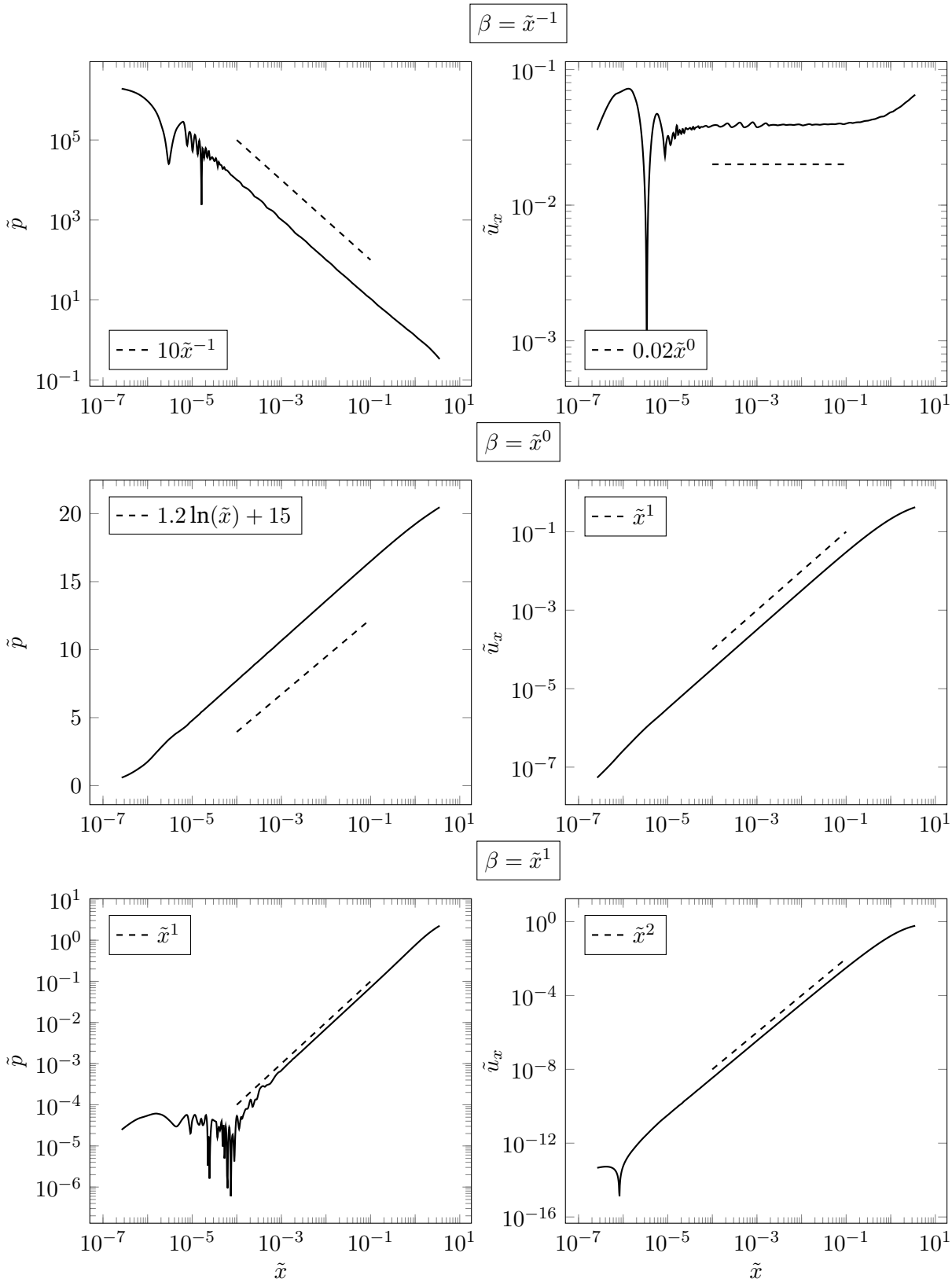

Figure 7.2: Pressure and velocity as the right contact point is approached for the flow in the wedge between two walls, using different wall slip functions for the lower moving wall, see Fig. 7.1

the Green solutions for the velocity and pressure are

$$\boldsymbol{u}_{3D} = \frac{\boldsymbol{F} \cdot \left(\mathbf{I}|\tilde{\boldsymbol{x}}|^2 + \tilde{\boldsymbol{x}} \otimes \tilde{\boldsymbol{x}}\right)}{8\pi\mu|\tilde{\boldsymbol{x}}|^3}, \tag{7.9a}$$

$$p_{3D} = \frac{\boldsymbol{F} \cdot \tilde{\boldsymbol{x}}}{4\pi|\tilde{\boldsymbol{x}}|^3}. \tag{7.9b}$$

By integration along the contact line the effect of a line force or 2D point force can be obtained:

$$\boldsymbol{u}_{2D} \propto \int \boldsymbol{u}_{3D} dz \approx \ln(\tilde{\boldsymbol{x}}), \tag{7.10a}$$

$$p_{2D} \propto \int p_{3D} dz \approx |\tilde{\boldsymbol{x}}|^{-1}. \tag{7.10b}$$

Another explanation is offered in the work by Fullana et al. (2023). There boundary conditions for the contact line and the slip wall are combined to obtain a single boundary condition:

$$\begin{aligned} &\sigma\left(\cos(\theta) - \cos(\theta_{\text{stat}})\right)\delta(\tilde{\boldsymbol{x}}) + \left(\mathbf{P}^{\partial\Omega}\left(\mu\left(\nabla\boldsymbol{u} + (\nabla\boldsymbol{u})^T\right)\boldsymbol{n}^{\partial\Omega}\right)\right) \cdot \hat{\boldsymbol{n}}^L \\ &\quad = -\underbrace{\left(\beta + \beta_L\right)}_{\beta}\left(\mathbf{P}^{\partial\Omega}\left(\boldsymbol{u} - \boldsymbol{s}\right)\right) \cdot \hat{\boldsymbol{n}}^L. \end{aligned} \tag{7.11}$$

Under the assumption that the friction parameter is just a constant and the velocity slip is smooth and bounded everywhere, the RHS of the above equation is a regular function. This means the LHS has to be a regular function as well. However, looking at the two LHS terms it is clear, that the contact line force is actually a distribution, located at the contact line, and not a regular function. Therefore, the shear stress must also possess a distributive character, to balance the contact line force. In their work, Fullana et al. (2023) suggest to relax the contact line force to a volumetric force, smeared out over a finite region around the contact line. This effectively regularizes the problem and the shear stress stays bounded at the contact line. However, this comes at the cost of loosing the sharpness of the original sharp interface model.

Regularization using a singular viscosity From the previous analysis we deduct that there are two main courses of action one may take. Either the distribution character of the contact line force is relaxed, by smearing the force over a finite region, as suggested by Fullana et al. (2023). Or the stresses must also possess distribution character at the contact line. At this point we follow the latter approach, while trying to obtain bounded velocity gradients. To achieve this goal the distribution, originally found in the velocity gradients, is shifted over to the viscosity. Two cases are investigated in which the viscosity is modeled to become infinite at the contact line, according to $1/Re = [\tilde{x}^{-1}, \tilde{x}^{-2}]$[1]. From the study of the Stokeslet we then expect the velocity to behave as $\boldsymbol{u} \propto [\tilde{x}, \tilde{x}^2]$ towards the contact point, which would also mean the velocity gradients stay bounded. Indeed, Fig. 7.4 shows exactly this behavior for the velocity in wall parallel direction. It is not shown here explicitly, but the pressure behavior is untouched by this adaption, except for the case $\beta = \tilde{x}^{-1}$, where now also $p \propto \tilde{x}^{-1}$. By introducing a viscosity that becomes singular at the contact line we are thus able to obtain a solution with bounded behavior of the velocity gradients as the contact line is approached.

[1] At this point this is merely a modeling experiment, missing a rigorous physical motivation for such a viscosity behavior.

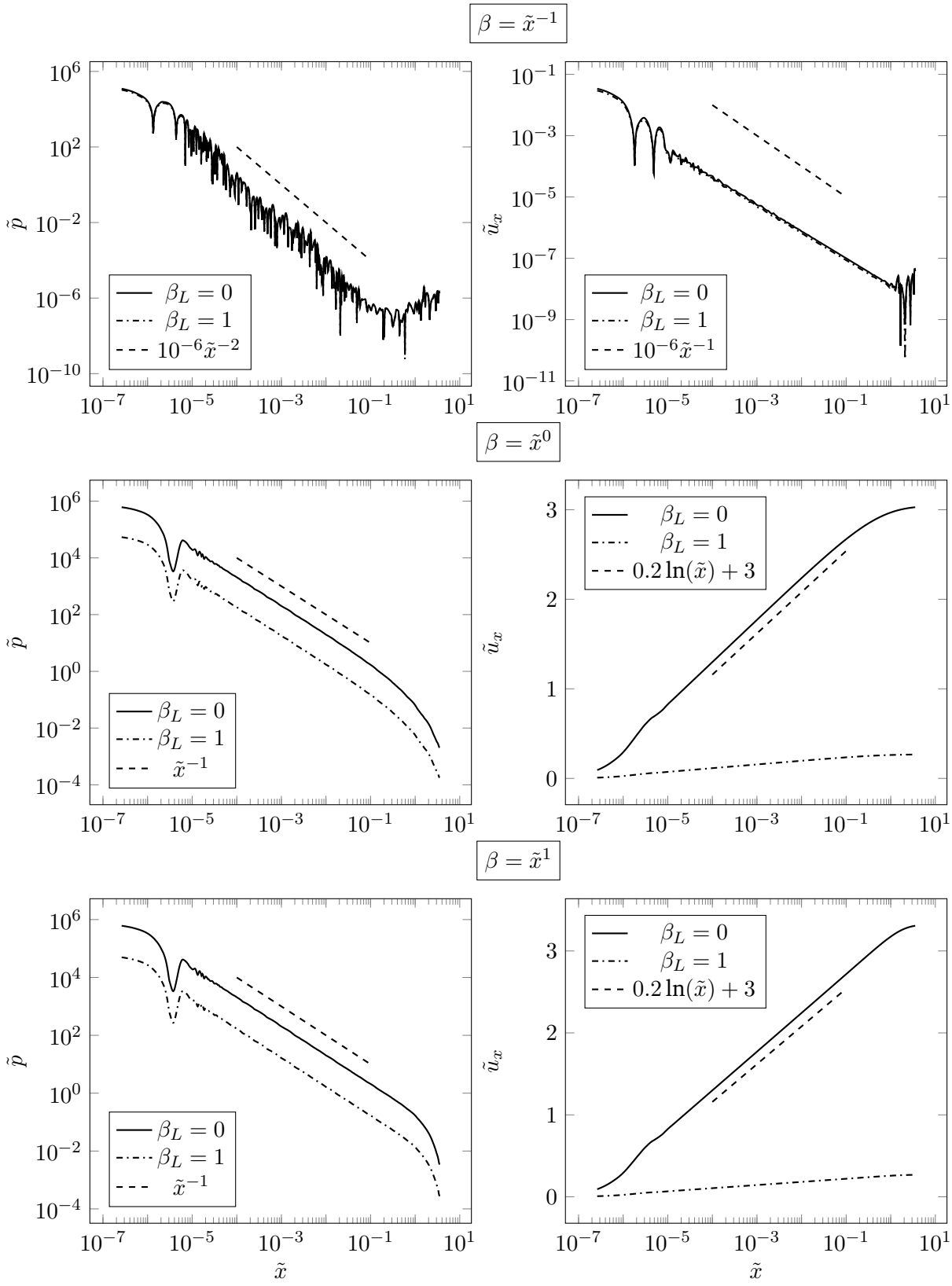

Figure 7.3: Pressure and velocity as the right contact point is approached for the flow in the wedge between a wall and free surface, using different wall and contact line slip functions. The flow is induced by the condition for the dynamic contact angle, as it is moved out-of-equilibrium.

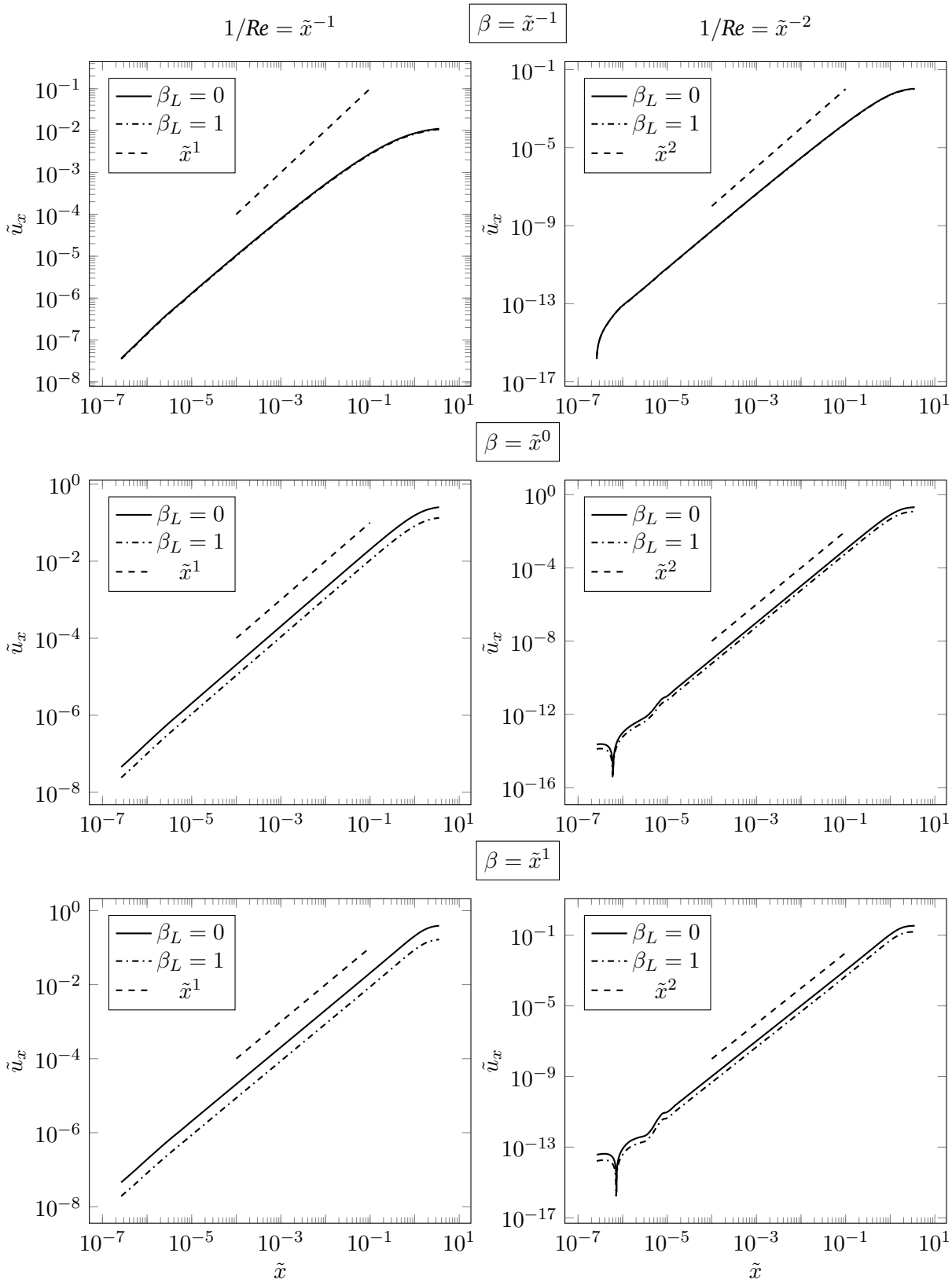

Figure 7.4: Velocity as the right contact point is approached for the flow in the wedge between a wall and free surface, using different wall and contact line slip functions. On the left and right results for different singular expressions for the viscosity as $\tilde{x} \to 0$ are compared.

7.1.2 Modeling of complex contact line behavior

In the previous subsection the qualitative influence of various types of models, for the boundary conditions, contact line conditions and viscous bulk modeling, on the pressure and velocity behavior towards the contact line are investigated. In this subsection we want to focus on the application of the direct introduction of a contact line force to enforce a condition of type Eqs. (7.1) and (7.2).

Dynamic contact angles in dependence of the velocity First, the capability of the method to adequately model relations between contact angle and contact line velocity, Eq. (7.1), is demonstrated by computing a two-phase Couette flow, cf. (Smuda and Kummer, 2021). In the domain of size $\Omega = [-5, 5] \times [-1, 1]$ a liquid slug is placed with the level set[2]

$$\varphi(x, y) = (x - 1.1)(x + 1.1). \tag{7.12}$$

The domain is meshed with a grid of size 15×3 and 2 levels of AMR are performed at the interface, the approximation degree is $k = 4$. The material parameters are set to $\theta_{\text{stat}} = \pi/2$, $We = Re = 1$. The upper and lower wall are dragged in opposing direction according to the velocity

$$u_y(x, y) = y. \tag{7.13}$$

Different combinations of wall boundary and contact line conditions are tried out. The wall the friction parameter is varied as $\beta = [0.0, 1.0, \infty]$ and at the contact line friction parameter as $\beta_L = [0.0, 0.5]$. Additionally, for the dynamic contact angle ($\beta_L = 0.5$) the exponent for the velocity-to-angle relation is varied as $\alpha = [0.5, 1.0, 2.0]$. The value of $\beta_L = 0.5$ is chosen deliberately, such that a dynamic equilibrium state with $\theta = \pi/2 \pm \pi/6$ at the advancing/receding contact line is approached. The simulation is then run until a time $t_{end} = 3$, with $\Delta t = 0.01$.
In Fig. 7.5 the interface position is displayed at $t = 0, 1, 2$ and 3 for the simulations with a linear dynamic contact angle, under variation of the wall boundary condition. The influence of the imposed boundary condition is immediately visible. For no-slip, $\beta = \infty$ the fluid sticks to the wall and moves with it. When a slip condition is assumed, $\beta = 1$, there is some slip involved and the contact points move relative to the wall. Finally, for freeslip, $\beta = 0$, force transmission between fluid and wall takes place only at the contact points, which results in even more slip and less overall movement of the interface.
Figure 7.6 shows the x-position, x-velocity and dynamic contact angle for the two contact points at the upper wall. The colors denote different contact anlge conditions and the marker types different conditions for the slip walls. There are two limiting cases. If the slip wall is set to no-slip, the contact line is moving with the wall, no matter what contact angle condition is chosen. In that sense, the no-slip condition overwrites the condition set at the contact line. The other limit is when no force is transmitted between wall and fluid, i.e., a freeslip wall together with the quasi-stationary contact angle condition is chosen. Then, as expected, nothing happens as no force is acting from the wall on the fluid. All other test cases display behavior between these two limits, evolving towards a dynamic equilibrium, where the amount of slip, the dynamic contact angle and the stresses are in balance.

[2] For this test case a variation of the level set algorithm is used, where each interface is described by a cubic spline with 30 equally spaced interpolation points. During the simulation the x-coordinate of these interpolation points is updated according to the point-wise interface velocity.

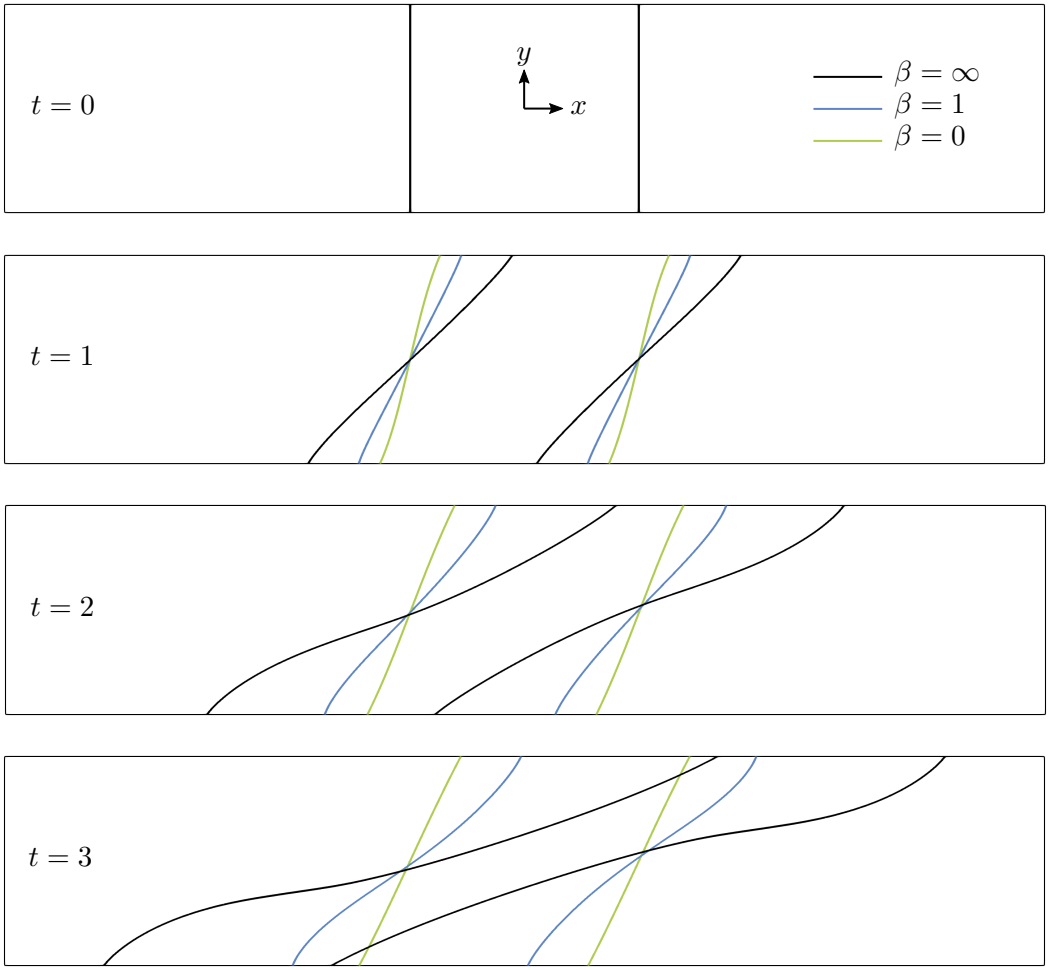

Figure 7.5: Interface positions for the two-phase Couette flow at different times and for differing slip boundary conditions. For the contact angle condition (7.1) $\beta_L = 0.5, \alpha = 1.0$ is chosen. The initially vertical liquid plug in the channel is sheared differently, depending on the wall slip in the specific simulation.

Finally, Fig. 7.7 plots the relation between contact line velocity and measured deviation in contact angle. As a reference the desired behavior is plotted as a thin solid line in the respective color. For a freeslip wall the dynamic contact angle approaches the prescribed behavior after a startup period. This is visible from the data points marked with circles. However, when $\beta \neq 0$, this relation is skewed towards the results obtained for a no-slip wall. When setting no slip the contact angle condition is completely overwritten and the behavior of the contact line is dominated by the bulk boundary condition. So as expected at least some slip has to be allowed for the contact line to be able to move relative to the wall. Additionally, there seems to be an intricate feedback between the wall and contact line boundary conditions, which makes it hard to predict the exact behavior of the contact line a-priori.

Contact angle hysteresis

In the last paragraph the capability of the method to handle different models for the dynamic contact angle is demonstrated. Another contact line behavior observed in experiments is contact angle hysteresis. In practice this is a result of the imperfection, e.g. surface roughness or chemical inhomogeneity, of technical surfaces (Wang et al., 2020; Marengo and Coninck, 2022). It describes the situation, where a contact line can pin until a certain threshold value for the contact angle is achieved. Only then the contact line starts to move. Additionally, this hysteresis may depend on the direction of movement of the contact line, described by the advancing and receding contact angle. To model this behavior without explicit meshing, e.g. surface roughness, the implementation shown in Eq. (A.14) is extended on the slip boundaries Γ_R to

$$\begin{cases} \oint_{\Sigma\cap(\Gamma_\mathrm{R})} \left(\sigma \boldsymbol{t}^\Sigma - \eta_4 \left(\left(\boldsymbol{u}^\Sigma - \boldsymbol{s}\right)\cdot\hat{\boldsymbol{n}}^L\right)\hat{\boldsymbol{n}}^L\right)\cdot\boldsymbol{v}\ \mathrm{d}l & \text{if} \quad \theta_\mathrm{rec} < \theta < \theta_\mathrm{adv} \\ \oint_{\Sigma\cap(\Gamma_\mathrm{R})} \left(\sigma\left(\boldsymbol{n}^{\partial\Omega}\cdot\boldsymbol{t}^\Sigma\right)\boldsymbol{n}^{\partial\Omega} + \sigma\cos(\theta_\mathrm{stat})\hat{\boldsymbol{n}}^L\right)\cdot\boldsymbol{v} & \\ \qquad -\left(\mathrm{sgn}((\boldsymbol{u}^\Sigma - \boldsymbol{s})\cdot\hat{\boldsymbol{n}}^L)\beta_L\left|(\boldsymbol{u}^\Sigma - \boldsymbol{s})\cdot\hat{\boldsymbol{n}}^L\right|^\alpha\right)\cdot\boldsymbol{v}\ \mathrm{d}l & \text{else} \end{cases}, \tag{7.14}$$

imposing a no-slip condition through a penalty when the contact angle is between the receding or advancing contact angle. The value for the penalty is chosen arbitrarily[3] to $\eta_4 = 100$. If the dynamic contact angle is outside these hysteresis limits, the condition for the dynamic contact angle (Eq. (7.1)) is employed.
To test whether this enables the numerical method to simulate this behavior, a droplet is placed on a plane vertical surface under the influence of gravity. We choose the values for the advancing and receding contact angle such that a static equilibrium is reached eventually. In this equilibrium state the forces at the contact line and the gravitational force are in balance. For an initially semi-circular 2D droplet of radius R, see Fig. 7.8, this equates to

$$\frac{V}{Fr} + \frac{1}{We}\left(\cos(\theta_{adv}) - \cos(\theta_{rec})\right) = 0, \tag{7.15a}$$

$$\left(\cos(\theta_{adv}) - \cos(\theta_{rec})\right) = -\frac{\pi R^2 We}{2Fr}. \tag{7.15b}$$

Two series of simulations are performed, with the equilibrium angle set to $\theta_\mathrm{stat} = \pi/2 = 90°$. One time the advancing contact angle is set to $\theta_{adv} = \theta_\mathrm{stat} + 15°$ and the receding contact angle is set to $\theta_{rec} = 0$. In this situation the receding contact line always pins, while the advancing contact line

[3] Further investigations are necessary to determine how this value should be chosen.

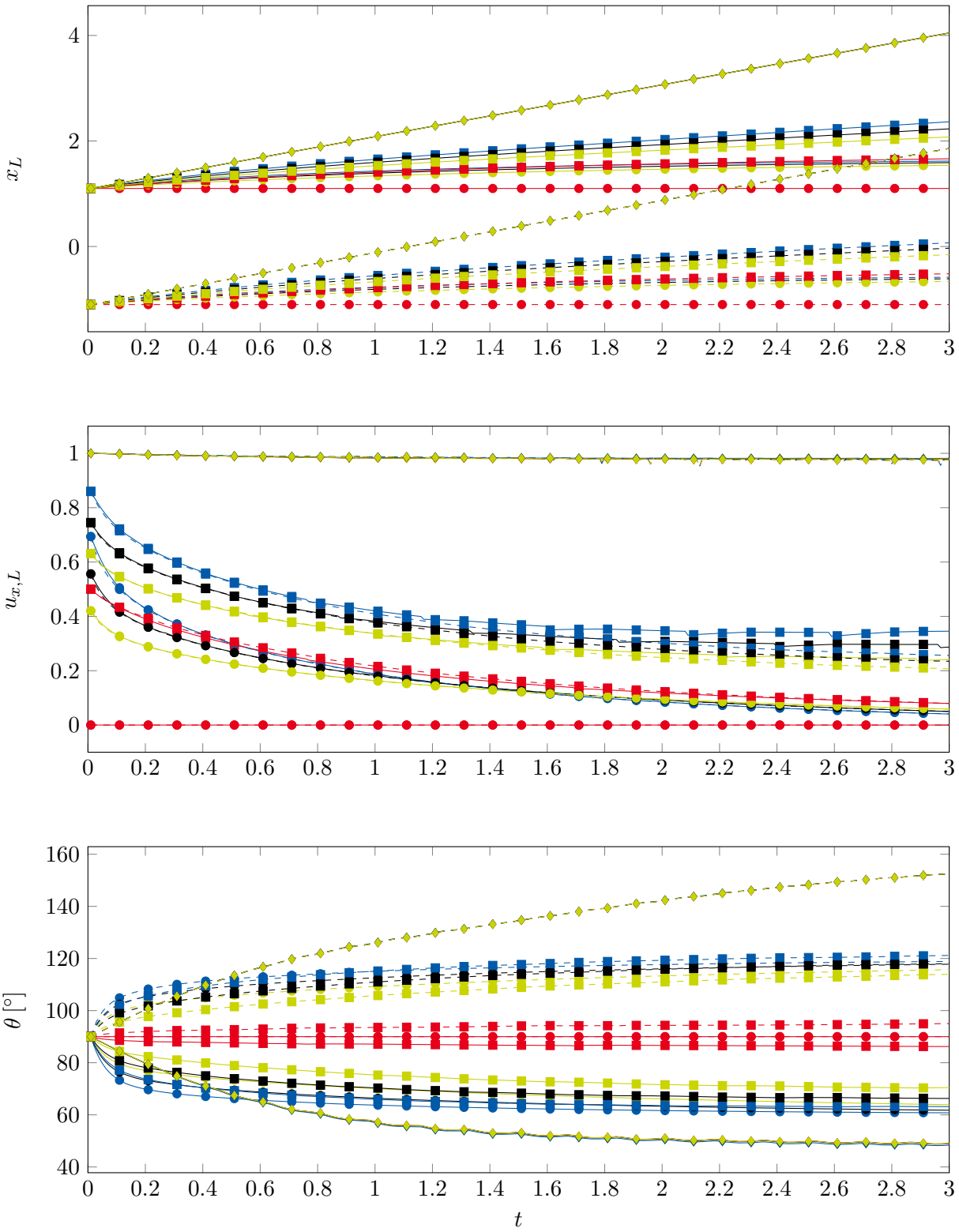

Figure 7.6: Temporal evolution of the position, velocity and angle of the contact points on the upper wall. The colors decode the contact angle condition, $\beta_L = 0$, $\alpha = 1$, $\beta_L = 0.5$, $\alpha = 0.5$, $\beta_L = 0.5$, $\alpha = 1$ and $\beta_L = 0.5$, $\alpha = 2$. The symbols distinguish the boundary conditions • $\beta = 0$, ■ $\beta = 1$ and ♦ $\beta = \infty$. Solid lines mark the right and dashed lines the left contact point.

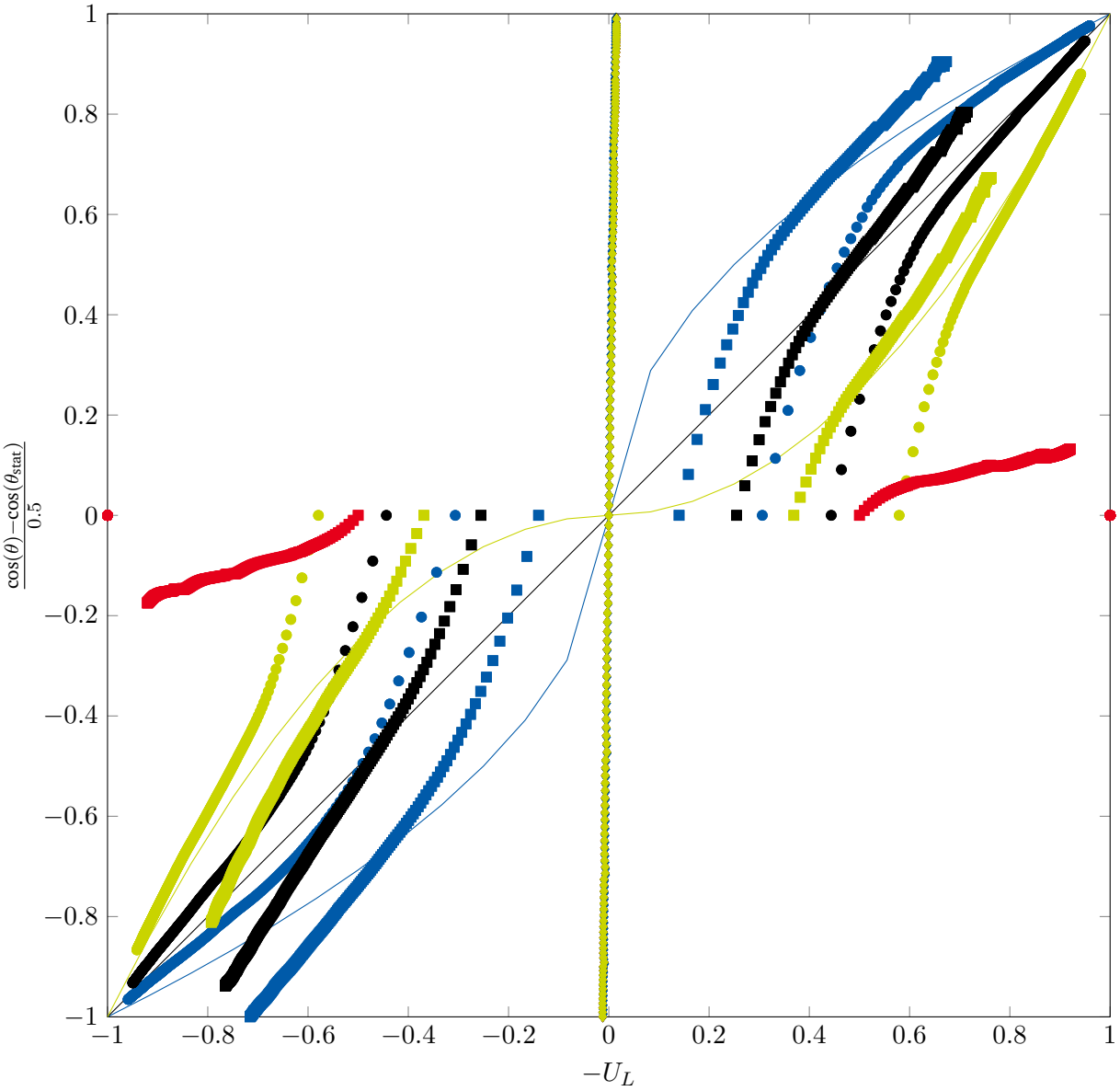

Figure 7.7: Relation between contact angle and contact line velocity. The colors decode the contact angle condition, $\beta_L = 0$, $\alpha = 1$, $\beta_L = 0.5$, $\alpha = 0.5$, $\beta_L = 0.5$, $\alpha = 1$ and $\beta_L = 0.5$, $\alpha = 2$. The symbols distinguish the boundary conditions • $\beta = 0$, ■ $\beta = 1$ and ♦ $\beta = \infty$. For reference the functions $\text{sgn}(x)\sqrt{|x|}$, x and $\text{sgn}(x)x^2$ are plotted as well

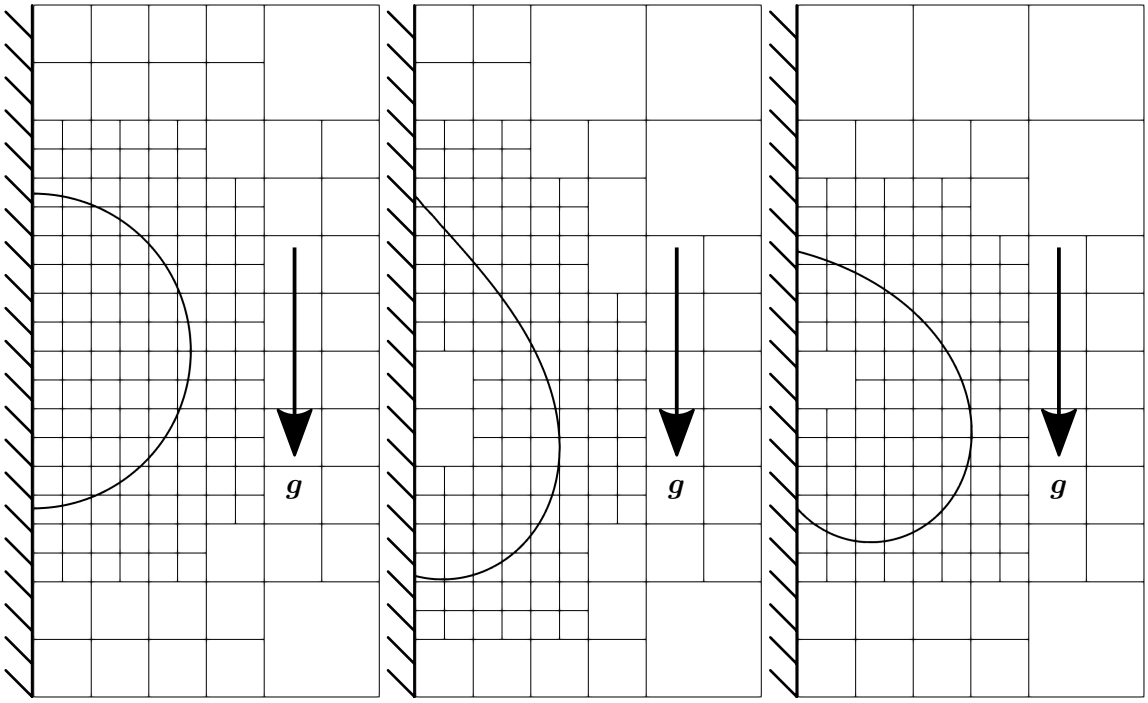

Figure 7.8: From left to right, initial state, and final states at $t = 3$ using a pinned receding and advancing contact line are shown.

pins until θ_{adv} is reached. Then it moves until the contact angle falls below this limit value again and the contact line pins again. With $R = 1$, $We = Re = 1$ and $Fr = \pi/2R^2$ we should observe a receding contact angle of $\theta_{rec} \approx 42.17°$, when the equilibrium state according to Eq. (7.15) is reached. For the second setup the situation is reversed. The receding contact angle is set to $\theta_{rec} = \theta_{\text{stat}} - 15°$, and the advancing to $\theta_{adv} = \pi$. Now, the advancing contact line always pins and the receding one exhibits a stick-slip kind of motion. The equilibrium value for the advancing contact angle is then $\theta_{adv} \approx 137.83°$. The same variation of boundary and contact line conditions as in the last section is employed, however here we display and discuss only the simulations using $\beta = 0$. The Froude number is chosen such that if one of the contact points does not carry any weight, i.e. $\theta = \pi/2$, the other one is still able to support the complete weight of the droplet, i.e. with $\theta = 0$ or π, which means $Fr = \pi/2\, R^2\, We$. The droplet is initialized with the level set

$$\varphi(x, y) = x^2 + y^2 - R^2, \tag{7.16}$$

on the domain $\Omega = [0, 2.2R] \times [-2.2R, 2.2R]$. The degree for the velocity is chosen to $k = 4$, the base grid has 3×6 cells and 2 levels of AMR are performed at the interface. The simulations run until $t_{end} = 3$, using a fixed time-step of $\Delta t = 0.01$. The initial state and final states for both test cases are displayed in Fig. 7.8.
In Fig. 7.9 the deviation from initial position, contact line velocity and contact angle for the receding and advancing contact point and both test cases are displayed. The first observation, which is especially noticeable when $\beta_L = 0$, is the stick-slip behavior of the moving contact point. The pinned contact point remains stationary, moving only slightly, which is probably a result of numerical diffusion or similar effects. When a dynamic contact angle model is employed the contact line velocity does not achieve as high values as in the quasi-stationary case, resulting in a less pronounced stick-slip behavior, with a higher frequency of slip events. The contact line

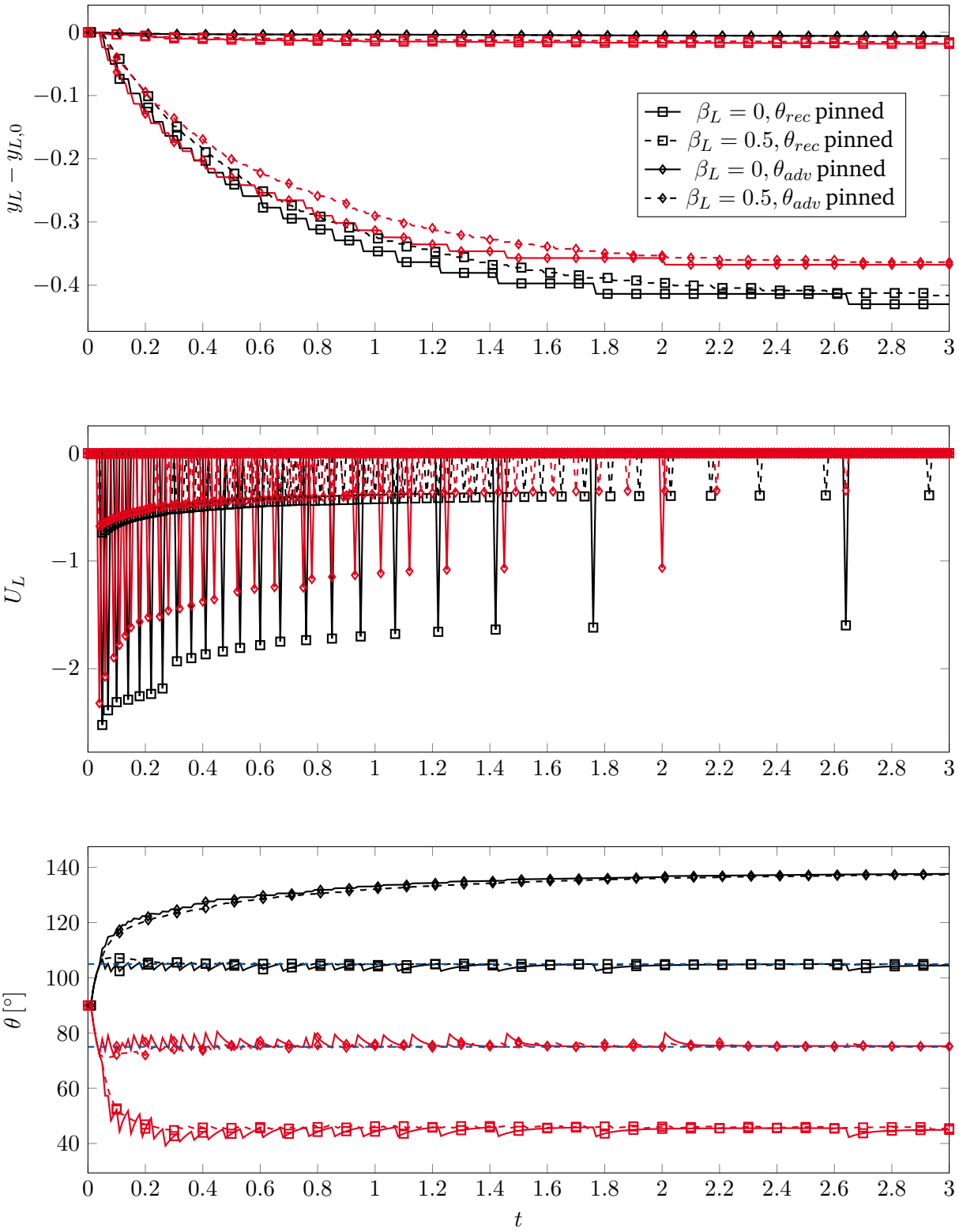

Figure 7.9: Contact point position, velocity and contact angle. Black denotes the advancing contact point, red the receding one. The hysteresis values for the two test cases are plotted as blue dashed lines for reference.

position and contact angle approached asymptotically are not impacted by the choice of contact angle condition. Additionally, the hysteresis values for the two test-cases are displayed in Fig. 7.9. It is visible, that as soon as the hysteresis value is reached, a slip event occurs, allowing the contact line to slip towards the equilibrium contact angle. Thus, the contact angle in the next time-step lies again in the range where the contact line pins. The contact line is then pinned until the hysteresis value is reached again.

7.2 Resolution of model contradicitions in contact line evaporation through interfacial slip

Scope of the following section is the investigation of a contradiction in the boundary and interfacial conditions at the three phase contact line when employing the model presented in Section 2.6.2. Firstly, the origin of this contradiction is discussed, followed by a numerical investigation of its influence on simulation results. Secondly, a model adaption, namely introduction of slip on the fluid-fluid interfaces, to alleviate this contradiction is introduced and the simulations are repeated to measure the effectiveness of this adaption.
The hypothesis is that in the optimal case, when using the XDG method presented in Chapter 4, a convergence order of h^{k+1} can be achieved, where h is a measure of the grid width and k the polynomial degree used to approximate the solution (Arnold et al., 2002; Di Pietro and Ern, 2012; Dolejší and Feistauer, 2015). However, having singularities in the solution or its derivatives prevents the method to achieve optimal performance. Therefore, this high-order method is sensitive to the presence of singularities and makes it possible to examine models for their regularity.
To investigate the influence the aforementioned contradiction and the proposed solution have on the numerical solution, we follow the approach chosen in the work of Smuda and Kummer (2021) for similar considerations in context of the generalized Navier boundary condition (Gerbeau and Lelièvre, 2009). Essentially, the idea is to compare the convergence order for a problem with singularities to a reference case without singularities, for example by disregarding evaporation. Afterwards, the solution approach is introduced and it is investigated whether the original order of convergence can be regained.

7.2.1 Evaporation Model

Starting point for the present investigation is the two-phase model and corresponding discretization for the incompressible Navier-Stokes and heat equations, including evaporation, presented in the work by Rieckmann et al. (2023e). In addition, this work introduces the handling of the contact line described in Smuda and Kummer (2021) into the evaporation model. The problem statement and its discretization are also discussed in Section 2.6.2 and Chapter 4.

Model contradiction at the contact line It was noted by Fricke et al. (2019) that this simple evaporation model possesses a contradiction at the contact line. This can be made visible by decomposition of the velocity jump in wall normal direction at the contact line. Due to the impermeability condition (Eq. (2.78), $\beta_N = 0$) it vanishes at the contact line. Simultaneously, the velocity can be expressed in terms of components normal to the surface, normal to the contact line

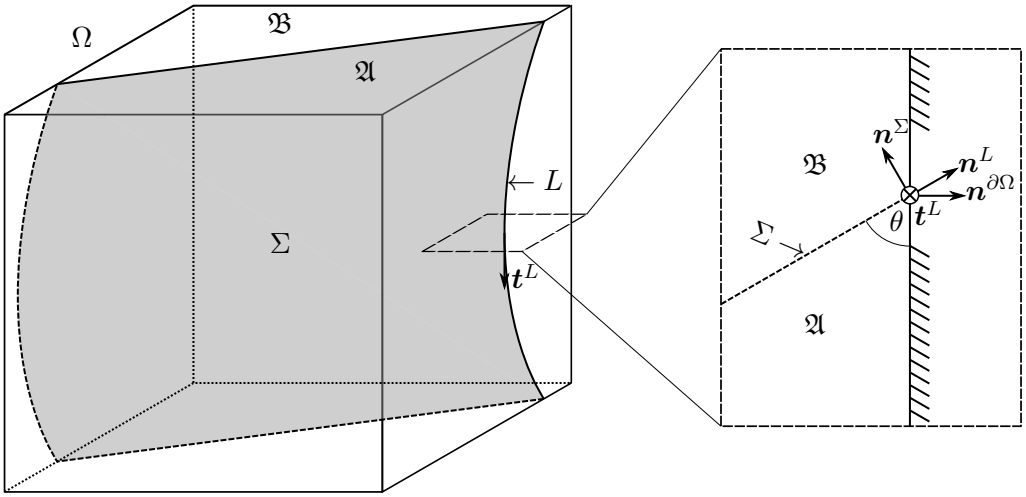

Figure 7.10: A fluid-fluid interface Σ, dividing the domain Ω into two phases $\mathfrak{A}$ and $\mathfrak{B}$, intersects a solid wall, the boundary $\partial\Omega$ of the displayed box. On the left the contact line tangent $\boldsymbol{t}^L$ and its corresponding sectional plane are displayed at one of the contact lines. On the right this section is enlarged and the normal vectors for interface $\boldsymbol{n}^\Sigma$, contact line $\boldsymbol{n}^L$ and wall $\boldsymbol{n}^{\partial\Omega}$ are depicted. For the tangent $\boldsymbol{t}^L = \boldsymbol{n}^\Sigma \times \boldsymbol{n}^L$ applies. The interface forms the angle θ with the solid wall at the contact line in the sectional plane.

(and tangential to the interface) and tangential to the contact line, given the respective projections $\mathbf{P}^\Sigma = \boldsymbol{n}^\Sigma \otimes \boldsymbol{n}^\Sigma$, $\mathbf{P}^L = \boldsymbol{n}^L \otimes \boldsymbol{n}^L$ and $\mathbf{P}^{\boldsymbol{t}} = \boldsymbol{t}^L \otimes \boldsymbol{t}^L$ (Fig. 7.10):

$$[\![\boldsymbol{u}]\!] \cdot \boldsymbol{n}^{\partial\Omega} = \left(\mathbf{P}^\Sigma [\![\boldsymbol{u}]\!] + \mathbf{P}^L [\![\boldsymbol{u}]\!] + \mathbf{P}^{\boldsymbol{t}} [\![\boldsymbol{u}]\!]\right) \cdot \boldsymbol{n}^{\partial\Omega} = 0. \tag{7.17}$$

As $\boldsymbol{t}^L \cdot \boldsymbol{n}^{\partial\Omega} = 0$ the last term vanishes. By inserting the contact angle θ, i.e., employing $\boldsymbol{n}^\Sigma \cdot \boldsymbol{n}^{\partial\Omega} = -\cos(\theta)$ and $\boldsymbol{n}^L \cdot \boldsymbol{n}^{\partial\Omega} = \sin(\theta)$, the wall normal velocity jump equals

$$-\cos(\theta) [\![\boldsymbol{u}]\!] \cdot \boldsymbol{n}^\Sigma + \sin(\theta) [\![\boldsymbol{u}]\!] \cdot \boldsymbol{n}^L = 0, \tag{7.18}$$

or

$$-\cos(\theta)\dot{m} \left[\!\left[\frac{1}{\rho}\right]\!\right] + \sin(\theta) [\![\boldsymbol{u}]\!] \cdot \boldsymbol{n}^L = 0, \tag{7.19}$$

by inserting Eq. (2.75) for the interface normal velocity jump. When assuming no-slip on the interface, this condition is only fulfilled in three special cases, when $[\![\rho]\!] = 0$, $\theta = \pi/2$ or $\dot{m} = 0$. In general, the two phases have different densities, the (dynamic) contact angle can assume arbitrary values and through the employed model (Eq. (2.75)) the (evaporative) massflux does not necessarily vanish at the contact line. Thus, we arrive at the conclusion that the evaporation model in the present formulation contains a contradiction at the contact line.
One possible remedy is to allow interfacial slip, such that an equilibrium between the surface normal and contact line normal velocity jump in Eq. (7.18) can develop. In the subsequent sections we will investigate the effect of this contradiction in the model on the numerical results and explore the impact of an interfacial slip as a possible remedy.

Table 7.1: Material properties for the numerical experiment

	Density ρ [kg/m^3]	Heat capacity $\hat{c}_p$ [J/(kg K)]	Thermal conductivity $\hat{k}$ [W/(m K)]	Dyn. viscosity μ [Pa s]
$\mathfrak{A}$	1.0	1.0	1.0	0.5
$\mathfrak{B}$	0.1	1.0	0.1	0.05

Latent heat $\hat{h}_{vap}$ [J/kg] $= [10^3, \infty]$[4], Surface tension σ [N/m] $= [0.0, 0.1]$,
Saturation temperature T_{sat} [K] $= 0.0$[5], Static contact angle $\theta_{\text{stat}} = [80°, 90°]$

Adapted model, introducing interfacial slip For the adapted model an interfacial slip is introduced in analogy to the Navier-slip boundary condition, i.e., on the interface the condition for the tangential jump in velocity is replaced by

$$-\beta_\Sigma \mathbf{P}^\Sigma [\![\boldsymbol{u}]\!] = \mathbf{P}^\Sigma \left(\{\{ \mu \left(\nabla \boldsymbol{u} + \nabla \boldsymbol{u}^T \right) \}\} \boldsymbol{n}^\Sigma \right). \tag{7.20}$$

To arrive at this result, we start from assuming a slip from either side of the interface:

$$-\mathbf{P}^\Sigma \left(\boldsymbol{u}_{\mathfrak{A}/\mathfrak{B}} - \boldsymbol{u}^\Sigma \right) = \alpha_{\mathfrak{A}/\mathfrak{B}} \mathbf{P}^\Sigma \left(\mathbf{S}_{\mathfrak{A}/\mathfrak{B}} \cdot \boldsymbol{n}_{\mathfrak{A}/\mathfrak{B}} \right) \quad , \ \alpha_{\mathfrak{A}/\mathfrak{B}} \geq 0. \tag{7.21}$$

In the present model the irreversible part of the stress tensor is $\mathbf{S} = \mu \left(\nabla \boldsymbol{u} + \nabla \boldsymbol{u}^T \right)$. Choosing $\alpha = 0$ would result in the usual no-slip interface. Applying Eq. (7.21) from both phases to eliminate the interface velocity we recover

$$-\mathbf{P}^\Sigma [\![\boldsymbol{u}]\!] = \mathbf{P}^\Sigma \left(\alpha_{\mathfrak{A}} \mathbf{S}_{\mathfrak{A}} \cdot \boldsymbol{n}^\Sigma + \alpha_{\mathfrak{B}} \mathbf{S}_{\mathfrak{B}} \cdot \boldsymbol{n}^\Sigma \right). \tag{7.22}$$

Equation (7.20) is then obtained by choosing the same slip coefficients from both sides ($\alpha_{\mathfrak{A}/\mathfrak{B}} = \alpha$) and introducing a new unified friction coefficient $\beta_\Sigma = 1/(2\alpha)$. For the numerical method we define $\alpha = L_\Sigma / (\mu_{\mathfrak{A}} + \mu_{\mathfrak{B}})$, introducing the interfacial slip length L_Σ as the sole parameter to tune the interfacial slip condition. The introduction of such a slip condition necessitates an adaption in the discretization of the interfacial terms. The required adaption is discussed in Appendix A.2. Therein, a few test cases are collected, which verify the slip implementation.

7.2.2 Numerical-experimental setup

In Smuda and Kummer (2021) a quasi-stationary solution for an out-of equilibrium ellipsoidal droplet was calculated. The authors continued to vary the friction parameters β, β_L and the equilibrium contact-angle θ_{stat} and assessed the experimental order of convergence (EOC) in velocity and pressure for each of these cases. In the present work we will follow the same approach to investigate the influence of the contradiction in the unmodified model. We will then introduce the interfacial slip and repeat the analysis for the adapted model. To simplify the analysis all calculations are quasi-steady state and linear, by omitting the temporal derivatives and non-linear terms (convective terms and recoil pressure) in Eq. (2.74) and Eq. (2.75). For all of the investigated cases the domain is a box of size $\Omega := [-1.5, 1.5]$ m $\times$ $[0, 1.5]$ m. On all boundaries we prescribe

[4] A formally infinite latent heat disables evaporation. On the solver side the corresponding term ($\dot{m}\hat{h}_{vap}$ in Eq. (2.75)) is excluded from the calculation if this value is detected.

[5] The temperature range is shifted for numerical reasons, the occurrence of absolute zero at this point has no physical significance.

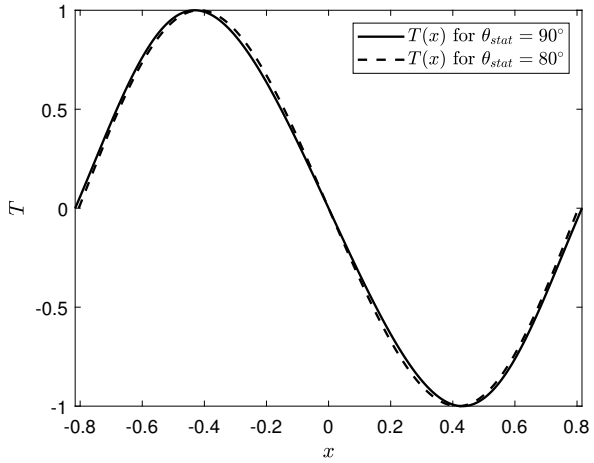

Figure 7.11: Prescribed temperature $T_{\partial\Omega}$ along the lower wall in $\mathfrak{A}$, for both investigated values of θ_{stat}. The functions resemble sin functions but not exactly.

freeslip ($\beta = 0, \beta_N = \infty$) and the wall temperature ($\beta_T = \infty$). The material properties for the setup are shown in Table 7.1. The interface is prescribed as an slightly out of equilibrium ellipsoidal droplet, to induce a capillary flow, with geometric contact angle $\theta = \theta_{\text{stat}}$:

$$\Sigma := \{\boldsymbol{x} \in \Omega \mid x^2/a^2 + (y - y_0)^2/b^2 - 1 = 0\}. \tag{7.23}$$

The shape parameters are set to $a = 0.816\,\text{m}$ and $b = 0.784\,\text{m}$. The center offset y_0 of the ellipsoid is chosen such that the geometric contact angle matches the static contact angle $y_0 = -b/\sqrt{1 + a^2/b^2 \tan(\theta)^2}$ the intersection points of the interface with the lower wall $\pm x_0 = \pm a \cos(\arcsin(y_0/b))$ are used to set the temperature boundary condition, see Fig. 7.11. It may seem simple to prescribe some boundary condition for the temperature. However, it proved to be quite challenging to choose a boundary condition such that the heat flux at the contact line is non-vanishing and the solution is sufficiently smooth to measure an close to optimal EOC. The profiles in Fig. 7.11 are based on an exact solution for the (temperature) Poisson equation (Polyanin, 2015, p. 788) in compliance with constant temperature T_{sat} along the interface of a circular droplet in the positive half plane.

In the first stage the analysis will still be restricted to material interfaces. The mass flux is excluded from the discrete system ($\hat{h}_{vap} \to \infty$) and no coupling between Navier-Stokes and heat equation takes place. We then vary the interfacial condition from no slip to free-slip $L_\Sigma = [0, 0.1, \infty]$ m and the prescribed contact angles $\theta_{\text{stat}} = [80°, 90°]$. This allows us to observe the EOC for pressure, velocity and temperature in absence of the contradiction occurring for non-zero mass fluxes. This analysis serves as the reference for the subsequent investigations.

In the second stage the influence of the contradiction in the evaporation model will be assessed. The enthalpy of evaporation is set to a finite value ($\hat{h}_{vap} = 10^3$ J/kg) and therefore a coupling between temperature and velocity is included. Due to evaporation a flow is induced, originating from the interface. By again varying the interfacial condition from no slip to free-slip $L_\Sigma = [0, 0.1, \infty]$ m and the prescribed contact angles $\theta_{\text{stat}} = [80°, 90°]$, we are able to observe the effects of evaporation and the contradiction on the EOC.

In the third stage the surface tension will be set to zero $\sigma = 0$ N/m, eliminating the influence of the capillary background flow. We then repeat the investigation carried out in the second stage. This allows us to purely focus on the flow resulting from evaporation.

Definition 7.1 (Case identification). *The cases will be labeled, explicitly containing the information about each of the free parameters, i.e.,*

$$\left[L_{\Sigma,[0,0.1,\infty]}, h_{v,[10^3,\infty]}, \sigma_{[0,0.1]}, \theta_{[80°,90°]}\right] . \tag{7.24}$$

Numerical procedure In the following paragraphs the results for the 3-staged investigation described in Section 7.2.2 are presented. We proceed exactly in the order of stages described and characterize the test cases based on the driving mechanism of the flow. To determine the EOC, the analysis is carried out on grids of size $\mathfrak{K}_h = [8 \times 4, 16 \times 8, 32 \times 16, 64 \times 32, 128 \times 64, 256 \times 128]$ and for polynomial orders $k = [2, 3, 4]$ for temperature and velocity field and $k - 1$ for the pressure field. The finest grid serves as the reference to calculate the approximate error in each field on the coarser grid levels. The optimal result for sufficiently smooth solutions is an EOC of h^{k+1}, see e.g. Arnold et al. (2002), a drastically reduced EOC implies limited smoothness of the solution.

Purely capillary flow In the first stage of the analysis no coupling between heat equation and Navier Stokes equation is established. Therefore, the flow in Fig. 7.13 is induced purely through capillarity, as the droplet is slightly deviated out of its equilibrium shape. Table 7.2 shows the EOC for the pressure, velocity and temperature fields for this stage, under variation of contact-angle and interfacial slip length. For $\theta_{\text{stat}} = 90°$ the EOC for pressure, velocity and temperature are

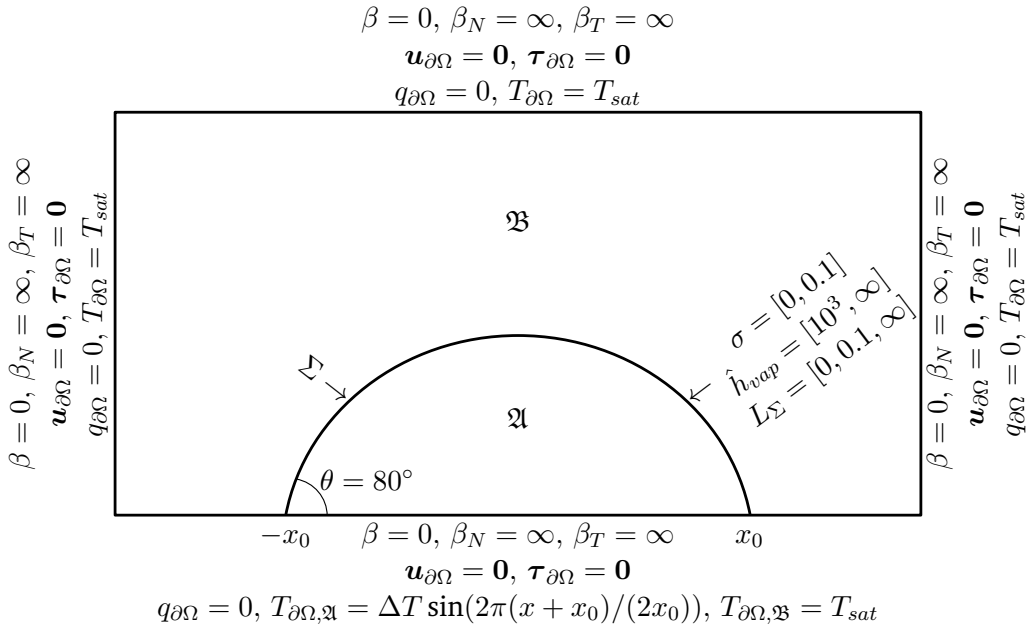

Figure 7.12: For the numerical experiments a slightly ellipsoidal droplet is placed on a free-slip wall at a prescribed temperature. The other three sides of the box are closed with constant temperature, freeslip walls. Due to the ellipsoidal shape, a capillary driven flow is induced. This is superposed with a flow due to evaporation, when the coupling between temperature and velocity is turned on ($\hat{h}_{vap} < \infty$). The temperature on the lower wall is prescribed according to Fig. 7.11 such that the same mass of fluid is evaporated on the left as vapor is condensed on the right side of the droplet.

Table 7.2: EOC, without evaporation $\hat{h}_{vap} = \infty$, with capillarity $\sigma \neq 0$

		$\theta_{\text{stat}} = 90°$			$\theta_{\text{stat}} = 80°$		
	k	$L_\Sigma = 0$	$L_\Sigma = 0.1$	$L_\Sigma = \infty$	$L_\Sigma = 0$	$L_\Sigma = 0.1$	$L_\Sigma = \infty$
$\|p - p_{ref}\|_{L^2(\Omega)}$							
	1	2.08	2.16	2.34	1.77	1.81	1.63
	2	3.02	3.17	3.45	1.93	1.95	1.61
	3	3.84	3.78	4.03	2.29	2.24	1.84
$\|\boldsymbol{u} - \boldsymbol{u}_{ref}\|_{L^2(\Omega)}$							
	2	3.09	2.99	3.24	2.67	2.81	2.37
	3	3.96	3.83	4.00	2.95	3.04	2.42
	4	4.81	4.67	4.68	2.76	2.81	2.09
$\|T - T_{ref}\|_{L^2(\Omega)}$							
	2	3.21	3.21	3.21	3.25	3.25	3.25
	3	3.90	3.90	3.90	3.89	3.89	3.89
	4	4.53	4.53	4.53	4.58	4.58	4.58

close to the optimal order. The introduction of slip on the interface has no significant impact on the EOC. When changing the contact-angle to $\theta_{\text{stat}} = 80°$ the EOC for pressure and velocity is reduced, with diminishing effect of a variation in polynomial degree. For the temperature the convergence order is higher, reaching almost the optimal order. Again, a variation of slip length has no significant impact on the EOC of pressure and velocity.

Superposed capillary and evaporative flow In the second stage of the analysis, a coupling between temperature gradients and velocity is introduced on the interface. The capillary flow, already present in the first stage, is thereby superposed by a flow driven through evaporation, as shown in Fig. 7.14. There, the jumps in interface normal velocity are visible in the discontinues change in arrow colors and size, especially at the contact points. The results of this study are assembled in Table 7.3. For the droplet with $\theta_{\text{stat}} = 90°$ the EOC for pressure and velocity are reduced to order 1 and 2 respectively. A variation of polynomial degrees and interfacial slip has no impact on the observed EOC. As no convective terms are included, there is no coupling

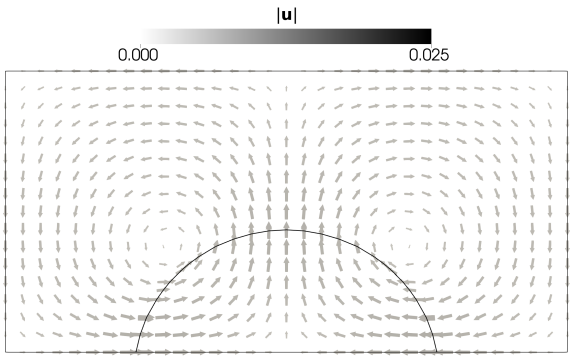

Figure 7.13: Vector field $\boldsymbol{u}$ for $[L_{\Sigma,0.1}, h_{v,\infty}, \sigma_{0.1}, \theta_{80°}]$. The flow induced by capillarity in this testcase is symmetric w.r.t. the y-axis.

Table 7.3: EOC, with evaporation $\hat{h}_{vap} \neq \infty$, with capillarity $\sigma \neq 0$

		$\theta_{\text{stat}} = 90°$			$\theta_{\text{stat}} = 80°$		
	k	$L_\Sigma = 0$	$L_\Sigma = 0.1$	$L_\Sigma = \infty$	$L_\Sigma = 0$	$L_\Sigma = 0.1$	$L_\Sigma = \infty$
$\|p - p_{ref}\|_{L^2(\Omega)}$							
	1	1.18	1.16	1.05	0.49	0.97	0.93
	2	1.10	1.04	1.03	0.19	1.00	1.10
	3	1.17	1.05	1.05	0.07	0.78	1.01
$\|\boldsymbol{u} - \boldsymbol{u}_{ref}\|_{L^2(\Omega)}$							
	2	2.28	2.30	2.34	1.48	2.19	2.36
	3	2.51	2.53	2.56	1.23	2.08	2.31
	4	2.49	2.51	2.57	1.13	1.88	2.32
$\|T - T_{ref}\|_{L^2(\Omega)}$							
	2	3.21	3.21	3.21	3.25	3.25	3.25
	3	3.90	3.90	3.90	3.89	3.89	3.89
	4	4.53	4.53	4.53	4.58	4.58	4.58

from velocities to temperature and the EOC for temperature is the same as in Table 7.2. The results for $\theta_{\text{stat}} = 80°$ are those in the center of this work, as here the effect of the observed model contradiction and its proposed solution can be investigated. The EOC for pressure in this case and a no-slip interface is reduced to 0.5 for the lowest investigated polynomial degree and decreases even further when increasing the polynomial degree. The EOC for velocity is around one order higher, but still reduced in comparison to the results without evaporation in Table 7.2. This loss of high-order convergence indicates some sort of singularity arising in the solution, which can be attributed to the contradiction Eq. (7.18) in the model, Figs. 7.17 to 7.16. When introducing slip on the interface, the model contradiction is resolved and the EOC for the $\theta_{\text{stat}} = 90°$ case, where the contradiction is also not present, is recovered. A further increase in slip on the interface, to free-slip, has no additional effect.

Purely evaporative flow In the final stage capillarity is turned off and the flow resulting from pure evaporation is investigated, see Fig. 7.15. This enables us to make a statement about the

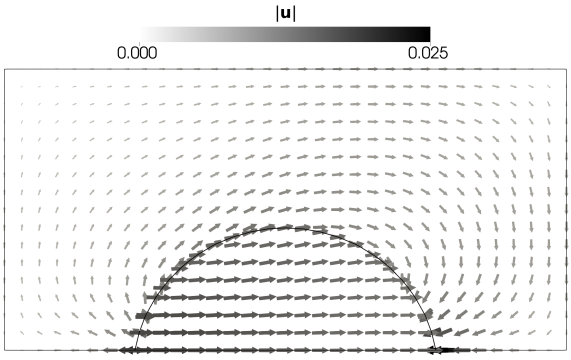

Figure 7.14: Vector field $\boldsymbol{u}$ for $\left[L_{\Sigma,0.1}, h_{v,10^3}, \sigma_{0.1}, \theta_{80°}\right]$. The flow induced by capillarity in this testcase is superposed with the anti-symmetric flow due to evaporation.

Table 7.4: EOC, with evaporation $\hat{h}_{vap} \neq \infty$, without capillarity $\sigma = 0$

		$\theta_{\text{stat}} = 90°$			$\theta_{\text{stat}} = 80°$		
	k	$L_\Sigma = 0$	$L_\Sigma = 0.1$	$L_\Sigma = \infty$	$L_\Sigma = 0$	$L_\Sigma = 0.1$	$L_\Sigma = \infty$
$\|p - p_{ref}\|_{L^2(\Omega)}$							
	1	1.18	1.17	1.07	0.49	0.97	0.94
	2	1.11	1.07	1.07	0.19	1.01	1.12
	3	1.20	1.14	1.13	0.07	0.85	1.08
$\|\boldsymbol{u} - \boldsymbol{u}_{ref}\|_{L^2(\Omega)}$							
	2	2.28	2.30	2.34	1.48	2.19	2.36
	3	2.51	2.53	2.56	1.23	2.08	2.31
	4	2.49	2.51	2.57	1.13	1.87	2.32
$\|T - T_{ref}\|_{L^2(\Omega)}$							
	2	3.21	3.21	3.21	3.25	3.25	3.25
	3	3.90	3.90	3.90	3.89	3.89	3.89
	4	4.53	4.53	4.53	4.58	4.58	4.58

interaction between evaporation induced and capillary flow. The results assembled in Table 7.4 show good agreement with the results from Table 7.3. This indicates, that the results and discussion of Table 7.3 are already dominated by the evaporative flow, without the capillary flow from Table 7.2 having too much of a regularizing influence.
In Fig. 7.16 the temperature field and pressure field near the right contact point are displayed. For the pressure a simulation without the contradiction $\left(\left[L_{\Sigma,0.0}, h_{v,10^3}, \sigma_{0.0}, \theta_{80°}\right]\right)$ is displayed on top and with contradiction $\left(\left[L_{\Sigma,\infty}, h_{v,10^3}, \sigma_{0.0}, \theta_{80°}\right]\right)$ on the bottom. Clearly, the pressure field is irregular in the lower picture and the magnitude of pressure $1-2$ order higher than in the upper one. This indicates some sort of singularity in the pressure caused by the contradiction in the model.
To complete the presentation and discussion we directly evaluate the LHS of Eq. (7.18) at the right point of contact. These results, together with the respective jumps in velocity are displayed in Table 7.5. As the boundary and interface conditions are enforced only weakly, even in absence of the contradiction, the jump in wall normal direction and the LHS of Eq. (7.18) do not vanish completely. However, in presence of the contradiction these values are several orders of magnitude

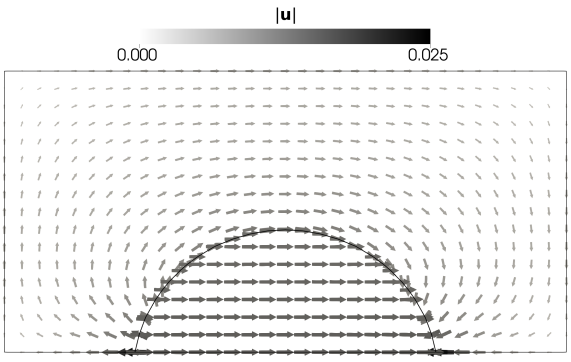

Figure 7.15: Vector field $\boldsymbol{u}$ for $\left[L_{\Sigma,0.1}, h_{v,10^3}, \sigma_{0.0}, \theta_{80°}\right]$. In this isolated setup the anti-symmetric structure of the flow field induced by evaporation is visible.

Table 7.5: Velocity jumps at the right contact point. The results are obtained for the finest grid and highest degree.

Case	$[\![\boldsymbol{u}\cdot\boldsymbol{n}^{\partial\Omega}]\!]$	$[\![\boldsymbol{u}\cdot\boldsymbol{n}^{\Sigma}]\!]$	$[\![\boldsymbol{u}\cdot\boldsymbol{n}^{L}]\!]$	Eq. (7.18)
$\left[L_{\Sigma,0.0}, h_{v,10^3}, \sigma_{0.0}, \theta_{90^\circ}\right]$	1.23×10^{-6}	3.27×10^{-2}	1.23×10^{-6}	1.23×10^{-6}
$\left[L_{\Sigma,0.0}, h_{v,\infty}, \sigma_{0.1}, \theta_{80^\circ}\right]$	1.15×10^{-8}	-3.54×10^{-9}	1.10×10^{-8}	1.15×10^{-8}
$\left[L_{\Sigma,0.0}, h_{v,10^3}, \sigma_{0.0}, \theta_{80^\circ}\right]$	-5.40×10^{-3}	3.63×10^{-2}	9.24×10^{-4}	-5.40×10^{-3}
$\left[L_{\Sigma,0.1}, h_{v,10^3}, \sigma_{0.0}, \theta_{80^\circ}\right]$	-1.29×10^{-5}	3.65×10^{-2}	6.42×10^{-3}	-1.29×10^{-5}
$\left[L_{\Sigma,\infty}, h_{v,10^3}, \sigma_{0.0}, \theta_{80^\circ}\right]$	2.10×10^{-6}	3.65×10^{-2}	6.44×10^{-3}	2.10×10^{-6}

higher. By introducing slip on the interface it is possible to recover the same magnitude for these measurements $\left(\left[L_{\Sigma,\infty}, h_{v,10^3}, \sigma_{0.0}, \theta_{80^\circ}\right]\right)$ as for the case where the contradiction is not present $\left(\left[L_{\Sigma,0.0}, h_{v,10^3}, \sigma_{0.0}, \theta_{90^\circ}\right]\right)$.

Flow behavior at the contact line To gain an even better insight into the flow at the contact line, the cases $\left[L_{\Sigma,0.0}, h_{v,10^3}, \sigma_{0.0}, \theta_{90^\circ}\right]$, $\left[L_{\Sigma,\infty}, h_{v,10^3}, \sigma_{0.0}, \theta_{90^\circ}\right]$, $\left[L_{\Sigma,0.0}, h_{v,10^3}, \sigma_{0.0}, \theta_{80^\circ}\right]$, and $\left[L_{\Sigma,\infty}, h_{v,10^3}, \sigma_{0.0}, \theta_{80^\circ}\right]$ are computed again on a highly resolved grid near the contact lines. The coarsest base grid (8×4) is used with 6 levels of AMR on the boundary and interface and 16 levels at the contact line, giving a minimum cell size of $h_{min} = 5.722\times10^{-6}$ m. This very fine resolution allows to resolve the fields very accurately towards the contact line and investigate the nature of still present singularities.
In Fig. 7.17 the pressure and velocities resulting from these calculations are plotted as a graph over the lower wall. The left images show the results for $\left[L_{\Sigma,0.0}, h_{v,10^3}, \sigma_{0.0}, \theta_{80^\circ}\right]$ and the right for $\left[L_{\Sigma,\infty}, h_{v,10^3}, \sigma_{0.0}, \theta_{80^\circ}\right]$. Both simulations exhibit sharp pressure spikes at the contact points. However, for the left side, using the no-slip interface, these spikes have a much larger magnitude and seem sharper. At first glance the x-component of the velocity seems smooth and of overall same behavior in both simulations. When looking closely though a small spike is visible in the left images at the contact points. The y-component of the velocity should vanish exactly, due to the

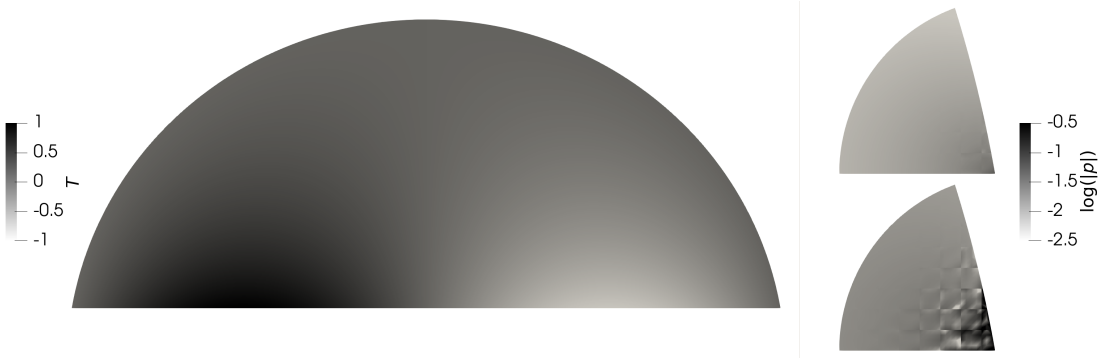

Figure 7.16: On the left the temperature field for the $\theta = 80^\circ$ droplet is shown. The right pictures show the magnitude of the pressure field for the simulations $\left[L_{\Sigma,\infty}, h_{v,10^3}, \sigma_{0.0}, \theta_{80^\circ}\right]$ (top) and $\left[L_{\Sigma,0.0}, h_{v,10^3}, \sigma_{0.0}, \theta_{80^\circ}\right]$ (bottom) at the right contact point. In the lower picture the effect of the model contradiction is visible in the ragged pressure field.

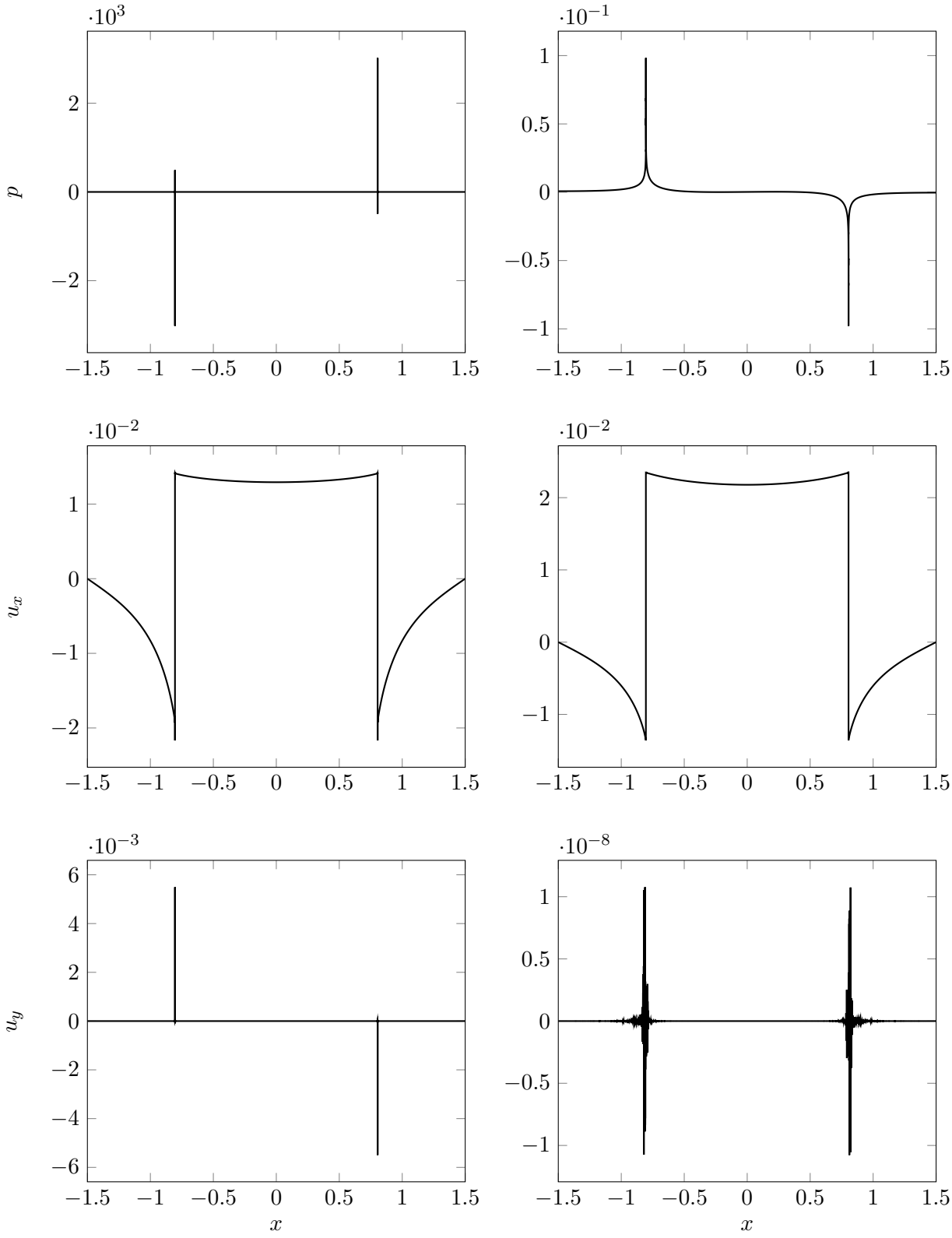

Figure 7.17: Profiles of pressure and velocities along the lower wall for no-slip ($\left[L_{\Sigma,0.0}, h_{v,10^3}, \sigma_{0.0}, \theta_{80^\circ}\right]$) on the left, and for freeslip ($\left[L_{\Sigma,\infty}, h_{v,10^3}, \sigma_{0.0}, \theta_{80^\circ}\right]$) on the right

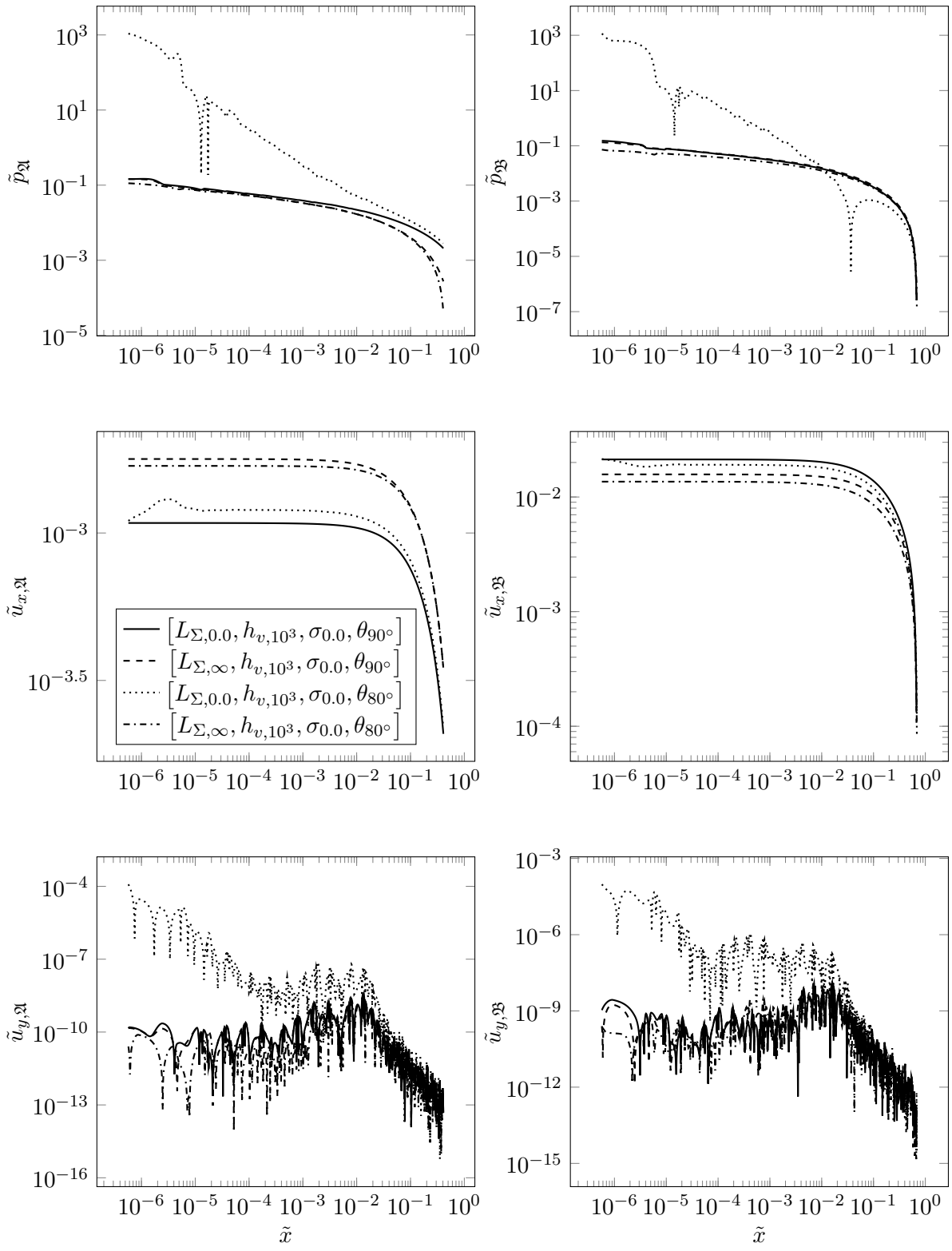

Figure 7.18: Log-log representation of the augmented pressure and velocities (Eq. (7.25)). The behavior from both sides $(\mathfrak{A}, \mathfrak{B})$ of the interface is displayed for the test cases shown in the key.

Table 7.6: Exponents for the pressure behavior towards the contact point as $\tilde{p} \propto \tilde{x}^{\vartheta}$

Case	$\vartheta_{\mathfrak{A}}$	$\vartheta_{\mathfrak{B}}$
$\left[L_{\Sigma,0.0}, h_{v,10^3}, \sigma_{0.0}, \theta_{90^\circ}\right]$	-0.18	-0.22
$\left[L_{\Sigma,\infty}, h_{v,10^3}, \sigma_{0.0}, \theta_{90^\circ}\right]$	-0.20	-0.20
$\left[L_{\Sigma,0.0}, h_{v,10^3}, \sigma_{0.0}, \theta_{80^\circ}\right]$	-1.09	-1.12
$\left[L_{\Sigma,\infty}, h_{v,10^3}, \sigma_{0.0}, \theta_{80^\circ}\right]$	-0.18	-0.15

impermeable wall. Both simulations violate this condition, especially towards the contact-points. As was seen for the pressure, the magnitude of this velocity component is again much larger for the simulation using a no-slip interface.
To even better understand the behavior of the fields at the contact points, we zoom in on the right contact point. In Fig. 7.18 the inner ($\mathfrak{A}$, left) and outer ($\mathfrak{B}$, right) solutions are distinguished. The fields are drawn in double logarithmic representation as

$$\tilde{f}_{\mathfrak{A}}(\tilde{x}) = \left| f_{\mathfrak{A}}(x_0 - \tilde{x}, 0) - f_{\mathfrak{A}}(0,0) \right|, \tag{7.25a}$$

$$\tilde{f}_{\mathfrak{B}}(\tilde{x}) = \left| f_{\mathfrak{B}}(x_0 + \tilde{x}, 0) - f_{\mathfrak{B}}(1.5,0) \right|. \tag{7.25b}$$

The pressure profile in the inner and outer solution displays very similar behavior. For the simulation $\left[L_{\Sigma,0.0}, h_{v,10^3}, \sigma_{0.0}, \theta_{80^\circ}\right]$ a $\tilde{p} \propto 1/\tilde{x}$ relation is visible, explaining the low convergence orders for this case in Table 7.4, as this would mean a singular pressure at the contact point. For all other cases the pressure becomes singular towards the contact point as well, however, with a much less severe exponent, measured to approximately $\tilde{p} \propto 1/\tilde{x}^{0.2}$. The measured exponents for the pressure are given in Table 7.6, and calculated from the range $\tilde{x} = [h_{min}/10, 1000\, h_{min}]$ by a linear regression from the log-log representation. The data lines for the x-velocity are smooth and do not diverge towards the contact point. The only interesting behavior here is the slight bump in the result of the case $\left[L_{\Sigma,0.0}, h_{v,10^3}, \sigma_{0.0}, \theta_{80^\circ}\right]$, forcing the θ_{80° velocity towards the same value as measured for θ_{90° at the contact point. This behavior is displayed in both the inner and outer solution. At last the data lines for the y-velocity shall be discussed. The first impression is, that these are very irregular, oscillating in the range 10^{-12} to 10^{-8} m/s. When the contact point is approached the velocity in the $\left[L_{\Sigma,0.0}, h_{v,10^3}, \sigma_{0.0}, \theta_{80^\circ}\right]$ simulation is about 4 magnitudes larger than in the other simulations. After a certain distance to the contact point ($\tilde{x} \approx 0.01$ m), the velocities for all simulations start to decline with approximately $\tilde{u_y} \propto 1/\tilde{x}^{2.5}$. Overall the log-log plots confirm the aforementioned observation, that the slip interface condition eliminates the contradiction Eq. (7.18) and the behavior of the θ_{90° case, where the contradiction is absent as well, can be recovered.

7.3 Transient simulations of contact line evaporation

A major part of the work conducted throughout this thesis was dedicated to performing simulations of the experiments conducted in the work of Schweikert et al. (2019). In those experiments a superheated wall is dragged out of a reservoir of some liquid (ethanol or the coolant FC-72) superposed by its vapor, both held at the saturation point, here this experiment is referred to as "heated wall" experiment. Depending on the dewetting velocity and superheat supplied through the wall either a contact line evaporation or microlayer evaporation is observed. The former

Table 7.7: Material properties of saturated ethanol at $300\,\mathrm{K}$ (Springer-Verlag GmbH, 2013)

	Density ρ [kg/m^3]	Heat capacity $\hat{c}_p$ [J/(kg K)]	Thermal conductivity $10^{-3}, \hat{k}$ [W/(m K)]	Dyn. viscosity $10^{-6}, \mu$ [Pa s]
liquid $\mathfrak{A}$	783.82	2.597	175.1	1043
vapor $\mathfrak{B}$	0.164	1.605	15.1	8.65

Latent heat $\hat{h}_{vap}$ [kJ/kg] $= 919.7$, Surface tension σ [N/m] $= 21.95 * 10^{-3}$,
Saturation temperature T_{sat} [K] $= 300$, Gravitational acceleration g [m/s^2] $= 9.81$

describes a regime, where the contact line only rises a small distance with the wall and evaporation mainly occurs at said contact line. Evaporation in this regime is strong enough to inhibit the formation of a liquid film on the wall. In the latter regime the contact line rises a considerable amount with the wall, until a nearly stationary thin film is developed. Evaporation occurs then not only at the contact line, but also over the length of this thin film. The aim of the numerical study was to retrieve better insight into the transition between these two regimes.
However, over the course of the simulations conducted towards this goal the real experimental setup proved too challenging to simulate directly. In Section 7.3.1 the difficulties hindering the simulation of the full setup are discussed. An extremely simplified simulation of the setup, allowing at least some insights is presented in Section 7.3.2. Finally, it was found that it may be necessary to include conjugate heat transfer in the solid wall. This is showcased in Section 7.3.3.

7.3.1 Heated wall - simulation runtime

The difficulties in simulating the setup presented in Schweikert et al. (2019) can be mainly attributed to computational cost. To this end we first review some relevant length scales in the plate coating process, cf. (Landau and Levich, 1942; Ryck and Quéré, 1998), for ethanol (Table 7.7). First, and independent we compute the capillary length, which we can use in the simulation to estimate the necessary extent of the domain to include for example the unperturbed formation of the meniscus at the wall:

$$a = \sqrt{\frac{\sigma}{\rho_{\mathfrak{A}} g}} \approx 0.0017\,\mathrm{m}. \tag{7.26}$$

Next, we calculate the capillary number, which depends on the dewetting velocity V of the wall. From the experiments we know these to be $V \approx \mathcal{O}(10^{-3}) - \mathcal{O}(10^{-2})$ m/s, which means

$$Ca = \frac{\mu_{\mathfrak{A}} V}{\sigma} = \mathcal{O}(10^{-4}). \tag{7.27}$$

From the Landau-Levich theory (Landau and Levich, 1942; Ryck and Quéré, 1998) for this regime where $Ca << 1$ the film thickness is expected to be

$$\delta = 0.94\, a\, Ca^{\frac{2}{3}} \approx 3\,\mu\mathrm{m}. \tag{7.28}$$

Now we have the difficulty that on the one hand we need to resolve length scales of a and on the other hand those of δ. Which means that the cell size is approximately $h_{min} \approx \delta$. Using the

Table 7.8: Material properties for the simplified setup

	Density ρ [kg/m^3]	Heat capacity $\hat{c}_p$ [J/(kg K)]	Thermal conductivity $\hat{k}$ [W/(m K)]	Dyn. viscosity μ [Pa s]
liquid $\mathfrak{A}$	1	0	1	1
vapor $\mathfrak{B}$	1	0	1	0.001
solid $\mathfrak{S}$	1	0	1	–
Latent heat $\hat{h}_{vap}$ [J/kg] $= 1$, Surface tension σ [N/m] $= 1$, Saturation temperature T_{sat} [K] $= 0$[6], Gravitational acceleration g [m/s^2] $= 4$				

capillary time-step from Section 6.1 we find a time-step size of

$$\Delta t \approx \sqrt{\frac{\rho_{\mathfrak{A}} + \rho_{\mathfrak{B}}}{2\pi\sigma} \left(\frac{h_{min}}{2k+1}\right)^3} \approx 3.5 \times 10^{-8} \text{ s} \tag{7.29}$$

for a moderate polynomial degree of $k = 2$. Also from the experiment we know the intended duration of the simulation to be $t_{end} \approx 1$ s. Putting all of this together we would therefore need

$$N_{\Delta t} = t_{end}/\Delta t = \mathcal{O}(10^7) \tag{7.30}$$

time-steps. Resolving the macroscopic length a and film thickness δ would mean we employ around

$$N_K = \approx \mathcal{O}((a/\delta)^2) \approx \mathcal{O}((10^3)^2) = \mathcal{O}(10^6) \tag{7.31}$$

cells in a 2D simulation. In practice this would be somewhat less by employing AMR, so lets assume $N_K = 10^5$. With $k = 2$ there are $(6, 6, 3) = 15$ DOFs for the two velocities and the pressure in each cell and finally the total number of DOFs becomes

$$N_{dof} = \mathcal{O}(10^6). \tag{7.32}$$

Now, we are not able to provide an exact number but from experience we estimate the solver needs around $\tau = 1$ to 10 min for a time-step with that amount of DOFs, which would mean the total simulation runtime would succumb to

$$T = N_{\Delta t}\tau \approx 10^7 \text{ min} \approx 10^5 \text{ h} \approx 10^4 \text{ d} \approx 19 \text{ years}. \tag{7.33}$$

Thus, it is beyond the capabilities of the solver at the current time to compute this experiment to its full extent. This estimation emphasizes the considerations made in Section 6.1 and the need for a fully implicit level set coupling able to handle larger time-steps. These considerations are valid even before taking into account long term stability of the solver, especially of the interface, which is very challenging for such inviscid materials.

[6]The temperature range is shifted for numerical reasons, the occurrence of absolute zero at this point has no physical significance.

7.3.2 Heated wall - simplified setup

To compute a simplified version of the heated wall experiment, using the system of equations from Section 2.6.2, the first drastic simplification is the choice of fictive material parameters. Table 7.8 shows the values chosen in this setup. Most noticeable vapor and liquid have the same density. So it is obvious that this setup is completely artificial, but this simplification together with the neglected heat capacities effectively decouples the solution of the heat equation and the flow solution, as according to Eq. (2.75) the velocity jump vanishes for equal densities and therefore the contradiction discussed in Section 7.2 is not present. This means the interface movement as described by Eq. (2.73) is influenced by evaporation, but there is no additional flow induced in the liquid/vapor bulks. These fluids are then placed in a domain of size $\Omega = [-5, 0]$ m $\times$ $[0, 15]$ m and subject to an gravitational acceleration of $g = 4$ m/s^2 in negative y-direction, such that the capillary length is $a = 0.5$ m. The equilibrium contact angle is set to $\theta_{\text{stat}} = \pi/2$ and the quasi-stationary contact angle model is employed ($\beta_L = 0$, Eq. (2.79)). The upper and lower walls are pressure outlets, with the pressure value prescribed according to the hydrostatic pressure for the initial state with a flat interface at $y_0 = 1$ m, shown on the left in Fig. 7.19, for which the level set

$$\varphi(x, y) = -y_0 + y \tag{7.34}$$

is used[7]. The left wall is set as a free-slip wall and the right one as a slip wall with $\beta_{\mathfrak{A}} = \beta_{\mathfrak{B}} = 1000$ Pa s/m, that is moving upward with $V_{wall} = 1$ m/s. The left, upper and lower boundaries are assumed adiabatic for the heat equation and through the right wall a constant heat flux is supplied only to the liquid phase. The domain is meshed with a 4×12 grid and 3 levels of AMR are used at the interface. The total duration for the simulations is $t_{end} = 12$ s with a fixed time-step size of $\Delta t = 0.01$ s.

In Fig. 7.19 the evolution of the liquid-vapor interface for heat fluxes of different intensity $\left(q_{\partial\Omega} = [0, 0.05, 0.1, 0.2] \text{ W/m}^2\right)$[8] is displayed. This effects evaporation of different amounts at the interface, draining the liquid film on the wall. Initially the interface is horizontal. After 1.5 s the formation of a dynamic meniscus is observable, due to the movement of the wall dragging the fluids along. At 3 s the differences between the simulations using different heat fluxes become more pronounced. The black line, where no heat flux is supplied and thus no evaporation occurs is rising higher than the other interfaces. Additionally, the formation of an inflection point is visible. Near the contact point the curvature is positive and becomes negative when moving away from the contact point. This initially positive curvature is less pronounced in the simulations with evaporation. At 6 s the "cold" interface starts to form a thin film on the wall, while the other interfaces approach the wall asymptotically without a region of a near constant thickness. Looking at the final time the simulations with the highest heat flux seem to have reached a nearly stationary state, as the contact point did not climb noticeably between 6 and 12 s. In contrast the "cold" interface still rises with the same constant velocity, now exhibiting a nicely formed film on the wall. The simulation with the lowest heat flux lies somewhat in between, still rising but at a considerably reduced velocity.

These observations are supported by the finding in Fig. 7.20. Here the contact point y-position, y-velocity, and contact angle are displayed. For the cold interface the contact point rises with a constant speed, slightly below the wall velocity due to the slip. The contact angle approaches a constant value, not equal to the equilibrium value. We explain this with the high friction value of

[7] For these simulations the "Fast-Marching" scheme described in Smuda and Kummer (2022) is employed.

[8] A positive value effects a heat flux in opposite direction of the boundary normal, which means heat is flowing into the domain.

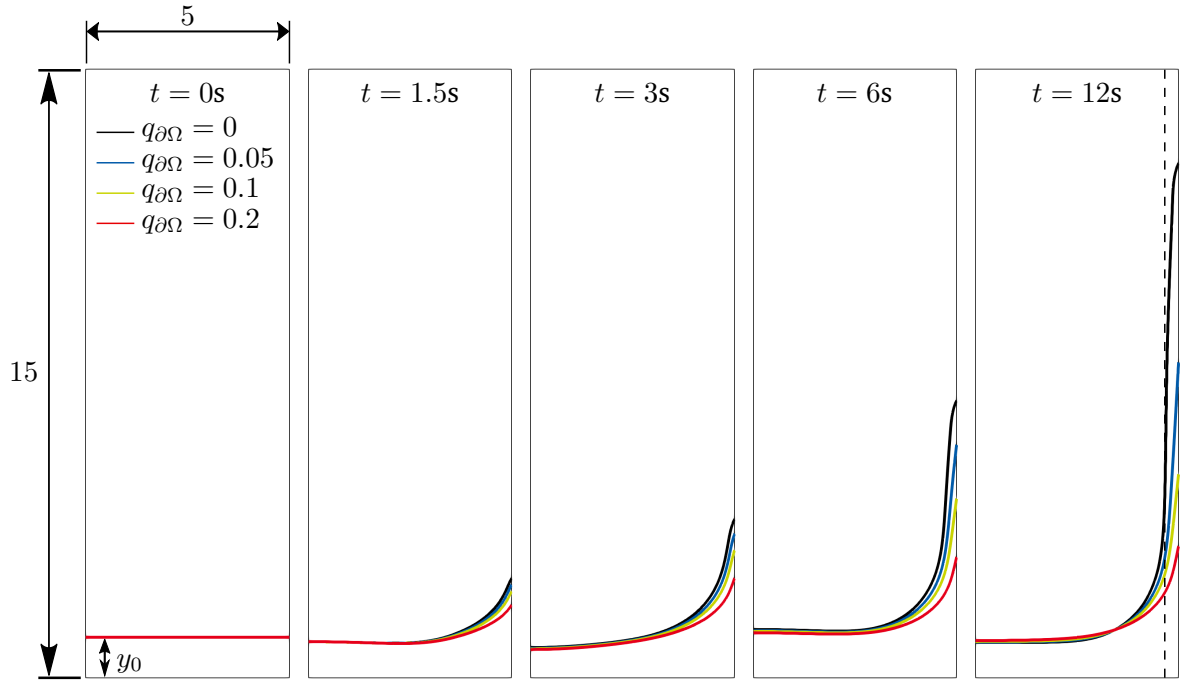

Figure 7.19: Evolution of the interface in the simplified setup for a heated wall getting dragged out of a liquid reservoir. Results for heat fluxes of different amounts supplied through the boundary are displayed. The dashed line in the last figure helps visualize the formation of a film of almost constant thickness.

$\beta = 1000$ Pa s/m. In Section 7.1, we observed that a no-slip condition effectively overwrites the contact line condition. This high friction value almost depicts a no-slip condition, and thus the quasi-stationary contact angle condition is not able to pull the contact angle to $\theta_{\text{stat}} = \pi/2$.
The blue data lines show the same measurements for the simulation with $q_{\partial\Omega} = 0.05$ W/m^2. The contact point always rises slower than in the "cold" simulation. As the contact point rises, more heat is supplied (as the whole wetted region is heated), which in turn means more evaporation at the interface and thus more film drainage. Therefore, the movement of the contact point is slowed down over the course of the simulation.
The green and orange lines display the same behavior. However, due to the higher heat fluxes the equilibrium, where the amount of liquid dragged into the film and evaporated over the length of the film is in balance, is reached sooner. This is noticeable as the point where the contact velocity approaches zero.
At last we want to look at the contact angles in the simulations with evaporation. What is somewhat surprising is that the approached asymptotic value for the lowest heat flux is furthest away from the value in the "cold" simulation. However, these asymptotic angles are not random and follow a strict pattern. When considering the equilibrium state we find $\boldsymbol{u}^\Sigma \cdot \boldsymbol{n}^\Sigma = 0$, which means

$$\boldsymbol{u}_{\mathfrak{A}} \cdot \boldsymbol{n}^\Sigma = \frac{\dot{m}}{\rho_{\mathfrak{A}}}. \tag{7.35}$$

For the high friction value we can estimate $\boldsymbol{u}_{\mathfrak{A}} \approx (0, V_{wall})^T$ and the interface normal at the contact point is $\boldsymbol{n}^\Sigma = (-\cos(\theta), \sin(\theta))^T$. This gives a relation between the contact angle and the

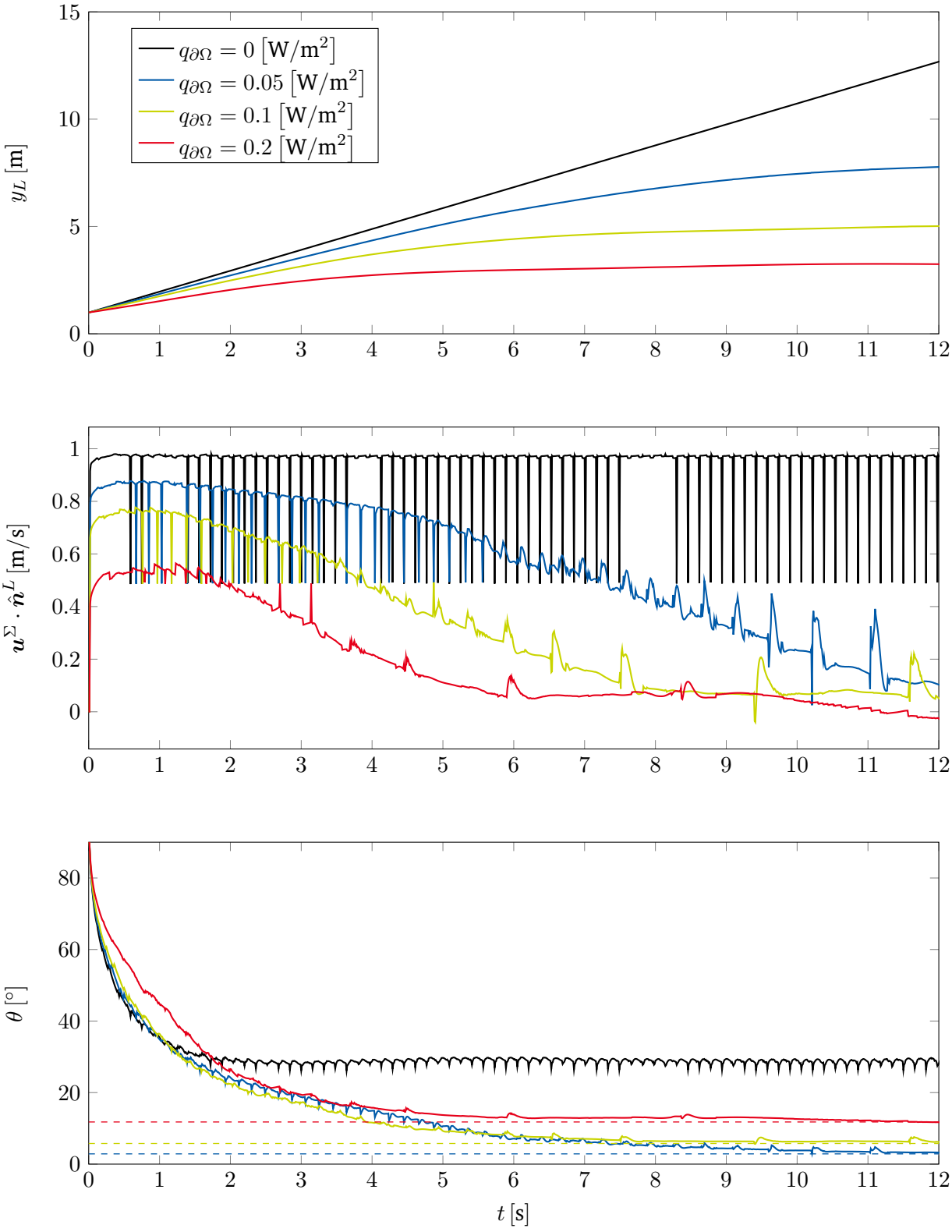

Figure 7.20: Contact point position, velocity and contact angle in the simplified heated wall simulation over the duration of the simulation

mass flux in the equilibrium state:

$$\sin(\theta) = \frac{\dot{m}}{\rho_{\mathfrak{A}} V_{wall}}. \tag{7.36}$$

To estimate the mass flux we repeat the same considerations for the temperature gradient. From the interface conditions (Eq. (2.75)) it is known that

$$\nabla T_{\mathfrak{A}} = -\frac{\dot{m}\hat{h}_{vap}}{\hat{k}_{\mathfrak{A}}} \boldsymbol{n}^{\Sigma}. \tag{7.37}$$

On the other hand, the heat flux at the boundary in wall normal direction is given by Eq. (2.78) as

$$\nabla T_{\mathfrak{A}} \cdot \boldsymbol{n}^{\partial\Omega} = q_{\partial\Omega}. \tag{7.38}$$

By inserting Eq. (7.37) in Eq. (7.38) the mass flux at the contact line in terms of the boundary heat flux is obtained as

$$\dot{m} = \frac{q_{\partial\Omega}}{\hat{h}_{vap} \cos(\theta)}. \tag{7.39}$$

Inserting Eq. (7.39) in Eq. (7.36) and applying an addition theorem for the trigonometric functions the expected contact angle for an equilibrium state is found to be

$$\theta = \frac{1}{2} \arcsin\left(2 \frac{q_{\partial\Omega}}{\hat{h}_{vap} \rho_{\mathfrak{A}} V_{wall}}\right). \tag{7.40}$$

These predicted values are displayed as dashed lines in Fig. 7.20. It is visible, that these predictions are accurate and approached in the actual simulations. At last we can calculate the film thickness for the "cold" simulation. To this end, we average the film thickness over the region from $y = 4$ m to $y = 10$ m to obtain $\delta \approx 0.29$ m. The capillary number for this setup is $Ca = 1$, which means we should observe the film thickness according to the "crossover" regime given by Ryck and Quéré (1998). There, the expression

$$Ca = 1.09 \left(\frac{\delta}{a}\right)^{3/2} + \left(\frac{\delta}{a}\right)^{2} \tag{7.41}$$

is given for the film thickness in dependence of the capillary number and capillary length, which is here $a = 0.5$ m. Thus, they predict a thickness of $\delta \approx 0.33$ m, which agrees well with the estimate derived from the simulation. It should be noted that the value from the simulation depends on the upper and lower cut-off values, determining whether the dynamic meniscus and the contact line still influence the instantaneous thickness. From this result also the discrepancy in the length scales present in this experiment is highlighted. It is visible from Fig. 7.19, that we need a domain size of several times the capillary length to capture the formation of the dynamic meniscus accurately. In addition we need to resolve the film thickness or even smaller scales at the contact line. We were able to simulate this setup for a capillary number of order $\mathcal{O}(1)$, where the film thickness is also of the same magnitude as the capillary length. However, for the capillary numbers used in real experiments the film would be much smaller, which underlines the point made in Section 7.3.1.

7.3.3 Heated wall - conjugate heat transfer

The results of the previous section emphasize how the heat flux from the wall into the liquid at the contact line influences the dewetting behavior. There, we assumed a constant heat flux in wall normal direction. However, in a realistic setup the heat flux is probably not constant at every point on the wall. Another often employed boundary condition is that of a constant wall temperature. But this is inappropriate for our simulation as a constant, compared to the saturation temperature superheated, temperature would effect a diverging heat flux at the contact line in the employed model. So the question is how can we obtain a boundary condition at the contact line that models the heat fluxes more accurately. The approach we want to showcase in this section is to actually include heat transfer in the wall to simulate the temperature field at the contact line more realistically.
To this end, we adapt the setup presented in Section 7.3.2 slightly. The domain is now of size $\Omega = [-5, 0]\,\text{m} \times [0, 5]\,\text{m}$ or when including the solid explicitly $\Omega = [-5, 1]\,\text{m} \times [0, 5]\,\text{m}$, see Fig. 7.21, and the right wall is not moving. The fluid-fluid interface is placed at $y_0 = 2.2$ m and if present the fluid-solid interface at $x_0 = 0$ m. The mesh contains one cell per unit length and 5 levels of AMR are employed at the fluid-fluid interface and 5 additional levels at the contact point. Two steady state simulations are performed, in the first the heat flux is set to $q_{\partial\Omega} = 0.2\ \text{W/m}^2$ and the solid is not included, the second simulation uses Eq. (2.77a) with $Q^\Sigma = 0.2\ \text{W/m}^2$, while including the solid explicitly. In both simulations the heating is done only along the liquid-solid interface, while no additional heat is supplied along the vapor-solid interface. The second condition can be thought of as a very thin film applied on the solid, which is then heated, e.g. by sending an electric current through it, very similar to what is done in the actual experiments (Schweikert et al., 2019).
The complex temperature field resulting from the three phase simulation is displayed in Fig. 7.21. The fluid-fluid interface (red) stays at saturation temperature everywhere. The fluid-solid interface (white) displays superheating when moving away from the contact point and approaches saturation

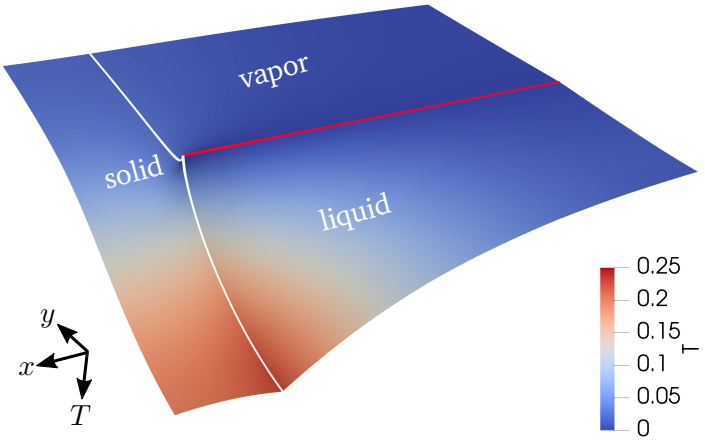

Figure 7.21: Elevated temperature field for the three phase showcase. The image is rotated such that the solid wall is on the left and the elevation is inverse to the calculated temperature. The fluid-fluid interface is highlighted in red, the fluid-solid one in white.

temperature at the contact point. The solid also exhibits a temperature gradient in y-direction, which corresponds to heat flowing from the heated part of the wall towards the passive part, that is from the solid-liquid to the solid-vapor interface.
In Fig. 7.22 the temperature and wall normal heat fluxes are displayed along the fluid-solid interface. In case of the three phase simulation these values are included from both sides of the interface, i.e. in $\mathfrak{A}$ or $\mathfrak{B}$ and $\mathfrak{S}$. From the temperature profile the complete thermal decoupling of the two fluid phases is visible. While the heated part of the wall (that in contact with $\mathfrak{A}$) reaches a certain superheat, the passive part remains at saturation temperature. If the solid phase is included this changes. Now the fluid phases are thermally coupled through the solid and heat can flow from the heated to the passive side. The wall does not reach as high superheating values as in the two phase case. However, now the passive part of the wall also exhibits some superheat. As intended the measured temperatures from solid and fluid phase align. The profiles for the heat flux show similar results. The dashed line, indicating the purely two phase setup, has a jump at the contact point, separating the heated from the passive part of the wall. With three phases it is possible to observe two non overlapping lines in the heated section. These lines show the heat flux in wall normal direction measured from fluid and solid wall respectively. The distance between these two lines is the heat source we placed on the interface. Further away from the contact point the results are similar to the two phase case. In the heated section a constant heat flux is approached and in the passive section it tends towards zero. In close proximity to the contact line this changes. There, a significant spike in heat flux can be observed. On the other side of the contact point no source is placed on the interface, which is why there the heat fluxes from both sides overlap.
The same measurements are taken for the fluid-fluid interface. As intended from the interface conditions the interface is at saturation temperature everywhere. Qualitatively the heat fluxes behave also similar, with two notable differences. In the two phase setup the vapor is basically completely passive, thus there is no heat flux from the vapor side to the interface. In the three phase simulation heat is flowing towards the interface from the liquid and the vapor side, for the latter mostly close to the contact point. The second observation is the amount of heat flowing to the interface at the contact point. In both simulations it reaches its maximum at the contact point. When all three phases are computed this maximum is considerably larger. In return the heat flux from the liquid to the interface is slightly higher in the two phase simulation, when measuring further away from the contact point.

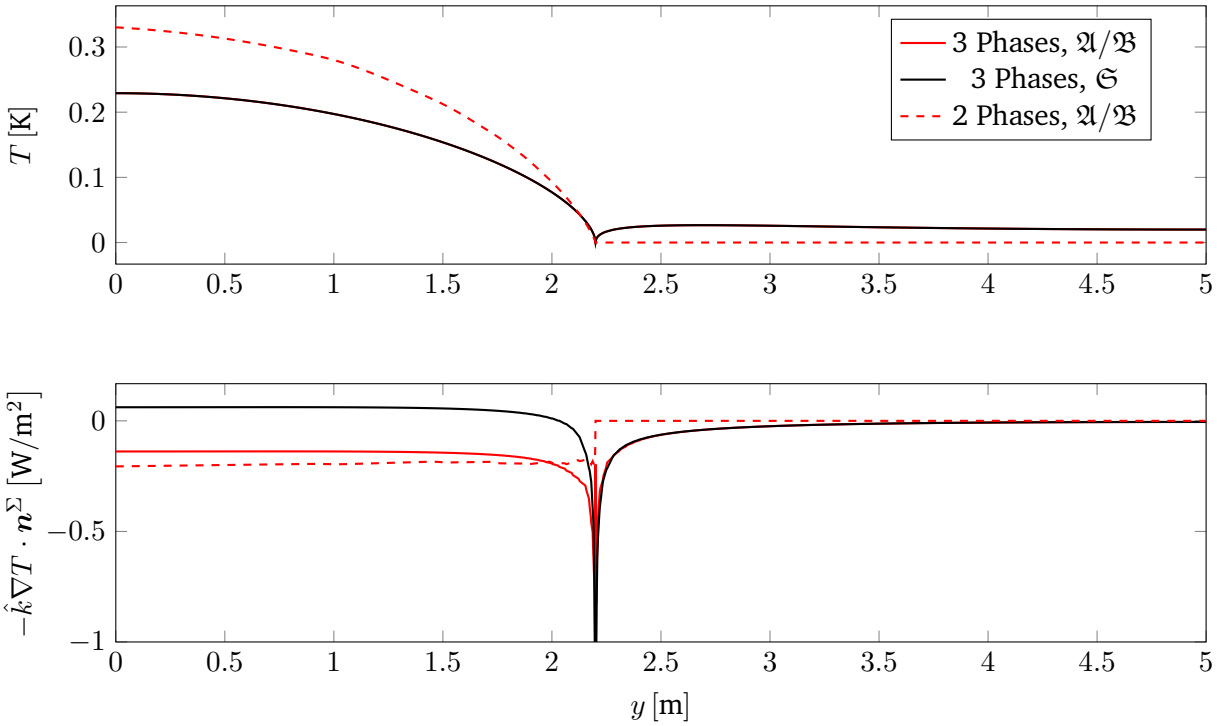

Figure 7.22: Temperature and (interface normal) heat flux along the fluid-solid interface

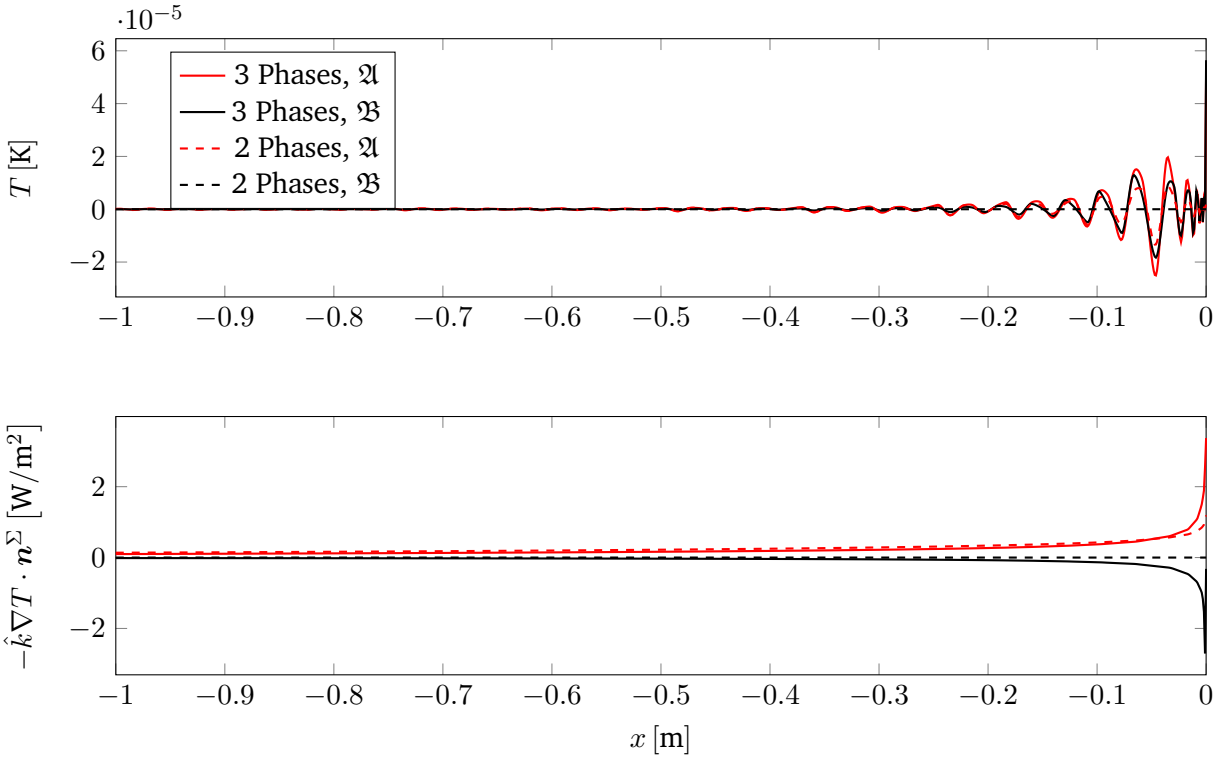

Figure 7.23: Temperature and (interface normal) heat flux along the fluid-fluid interface

7.4 Conclusion

In this chapter the focus is shifted from pure two-phase (or multiphase problems) to special two-phase problems, containing a three phase contact line. For Section 7.1 evaporation and even the computation of the second phase are neglected to focus purely on the dynamics of the contact line in the XDG method presented in Chapter 4. The capability of the method handling various contact line models to take into account complex behavior like contact angle hysteresis is examined. Several independent studies are conducted. First, the contact line behavior excluded and the focus lies on the behavior of the fluid pressure and velocity in a sharp corner depending on the slip boundary condition set on the solid wall. We were able to confirm findings obtained analytically and observed the presence of singularities, when a no-slip condition is enforced. This first analysis also emphasized the capability of the method to make these singularities visible by using high approximation orders and AMR. The second study shifted the focus to the behavior of pressure and velocity towards the contact line in dependence of different contact line models. For all variations a logarithmic singularity in the velocity and a rational singularity for the pressure is observed when approaching the contact line. This result again agrees well with the analytical study of the problem considering Green's solutions to Stokes equation when introducing a line force. To regularize the velocities we proposed to introduce a singular viscosity at the contact line. With this adaption in the model we were indeed able to obtain regular behavior of the velocity towards the contact line, while the pressure behavior remained unaltered. The last two studies focused then on the possibilities offered through the introduction of such contact line forces. First, different conditions for the dynamic contact angle were tested in a two-phase Couette flow. We found that the method is indeed able to model the behavior of the contact line in accordance to such dynamic conditions. However, it became evident that there is some kind of complex interaction between the contact line and bulk boundary condition influencing the behavior of the dynamic contact angle. In the limiting case of a no-slip boundary condition the dynamic contact angle condition is even overwritten altogether. In the last study we examined if the method is able to model contact angle hysteresis. For this we received a positive result with the method replicating pinning and stick-slip behavior of the contact lines as expected from the prescribed conditions.

In Section 7.2 evaporation and the second phase are included again, but for the moment any movement of the interface is excluded. Over the course of that section the evaporation model, Section 2.6.2, at the contact line is discussed. It is observed that this model is in contradiction with the impermeability of the wall at the contact line. The effect and possible resolution of this contradiction is investigated in a series of convergence studies. The experimental orders of convergence in pressure, velocity and temperature in test cases excluding and including evaporation and under conditions where the contradiction is or is not present are investigated. Furthermore, a modification in the model to alleviate the contradiction, namely the introduction of slip on the interface, is proposed. In the absence of evaporation we are able to confirm the optimal convergence order for the XDG based discretization. With evaporation present the convergence orders are reduced, but still of order higher than one. Under conditions where the contradiction is present a further decrease in convergence order is observed, that could be recovered through the introduction of slip on the interface. Finally, the findings are emphasized by displaying the profiles of pressure and velocity in the limit as the contact line is approached. In double logarithmic representation the severe singularity in the pressure profile when the contradiction is present becomes visible. With the introduction of slip on the interface this singularity is defused

substantially. The same pressure behavior as in the cases where the contradiction is not present by design is regained.

Subsequently, an experiment of the superordinate project, Sonderforschungsbereich/Collaborative Research Center 1194 (SFB/CRC 1194) (Schweikert et al., 2019), is examined in Section 7.3. In this setup a heated wall is dragged out of a liquid reservoir and the dewetting of the wall is investigated. The real experimental setup proofed to be too challenging for the method, in terms of expected runtime and numerical stability, but a simplified version of this experiment is simulated numerically. For this simplified version, the fluid velocities are assumed to be equal, which effectively decouples the temperature and flow solutions, simplifying the problem, while being an obviously non-physical assumption. We then computed the dewetting of the wall without evaporation and with heat fluxes of different magnitude supplied through the wall. We were able to match the observed contact angles when a stationary state is reached to an analytical prediction derived from the boundary conditions. Additionally, the film thickness observed in this plate coating simulation matches the analytical prediction closely. The chapter closes with a showcase simulation, where heat conduction is calculating in the third phase, i.e. the solid wall, explicitly. It is observed that the solid builds a thermal bridge between the two fluid phases, coupling them thermally and forming a complex temperature field in proximity to the contact line. This showcase emphasizes the importance of including heat transport in the solid, as it displayed a huge impact on the heat fluxes measured at the contact line.

8 Conclusion

To conclude this thesis we want to summarize the contents, highlighting the main advancements and findings. Finally, a small outlook is given on which matters present themselves as most pressing when trying to simulate contact lines and evaporation with the extended discontinuous Galerkin (XDG) method.

8.1 Summary

After introducing the mathematical model used in Chapter 2 and the fundamentals of the numerical method in Chapter 3, the XDG based solver to simulate multiphase flows with evaporation and contact lines is described in Chapter 4. This work then features three chapters with results to single-phase flows (Chapter 5), two-phase flows without contact lines (Chapter 6) and two-phase flows with contact lines (Chapter 7).

Regarding the single-phase flow in Chapter 5, first the Stokes flow through the nip between two printing cylinders is investigated in Section 5.1. The numerical results provide solutions for the pressure and velocity fields as the distance between the cylinders tends towards zero. By following this approach a connection is verified, relating the numerically measured pressure gradients at stagnation points in the flow to experimentally observed finger patterns, belonging to the so-called lamella splitting regime.
This analysis is extended in Section 5.2. There, analytical homogeneous solutions to the Stokes flow between the two cylinders are constructed using the bipolar coordinate (BPC) system. According to these analytical solutions the formation of viscous vortices is possible in the nip. These findings are verified by numerical simulations, using the analytical solution as boundary conditions, and resulting in the same flow patterns further away from the boundaries.

The role of capillary waves in multiphase simulations is reviewed in Section 6.1. It is postulated and then verified that the propagation speed of these waves results in a severe time-step restriction for the proposed method. This restricting necessitates to scale the time-step size in relation to the grid size as $\Delta t \propto h^{1.5}$.
In Section 6.2 the idea of a hybrid phase field level set method, combining a sharp interface flow solution with a diffuse interface level set solution is explored. It is found that the phase field level set method has some advantages with respect to overall stability and not requiring an additional reinitialization. However, this is offset by the disadvantages, namely that it is not clear how to choose the additional parameters for the phase field and that it is computationally more expensive to solve, due to the implicit nonlinear solution procedure. Further, the contact angle boundary condition for level set and flow solution do not have the same fix points. Therefore, this hybrid method is not further pursued.

Some additional insights on the behavior of the solver are presented in Section 6.3. First, the sensitivity of the achievable convergence orders in dependence of the boundary conditions is investigated. It turned out that even the prescription of smooth boundary values can result in a decay of convergence order. It is therefore of utmost importance to appropriately choose the boundary conditions if high order convergence is the aim. Second, the optimal approximation orders for the coupling between temperature and velocity fields is tested. The results indicate that in opposition to what is chosen throughout this work, a temperature field of one polynomial order higher than the velocity field is optimal, when evaporation is included. However, the results are not conclusive and additional numerical analysis of this matter is necessary.
Finally, Section 6.4 validates the implementation of evaporation in the XDG method. To this end a series of established 1D, 2D and 3D test cases is computed. The results are compared to analytical and other numerical solutions from literature and show good agreement. With the XDG based method similar errors are achieved, while using less degrees of freedom (DOFs). For the 3D test case even second order spatial convergence is obtained.

For the last result Chapter 7 finally the contact line is included. In Section 7.1 the dynamics of the contact line are reviewed. First, a droplet is placed on a plate and fixed in place, while capillary effects are turned off. The wall is then drawn out from under the droplet and the influence of the wall boundary condition on the flow in the sharp corners are investigated. The singularities arising in the pressure and velocity fields near the contact line match the predictions obtained from theoretical analysis. For the second test, the plate is stationary and capillary effects are switched on. The static contact angle is prescribed such that the droplet is not in equilibrium. Thereby, a contact line force is present, trying to move the contact line towards the equilibrium state. Again, singularities in the pressure and velocity fields are observable, caused by the introduction of a line force into the model. Finally, an approach is suggested to transfer the singularity from the velocity field into the viscosity, which is modeled based on the distance to the contact line. This procedure makes it possible to regularize the velocity field.
Another test confirms the behavior of the dynamic contact angle in relation to the slip velocity as prescribed by the contact angle model. A good agreement of the expected with the actually obtained relation is achieved. However, the dynamic contact angle in actual simulations is not only governed by the contact angle condition, but also influenced by the slip boundary condition set for the bulk of the fluid. At last it is showcased how more complex wetting behavior can be taken into account in the presented method. This is demonstrated at the example of contact angle hysteresis for a sliding droplet.
When including evaporation into the simulation of wetting a contradiction in the interface and wall boundary conditions of the used model can be observed. Section 7.2 investigates the influence this contradiction poses onto the numerical solution. It is observed that the presence of this contradiction results in a reduced convergence order of the scheme. To resolve this issue the use of slip on the interface is proposed and implemented. This adapted model does not possess the contradiction anymore and it is possible to regain a higher convergence order, albeit not the optimal one.
In the last section, Section 7.3, it is attempted to calculate a real experiment, conducted as part of the Sonderforschungsbereich/Collaborative Research Center 1194 (SFB/CRC 1194). There a heated wall is dragged out of a liquid reservoir. The amount of heat supplied influences strongly the observed wetting behavior. However, due to the limitations in solver stability and time-step restriction the numerical setup is drastically simplified. Nevertheless, the simplified setup makes it possible to draw a few meaningful conclusions. First, the thickness of the film forming on the wall when no evaporation is presented is in good agreement with theoretical predictions. When

evaporation is introduced in varying amounts, stronger evaporation leads to shorter and thinner films. Additionally, the way the heat flux boundary condition is applied, makes it possible to predict the contact angle that is approached when the system reaches a dynamic equilibrium. Indeed the measured angles approach these predictions asymptotically. Finally, it is showcased that to obtain a more accurate representation of the heat fluxes near the three-phase contact line it is necessary to include heat transfer in the solid wall explicitly in the simulation.

Finally, we would like to return to the objective formulated at the beginning. We succeeded in implementing the XDG method to simulate multiphase flows with evaporation and contact lines. The method is verified in multiple test cases and then used as suggested to zoom into the contact line. We presented multiple investigations focusing on the behavior of the used wetting/evaporation model at the contact line and experimented with several extensions to the models. Thereby, we were able to demonstrate the capability of the method to be used as a tool in the development and evaluation of novel multiphase models. This work, therefore, contributes significantly to the advancement of the XDG method for coupled multiphysics multiphase problems.

8.2 Outlook

During some of the test cases conducted as part of this thesis the capillary time-step restriction proved to be very limiting, necessitating an otherwise unnecessary small time-step size. This resulted in greatly prolonged simulation times and made the computation of some tests unfeasible. This applies in particular to calculations in which material and process properties from practical applications are to be used. It is therefore of great importance to breach this capillary time-step restriction and also to stabilize the coupling between interface and flow solution. Possible approaches include to construct an implicit fully coupled solver that computes the interface and flow solutions without a splitting procedure. Another idea is to stabilize the method by blending over from a diffuse interface solution to the sought after sharp interface one in an iterative relaxation scheme.

The sole setting for evaporation in this work were single component systems, where the mass transfer is caused by heat fluxes at the interface, staying at saturation temperature. However, there are also other modes, which can play a role in real-life applications. This includes mass transfer at the interface due to concentration gradients, e.g. the evaporation of a volatile liquid into a surrounding gas, or isothermal evaporation/condensation caused by a change in ambient pressure. In the implemented method such effects are not yet regarded and would require additional extension or even different models to be considered.

At last it was discovered that the method can be used as a kind of detector for irregularities, in particular near the contact line, in the models used. It is still an open question how to construct a completely singularity free hydrodynamic sharp interface model. A possible route to achieve this task could be to include several regularizing microscopic effects. However, there the question arises how these can be made accessible without resolving microscopic scales explicitly, which is usually not wanted for performance reasons, for example.

Bibliography

Amestoy, P. R., Duff, I. S., L'Excellent, J.-Y., and Koster, J. (2001). "A Fully Asynchronous Multifrontal Solver Using Distributed Dynamic Scheduling". In: *SIAM Journal on Matrix Analysis and Applications* 23.1, pp. 15–41. ISSN: 0895-4798. DOI: 10.1137/S0895479899358194.

Amestoy, P. R., Guermouche, A., L'Excellent, J.-Y., and Pralet, S. (2006). "Hybrid scheduling for the parallel solution of linear systems". In: *Parallel Computing* 32.2, pp. 136–156. ISSN: 01678191. DOI: 10.1016/j.parco.2005.07.004.

Anderson, D. M., McFadden, G. B., and Wheeler, A. A. (1998). "DIFFUSE-INTERFACE METHODS IN FLUID MECHANICS". In: *Annual Review of Fluid Mechanics* 30.1, pp. 139–165. ISSN: 0066-4189. DOI: 10.1146/annurev.fluid.30.1.139.

Arnold, D. N., Brezzi, F., Cockburn, B., and Marini, L. D. (2002). "Unified Analysis of Discontinuous Galerkin Methods for Elliptic Problems". In: *SIAM Journal on Numerical Analysis* 39.5, pp. 1749–1779. ISSN: 0036-1429. DOI: 10.1137/S0036142901384162.

Badalassi, V. E., Ceniceros, H. D., and Banerjee, S. (2003). "Computation of multiphase systems with phase field models". In: *Journal of Computational Physics* 190.2, pp. 371–397. ISSN: 00219991. DOI: 10.1016/S0021-9991(03)00280-8.

Bastian, P. and Engwer, C. (2009). "An unfitted finite element method using discontinuous Galerkin". In: *International Journal for Numerical Methods in Engineering* 79.12, pp. 1557–1576. ISSN: 0029-5981. DOI: 10.1002/nme.2631.

Basting, C. and Kuzmin, D. (2013). "A minimization-based finite element formulation for interface-preserving level set reinitialization". In: *Computing* 95.S1, pp. 13–25. ISSN: 0010-485X. DOI: 10.1007/s00607-012-0259-z.

Baus, M. and Tejero, C. F. (2021). *Equilibrium Statistical Physics*. Cham: Springer International Publishing. ISBN: 978-3-030-75431-0. DOI: 10.1007/978-3-030-75432-7.

Beck, L. and Kummer, F. (2023). *High-Order Numerical Integration on Domains Bounded by Intersecting Level Sets*. arXiv: 2308.10698 [math.NA].

Benkreira, H. and Cohu, O. (1998). "Direct forward gravure coating on unsupported web". In: *Chemical engineering science* 55.6, pp. 1223–1231.

Blake, T. D. (2006). "The physics of moving wetting lines". In: *Journal of colloid and interface science* 299.1, pp. 1–13. DOI: 10.1016/j.jcis.2006.03.051.

Bluman, G. W. and Gregory, R. D. (1985). "On transformations of the biharmonic equation". In: *Mathematika* 32.1, pp. 118–130. DOI: 10.1112/s0025579300010937.

Bonn, D., Eggers, J., Indekeu, J., Meunier, J., and Rolley, E. (2009). "Wetting and spreading". In: *Reviews of Modern Physics* 81.2, pp. 739–805. ISSN: 0034-6861. DOI: 10.1103/RevModPhys.81.739.

Bornemann, N., Sauer, H. M., and Dörsam, E. (2011). "Gravure Printed Ultrathin Layers of Small-Molecule Semiconductors on Glass". In: *J. Imaging Sci. Technol.* 55, p. 040201. DOI: 10.2352/J.ImagingSci.Technol.2011.55.4.040201.

Brumm, P., Sauer, H. M., and Dörsam, E. (2019). “Scaling Behavior of Pattern Formation in the Flexographic Ink Splitting Process”. In: *Colloids and Interfaces* 3.1, p. 37. DOI: doi.org/10.3390/colloids3010037.

Brumm, P., Weber, T. E., Sauer, H. M., and Dörsam, E. (2021). “Ink splitting in gravure printing: localization of the transition from dots to fingers”. In: *J. Print Media Technol. Res.* 10.2, pp. 81–93. DOI: 10.14622/JPMTR-2016.

Bureš, L. and Sato, Y. (2021a). “Direct numerical simulation of evaporation and condensation with the geometric VOF method and a sharp-interface phase-change model”. In: *International Journal of Heat and Mass Transfer* 173, p. 121233. ISSN: 00179310. DOI: 10.1016/j.ijheatmasstransfer.2021.121233.

Bureš, L. and Sato, Y. (2021b). “On the modelling of the transition between contact-line and microlayer evaporation regimes in nucleate boiling”. In: *Journal of Fluid Mechanics* 916. ISSN: 0022-1120. DOI: 10.1017/jfm.2021.204.

Caginalp, G. (1986). “An analysis of a phase field model of a free boundary”. In: *Archive for Rational Mechanics and Analysis* 92.3, pp. 205–245. ISSN: 0003-9527. DOI: 10.1007/BF00254827.

Cahn, J. W. (1959). “Free Energy of a Nonuniform System. II. Thermodynamic Basis”. In: *The Journal of Chemical Physics* 30.5, pp. 1121–1124. ISSN: 0021-9606. DOI: 10.1063/1.1730145.

Cahn, J. W. and Hilliard, J. E. (1958). “Free Energy of a Nonuniform System. I. Interfacial Free Energy”. In: *The Journal of Chemical Physics* 28.2, pp. 258–267. ISSN: 0021-9606. DOI: 10.1063/1.1744102.

Cahn, J. W. and Hilliard, J. E. (1959). “Free Energy of a Nonuniform System. III. Nucleation in a Two–Component Incompressible Fluid”. In: *The Journal of Chemical Physics* 31.3, pp. 688–699. ISSN: 0021-9606. DOI: 10.1063/1.1730447.

Carvalho, M. S. and Scriven, L. E. (1997). “Deformable roll coating flows: steady state and linear perturbation analysis”. In: *J. Fluid Mech.* 339, pp. 143–172.

Casademunt, J. (2004). “Viscous fingering as a paradigm of interfacial pattern formation: recent results and new challenges”. In: *Chaos (Woodbury, N.Y.)* 14.3, pp. 809–824. ISSN: 1054-1500. DOI: 10.1063/1.1784931.

Cen, J., Kitsomboonloha, R., and Subramanian, V. (2014). “Cell Filling in Gravure Printing for Printed Electronics”. In: *Langmuir* 30, pp. 13716–13726. DOI: dx.doi.org/10.1021/la503180a.

Chandrasekhar, S. (1961). *Hydrodynamic and hydromagnetic stability*.

Cheng, Y. and Shu, C.-W. (2007). “A discontinuous Galerkin finite element method for directly solving the Hamilton–Jacobi equations”. In: *Journal of Computational Physics* 223.1, pp. 398–415. ISSN: 00219991. DOI: 10.1016/j.jcp.2006.09.012.

Cockburn, B. and Shu, C.-W. (2001). “Runge–Kutta Discontinuous Galerkin Methods for Convection-Dominated Problems”. In: *Journal of Scientific Computing* 16.3, pp. 173–261. ISSN: 08857474. DOI: 10.1023/A:1012873910884.

Colinet, P. and Rednikov, A. (2011). “On integrable singularities and apparent contact angles within a classical paradigm”. In: *The European Physical Journal Special Topics* 197.1, pp. 89–113. ISSN: 1951-6355. DOI: 10.1140/epjst/e2011-01443-x.

Coyle, D. J., Macosko, C. W., and Scriven, L. E. (1990). “The Fluid Dynamics of Reverse Roll Coating”. In: *AlChE Journal* 36.2, pp. 161–174.

Deegan, R. D., Bakajin, O., Dupont, T. F., Huber, G., Nagel, S. R., and Witten, T. A. (2000). “Contact line deposits in an evaporating drop”. In: *Physical review. E, Statistical physics, plasmas, fluids, and related interdisciplinary topics* 62.1, pp. 756–765. ISSN: 1063-651X. DOI: 10.1103/physreve.62.756.

Denner, F., Evrard, F., and van Wachem, B. (2022). “Breaching the capillary time-step constraint using a coupled VOF method with implicit surface tension”. In: *Journal of Computational Physics* 459, p. 111128. ISSN: 00219991. DOI: 10.1016/j.jcp.2022.111128.

Denner, F. and van Wachem, B. G. (2015). “Numerical time-step restrictions as a result of capillary waves”. In: *Journal of Computational Physics* 285, pp. 24–40. ISSN: 00219991. DOI: 10.1016/j.jcp.2015.01.021.

Dhir, V. K., Warrier, G. R., and Aktinol, E. (2013). “Numerical Simulation of Pool Boiling: A Review”. In: *Journal of Heat Transfer* 135.6. ISSN: 0022-1481. DOI: 10.1115/1.4023576.

Di Pietro, D. A. and Ern, A. (2012). *Mathematical Aspects of Discontinuous Galerkin Methods*. Vol. 69. Berlin, Heidelberg: Springer Berlin Heidelberg. ISBN: 978-3-642-22979-4. DOI: 10.1007/978-3-642-22980-0.

Diddens, C. (2017). “Detailed finite element method modeling of evaporating multi-component droplets”. In: *Journal of Computational Physics* 340, pp. 670–687. ISSN: 00219991. DOI: 10.1016/j.jcp.2017.03.049.

Dodds, S., Carvalho, M. S., and Kumar, S. (2009). “Stretching and slipping of liquid bridges near plates and cavities”. In: *Phys. Fluids* 21, p. 092103. DOI: 10.1063/1.3212963.

Dodds, S., Carvalho, M. S., and Kumar, S. (2011a). “Stretching Liquid Bridges with Bubbles: The Effect of Air Bubbles on Liquid Transfer”. In: *Langmuir* 27.5, pp. 1556–1559. DOI: 10.1021/la104369z.

Dodds, S., Carvalho, M. S., and Kumar, S. (2011b). “Stretching liquid bridges with moving contact lines: The role of inertia”. In: *Phys. Fluids* 23, p. 092101. DOI: 10.1063/1.3623427.

Dodds, S., Carvalho, M. S., and Kumar, S. (2012). “The dynamics of three-dimensional liquid bridges with pinned and moving contact lines”. In: *J. Fluid. Mech.* 707, pp. 521–540. DOI: 10.1017/jfm.2012.296.

Dolejší, V. and Feistauer, M. (2015). *Discontinuous Galerkin Method*. Vol. 48. Cham: Springer International Publishing. ISBN: 978-3-319-19266-6. DOI: 10.1007/978-3-319-19267-3.

Dorrepaal, J. M. and O’Neill, M. E. (1979). “The existence of free eddies in a streaming stokes flow”. In: *The Quarterly Journal of Mechanics and Applied Mathematics* 32.2, pp. 95–107. DOI: 10.1093/qjmam/32.2.95.

Elsayad, S., Morsy, F., El-Sherbiny, S., and Abdou, E. (2002). “Some factors affecting ink transfer in gravure printing”. In: *Pigment & Resin Technology* 31.4, pp. 234–240. ISSN: 1559-128X. DOI: 10.1108/03699420210432429.

Feng, X., Li, Y., and Xing, Y. (2016). “Analysis of Mixed Interior Penalty Discontinuous Galerkin Methods for the Cahn–Hilliard Equation and the Hele–Shaw Flow”. In: *SIAM Journal on Numerical Analysis* 54.2, pp. 825–847. ISSN: 0036-1429. DOI: 10.1137/15M1009962.

Franz, B., Sielaff, A., and Stephan, P. (2021). “Numerical Investigation of Successively Nucleating Bubbles During Subcooled Flow Boiling of FC-72 in Microgravity”. In: *Microgravity Science and Technology* 33.2. ISSN: 0938-0108. DOI: 10.1007/s12217-021-09876-6.

Fricke, M., Köhne, M., and Bothe, D. (2019). “A kinematic evolution equation for the dynamic contact angle and some consequences”. In: *Physica D: Nonlinear Phenomena* 394, pp. 26–43. ISSN: 01672789. DOI: 10.1016/j.physd.2019.01.008.

Fullana, T., Kulkarni, Y., Fricke, M., Popinet, S., Afkhami, S., Bothe, D., and Zaleski, S. (2023). *A consistent treatment of dynamic contact angles in the sharp-interface framework with the generalized Navier boundary condition*. DOI: 10.5281/zenodo.10142048.

Gal, C. G. and Grasselli, M. (2010). “Asymptotic behavior of a Cahn–Hilliard–Navier–Stokes system in 2D”. In: *Annales de l’Institut Henri Poincaré C, Analyse non linéaire* 27.1, pp. 401–436. ISSN: 0294-1449. DOI: 10.1016/j.anihpc.2009.11.013.

Gallot, S., Hulin, D., and Lafontaine, J. (2004). *Riemannian Geometry*. Berlin, Heidelberg: Springer Berlin Heidelberg. ISBN: 978-3-540-20493-0. DOI: 10.1007/978-3-642-18855-8.

Gaskell, P. H., Innes, G. E., and Savage, M. D. (1998). "An experimental investigation of meniscus roll coating". In: *Journal of Fluid Mechanics* 355, pp. 17–44. ISSN: 0022-1120. DOI: 10.1017/S0022112097007398.

Gell-Mann, M. and Low, F. E. (1954). "Quantum Electrodynamics at Small Distances". In: *Phys. Rev.* 95 (5), pp. 1300–1312. DOI: 10.1103/PhysRev.95.1300.

Gerbeau, J.-F. and Lelièvre, T. (2009). "Generalized Navier boundary condition and geometric conservation law for surface tension". In: *Computer Methods in Applied Mechanics and Engineering* 198.5-8, pp. 644–656. ISSN: 00457825. DOI: 10.1016/j.cma.2008.09.011.

Gibou, F., Chen, L., Nguyen, D., and Banerjee, S. (2007). "A level set based sharp interface method for the multiphase incompressible Navier–Stokes equations with phase change". In: *Journal of Computational Physics* 222.2, pp. 536–555. ISSN: 00219991. DOI: 10.1016/j.jcp.2006.07.035.

Gottlieb, S. and Shu, C.-W. (1998). "Total variation diminishing Runge-Kutta schemes". In: *Mathematics of Computation* 67.221, pp. 73–85. ISSN: 0025-5718. DOI: 10.1090/S0025-5718-98-00913-2.

Gründing, D., Smuda, M., Antritter, T., Fricke, M., Rettenmaier, D., Kummer, F., Stephan, P., Marschall, H., and Bothe, D. (2020). "A comparative study of transient capillary rise using direct numerical simulations". In: *Applied Mathematical Modelling* 86, pp. 142–165. ISSN: 0307904X. DOI: 10.1016/j.apm.2020.04.020.

Hairer, E., Nørsett, S. P., and Wanner, G. (1993). *Nonstiff problems*. 2., rev. ed. Vol. 8. Springer series in computational mathematics. Berlin: Springer. ISBN: 978-3-540-56670-0.

Hairer, E. and Wanner, G. (1996). *Solving Ordinary Differential Equations II*. Vol. 14. Berlin, Heidelberg: Springer Berlin Heidelberg. ISBN: 978-3-642-05220-0. DOI: 10.1007/978-3-642-05221-7.

Happel, J. and Brenner, H. (1981). *Low Reynolds number hydrodynamics*. Springer Netherlands. DOI: 10.1007/978-94-009-8352-6.

Hoda, N. and Kumar, S. (2008). "Boundary integral simulations of liquid emptying from a model gravure cell". In: *Phys. Fluids* 20, p. 092106. DOI: 10.1063/1.2980035.

Holden, H., Karlsen, K. H., Lie, K.-A., and Risebro, N. H. (2010). *Splitting Methods for Partial Differential Equations with Rough Solutions*. EMS Press. ISBN: 978-3-03719-078-4. DOI: 10.4171/078.

Holland, F. A. and Bragg, R. (1995). *Fluid Flow for Chemical Engineers*. Elsevier. ISBN: 9780340610589. DOI: 10.1016/B978-0-340-61058-9.X5000-2.

Huang, C. H., Carvalho, M. S., and Kumar, S. (2016). "Stretching liquid bridges with moving contact lines: comparison of liquid-transfer predictions and experiments". In: *Soft Matter* 12, pp. 7457–7469. DOI: 10.1039/c6sm00876c.

Huang, W.-X., Lee, S.-H., Sung, H. J., Lee, T.-M., and Kim, D.-S. (2008). "Simulation of liquid transfer between separating walls for modeling micro-gravure-offset printing". In: *International Journal of Heat and Fluid Flow* 29.5, pp. 1436–1446. ISSN: 0142727X. DOI: 10.1016/j.ijheatfluidflow.2008.07.002.

Hübner, G. (1991). "Ein Beitrag zum Problem der Flüssigkeitsspaltung in der Drucktechnik". Dissertation. TU Darmstadt.

Huh, C. and Scriven, L. (1971). "Hydrodynamic model of steady movement of a solid/liquid/fluid contact line". In: *Journal of colloid and interface science* 35.1, pp. 85–101. DOI: 10.1016/0021-9797(71)90188-3.

Hysing, S., Turek, S., Kuzmin, D., Parolini, N., Burman, E., Ganesan, S., and Tobiska, L. (2009). "Quantitative benchmark computations of two–dimensional bubble dynamics". In: *International Journal for Numerical Methods in Fluids* 60.11, pp. 1259–1288. ISSN: 0271-2091. DOI: 10.1002/fld.1934.

Ishii, M. and Hibiki, T. (2011). *Thermo-Fluid Dynamics of Two-Phase Flow*. New York, NY: Springer New York. ISBN: 978-1-4419-7984-1. DOI: 10.1007/978-1-4419-7985-8.

Jeffery, G. B. (1922). "The rotation of two circular cylinders in a viscous fluid". en. In: *Proc. R. Soc. Lond. A Math. Phys. Sci.* 101.709, pp. 169–174.

Kay, D., Styles, V., and Süli, E. (2009). "Discontinuous Galerkin Finite Element Approximation of the Cahn–Hilliard Equation with Convection". In: *SIAM Journal on Numerical Analysis* 47.4, pp. 2660–2685. ISSN: 0036-1429. DOI: 10.1137/080726768.

Kazakova, A. O. (2020). "Application of bipolar coordinates to the analysis of the structure of viscous fluid flow between two rotating cylinders". In: *Journal of Physics: Conference Series* 1679, p. 022068. DOI: 10.1088/1742-6596/1679/2/022068.

Kennedy, C. A. and Carpenter, M. H. (2016). *Diagonally Implicit Runge-Kutta Methods for Ordinary Differential Equations. A Review*. Ed. by NASA Langley Research Center.

Khandavalli, S., Lee, J. A., Pasquali, M., and Rothstein, J. P. (2015). "The effect of shear-thickening on liquid transfer from an idealized gravure cell". In: *J. Non-Newton. Fluid Mech.* 221, pp. 55–65. DOI: 10.1016/j.jnnfm.2015.03.007.

Khandavalli, S. and Rothstein, J. P. (2017). "Ink transfer of non-Newtonian fluids from an idealized gravure cell: The effect of shear and extensional deformation". In: *J. Non-Newton. Fluid Mech.* 243, pp. 16–26. DOI: 10.1016/j.jnnfm.2017.02.005.

Kummer, F. (2017). "Extended discontinuous Galerkin methods for two-phase flows: the spatial discretization". In: *International Journal for Numerical Methods in Engineering* 109.2, pp. 259–289. ISSN: 0029-5981. DOI: 10.1002/nme.5288.

Kummer, F. and Müller, B. (2021). *Script to High-Accuracy methods for Computational Fluid Dynamics*. Technical University Darmstadt, Chair of Fluid Dynamics.

Kummer, F., Müller, B., Klein, B., Emamy, N., Mousavi, R., Klingenberg, D., Benjamin, D., Geisenhofer, M., Smuda, M., Dierkes, D., Kikker, A., Krause, D., Utz, T., Kallendorf, C., Krämer-Eis, S., and Vandergrift, J. (2023). *BoSSS*. DOI: 10.5281/ZENODO.8386633.

Kummer, F., Müller, B., and Utz, T. (2018). "Time integration for extended discontinuous Galerkin methods with moving domains". In: *International Journal for Numerical Methods in Engineering* 113.5, pp. 767–788. ISSN: 0029-5981. DOI: 10.1002/nme.5634.

Kunkelmann, C. and Stephan, P. (2009). "CFD Simulation of Boiling Flows Using the Volume-of-Fluid Method within OpenFOAM". In: *Numerical Heat Transfer, Part A: Applications* 56.8, pp. 631–646. ISSN: 1040-7782. DOI: 10.1080/10407780903423908.

Kunkelmann, C. and Stephan, P. (2010). "Numerical simulation of the transient heat transfer during nucleate boiling of refrigerant HFE-7100". In: *International Journal of Refrigeration* 33.7, pp. 1221–1228. ISSN: 01407007. DOI: 10.1016/j.ijrefrig.2010.07.013.

Landau, L. D. and Levich, B. (1942). "Dragging of a Liquid by a Moving Plate". In: *Acta Physicochim. URSS* 17. Ed. by D. ter Haar. DOI: 10.1016/b978-0-08-010586-4.50053-5.

Liu, C. and Riviere, B. (2018). *Numerical analysis of a discontinuous Galerkin method for Cahn-Hilliard-Navier-Stokes equations*. DOI: 10.48550/arXiv.1807.02725.

Lukyanov, A. V. and Pryer, T. (2017). "Hydrodynamics of Moving Contact Lines: Macroscopic versus Microscopic". In: *Langmuir : the ACS journal of surfaces and colloids* 33.34, pp. 8582–8590. DOI: 10.1021/acs.langmuir.7b02409.

Manzanero, J., Rubio, G., Kopriva, D. A., Ferrer, E., and Valero, E. (2020). "Entropy–stable discontinuous Galerkin approximation with summation–by–parts property for the incompressible Navier–Stokes/Cahn–Hilliard system". In: *Journal of Computational Physics* 408, p. 109363. ISSN: 00219991. DOI: 10.1016/j.jcp.2020.109363.

Marengo, M. and Coninck, J. de (2022). *The Surface Wettability Effect on Phase Change*. Cham: Springer International Publishing. DOI: 10.1007/978-3-030-82992-6.

Marsden, J. E., Sirovich, L., Antman, S. S., Hesthaven, J. S., and Warburton, T. (2008). *Nodal Discontinuous Galerkin Methods*. Vol. 54. New York, NY: Springer New York. ISBN: 978-0-387-72065-4. DOI: 10.1007/978-0-387-72067-8.

Marsden, J. E. and Hughes, T. J. R. (1994). *Mathematical foundations of elasticity*. Dover ed., ... an unabridged, corr. republ. of the first publ. Dover books on mathematics. Mineola, NY: Dover. ISBN: 9780486678658.

Mirjalili, S., Jain, S. S., and Dodd, M. (2017). "Interface-capturing methods for two-phase flows: An overview and recent developments". In: *Center for Turbulence Research Annual Research Briefs* 2017.117-135, p. 13.

Moffatt, H. K. (1964). "Viscous and resistive eddies near a sharp corner". In: *Journal of Fluid Mechanics* 18.1, pp. 1–18. DOI: 10.1017/s0022112064000015.

Moon, P. and Spencer, D. E. (1971). *Field Theory Handbook*. Springer Berlin Heidelberg. DOI: 10.1007/978-3-642-83243-7.

Mos, N., Dolbow, J., and Belytschko, T. (1999). "A finite element method for crack growth without remeshing". In: *International Journal for Numerical Methods in Engineering* 46.1, pp. 131–150. ISSN: 0029-5981. DOI: 10.1002/(SICI)1097-0207(19990910)46:1{\textless}131::AID-NME726{\textgreater}3.0.CO;2-J.

Müller, W. (1942). "Ebene Spannungs- und Strömungsfelder mit zwei kreiszylindrischen Grenzen". In: *Ingenieur-Archiv* 13.1, pp. 37–58. DOI: 10.1007/bf02107475.

Newbry, M. (2017). *Water droplets*. URL: https://web.archive.org/web/20170716153904/https%3A//images.unsplash.com/photo-1490713230272-bf236b61ad43 (visited on 05/24/2024).

Osher, S. and Fedkiw, R. P. (2001). "Level Set Methods: An Overview and Some Recent Results". In: *Journal of Computational Physics* 169.2, pp. 463–502. ISSN: 00219991. DOI: 10.1006/jcph.2000.6636.

Osher, S. and Sethian, J. A. (1988). "Fronts propagating with curvature-dependent speed: Algorithms based on Hamilton-Jacobi formulations". In: *Journal of Computational Physics* 79.1, pp. 12–49. ISSN: 00219991. DOI: 10.1016/0021-9991(88)90002-2.

Owkes, M. and Desjardins, O. (2013). "A discontinuous Galerkin conservative level set scheme for interface capturing in multiphase flows". In: *Journal of Computational Physics* 249, pp. 275–302. ISSN: 00219991. DOI: 10.1016/j.jcp.2013.04.036.

Pawlowski, R. P., Shadid, J. N., Simonis, J. P., and Walker, H. F. (2006). "Globalization Techniques for Newton–Krylov Methods and Applications to the Fully Coupled Solution of the Navier–Stokes Equations". In: *SIAM Review* 48.4, pp. 700–721. ISSN: 0036-1445. DOI: 10.1137/S0036144504443511.

Pitts, E. and Greiller, J. (1961). "The flow of thin liquid films between rollers". In: *Journal of Fluid Mechanics* 11.1, pp. 33–50. DOI: 10.1017/s0022112061000846.

Polyanin, A. D. (2015). *Handbook of Linear Partial Differential Equations for Engineers and Scientists, Second Edition*. 2nd ed. s.l.: CRC Press. ISBN: 978-1-4665-8149-4.

Prosperetti, A. and Tryggvason, G. (2009). *Computational Methods for Multiphase Flow*. Cambridge University Press. ISBN: 9780521847643. DOI: 10.1017/CBO9780511607486.

Rednikov, A. Y. and Colinet, P. (2019). “Contact-line singularities resolved exclusively by the Kelvin effect: volatile liquids in air”. In: *Journal of Fluid Mechanics* 858, pp. 881–916. ISSN: 0022-1120. DOI: 10.1017/jfm.2018.760.

Rednikov, A. and Colinet, P. (2013). “Singularity-free description of moving contact lines for volatile liquids”. In: *Physical review. E, Statistical, nonlinear, and soft matter physics* 87.1, p. 010401. ISSN: 1539-3755. DOI: 10.1103/PhysRevE.87.010401.

Reed, W. H. and Hill, T. R. (1973). “Triangular mesh methods for the neutron transport equation”. In.

Reusken, A., Xu, X., and Zhang, L. (2017). “Finite element methods for a class of continuum models for immiscible flows with moving contact lines”. In: *International Journal for Numerical Methods in Fluids* 84.5, pp. 268–291. ISSN: 02712091. DOI: 10.1002/fld.4349.

Rieckmann, M. (2024). *The Extended Discontinuous Galerkin Method for Evaporation and Contact Lines: Supplementary Material*. DOI: https://doi.org/10.48328/tudatalib-1492.

Rieckmann, M., Brumm, P., Sauer, H. M., Dörsam, E., and Kummer, F. (2023a). *Supplementary Data: Pressure and shear flow singularities: fluid splitting and printing nip hydrodynamics*. DOI: 10.48328/tudatalib-1057.

Rieckmann, M., Smuda, M., and Kummer, F. (2023b). *Numerical Data: The extended Discontinuous Galerkin method for two-phase flows with evaporation*. DOI: https://doi.org/10.48328/tudatalib-1155.

Rieckmann, M. E., Brumm, P., Sauer, H. M., Dörsam, E., and Kummer, F. (2023c). “Pressure and shear flow singularities: Fluid splitting and printing nip hydrodynamics”. In: *Physics of Fluids* 35.3. ISSN: 1070-6631. DOI: 10.1063/5.0139000.

Rieckmann, M., Brumm, P., Sauer, H. M., Doersam, E., Kummer, F., and TU Darmstadt (2023d). *SUPPLEMENTARY NUMERICAL DATA: Pressure and shear flow singularities: fluid splitting and printing nip hydrodynamics*. DOI: 10.48328/tudatalib-1079.2.

Rieckmann, M., Smuda, M., Stephan, P., and Kummer, F. (2023e). “The extended Discontinuous Galerkin method for two-phase flows with evaporation”. In: *Journal of Computational Physics*, p. 112716. ISSN: 00219991. DOI: 10.1016/j.jcp.2023.112716.

Ryck, A. de and Quéré, D. (1998). “Gravity and Inertia Effects in Plate Coating”. In: *Journal of colloid and interface science* 203.2, pp. 278–285. DOI: 10.1006/jcis.1998.5444.

Saffman, P. G. and Taylor, G. (1958). “The penetration of a fluid into a porous medium or Hele-Shaw cell containing a more viscous liquid”. In: *British Journal of Applied Physics* 245.1242, pp. 312–329. ISSN: 0080-4630. DOI: 10.1098/rspa.1958.0085.

Sato, Y. and Ničeno, B. (2013). “A sharp-interface phase change model for a mass-conservative interface tracking method”. In: *Journal of Computational Physics* 249, pp. 127–161. ISSN: 00219991. DOI: 10.1016/j.jcp.2013.04.035.

Sauer, H. M., Daume, D., and Dörsam, E. (2015). “Lubrication theory of ink hydrodynamics in the flexographic printing nip”. In: *J. Print Media Technol. Res* 4.3, pp. 163–172. DOI: 10.14622/JPMTR-1426.

Sauer, H. M., Roisman, I. V., Dörsam, E., and Tropea, C. (2018). “Fast liquid sheet and filament dynamics in the fluid splitting process”. In: *Colloids and Surfaces A* 557, pp. 20–27. DOI: 10.1016/j.colsurfa.2018.05.101.

Saye, R. I. (2015). “High-Order Quadrature Methods for Implicitly Defined Surfaces and Volumes in Hyperrectangles”. In: *SIAM Journal on Scientific Computing* 37.2, A993–A1019. ISSN: 1064-8275. DOI: 10.1137/140966290.

Schäfer, J. (2020). “In situ Untersuchung der hochdynamischen Grenzflächeninstabilität im Zylinderspalt”. PhD thesis. TU Darmstadt. DOI: 10.25534/tuprints-00014204.

Schäfer, J., Roisman, I. V., Sauer, H. M., and Dörsam, E. (2019). “Millisecond fluid pattern formation in the nip of a gravure printing machine”. In: *Colloids and Surfaces A* 575, pp. 222–229. DOI: 10.1016/j.colsurfa.2019.04.085.

Schenk, O. and Gärtner, K. (2006). “On Fast Factorization Pivoting Methods for Sparse Symmetric Indefinite Systems”. In: *Electronic Transactions on Numerical Analysis* 23, pp. 158–179.

Schwartz, L. W. (2002). “Numerical modeling of liquid withdrawal from gravure cavities in coating operations; the effect of cell pattern”. In: *J. Eng. Math.* 42, pp. 243–253.

Schweikert, K., Sielaff, A., and Stephan, P. (2019). “On the transition between contact line evaporation and microlayer evaporation during the dewetting of a superheated wall”. In: *International Journal of Thermal Sciences* 145, p. 106025. ISSN: 12900729. DOI: 10.1016/j.ijthermalsci.2019.106025.

Scriven, L. E. (1959). “On the dynamics of phase growth”. In: *Chemical Engineering Science* 10.1-2, pp. 1–13. ISSN: 00092509. DOI: 10.1016/0009-2509(59)80019-1.

Seppecher, P. (1996). “Moving contact lines in the Cahn-Hilliard theory”. In: *International Journal of Engineering Science* 34.9, pp. 977–992. ISSN: 00207225. DOI: 10.1016/0020-7225(95)00141-7.

Shahbazi, K. (2005). “An explicit expression for the penalty parameter of the interior penalty method”. In: *Journal of Computational Physics* 205.2, pp. 401–407. ISSN: 00219991. DOI: 10.1016/j.jcp.2004.11.017.

Shahbazi, K., Fischer, P. F., and Ethier, C. R. (2007). “A high-order discontinuous Galerkin method for the unsteady incompressible Navier–Stokes equations”. In: *Journal of Computational Physics* 222.1, pp. 391–407. ISSN: 00219991. DOI: 10.1016/j.jcp.2006.07.029.

Slattery, J. C. (2005). *Advanced transport phenomena*. Cambridge series in chemical engineering. Cambridge et al.: Cambridge University Press. ISBN: 9780511800238. DOI: 10.1017/CBO9780511800238.

Slattery, J. C., Sagis, L., and Oh, E.-S. (2007). *Interfacial transport phenomena*. 2. ed. New York, NY: Springer. ISBN: 0-387-38438-3.

Smith, G. (2008). “Newton’s Philosophiae Naturalis Principia Mathematica”. In: *The Stanford Encyclopedia of Philosophy*. Ed. by E. N. Zalta. Winter 2008. https://plato.stanford.edu/archives/win2008/entries/newton-principia/, Accessed: 24.05.2024. Metaphysics Research Lab, Stanford University.

Smuda, M. (2021). “Direct Numerical Simulation of Multi-Phase Flows using Extended Discontinuous Galerkin Methods”. PhD thesis. TU Darmstadt. DOI: 10.26083/TUPRINTS-00017376.

Smuda, M. and Kummer, F. (2021). “The extended discontinuous Galerkin method adapted for moving contact line problems via the generalized Navier boundary condition”. In: *International Journal for Numerical Methods in Fluids* 93.9, pp. 2921–2945. ISSN: 0271-2091. DOI: 10.1002/fld.5016.

Smuda, M. and Kummer, F. (2022). “On a marching level–set method for extended discontinuous Galerkin methods for incompressible two–phase flows: Application to two–dimensional settings”. In: *International Journal for Numerical Methods in Engineering* 123.1, pp. 197–225. ISSN: 0029-5981. DOI: 10.1002/nme.6853.

Snoeijer, J. H. and Andreotti, B. (2013). “Moving Contact Lines: Scales, Regimes, and Dynamical Transitions”. In: *Annual Review of Fluid Mechanics* 45.1, pp. 269–292. ISSN: 0066-4189. DOI: 10.1146/annurev-fluid-011212-140734.

Son, G. and Dhir, V. K. (1998). “Numerical Simulation of Film Boiling Near Critical Pressures With a Level Set Method”. In: *Journal of Heat Transfer* 120.1, pp. 183–192. ISSN: 0022-1481. DOI: 10.1115/1.2830042.

Springer-Verlag GmbH (2013). *VDI-Wärmeatlas*. Berlin, Heidelberg: Springer Berlin Heidelberg. DOI: 10.1007/978-3-642-19981-3.

Sprittles, J. E. and Shikhmurzaev, Y. D. (2011). "Viscous flow in domains with corners: Numerical artifacts, their origin and removal". In: *Computer Methods in Applied Mechanics and Engineering* 200.9-12, pp. 1087–1099. ISSN: 00457825. DOI: 10.1016/j.cma.2010.12.005.

Stephan, P., Schaber, K., Stephan, K., and Mayinger, F. (2013). *Thermodynamik: Grundlagen und technische Anwendungen*. 19., erg. Aufl. Springer-Lehrbuch. Berlin: Springer. ISBN: 9783642300981. DOI: 10.1007/978-3-642-30098-1.

Stückelberg, E. C. G. and Petermann, A. (1953). "On the Normalizations of Quantum Theory Constants". In: *Helv. Phys. Acta* 2, p. 499.

Tanguy, S., Ménard, T., and Berlemont, A. (2007). "A Level Set Method for vaporizing two-phase flows". In: *Journal of Computational Physics* 221.2, pp. 837–853. ISSN: 00219991. DOI: 10.1016/j.jcp.2006.07.003.

Toprak, M., Rieckmann, M., and Kummer, F. (2024). *Cell agglomeration strategy for cut cells in eXtended discontinuous Galerkin methods*. DOI: 10.48550/arXiv.2404.15285.

Tryggvason, G., Bunner, B., Ebrat, O., and Tauber, W. (1998). "Computations of multiphase flows by a finite difference/front tracking method. I. Multi-fluid flows". In: *Lecture Series-von Karman Institute For Fluid Dynamics*, pp. 7–7.

Utz, T., Kummer, F., and Oberlack, M. (2017). "Interface-preserving level-set reinitialization for DG-FEM". In: *International Journal for Numerical Methods in Fluids* 84.4, pp. 183–198. ISSN: 0271-2091. DOI: 10.1002/fld.4344.

Voinov, O. V. (1976). "Hydrodynamics of wetting". In: *Fluid Dynamics* 11.5, pp. 714–721. ISSN: 0015-4628. DOI: 10.1007/BF01012963.

Voß, C. (2002). "Analytische Modellierung, experimentelle Untersuchungen und dreidimensionale Gitter-Boltzmann Simulation der quasistatischen und instabilen Farbspaltung". PhD thesis. Wuppertal, Germany: University of Wuppertal.

Wakiya, S. (1975a). "Application of Bipolar Coordinates to the Two-Dimensional Creeping Motion of a Liquid. I. Flow over a Projection or a Depression on a Wall". In: *Journal of the Physical Society of Japan* 39.4, pp. 1113–1120. DOI: 10.1143/jpsj.39.1113.

Wakiya, S. (1975b). "Application of Bipolar Coordinates to the Two-Dimensional Creeping Motion of a Liquid. II. Some Problems for Two Circular Cylinders in Viscous Fluid". In: *Journal of the Physical Society of Japan* 39.6, pp. 1603–1607. DOI: 10.1143/jpsj.39.1603.

Wakiya, S. (1978). "Application of Bipolar Coordinates to the Two-Dimensional Creeping Motion of a Liquid. III. Separation in Stokes Flows". In: *Journal of the Physical Society of Japan* 45.5, pp. 1756–1763. DOI: 10.1143/jpsj.45.1756.

Wang, J., Wu, Y., Cao, Y., Li, G., and Liao, Y. (2020). "Influence of surface roughness on contact angle hysteresis and spreading work". In: *Colloid and Polymer Science* 298.8, pp. 1107–1112. ISSN: 0303-402X. DOI: 10.1007/s00396-020-04680-x.

Wang, Y. and Cai, J. (2017). "Numerical investigation on bubble evolution during nucleate boiling using diffuse interface method". In: *International Journal of Heat and Mass Transfer* 112, pp. 28–38. ISSN: 00179310. DOI: 10.1016/j.ijheatmasstransfer.2017.04.109.

Welch, S. W. and Wilson, J. (2000). "A Volume of Fluid Based Method for Fluid Flows with Phase Change". In: *Journal of Computational Physics* 160.2, pp. 662–682. ISSN: 00219991. DOI: 10.1006/jcph.2000.6481.

Wells, G. N., Kuhl, E., and Garikipati, K. (2006). "A discontinuous Galerkin method for the Cahn–Hilliard equation". In: *Journal of Computational Physics* 218.2, pp. 860–877. ISSN: 00219991. DOI: 10.1016/j.jcp.2006.03.010.

Wu, J.-T., Carvalho, M. S., and Kumar, S. (2019a). “Effects of Shear and Extensional Rheology on Liquid Transfer between Two Flat Surfaces”. In: *J. Non-Newtonian Fluid Mech.* 274, p. 104173. DOI: 10.1016/j.jnnfm.2019.104173.

Wu, J.-T., Carvalho, M. S., and Kumar, S. (2019b). “Emptying of Gravure Cavities containing Shear-thinning Liquids”. In: *J. Non-Newtonian Fluid Mech.* 268, pp. 46–55. DOI: 10.1016/j.jnnfm.2019.04.001.

Xia, Y., Xu, Y., and Shu, C.-W. (2007). “Local discontinuous Galerkin methods for the Cahn–Hilliard type equations”. In: *Journal of Computational Physics* 227.1, pp. 472–491. ISSN: 00219991. DOI: 10.1016/j.jcp.2007.08.001.

Yang, L. (2013). “A physical model for liquid movement into a porous substrate under the action of a pressure pulse”. In: *Nordic Pulp and Paper Research Journal* 28.1, p. 94.

Yin, X. and Kumar, S. (2006). “Flow visualization of the liquid-emptying process in scaled-up gravure grooves and cells”. In: *Chem. Eng. Sci.* 61, pp. 1146–1156. DOI: 10.1016/j.ces.2005.07.039.

Yue, P., Zhou, C., and Feng, J. J. (2010). “Sharp-interface limit of the Cahn–Hilliard model for moving contact lines”. In: *Journal of Fluid Mechanics* 645, pp. 279–294. ISSN: 0022-1120. DOI: 10.1017/S0022112009992679.

A Appendix

A.1 Integral forms of the spatial discretization

When following the extended discontinuous Galerkin (XDG) discretization procedure as presented in Section 3.2 we finally obtain a discrete equation of the form of Eq. (4.3), Eq. (4.6) or Eq. (4.9). In this section we want to expand these abstract operators in integral form. Usually all terms independent of the solution variables are collected on the right-hand side (RHS), in the form denoted by the letter s. We deviate here a bit from this notation, to emphasize how the boundary conditions are implemented for each contribution (convective, viscous etc.) separately. In Section 2.6 the boundary conditions are written in a non-conventional form. Here we distinguish the limiting cases of Dirichlet Γ_D and Neumann Γ_N and Robin Γ_R boundaries (which may differ for energy and momentum equations) explicitly. For all three systems presented in Section 2.6 the integrals over the fluid bulk $\mathfrak{K}_h^\mathrm{X}$, inner edges Γ_int (excluding the interface) and boundaries are the same. They only differ in the implementation of the interfacial integral over Σ. If different from the interface discretization for the material two-phase flow Section 2.6.1, the interface terms used for the two-phase flow with evaporation, Section 2.6.2, will be marked in red and for the free surface flow, Section 2.6.3, in blue, completely replacing the "standard" black contribution. For shorter notation and better readability the identity $\dot{m} = (\left[\!\left[\hat{k}\nabla_h T\right]\!\right] \cdot \boldsymbol{n}^\Sigma)/\hat{h}_{vap}$ is used. I.e. $\dot{m}$ is a function of T or to be precise its gradients. In case the third (solid) phase is included in the computation the same fluxes as on boundary edges are employed on the respective interface, with the exception of the diffusive term in the heat equations, where a separate remark will be made.

A.1.1 Temporal terms

The temporal form in Eq. (4.6) can be separated in a momentum and temperature contribution:

$$m((\boldsymbol{u}, T), (\boldsymbol{v}, r)) = m_u(\boldsymbol{u}, \boldsymbol{v}) + m_T(T, r). \tag{A.1}$$

The momentum contribution m_u is exactly the temporal form used in Eq. (4.3) and Eq. (4.9), where the subindex was dropped (the same is true for all other forms we will consider). Expanded into the single contributions these forms become

$$m_u(\boldsymbol{u}, \boldsymbol{v}) = \int_{\mathfrak{K}_h^\mathrm{X}} \frac{\partial \boldsymbol{u}}{\partial t} \cdot \boldsymbol{v} \ \mathrm{d}V + \oint_{\Gamma_\mathrm{int}} 0 \ \mathrm{d}S + \oint_{\Gamma_\mathrm{D}} 0 \ \mathrm{d}S + \oint_{\Gamma_\mathrm{N}} 0 \ \mathrm{d}S + \oint_{\Gamma_\mathrm{R}} 0 \ \mathrm{d}S + \oint_{\Sigma} 0 \ \mathrm{d}S, \tag{A.2}$$

$$m_T(T, r) = \int_{\mathfrak{K}_h^\mathrm{X}} \frac{\partial T}{\partial t} \cdot r \ \mathrm{d}V + \oint_{\Gamma_\mathrm{int}} 0 \ \mathrm{d}S + \oint_{\Gamma_\mathrm{D}} 0 \ \mathrm{d}S + \oint_{\Gamma_\mathrm{N}} 0 \ \mathrm{d}S + \oint_{\Gamma_\mathrm{R}} 0 \ \mathrm{d}S + \oint_{\Sigma} 0 \ \mathrm{d}S. \tag{A.3}$$

For completeness, also integrals equating to 0 are included.

A.1.2 Convective terms

Again the combined convective form containing momentum and energy contributions can be splitted into the contributions from either equation:

$$c(\boldsymbol{u},(\boldsymbol{u},T),(\boldsymbol{v},r)) = c_u(\boldsymbol{u},(\boldsymbol{u},T),\boldsymbol{v}) + c_T(\boldsymbol{u},T,r). \tag{A.4}$$

In case evaporation is present the convective form does also depend on the temperature solution. If no evaporation is considered, i.e. the systems of Eq. (4.3) or Eq. (4.9) are used, the red terms can be ignored. The momentum contribution is implemented as

$$\begin{aligned}
c_u(\boldsymbol{u},(\boldsymbol{u},T),\boldsymbol{v}) = &\int_{\Re_h^X} -\rho\boldsymbol{u}\otimes\boldsymbol{u} : \nabla_h\boldsymbol{v} \ \mathrm{d}V + \oint_{\Gamma_{\text{int}}} \rho((\{\{\boldsymbol{u}\otimes\boldsymbol{u}\}\}\,\boldsymbol{n}^{\Gamma}) + \eta_1 [\![\boldsymbol{u}]\!])\cdot[\![\boldsymbol{v}]\!] \ \mathrm{d}S \\
&+ \oint_{\Gamma_{\text{D}}} \rho(((\frac{\boldsymbol{u}\otimes\boldsymbol{u}+\boldsymbol{s}\otimes\boldsymbol{s}}{2})\boldsymbol{n}^{\partial\Omega}) + \eta_1(\boldsymbol{u}-\boldsymbol{s}))\cdot\boldsymbol{v} \ \mathrm{d}S \\
&+ \oint_{\Gamma_{\text{N}}} \rho((\boldsymbol{u}\otimes\boldsymbol{u})\boldsymbol{n}^{\partial\Omega})\cdot\boldsymbol{v} \ \mathrm{d}S + \oint_{\Gamma_{\text{R}}} \rho(((\frac{\boldsymbol{u}\otimes\boldsymbol{u}+\boldsymbol{s}\otimes\boldsymbol{s}}{2})\boldsymbol{n}^{\partial\Omega}) + \eta_1(\boldsymbol{u}-\boldsymbol{s}))\cdot\boldsymbol{v} \ \mathrm{d}S \\
&+ \oint_{\Sigma} \rho((\{\{\boldsymbol{u}\otimes\boldsymbol{u}\}\}\,\boldsymbol{n}^{\Sigma}) + \eta_1 [\![\boldsymbol{u}]\!])\cdot[\![\boldsymbol{v}]\!] \ \mathrm{d}S \\
&+ \oint_{\Sigma} \rho((\{\{\boldsymbol{u}\otimes\boldsymbol{u}\}\}\,\boldsymbol{n}^{\Sigma}) + \eta_1([\![\boldsymbol{u}]\!] - \dot{m}\,[\![\rho^{-1}]\!]\,\boldsymbol{n}^{\Sigma}))\cdot[\![\rho\boldsymbol{v}]\!] \\
&\quad +((\{\{\boldsymbol{u}\}\}\cdot\boldsymbol{n}^{\Sigma})\dot{m}\,[\![\rho^{-1}]\!]\,\boldsymbol{n}^{\Sigma} + \{\{\boldsymbol{u}\}\}([\![\boldsymbol{u}]\!]\cdot\boldsymbol{n}^{\Sigma}))\cdot\{\{\rho\boldsymbol{v}\}\} \ \mathrm{d}S \\
&+ \oint_{\Sigma} \begin{cases} \frac{1}{2}\rho\left((\boldsymbol{u}\otimes\boldsymbol{u})\,\boldsymbol{n}^{\Sigma} + \eta_1\boldsymbol{u}\right)\cdot(\boldsymbol{v}) \\ \rho\left((\boldsymbol{u}\otimes\boldsymbol{u})\,\boldsymbol{n}^{\Sigma}\right)\cdot(\boldsymbol{v}) \quad \text{if } \beta_\Sigma \neq \infty \text{ in Eq. (2.84)} \end{cases} \mathrm{d}S,
\end{aligned} \tag{A.5}$$

following the procedure proposed in Shahbazi et al. (2007). For each edge the maximum penalty of the both neighboring cells i, j is chosen. The penalty is computed from the mean velocity $\bar{\boldsymbol{u}}$ in those cells

$$\begin{aligned}
\eta_1 &= \frac{1}{2}\max(\eta_i,\eta_j), \\
\eta_i &= 2|\bar{\boldsymbol{u}}_i\cdot\boldsymbol{n}^{\partial\Omega}|,
\end{aligned} \tag{A.6}$$

ensuring a sufficient stabilization of the convective term. For the heat equation we define

$$
\begin{aligned}
c_T(\boldsymbol{u}, T, r) = &\int_{\mathfrak{K}_h^{\mathrm{X}}} \rho \hat{c} \boldsymbol{u} \cdot \nabla_h T r \ \mathrm{d}V \\
&+ \oint_{\Gamma_{\text{int}}} -\rho \hat{c} \left(\frac{\min\left(\boldsymbol{u}^- \cdot \boldsymbol{n}^\Gamma, \boldsymbol{u}^+ \cdot \boldsymbol{n}^\Gamma\right) - \left|\min\left(\boldsymbol{u}^- \cdot \boldsymbol{n}^\Gamma, \boldsymbol{u}^+ \cdot \boldsymbol{n}^\Gamma\right)\right|}{2} r^- \right. \\
&\left. + \frac{\max\left(\boldsymbol{u}^- \cdot \boldsymbol{n}^\Gamma, \boldsymbol{u}^+ \cdot \boldsymbol{n}^\Gamma\right) + \left|\max\left(\boldsymbol{u}^- \cdot \boldsymbol{n}^\Gamma, \boldsymbol{u}^+ \cdot \boldsymbol{n}^\Gamma\right)\right|}{2} r^+ \right) [\![T]\!] \ \mathrm{d}S \\
&+ \oint_{\Gamma_{\mathrm{D}}} -\rho \hat{c} \left(\frac{\boldsymbol{u} \cdot \boldsymbol{n}^{\partial\Omega} - |\boldsymbol{u} \cdot \boldsymbol{n}^{\partial\Omega}|}{2} - \frac{\boldsymbol{u} \cdot \boldsymbol{n}^{\partial\Omega} + |\boldsymbol{u} \cdot \boldsymbol{n}^{\partial\Omega}|}{2} \right) (T - T_D) r \ \mathrm{d}S \\
&+ \oint_{\Gamma_{\mathrm{N}}} 0 \ \mathrm{d}S + \oint_{\Gamma_{\mathrm{R}}} \text{Not implemented!}^1 \ \mathrm{d}S \\
&+ \oint_{\Sigma} -\rho_{\mathfrak{A}} \hat{c}_{\mathfrak{A}} \left(\frac{\boldsymbol{u}_{\mathfrak{A}} \cdot \boldsymbol{n}^\Sigma - |\boldsymbol{u}_{\mathfrak{A}} \cdot \boldsymbol{n}^\Sigma|}{2} - \frac{\boldsymbol{u}_{\mathfrak{A}} \cdot \boldsymbol{n}^\Sigma + |\boldsymbol{u}_{\mathfrak{A}} \cdot \boldsymbol{n}^\Sigma|}{2} \right) (T_{\mathfrak{A}} - T_{sat}) r_{\mathfrak{A}} \\
&\quad - \rho_{\mathfrak{B}} \hat{c}_{\mathfrak{B}} \left(\frac{\boldsymbol{u}_{\mathfrak{B}} \cdot \boldsymbol{n}^\Sigma - |\boldsymbol{u}_{\mathfrak{B}} \cdot \boldsymbol{n}^\Sigma|}{2} - \frac{\boldsymbol{u}_{\mathfrak{B}} \cdot \boldsymbol{n}^\Sigma + |\boldsymbol{u}_{\mathfrak{B}} \cdot \boldsymbol{n}^\Sigma|}{2} \right) (T_{\mathfrak{B}} - T_{sat}) r_{\mathfrak{B}} \ \mathrm{d}S,
\end{aligned}
\tag{A.7}
$$

employing a flux similar to Cheng and Shu (2007). By using the min, max functionals in the numerical flux, the transport direction is taken into account and the convective term is stabilized analogous to an upwind formulation.

[1] To simulate while using such conditions, convection in the heat equation has to be omitted. Usually the temperature slip boundary is an impermeable wall, such that there is no convective flux through the wall though.

A.1.3 Pressure gradient and velocity divergence terms

The pressure gradient and velocity divergence are discretized using a straight-forward central flux as

$$
\begin{aligned}
b((p,T),\boldsymbol{v}) = &\int_{\mathfrak{K}_h^X} -p\nabla_h\cdot(\boldsymbol{v})\ \mathrm{d}V + \oint_{\Gamma_{\text{int}}} \{\{p\}\}\ [\![\boldsymbol{v}]\!]\cdot\boldsymbol{n}^{\Gamma}\ \mathrm{d}S \\
&+ \oint_{\Gamma_D} p\boldsymbol{v}\cdot\boldsymbol{n}^{\partial\Omega}\ \mathrm{d}S + \oint_{\Gamma_N} 0\ \mathrm{d}S + \oint_{\Gamma_R} p\boldsymbol{v}\cdot\boldsymbol{n}^{\partial\Omega}\ \mathrm{d}S \\
&+ \oint_{\Sigma} \{\{p\}\}\ [\![\boldsymbol{v}]\!]\cdot\boldsymbol{n}^{\Sigma}\ \mathrm{d}S \\
&+ \oint_{\Sigma} \begin{cases} p\left(\boldsymbol{v}\cdot\boldsymbol{n}^{\Sigma}\right) \\ 0 \quad \text{if interface is moveable } (\beta_\Sigma \neq \infty \text{ in Eq. (2.84))} \end{cases} \mathrm{d}S, \\
-b(q,(\boldsymbol{u},T)) = &\int_{\mathfrak{K}_h^X} -q\nabla_h\cdot(\boldsymbol{u})\ \mathrm{d}V + \oint_{\Gamma_{\text{int}}} \{\{q\}\}\ [\![\boldsymbol{u}]\!]\cdot\boldsymbol{n}^{\Gamma}\ \mathrm{d}S \\
&+ \oint_{\Gamma_D} q(\boldsymbol{u}-\boldsymbol{s})\cdot\boldsymbol{n}^{\partial\Omega}\ \mathrm{d}S + \oint_{\Gamma_N} 0\ \mathrm{d}S + \oint_{\Gamma_R} q(\boldsymbol{u}-\boldsymbol{s})\cdot\boldsymbol{n}^{\partial\Omega}\ \mathrm{d}S \\
&+ \oint_{\Sigma} \{\{q\}\}\ [\![\boldsymbol{u}]\!]\cdot\boldsymbol{n}^{\Sigma}\ \mathrm{d}S + \oint_{\Sigma} \{\{q\}\}\left([\![\boldsymbol{u}]\!]\cdot\boldsymbol{n}^{\Sigma} - \dot{m}\,[\![\rho^{-1}]\!]\right)\mathrm{d}S \\
&+ \oint_{\Sigma} \begin{cases} q\left(\boldsymbol{u}\cdot\boldsymbol{n}^{\Sigma}\right) \\ 0 \quad \text{if interface is moveable } (\beta_\Sigma \neq \infty \text{ in Eq. (2.84))} \end{cases} \mathrm{d}S.
\end{aligned}
\tag{A.8, A.9}
$$

A.1.4 Diffusion terms

In the momentum and heat equation a diffusive term is present:

$$
a((\boldsymbol{u},T),(\boldsymbol{v},r)) = a_u((\boldsymbol{u},T),\boldsymbol{v}) + a_T(T,r). \tag{A.10}
$$

These are discretized as

$$
\begin{aligned}
a_u((\boldsymbol{u},T),\boldsymbol{v}) = &\int_{\mathfrak{K}_h^X} \mu(\nabla_h \boldsymbol{u} + \nabla_h \boldsymbol{u}^\mathrm{T}) : \nabla_h \boldsymbol{v} \ \mathrm{d}V \\
&+ \oint_{\Gamma_\mathrm{int}} -(\{\{\mu(\nabla_h \boldsymbol{u} + \nabla_h \boldsymbol{u}^\mathrm{T})\}\}\, \boldsymbol{n}^\Gamma) \cdot [\![\boldsymbol{v}]\!] - (\{\{\mu(\nabla_h \boldsymbol{v} + \nabla_h \boldsymbol{v}^\mathrm{T})\}\}\, \boldsymbol{n}^\Gamma) \cdot [\![\boldsymbol{u}]\!] \\
&\quad + 2\eta_2 [\![\boldsymbol{u}]\!] \cdot [\![\boldsymbol{v}]\!] \ \mathrm{d}S \\
&+ \oint_{\Gamma_\mathrm{D}} -\mu((\nabla_h \boldsymbol{u} + \nabla_h \boldsymbol{u}^\mathrm{T})\boldsymbol{n}^{\partial\Omega}) \cdot \boldsymbol{v} - \mu((\nabla_h \boldsymbol{v} + \nabla_h \boldsymbol{v}^\mathrm{T})\boldsymbol{n}^{\partial\Omega}) \cdot (\boldsymbol{u} - \boldsymbol{s}) \\
&\quad + 2\eta_2 (\boldsymbol{u} - \boldsymbol{s}) \cdot \boldsymbol{v} \ \mathrm{d}S + \oint_{\Gamma_\mathrm{N}} -\boldsymbol{g}_N \cdot \boldsymbol{v} \ \mathrm{d}S \\
&+ \oint_{\Gamma_\mathrm{R}} \beta \left(\mathbf{P}^{\partial\Omega}(\boldsymbol{u} - \boldsymbol{s})\right) \cdot \left(\mathbf{P}^{\partial\Omega}\boldsymbol{v}\right) - \mu \left((\nabla_h \boldsymbol{u} + \nabla_h \boldsymbol{u}^\mathrm{T})\boldsymbol{n}^{\partial\Omega}\right) \cdot \boldsymbol{n}^{\partial\Omega} \left(\boldsymbol{v} \cdot \boldsymbol{n}^{\partial\Omega}\right) \\
&\quad - \mu \left((\nabla_h \boldsymbol{v} + \nabla_h \boldsymbol{v}^\mathrm{T})\boldsymbol{n}^{\partial\Omega}\right) \cdot \boldsymbol{n}^{\partial\Omega} \left((\boldsymbol{u} - \boldsymbol{s}) \cdot \boldsymbol{n}^{\partial\Omega}\right) \\
&\quad + 2\eta_2 \left((\boldsymbol{u} - \boldsymbol{s}) \cdot \boldsymbol{n}^{\partial\Omega}\right) \left(\boldsymbol{v} \cdot \boldsymbol{n}^{\partial\Omega}\right) \ \mathrm{d}S \\
&+ \oint_{\Sigma} -(\{\{\mu(\nabla_h \boldsymbol{u} + \nabla_h \boldsymbol{u}^\mathrm{T})\}\}\, \boldsymbol{n}^\Sigma) \cdot [\![\boldsymbol{v}]\!] - (\{\{\mu(\nabla_h \boldsymbol{v} + \nabla_h \boldsymbol{v}^\mathrm{T})\}\}\, \boldsymbol{n}^\Sigma) \cdot [\![\boldsymbol{u}]\!] \\
&\quad + \eta_2 [\![\boldsymbol{u}]\!] \cdot [\![\boldsymbol{v}]\!] \ \mathrm{d}S \\
&+ \oint_{\Sigma} -(\{\{\mu(\nabla_h \boldsymbol{u} + \nabla_h \boldsymbol{u}^\mathrm{T})\}\}\, \boldsymbol{n}^\Sigma) \cdot [\![\boldsymbol{v}]\!] - (\{\{\mu(\nabla_h \boldsymbol{v} + \nabla_h \boldsymbol{v}^\mathrm{T})\}\}\, \boldsymbol{n}^\Sigma) \cdot [\![\boldsymbol{u}]\!] \\
&\quad + \eta_2 [\![\boldsymbol{u}]\!] \cdot [\![\boldsymbol{v}]\!] + (\dot{m}\, [\![\rho^{-1}]\!]\, \boldsymbol{n}^\Sigma) \cdot (\{\{\mu(\nabla_h \boldsymbol{v} + \nabla_h \boldsymbol{v}^\mathrm{T})\}\}\, \boldsymbol{n}^\Sigma - \eta_2 [\![\boldsymbol{v}]\!]) \ \mathrm{d}S \\
&+ \oint_{\Sigma} \begin{cases} -\mu \left((\nabla_h \boldsymbol{u})\boldsymbol{n}^\Sigma\right) \cdot \boldsymbol{n}^\Sigma \left(\boldsymbol{v} \cdot \boldsymbol{n}^\Sigma\right) - \mu \left((\nabla_h \boldsymbol{v})\boldsymbol{n}^\Sigma\right) \cdot \boldsymbol{n}^\Sigma \left(\boldsymbol{u} \cdot \boldsymbol{n}^\Sigma\right) \\ +\eta_2 \left(\boldsymbol{u} \cdot \boldsymbol{n}^\Sigma\right) \left(\boldsymbol{v} \cdot \boldsymbol{n}^\Sigma\right) \\ 0 \quad \text{if interface is moveable } (\beta_\Sigma \neq \infty \text{ in Eq. (2.84)}) \end{cases} \mathrm{d}S,
\end{aligned}
\tag{A.11}
$$

and

$$
\begin{aligned}
a_T(T,r) = &\int_{\mathfrak{K}_h^X} \hat{k} \nabla_h T \cdot \nabla_h r \ \mathrm{d}V \\
&+ \oint_{\Gamma_\mathrm{int}} -\left\{\left\{\hat{k}\nabla_h T\right\}\right\} \cdot \boldsymbol{n}^\Gamma [\![r]\!] - \left\{\left\{\hat{k}\nabla_h r\right\}\right\} \cdot \boldsymbol{n}^\Gamma [\![T]\!] + \eta_3 [\![T]\!]\, [\![r]\!] \ \mathrm{d}S \\
&+ \oint_{\Gamma_\mathrm{D}} -\hat{k}\nabla_h T \cdot \boldsymbol{n}^{\partial\Omega} r - \hat{k}\nabla_h r \cdot \boldsymbol{n}^{\partial\Omega}(T - T_D) + \eta_3 (T - T_D) r \ \mathrm{d}S \\
&+ \oint_{\Gamma_\mathrm{N}} -q_N r \ \mathrm{d}S + \oint_{\Gamma_\mathrm{R}} \beta_T (T - T_D) r \ \mathrm{d}S \\
&+ \oint_{\Sigma} -\hat{k}_{\mathfrak{A}} \nabla_h T_{\mathfrak{A}} \cdot \boldsymbol{n}^\Sigma r_{\mathfrak{A}} - \hat{k}_{\mathfrak{A}} \nabla_h r_{\mathfrak{A}} \cdot \boldsymbol{n}^\Sigma (T_{\mathfrak{A}} - T_{sat}) \\
&\quad - \hat{k}_{\mathfrak{B}} \nabla_h T_{\mathfrak{B}} \cdot (-\boldsymbol{n}^\Sigma) r_{\mathfrak{B}} - \hat{k}_{\mathfrak{B}} \nabla_h r_{\mathfrak{B}} \cdot (-\boldsymbol{n}^\Sigma)(T_{\mathfrak{B}} - T_{sat}) \\
&\quad + \eta_3 (T_{\mathfrak{A}} - T_{sat}) r_{\mathfrak{A}} + \eta_3 (T_{\mathfrak{B}} - T_{sat}) r_{\mathfrak{B}} \ \mathrm{d}S \\
&+ \oint_{\Sigma} -Q^\Sigma \{\{r\}\} - \left\{\left\{\hat{k}\nabla_h T\right\}\right\} \cdot \boldsymbol{n}^\Gamma [\![r]\!] - \left\{\left\{\hat{k}\nabla_h r\right\}\right\} \cdot \boldsymbol{n}^\Gamma [\![T]\!] + \eta_3 [\![T]\!]\, [\![r]\!] \ \mathrm{d}S.
\end{aligned}
\tag{A.12}
$$

The penalties η_2, η_3 are again chosen in accordance to Shahbazi (2005), see Eq. (4.42). Note the orange interface integral in Eq. (A.12). This integral is used on the fluid-solid interface if present.

Keep in mind, that the free surface system, Section 2.6.3, does not use the transpose of the velocity gradient and potentially employs dimensionless numbers instead of material parameters. This is of course considered in the actual implementation, but not explicitly shown here, as it would unnecessarily inflate the presentation. Additionally, as the free surface system only computes one phase no averages or jumps occur on the interface, instead the values of the only active phase are used.

A.1.5 Recoil pressure

The recoil pressure $-\dot{m}\,[\![\boldsymbol{u}]\!]$, see Eq. (2.75), is the only interface contribution that is not dissolved in the forms given above. Therefore, it is included by

$$d(T,\boldsymbol{v}) = \oint_{\Sigma} -\dot{m}^2\,\left[\left[\rho^{-1}\right]\right]\boldsymbol{n}^{\Sigma}\cdot\,\{\{\boldsymbol{v}\}}\;\mathrm{d}S. \tag{A.13}$$

Note that this is a nonlinear form due to the occurrence of $\dot{m}^2$.

A.1.6 Surface tension

Usually the boundary contributions not dependent on the solution are collected in the right hand side. However, here we have written them into the differential forms on the left hand side for traceability. Thus, the right hand side only contains the surface tension force and source terms such as gravitational forces (or other volume sources):

$$\begin{aligned} s(\boldsymbol{v},q,r) = &\int_{\mathfrak{K}_h^{\mathrm{X}}} \rho\boldsymbol{g}\cdot\boldsymbol{v}\;\mathrm{d}V \\ &+\oint_{\Sigma} -\sigma\mathbf{P}^{\Sigma}:\,\{\{\nabla_{\Sigma}\boldsymbol{v}\}}\;\mathrm{d}S+\oint_{\Sigma\cap(\Gamma_{\mathrm{int}})}\sigma\,\{\{\boldsymbol{t}^{\Sigma}\}}\cdot\,[\![\,\{\{\boldsymbol{v}\}}]\!]\;\mathrm{d}l \\ &+\oint_{\Sigma\cap(\Gamma_{\mathrm{D}})}\sigma\left(\boldsymbol{n}^{\partial\Omega}\cdot\boldsymbol{t}^{\Sigma}\right)\boldsymbol{n}^{\partial\Omega}\cdot\,\{\{\boldsymbol{v}\}}\;\mathrm{d}l+\oint_{\Sigma\cap(\Gamma_{\mathrm{N}})}\sigma\boldsymbol{t}^{\Sigma}\cdot\,\{\{\boldsymbol{v}\}}\;\mathrm{d}l \\ &+\oint_{\Sigma\cap(\Gamma_{\mathrm{R}})}\left(\sigma\left(\boldsymbol{n}^{\partial\Omega}\cdot\boldsymbol{t}^{\Sigma}\right)\boldsymbol{n}^{\partial\Omega}+\sigma\cos(\theta_{\mathrm{stat}})\hat{\boldsymbol{n}}^{L}-\beta_L\left((\boldsymbol{u}^{\Sigma}-\boldsymbol{s})\cdot\hat{\boldsymbol{n}}^{L}\right)\hat{\boldsymbol{n}}^{L}\right)\cdot\,\{\{\boldsymbol{v}\}}\;\mathrm{d}l. \end{aligned} \tag{A.14}$$

These are dependent on the interface position, but not on the flow solution. The implementation uses the Laplace-Beltrami operator and surface divergence theorem, cf. Smuda (2021) and Gallot et al. (2004), and Definition 2.6. Note the occurence of the term $[\![\,\{\{\boldsymbol{v}\}}]\!]$ on the intersection of interface and inner edges. To be more specific, what is meant here is the jump (from one cell to the other) of the average (from both sides of the interface) in the test function. $\boldsymbol{t}^{\Sigma}$ is the vector that is tangential to the interface and normal to the respective edge, i.e.

$$\boldsymbol{t}^{\Sigma}=\frac{\mathbf{P}^{\Sigma}\boldsymbol{n}^{\Gamma}}{|\mathbf{P}^{\Sigma}\boldsymbol{n}^{\Gamma}|}. \tag{A.15}$$

A.2 Adapted discretization for interfacial slip

To account for the presence of slip on the interface, a few modifications to the discretization introduced in Rieckmann et al. (2023e), or Appendix A.1 respectively, are necessary. To allow slip at all, the SIP form in the viscous terms is splitted into the surface normal and tangential part. Then the tangential slip can be introduced analogous to a Neumann boundary condition:

$$\begin{aligned}\oint_\Sigma &- (\{\{\mu(\nabla_h \boldsymbol{u} + \nabla_h \boldsymbol{u}^{\mathrm{T}})\}\}\, \boldsymbol{n}^\Sigma)\cdot\boldsymbol{n}^\Sigma(\,[\![\boldsymbol{v}]\!]\cdot\boldsymbol{n}^\Sigma) - (\{\{\mu(\nabla_h \boldsymbol{v} + \nabla_h \boldsymbol{v}^{\mathrm{T}})\}\}\, \boldsymbol{n}^\Sigma)\cdot\boldsymbol{n}^\Sigma(\,[\![\boldsymbol{u}]\!]\cdot\boldsymbol{n}^\Sigma)\\ &+ \eta_2(\,[\![\boldsymbol{u}]\!]\cdot\boldsymbol{n}^\Sigma)(\,[\![\boldsymbol{v}]\!]\cdot\boldsymbol{n}^\Sigma) + (\dot{m}\,[\![\rho^{-1}]\!]\,\boldsymbol{n}^\Sigma)\cdot(\{\{\mu(\nabla_h \boldsymbol{v} + \nabla_h \boldsymbol{v}^{\mathrm{T}})\}\}\, \boldsymbol{n}^\Sigma - \eta_2\,[\![\boldsymbol{v}]\!])\\ &+\beta_\Sigma(\mathbf{P}^\Sigma\,[\![\boldsymbol{u}]\!])\cdot(\mathbf{P}^\Sigma\,[\![\boldsymbol{v}]\!])\;\mathrm{d}S.\end{aligned} \tag{A.16}$$

All additions/modifications are marked in red. As the tangential velocities are not necessarily continuous anymore the recoil pressure is not acting solely in interface normal direction. This is accounted for by introducing a tangential recoil:

$$\oint_\Sigma -\dot{m}(\dot{m}\,[\![\rho^{-1}]\!]\,\boldsymbol{n}^\Sigma + \mathbf{P}^\Sigma\,[\![\boldsymbol{u}]\!])\cdot\{\{\boldsymbol{v}\}\}\;\mathrm{d}S. \tag{A.17}$$

Finally, the original implementation of the convective term in the momentum balance implicitly enforces continuity in tangential velocity. By omitting the tangential velocity jump from the convective flux on the interface this restriction is removed. The final interface form is

$$\begin{aligned}\oint_\Sigma &((\{\{\boldsymbol{u}\otimes\boldsymbol{u}\}\}\,\boldsymbol{n}^\Sigma) + \eta_1(\,[\![\boldsymbol{u}]\!] - \dot{m}\,[\![\rho^{-1}]\!]\,\boldsymbol{n}^\Sigma))\cdot\,[\![\rho\boldsymbol{v}]\!] + ((\{\{\boldsymbol{u}\}\}\cdot\boldsymbol{n}^\Sigma)\dot{m}\,[\![\rho^{-1}]\!]\,\boldsymbol{n}^\Sigma\\ &+\{\{\boldsymbol{u}\}\}\,([\![\boldsymbol{u}]\!]\cdot\boldsymbol{n}^\Sigma))\cdot\,\{\{\rho\boldsymbol{v}\}\} - \mathbf{P}^\Sigma\,[\![\boldsymbol{u}]\!]\cdot(\eta_1\,[\![\rho\boldsymbol{v}]\!] - (\{\{\boldsymbol{u}\}\}\cdot\boldsymbol{n}^\Sigma)\,\{\{\rho\boldsymbol{v}\}\})\;\mathrm{d}S.\end{aligned} \tag{A.18}$$

In the next section these three necessary adaptions are verified with a series of testcase increasing in complexity.

A.2.1 Verification of the interfacial slip implementation

The implementation of the interfacial slip is verified with a steady plane shear flow in three stages. Firstly, a material interface is regarded. Due to the nature of the shear flow in that case all convective terms vanish. There is no heat flow present, and the only non vanishing field is the streamwise velocity. Secondly, heat flux is included and the interface is non-material. The massflux across the interfacce, paired with the slip, causes a discontinuity in the tangential stresses. The convective terms are artificially neglected, such that the fields are either constant or linear. Thirdly, convection is included. Through the coupling of the streamwise and spanwise velocities the streamwise velocity and temperature fields show exponential behavior. The pressure and spanwise velocity fields remain constant with a jump at the interface. The boundary conditions are chosen as periodic in streamwise direction. In all cases the fields are functions of the coordinate $y \in [-1, 1]$, the interface is positioned parallel to the plates at $y = 0$.

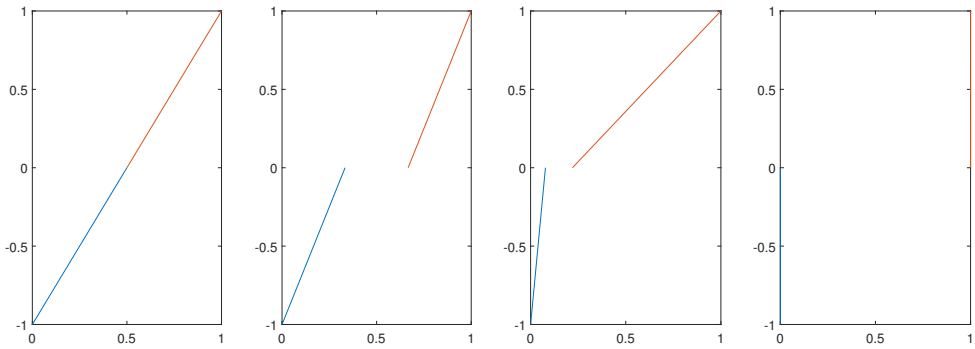

Figure A.1: Streamwise velocity for (from left to right) $\mu_{\mathfrak{A}} = 1, \mu_{\mathfrak{B}} = 1, L_\Sigma = 0$, $\mu_{\mathfrak{A}} = 1, \mu_{\mathfrak{B}} = 1, L_\Sigma = 1$, $\mu_{\mathfrak{A}} = 1, \mu_{\mathfrak{B}} = 0.1, L_\Sigma = 1$, $\mu_{\mathfrak{A}} = 1, \mu_{\mathfrak{B}} = 0.11, L_\Sigma = \infty$

Case 1 : Material interface, no convection For this case the lower plate is stationary and the upper plate moves with a fixed velocity. On both plates no-slip conditions are imposed:

$$\boldsymbol{u}_{\mathfrak{A}}(-1) = (0,0)^T, \tag{A.19a}$$
$$\boldsymbol{u}_{\mathfrak{B}}(1) = (1,0)^T. \tag{A.19b}$$

The reduced system

$$\nabla \cdot (\boldsymbol{u}) = 0, \tag{A.20a}$$
$$0 = -\nabla p + \mu \nabla \cdot \left(\nabla \boldsymbol{u} + \nabla \boldsymbol{u}^{\mathrm{T}}\right), \tag{A.20b}$$

is solved. Taking into account the slip length L_Σ the solution is:

$$p_{\mathfrak{A}}(y) = 0, \tag{A.21a}$$
$$p_{\mathfrak{B}}(y) = 0, \tag{A.21b}$$
$$\boldsymbol{u}_{\mathfrak{A}}(y) = \left(\frac{\mu_{\mathfrak{B}}(\mu_{\mathfrak{A}} + \mu_{\mathfrak{B}})}{\mu_{\mathfrak{A}}\mu_{\mathfrak{B}} + \mu_{\mathfrak{A}}^2 + \mu_{\mathfrak{B}}^2 + 2L_\Sigma \mu_{\mathfrak{A}}\mu_{\mathfrak{B}}}(y+1), 0\right)^T, \tag{A.21c}$$
$$\boldsymbol{u}_{\mathfrak{B}}(y) = \left(\frac{\mu_{\mathfrak{A}}(\mu_{\mathfrak{A}} + \mu_{\mathfrak{B}})}{\mu_{\mathfrak{A}}\mu_{\mathfrak{B}} + \mu_{\mathfrak{A}}^2 + \mu_{\mathfrak{B}}^2 + 2L_\Sigma \mu_{\mathfrak{A}}\mu_{\mathfrak{B}}} y + \frac{\mu_{\mathfrak{B}}(\mu_{\mathfrak{A}} + \mu_{\mathfrak{B}} + 2L_\Sigma \mu_{\mathfrak{A}})}{\mu_{\mathfrak{A}}\mu_{\mathfrak{B}} + \mu_{\mathfrak{A}}^2 + \mu_{\mathfrak{B}}^2 + 2L_\Sigma \mu_{\mathfrak{A}}\mu_{\mathfrak{B}}}, 0\right)^T. \tag{A.21d}$$

Figure A.1 shows a sample of the streamwise velocity for different viscosities and slip lengths.

Case 2 : Non-Material interface, no convection Compared to the first case transpiation is added on the lower wall, while the upper wall is substituted for a Neumann boundary condition:

$$\boldsymbol{u}_{\mathfrak{A}}(-1) = (0, \frac{\dot{m}}{\rho_{\mathfrak{A}}})^T, \tag{A.22a}$$
$$(-p_{\mathfrak{B}}(1)\mathbf{I} + \mu_{\mathfrak{B}}(\nabla \boldsymbol{u}_{\mathfrak{B}}(1) + \nabla \boldsymbol{u}_{\mathfrak{B}}{}^{\mathrm{T}}(1)))(\boldsymbol{n}^{\partial\Omega}) = (\mu_{\mathfrak{B}}\dot{\gamma}, 0)^T = (\frac{1}{2}\mu_{\mathfrak{B}} e^{-L_\Sigma}, 0)^T, \tag{A.22b}$$
$$\hat{k}_{\mathfrak{A}} \nabla T(0) \cdot \boldsymbol{n}^{\partial\Omega} = \dot{m}\hat{h}_{vap}, \tag{A.22c}$$
$$T_{\mathfrak{B}}(1) = 0. \tag{A.22d}$$

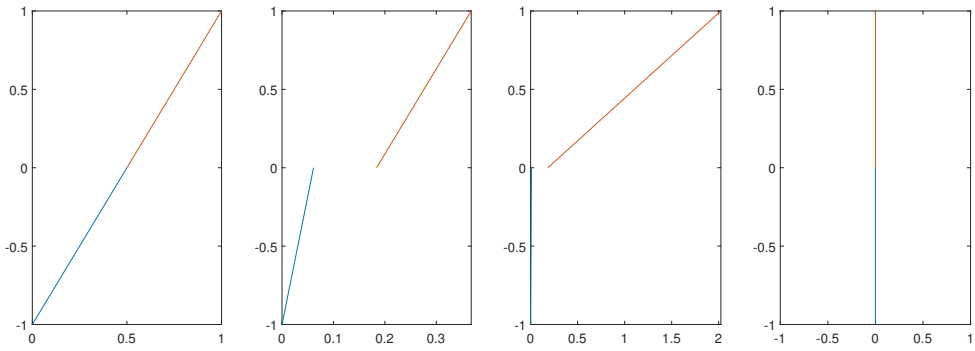

Figure A.2: Streamwise velocity for (from left to right) $\mu_{\mathfrak{A}} = 1, \mu_{\mathfrak{B}} = 1, L_\Sigma = 0, \dot{m} = 1$, $\mu_{\mathfrak{A}} = 1, \mu_{\mathfrak{B}} = 1, L_\Sigma = 1, \dot{m} = 1$, $\mu_{\mathfrak{A}} = 1, \mu_7 = 0.1, L_\Sigma = 1, \dot{m} = 1$, $\mu_{\mathfrak{A}} = 1, \mu_{\mathfrak{B}} = 0.11, L_\Sigma = \infty, \dot{m} = 1$

Remark on the temperature boundary condition. In the implementation of the testcase due to the absence of convection the heatflux is prescribed not at the interface, but on the lower boundary. Now the system

$$\nabla \cdot (\boldsymbol{u}) = 0, \tag{A.23a}$$

$$0 = -\nabla p + \mu \nabla \cdot \left(\nabla \boldsymbol{u} + \nabla \boldsymbol{u}^{\mathrm{T}}\right), \tag{A.23b}$$

$$0 = \hat{k} \nabla \cdot (\nabla T) \tag{A.23c}$$

is solved. Apart from viscosity the following material parameters are used, i.e., $\rho_{\mathfrak{A}} = 1000, \rho_{\mathfrak{B}} = 1.2$, $\hat{c}_{\mathfrak{A}} = 2.5, \hat{c}_{\mathfrak{B}} = 1.85$, $\hat{k}_{\mathfrak{A}} = 0.6, \hat{k}_{\mathfrak{B}} = 0.02$ and $\hat{h}_{vap} = 12000$. Taking into account the slip length L_Σ and massflux $\dot{m}$ the solution is:

$$p_{\mathfrak{A}}(y) = -\dot{m}^2 \left(\frac{1}{\rho_{\mathfrak{A}}} - \frac{1}{\rho_{\mathfrak{B}}}\right), \tag{A.24a}$$

$$p_{\mathfrak{B}}(y) = 0, \tag{A.24b}$$

$$\boldsymbol{u}_{\mathfrak{A}}(y) = \left(\dot{\gamma} \frac{\mu_{\mathfrak{B}}(\mu_{\mathfrak{A}} + \mu_{\mathfrak{B}} - \dot{m} L_\Sigma)}{\mu_{\mathfrak{A}}\mu_{\mathfrak{B}} + \mu_{\mathfrak{A}}^2 + L_\Sigma \dot{m} \mu_{\mathfrak{A}}} (y+1), \frac{\dot{m}}{\rho_{\mathfrak{A}}}\right)^T, \tag{A.24c}$$

$$\boldsymbol{u}_{\mathfrak{B}}(y) = \left(\dot{\gamma} y + \dot{\gamma} \frac{\mu_{\mathfrak{B}}(\mu_{\mathfrak{A}} + \mu_{\mathfrak{B}} - \dot{m} L_\Sigma + 2 L_\Sigma \mu_{\mathfrak{A}})}{\mu_{\mathfrak{A}}\mu_{\mathfrak{B}} + \mu_{\mathfrak{A}}^2 + L_\Sigma \dot{m} \mu_{\mathfrak{A}}}, \frac{\dot{m}}{\rho_{\mathfrak{B}}}\right)^T, \tag{A.24d}$$

$$T_{\mathfrak{A}}(y) = -\frac{\dot{m} \hat{h}_{vap}}{\hat{k}_{\mathfrak{A}}} y, \tag{A.24e}$$

$$T_{\mathfrak{B}}(y) = 0. \tag{A.24f}$$

Figure A.2 shows a sample of the streamwise velocity for different viscosities and slip lengths.

Case 3 : Non-Material interface, convection In the last testcase the convective terms are included. The same boundary conditions as in case 2 are used:

$$\boldsymbol{u}_{\mathfrak{A}}(-1) = (0, \frac{\dot{m}}{\rho_{\mathfrak{A}}})^T, \tag{A.25a}$$

$$(-p_{\mathfrak{B}}(1)\mathbf{I} + \mu_{\mathfrak{B}}(\nabla \boldsymbol{u}_{\mathfrak{B}}(1) + \nabla \boldsymbol{u}_{\mathfrak{B}}{}^{\mathrm{T}}(1)))(\boldsymbol{n}^{\partial\Omega}) = (\mu_{\mathfrak{B}}\dot{\gamma}, 0)^T = (\frac{1}{2}\mu_{\mathfrak{B}}e^{-L_\Sigma}, 0)^T, \tag{A.25b}$$

$$\hat{k}_{\mathfrak{A}}\nabla T(0) \cdot \boldsymbol{n}^{\partial\Omega} = \dot{m}\hat{h}_{vap}, \tag{A.25c}$$

$$T_{\mathfrak{B}}(1) = 0. \tag{A.25d}$$

For the implementation instead of a heat flux the temperature on the lower boundary, according to the analytical solution presented here, is prescribed. The final system is then

$$\nabla \cdot (\boldsymbol{u}) = 0, \tag{A.26a}$$

$$\rho \boldsymbol{u} \cdot \nabla \boldsymbol{u} = -\nabla p + \mu \nabla \cdot \left(\nabla \boldsymbol{u} + \nabla \boldsymbol{u}^{\mathrm{T}}\right), \tag{A.26b}$$

$$\rho \hat{c} \boldsymbol{u} \cdot \nabla T = \hat{k} \nabla \cdot (\nabla T). \tag{A.26c}$$

The material parameters remain unchanged from case 2. The solution in streamwise velocity and the temperature field is then, due to the superposed spanwise velocity, not linear in y anymore, but shows exponential behavior:

$$p_{\mathfrak{A}}(y) = -\dot{m}^2(\frac{1}{\rho_{\mathfrak{A}}} - \frac{1}{\rho_{\mathfrak{B}}}), \tag{A.27a}$$

$$p_{\mathfrak{B}}(y) = 0, \tag{A.27b}$$

$$\begin{aligned}\boldsymbol{u}_{\mathfrak{A}}(y) = \Bigg(&\dot{\gamma}\mu_{\mathfrak{B}}e^{-\frac{\dot{m}}{\mu_{\mathfrak{B}}}}\frac{\mu_{\mathfrak{A}} + \mu_{\mathfrak{B}} - \dot{m}L_\Sigma}{\dot{m}(\mu_{\mathfrak{A}} + \mu_{\mathfrak{B}} + \dot{m}L_\Sigma)}e^{\frac{\dot{m}}{\mu_{\mathfrak{A}}}y}, \\ &+ \dot{\gamma}\mu_{\mathfrak{B}}e^{-\frac{\dot{m}}{\mu_{\mathfrak{A}}}}e^{-\frac{\dot{m}}{\mu_{\mathfrak{B}}}}\frac{\mu_{\mathfrak{A}} + \mu_{\mathfrak{B}} - \dot{m}L_\Sigma}{\dot{m}(\mu_{\mathfrak{A}} + \mu_{\mathfrak{B}} + \dot{m}L_\Sigma)}, \frac{\dot{m}}{\rho_{\mathfrak{A}}}\Bigg)^T,\end{aligned} \tag{A.27c}$$

$$\boldsymbol{u}_{\mathfrak{B}}(y) = \left(\dot{\gamma}\mu_{\mathfrak{B}}e^{-\frac{\dot{m}}{\mu_{\mathfrak{B}}}}\frac{1}{\dot{m}}e^{\frac{\dot{m}}{\mu_{\mathfrak{B}}}y} - \dot{\gamma}\mu_{\mathfrak{B}}e^{-\frac{\dot{m}}{\mu_{\mathfrak{A}}}}e^{-\frac{\dot{m}}{\mu_{\mathfrak{B}}}}\frac{\mu_{\mathfrak{A}} + \mu_{\mathfrak{B}} - \dot{m}L_\Sigma}{\dot{m}(\mu_{\mathfrak{A}} + \mu_{\mathfrak{B}} + \dot{m}L_\Sigma)}, \frac{\dot{m}}{\rho_{\mathfrak{B}}}\right)^T, \tag{A.27d}$$

$$T_{\mathfrak{A}}(y) = -\frac{\hat{h}_{vap}}{\hat{c}_{\mathfrak{A}}}e^{\frac{\dot{m}\hat{c}_{\mathfrak{A}}}{\hat{k}_{\mathfrak{A}}}y} + \frac{\hat{h}_{vap}}{\hat{c}_{\mathfrak{A}}}, \tag{A.27e}$$

$$T_{\mathfrak{B}}(y) = 0. \tag{A.27f}$$

Figure A.3 shows a sample of the streamwise velocity for different viscosities and slip lengths.

A.2.2 Sensitivity of temperature boundary condition

In Section 6.3 the sensitivity of XDG results w.r.t. the smoothness of boundary conditions and exact solutions is discussed. While preparing the simulations presented in Section 7.2.2 it became evident that these considerations were especially relevant for the studies performed there. Initially an attempt was made to prescribe a simple sine profile on the lower wall in Fig. 7.12. However, it was noted that special care has to be taken to prescribe a temperature boundary condition corresponding to a smooth solution to the Poisson problem inside the droplet and obtain a high

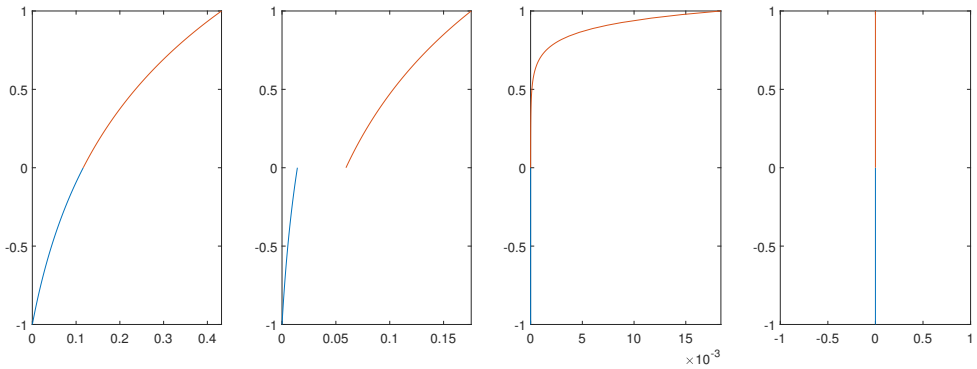

Figure A.3: Streamwise velocity for (from left to right) $\mu_{\mathfrak{A}} = 1, \mu_{\mathfrak{B}} = 1, L_\Sigma = 0, \dot{m} = 1$, $\mu_{\mathfrak{A}} = 1, \mu_{\mathfrak{B}} = 1, L_\Sigma = 1, \dot{m} = 1$, $\mu_{\mathfrak{A}} = 1, \mu_{\mathfrak{B}} = 0.1, L_\Sigma = 1, \dot{m} = 1$, $\mu_{\mathfrak{A}} = 1, \mu_{\mathfrak{B}} = 0.11, L_\Sigma = \infty, \dot{m} = 1$

EOC. To this end the solution to the Poisson problem inside a circle according to Polyanin (2015, p. 788) is considered. The solution for the temperature is given by the convolution

$$T(r,\varphi) = \frac{1}{2\pi}\int_0^{2\pi} f(\psi)\frac{R^2 - r^2}{r^2 - 2Rrcos(\varphi - \psi) + R^2}\, d\psi. \tag{A.28}$$

The function $f(\psi)$ corresponds to the temperature prescribed on the boundary of the circle at $r = R$. For this the piecewise function

$$f(\psi) = \begin{cases} 6(\frac{\psi-1.15\pi}{0.1\pi})^5 - 15(\frac{\psi-1.15\pi}{0.1\pi})^4 + 10(\frac{\psi-1.15\pi}{0.1\pi})^3 & 1.15\pi < \psi < 1.25\pi \\ 1 - 6(\frac{\psi-1.25\pi}{0.1\pi})^5 - 15(\frac{\psi-1.25\pi}{0.1\pi})^4 + 10(\frac{\psi-1.25\pi}{0.1\pi})^3 & 1.25\pi < \psi < 1.35\pi \\ -6(\frac{\psi-1.65\pi}{0.1\pi})^5 - 15(\frac{\psi-1.65\pi}{0.1\pi})^4 + 10(\frac{\psi-1.65\pi}{0.1\pi})^3 & 1.65\pi < \psi < 1.75\pi \\ -1 + 6(\frac{\psi-1.75\pi}{0.1\pi})^5 - 15(\frac{\psi-1.75\pi}{0.1\pi})^4 + 10(\frac{\psi-1.75\pi}{0.1\pi})^3 & 1.75\pi < \psi < 1.85\pi \\ 0 \quad \text{else} \end{cases} \tag{A.29}$$

is chosen. This function is C^∞ and ensures saturation temperature $T_{sat} = 0$ along the boundary of the circle in the positive half plane, as is the case in the testcases of Section 7.2. Various functions were tested beforehand, giving different EOC when applied in the actual setup. Therefore, this choice is somewhat arbitrary but complies with all the necessary conditions. These are saturation temperature at the interface, a non-zero heat flux at the contact line, vanishing total heat flux and a smooth solution for the temperature inside the droplet. To obtain the boundary condition on the lower wall for the testcases considered in this work, Eq. (A.28) is evaluated at $-y_0$ and mapped to cartesian coordinates. Finally x is rescaled using x_0, cf. Section 7.2.2, and the temperature such that the extremal values are ± 1, giving the shape displayed in Fig. 7.11.